



Kent Academic Repository

Avdellidou, Chrysoula (2016) *Hypervelocity impacts in the Solar System: An experimental investigation on the fate of the impactor*. Doctor of Philosophy (PhD) thesis, University of Kent, CAPS.

Downloaded from

<https://kar.kent.ac.uk/54994/> The University of Kent's Academic Repository KAR

The version of record is available from

This document version

UNSPECIFIED

DOI for this version

Licence for this version

UNSPECIFIED

Additional information

Versions of research works

Versions of Record

If this version is the version of record, it is the same as the published version available on the publisher's web site. Cite as the published version.

Author Accepted Manuscripts

If this document is identified as the Author Accepted Manuscript it is the version after peer review but before type setting, copy editing or publisher branding. Cite as Surname, Initial. (Year) 'Title of article'. To be published in *Title of Journal*, Volume and issue numbers [peer-reviewed accepted version]. Available at: DOI or URL (Accessed: date).

Enquiries

If you have questions about this document contact ResearchSupport@kent.ac.uk. Please include the URL of the record in KAR. If you believe that your, or a third party's rights have been compromised through this document please see our [Take Down policy](https://www.kent.ac.uk/guides/kar-the-kent-academic-repository#policies) (available from <https://www.kent.ac.uk/guides/kar-the-kent-academic-repository#policies>).

*Hypervelocity impacts in the Solar System: An
experimental investigation on the fate of the
impactor.*

by

Chrysoula Avdellidou

Thesis for the degree of Doctor of Philosophy



Centre for Astrophysics and Planetary Science

School of Physical Sciences

University of Kent

April 2016

To Marco, the best astronomer

Declarations

The content herein was composed by the author, and has not been submitted for that purposes of a qualification at any other institution or for any other degree.

The content of Chapter 3 and a part of the content of Chapter 4 has already been published as Avdellidou et al. (2016) in *Monthly Notices of the Royal Astronomical Society (MNRAS)* and therefore is adopted and expanded in this thesis.

The rest of the Chapter 4 is going to be submitted by Avdellidou et al. (in preparation) as another contribution in *Monthly Notices of the Astronomical Society (MNRAS)*.

The results of Chapter 4 that are based on the hydro-code simulations, were primarily done by author's advisor, *Dr. M.C. Price*, and were included in the Avdellidou et al. (2016).

The Main Belt Asteroid catalogue used in Chapter 5 was constructed and provided by *Dr. Marco Delbo'* from Observatoire de la Côte d'Azur. Part of the Chapter 5 consists of preliminary results and will be included in a future work in collaboration with *Dr. Marco Delbo'*.

Abstract

Collisions is one of the most important processes in the Solar System that have played a significant role in its evolution for 4.5 Gy. They are responsible for the formation of asteroid families, craters and regolith production on bodies surfaces. Moreover they pose a hazard for our planet's environment, human civilisation and space assets. Impacts have shaped the asteroids and their surfaces and recently there are indications that they are also responsible for the creation of multi-lithology asteroids. The effectiveness of this process lies, apart from the collisional speed and angle, on the physical parameters of both the target and the impactor. A plethora of laboratory experiments are devoted to study the outcome of impacts, from low speeds of a few m/s to greater speeds of several km/s. In addition space missions; such as Deep Impact (NASA) in the past and AIDA (ESA/NASA) hopefully in the near future, are aiming to perform hyper-velocity impact experiments at large scales. Although there is advance in our understanding of crater formation, target fragmentation and ejecta speeds, however the fate of the impactor is still very poorly constrained. Experiments so far were focused using materials not directly relevant to the composition of asteroids.

We start an investigation for the impactors' fate, by using lithological projectiles that impacted three different types of targets with different material and bulk porosities. For this experimental campaign was used the Light Gas Gun (LGG) of the Impact Group at the University of Kent. The study was focused on three main topics: i) the fragmentation of the impactor, ii) the implantation of exogenous material onto the target and iii) the inspection of the final state of the projectile.

This Thesis is divided in six Chapters. The first two, Chapters 1 and 2, are giving a review of recent advances of small bodies studies, the importance of collisions in the Solar System, and a brief description of the laboratory impact experiments, providing the current state of research on the fate of projectiles. Some open questions lead to the explanation of the aim of this study. In Chapter 3 are described the series of experiments performed, explaining the analysis methods were developed and the way that the main topics of fragmentation, implantation and characterisation of the impactor were studied. All the results for each one of these topics, along with the difficulties during the experimental procedure are provided in Chapter 4. In Chapter 5 we discuss the results giving the implications, attempting to place the outcome in the big picture of the small bodies collisions. In the last Chapter 6 there is a summary of this work, providing also possible future ideas for the continuation of this study.

Acknowledgements

There is a series of circumstances and people that helped to fulfil this Doctoral Thesis. First of all I would like to thank my parents for all the financial and psychological support during all these years that I am living abroad. That was the most essential aspect in order to complete my work. Everything started at my previous University in Greece, where *Profs. J. H. Seiradakis* and *K. Tsiganis*, gave me the opportunity to work on asteroid observations, a very different project compared to the previous they allocated to students. Therefore my appreciation for them is enormous. In turn, I would like to thank my current supervisor *Dr. Mark C. Price*, for trusting and giving me the opportunity to step in the field of laboratory experiments. Due to his constant help and support I managed, in almost a year, to complete all the laboratory work and analysis of my results. In addition I would like to thank *Mr. Mike Cole*, the laboratory experimental officer, who did always his best to prepare successfully the shots for my project and advised carefully whenever I had a problem in experiments. Moreover, *Prof. Michael Smith*, was the key person who actually helped for my transition into the laboratory work, trusted me to write the big grant application for our Beacon Observatory, which we finally obtained and suggested me as the *Best Physics PhD student for 2015*, a title that I finally obtained.

During these years two very important people helped and advised me on any topic I had to deal with; relevant to Physics and programming. Even when they had different point of view and we argued, they always tried the best for me, no matter the amount of time they had to spend. These precious friends and colleagues are *Dr. Timothy Kinnear* and *Dr. Panos Ioannidis*, the Python gurus.

I would like to thank my super girls *Morena Pappalardo*, *Evi Paraschou* and *Rebecca Lindsay* for just being there, like rocks (although they are beautiful flowers), by my side on everything that I was doing. Thank you so much, you are my family!

I was so lucky to meet (again), in the middle of my studies, my amazing man who was the one who believed so much to me and proposed the topic of research that this Thesis is based on. He is the source of inspiration and my motivation on everything I do until this very moment. He is with me, every minute of the day, always patient, helping with his unique way, although he leaves thousands of kilometres away. He is the most intelligent person I have ever met and a great astronomer, trying to answer the big questions of our Solar System. *Dr. Marco Delbo*, my love and admiral for you is beyond words. I wish one day to be like you. Thank you.

Contents

Declarations	iii
Abstract	iv
Acknowledgements	v
1 Introduction	1
1.1 Small Bodies in the Solar System	3
1.1.1 Main Belt Asteroids	4
1.1.2 Main Reservoirs of Icy Bodies	11
1.1.3 A quick overview	21
1.2 Collisions in the Solar System	21
1.2.1 Formation of Families of Small Bodies	21
1.2.2 Cratering and Regolith Production	23
1.2.3 Linking meteorites with their parent asteroidal bodies	27
1.2.4 Impacts as Drivers for Life	28
1.2.5 Impacts as a Hazard for Life and Space Assets	30
1.3 Approaches to Physics of Collisions	32
1.3.1 Laboratory Impact Experiments	34
1.3.2 Relevance of Space Missions and Large Scale Experiments to Impacts	35
1.4 Thesis Overview	38
2 The State of the Impactor after Hypervelocity Collisions	40
2.1 Introduction to the Problem	40
2.1.1 Exogenous Material on Asteroids	41
2.1.2 Multi-lithology Meteorites from Multi-Lithology Asteroids?	45
2.2 Open questions	47
2.3 Current Status of Experimental Research	48
2.4 Aim of the Study	51

3	Survival of the Impactor in Hypervelocity Impacts:	
	An Experimental Approach	52
3.1	Projectile and Target Materials	54
	3.1.1 Projectiles	54
	3.1.2 Targets	57
3.2	Experimental Protocol	62
	3.2.1 The Light-Gas Gun	63
	3.2.2 Experimental Setup	65
3.3	Data Analysis Methods and Tools	67
	3.3.1 Analysis Devices	67
	3.3.2 Analysis 1: Projectile Fragmentation–Largest recovered fragment and SFDs of ejecta	70
	3.3.3 Analysis 2: Implantation on Target	80
	3.3.4 Analysis 3: Final State of the Projectile	81
4	Experimental Results:	
	Fragmentation, Implantation and Final State of the Projectile	83
4.1	Projectile Fragmentation	84
	4.1.1 Low porosity targets	84
	4.1.2 High porosity targets	91
	4.1.3 Summary	94
4.2	Projectile Implantation in the Target	100
	4.2.1 Low porosity targets	101
	4.2.2 High porosity targets	101
	4.2.3 Summary	105
4.3	The Final State of the Projectile	106
	4.3.1 Raman Spectra	106
	4.3.2 Additional Hydro-Code Simulations	116
	4.3.3 Summary	117
4.4	Complications encountered in the experimental programme	119
	4.4.1 Impact speed limit	119
	4.4.2 Missing Basalt Shots	121
	4.4.3 Contamination of the targets	122
	4.4.4 Summary	125
5	Contextual Overview	128
5.1	Discussion of the Results	128
5.2	Implications for Asteroid Collisions	139
	5.2.1 Porosity of Asteroids	139
	5.2.2 How Does Porosity Affect the Outcome of Asteroid Collisions?	143
5.3	Can we Make a Multi-Lithology Body?	147

5.4	Summary	151
6	Conclusions	156
6.1	Summary of the work	157
6.2	Thoughts for future work	160
A	Appendix	173
A.0.1	Conversion of BTM to FITS files	173
A.0.2	Photometry routine of fragments	174
A.0.3	Flags of Source Extractor (SExtractor v2.13 User's Manual)	176
A.0.4	Identification of Raman spectra peaks P_1 and P_2	177
B	Appendix	179
B.0.5	Fragmentation: Run#2 (with $z = \times 150$)	180
B.0.6	Fragmentation: Run#2 (with $z = \times 300$)	188
B.0.7	Fragmentation: Run#3	195
B.0.8	Raman spectra: Run#1	201
B.0.9	Raman spectra: Run#2	213
B.0.10	Raman spectra: Run#3	218
C	Appendix	222
C.0.11	List of Publications	222
C.1	<i>Attached paper: Avdellidou et al. 2016 (MNRAS)</i>	223
C.2	<i>Attached paper: Ioannidis et al. 2014 (A&A)</i>	232

List of Figures

1.1	Main areas of small bodies in the Solar System. Due to the logarithmic scale of the diagram the orbits of the Mercury, Venus and Mars are not indicated. Modified image from Michele Serrano.	3
1.2	Spectra signatures of the three main complexes and End Members. Image modified from DeMeo et al. (2009).	6
1.3	As NASA's Dawn spacecraft was approaching the asteroid (1) Ceres bright spots in the Occator crater were revealed. Images modified from NASA (2016).	11
1.4	Estimated macroporosities of 32 small bodies according to studies by (Britt et al. 2006). It is a clear demonstration that the average macroporosity of the C-type asteroids is larger than S-types. Moreover, the most massive small bodies are more coherent, indicating that they were not fractured by impacts, but kept their primitive structure and survived the evolution of the Solar System.	15
1.5	D/H ratio of several small bodies in comparison with Earth's ratio. Image adapted from Hartogh et al. (2011).	20
1.6	Left panel: In yellow are plotted the families in contrast to the background population in red. Right panel: A sample of 25,000 asteroids observed from SDSS and WISE are plotted in different colours indicating their albedo differences between the different families. Image from Nesvorny et al. (2015).	22
1.7	Images of regolith covered surfaces of several asteroids. (a) Image of asteroid (21) Lutetia taken from Rosetta spacecraft. (b)Image of asteroid (4) Vesta from the Dawn space mission. (c) Image of asteroid (433) Eros from NEAR-Shoemaker mission and (d) of asteroid (25143) Itokawa from Hayabusa mission.	24

1.8	Size distribution of NEAs above a specific absolute magnitude. The line of circles represents the estimated total population, while the solid line is the observed one to 2014. The calculation of the size from the absolute magnitude is done by assuming an albedo of $p_V = 0.14$. For each size is calculated the impact energy along with the impact probability for an object with a given diameter and larger. Image adapted and modified from Harris et al. (2015).	26
1.9	Classification of the meteorite types. Figure adapted and modified from Weisberg et al. (2006).	29
1.10	Images from the Deep Impact spacecraft flyby to the comet 9P/Tempel 1 at different times: a) prior to the impact, b) soon after and, c) later showing the impact ejecta plume development Richardson & Melosh (2013).	37
1.11	The concept of the AIDA space mission from ESA (2016).	38
2.1	Images takes from NASA's Dawn space mission to asteroid (4) Vesta (2011–2012), revealing dark material inside (a) and around (b) impact craters as well as on the top of 'hills' (c). Images from NASA (2016). .	42
2.2	Images of the so-called 'Black Boulder' on asteroid (25143) Itokawa, taken from JAXA's Hayabusa space mission (Hirata & Ishiguro 2011). .	44
2.3	Images taken by the Rosetta space mission during the fly-by to asteroid (21) Lutetia, showing (a) the geological variability map of the asteroid's surface and (b) the Baetica crater cluster. The black dot in (a) denotes the north pole of the asteroid. The Baetica region is the youngest area on the asteroid's surface. Images taken from Thomas et al. (2012) and Schröder et al. (2015).	45
3.1	The experimental set-up, used for the icy (a) and regolith-like (b) targets, showing the projectile, which was placed inside a sabot (isoplast cylinder to hold the projectile at the beginning of the launch), inside the two-stage LGG, and the configuration of the target chamber (Avdellidou et al. 2016). The projectile impacts the target at 0° with respect to its trajectory (dashed line). The ejecta collection funnel (a) was aligned with the flight path of the projectile and the centre of the target. It contained water-ice layers in order to collect the projectile's debris after the impact. For the regolith shots a plastic tube was used to capture all the ejecta with no extra coating (b).	53
3.2	Front (a) and back (b) side of peridots and spherical (c) basalt projectiles that were used for this work. (Image credit: Taken by author.)	56

3.3	The three different targets that were used in the experiments we made of a) solid water ice with porosity <10%, b) crushed water ice with porosity $\sim 40\%$ and c) CaCO_3 powder with porosity $\sim 70\%$. (Image credit: Taken by author.)	58
3.4	The liquid nitrogen freezer in the Impact Lab where the targets were frozen down to -130°C before each shot. Image credit: Taken by author.	59
3.5	For Run#2 the icy target was prepared by spraying high purity water into liquid nitrogen. Image credit: Taken by author.	60
3.6	The projectile is placed inside a sabot. During flight, the four quarters of the sabot are removed by centripetal forces and only the projectile reaches the target.	64
3.7	The two-stage Light Gas Gun of the Impact Group, University of Kent. Image credit: Impact Lab.	65
3.8	For Run#1 and Run#2 a plastic funnel with an internal water-ice internal coating was used to capture the ejecta, for Run#3 the funnel was replaced with a plastic transparent tube that covered the whole length of the chamber.	66
3.9	(a) The Raman spectrometer and (b) the SEM of the University of Kent. Image credit: Impact Lab	68
3.10	After each shot the melt water (Run#1) or the solution (Run#3) was filtered through PTFE filters with hole sizes $0.1\text{--}5\ \mu\text{m}$. Image credit: Taken by the author.	70
3.11	(a) The background Bremsstrahlung radiation measured using a blank filter and the (b) superimposed X-ray lines using a filter with material from ejecta and gun debris. The red solid line indicates the area of Mg in the energy spectrum. The X-ray lines of C and F correspond to the PTFE filter that was used in both cases. Both were point spectra. . . .	73
3.12	Comparison between aperture and ISO photometry method with SExtractor. In the first case it identifies the centre of the light source analysing the pixels which are enclosed in the circle, product of the FWHM of the source. In the second case it analyses all the illuminated pixels of the light source according to area and pixel value thresholds that the user sets (e.g. in this example ISO leaves out the light grey pixels as their value is lower than the set threshold) (Bertin & Arnouts 1996).	76

3.13	BSE image showing that the fragments of the projectile are mixed with other material from the gun (a). As the projectile is Mg-rich it gives a strong signal in Mg X-ray maps (b). Considering also that there are no other sources of Mg contamination, these maps are used as the main dataset for the analysis. SExtractor identifies each fragment and reproduces another image containing only the pixels which contain information according to the given threshold (c). Images taken from Avdellidou et al. (2016).	79
4.1	Differential (top) and cumulative (bottom) SFD of ejecta fragments of indicative shots in Run#1 (magnification $\times 300$), showing no significant change, apart from the 0.60 km/s shot, with increasing speed (Avdellidou et al. 2016). The red dashed lines indicate the threshold range of the detection limit.	88
4.2	Mass ratio of the largest surviving fragment of the impactor versus the energy density, Q_{im} , for speed ranges 0.38–2.71 km/s and 1.49–3.03 km/s for olivine and basalt respectively in Run#1. The dashed lines correspond to the best-fitting curves using Eq.4.1 (Avdellidou et al. 2016).	90
4.3	Differential (top) and cumulative (bottom) SFD of the ejecta fragments of indicative shots in Run#2 (magnification $\times 150$), showing no significant change with increasing speed, apart from the impact speed at 1.33 km/s that appears shallower (Avdellidou et al. in prep.). The red dashed lines indicate the threshold range of the detection limit.	96
4.4	Differential (top) and cumulative (bottom) SFD of the ejecta fragments of indicative shots in Run#2 (magnification $\times 300$), showing no significant change with increasing speed (Avdellidou et al. in prep.). The red dashed lines indicate the threshold range of the detection limit.	97
4.5	Differential (top) and cumulative (bottom) SFD of the ejecta fragments of indicative shots of Run#3 (magnification $\times 100$), showing no significant change with increasing speed, except the distribution at 1.25 km/s that appears to be steeper (Avdellidou et al. in prep.). The red dashed lines indicate the threshold range of the detection limit.	98
4.6	Mass ratio of the largest surviving peridot fragment of the impactor versus the energy density, Q_{im} and the impact velocity, v , using data from Run#2 and Run#3 (Avdellidou et al. in prep.). The dashed lines correspond to the best-fitting curves using Eq.4.1 ((Avdellidou et al. 2016)).	99
4.7	Some of the largest recovered fragments from the experiments on the non-porous water-ice target (speeds: (a) before shot, (b) 0.6 km/s, (c) 1.3 km/s and (d) 2.1 km/s). As the collisional speed was increased the recovered fragments were more white, indication that were more fractured.107	

4.8	At 0.608 km/s none of the shifts exceed the precision of the instrument, whilst for the 2.16 km/s shot a shift in P_1 and P_2 olivine lines was observed to be 1.49 cm^{-1} and 1.08 cm^{-1} respectively.	109
4.9	Raman spectra of large fragment that recovered after shots (solid line) during Run#2, in comparison with the reference (dashed line). No significant change above the instrument precision was observed in the P_1 and P_2 olivine lines.	110
4.10	Raman spectra of large fragment that recovered after shots (solid line) during Run#3, in comparison with the reference (dashed line). No significant change above the instrument precision was observed in the P_1 and P_2 olivine lines.	111
4.11	The change in separation, ω , of the P_1 and P_2 olivine lines was calculated for all the big surviving fragments in the range of impact speeds 0.608–2.71 km/s.	113
4.12	The change in separation, ω , of the P_1 and P_2 olivine lines was calculated for all the big surviving fragments in the range of impact speeds 0.61–3.08 km/s.	114
4.13	The change in separation, ω , of the P_1 and P_2 olivine lines was calculated for all the big surviving fragments in the range of impact speeds 0.93–2.67 km/s. Notice that at the highest speed shot at 2.67 km/s, the separation slightly exceeds the resolution limit for both fragments. . . .	115
4.14	The gas diverter is a metallic funnel that is placed in between the target chamber and the gun. Several projectiles hit the back of the funnel leaving traces of damage.	120
4.15	Images using different magnifications of the residue layer found after filtering the HPLC water that was previously frozen down to -130°C . . .	123
4.16	The composition of the residue layer. Spectrum taken from the same region as the SEM image in Fig. 4.15.	124
4.17	BSE Images of different magnifications of the residue layer found after filtering the dissolved CaCO_3 targets.	126
4.18	The composition of the residue layer. EDX spectrum taken from the same region as the SEM image in Fig. 4.17.	126
5.1	The largest recovered fragments from all Runs. The dashed lines correspond to the best fitting of a power law as shown in Eq. 4.1. The red solid line shows the limit for the catastrophic disruption of the projectile, when $M_{1,f}/M_{im}=0.5$	130

5.2	Phase diagram of forsterite olivine (Fei & Bertka 1999). AUTODYN simulations (see Table 4.13) gave for the 3.50 km/s impact speed of peridot onto non-porous water-ice target $P_{\max}=10.2$ GPa and $T_P=80^\circ C$. The temperatures we calculated are below the range of the phase diagram, indicating that the recovered fragments were still in the olivine phase (a).	133
5.3	Macroporosities and bulk porosities of individual asteroids of the different types. Top: Are defined the three groups of objects according to their porosity values. Bottom: The average porosity for C-types is larger than the S-types, with $\sim 30\%$ and $\sim 40\%$ respectively (Britt et al. 2002).	141
5.4	Densities (top) and macroporosities (bottom) of six groups of small bodies including TNOs, comets and the four types of asteroids vs. their mass. The size of the markers correspond to the objects' diameters (Carry 2012).	142
5.5	Structure of the asteroids surfaces, showing a very high porosity in the first mm which can be explained either by cohesive forces (right side) or by small particles floating (left side). Model adapted and modified from Vernazza et al. (2012).	143
5.6	Mass ratio of the escaped ejecta material from the large craters from asteroids Mathilde, Eros, Ida and the martian satellites Phobos and Deimos as a function of the body's porosity. Image adapted and modified from Housen & Holsapple (2003).	145
5.7	Meteorites that have been found worldwide until 2013. The vast majority belongs to the ordinary chondrites, while the carbonaceous chondrites are only a small fraction of the chondrite population, with the vast majority being ordinary chondrites (http://meteorites.wustl.edu/meteorite_types.htm).	146
5.8	Semi-major axis (a) vs. eccentricity (e): Main Belt asteroids with different albedos that have non-zero impact probability on asteroid Polana, with collisional speed up to 0.5 km/s. The grey dots correspond to all the Main Belt population with known albedos and diameters, while the cyan square represents Polana.	152
5.9	Semi-major axis (a) vs. eccentricity (e): Main Belt asteroids with different albedos that have non-zero impact probability on Polana, with collisional speeds up to 1.0 and 2.0 km/s respectively. The grey dots correspond to all the Main Belt population with known albedos and diameters, while the cyan square represents Polana. As the impact speed threshold increases, the population of potential impactors in the current Main Belt increases too.	153

5.10	Semi-major axis (a) vs. sin of inclination (sini): Main Belt asteroids with different albedos that have non-zero impact probability on Polana, with collisional speeds up 1.0 and 2.0 km/s respectively. The grey dots correspond to all the Main Belt population with known albedos and diameters, while the cyan square represents Polana. As the impact speed threshold increases, the population of potential impactors in the current Main Belt increases too.	154
5.11	SFDs of the current MB population that could impact Polana at 0.5, 1.0 and 2.0 km/s. By extrapolating linearly the slopes, we obtained the impactors' population down to 100 m in diameter. The dashed lines correspond to the fitting of the slope for the estimation of the impactors population down to 100 m in size.	155
B.1	Differential (top) and cumulative (bottom) SFD of Run#2 (with $z = \times 150$).	180
B.2	Differential (top) and cumulative (bottom) SFD of Run#2 (with $z = \times 150$).	181
B.3	Differential (top) and cumulative (bottom) SFD of Run#2 (with $z = \times 150$).	182
B.4	Differential (top) and cumulative (bottom) SFD of Run#2 (with $z = \times 150$).	183
B.5	Differential (top) and cumulative (bottom) SFD of Run#2 (with $z = \times 150$).	184
B.6	Differential (top) and cumulative (bottom) SFD of Run#2 (with $z = \times 150$).	185
B.7	Differential (top) and cumulative (bottom) SFD of Run#2 (with $z = \times 150$).	186
B.8	Differential (top) and cumulative (bottom) SFD of Run#2 (with $z = \times 150$).	187
B.9	Differential (top) and cumulative (bottom) SFD of Run#2 (with $z = \times 300$).	188
B.10	Differential (top) and cumulative (bottom) SFD of Run#2 (with $z = \times 300$).	189
B.11	Differential (top) and cumulative (bottom) SFD of Run#2 (with $z = \times 300$).	190
B.12	Differential (top) and cumulative (bottom) SFD of Run#2 (with $z = \times 300$).	191
B.13	Differential (top) and cumulative (bottom) SFD of Run#2 (with $z = \times 300$).	192
B.14	Differential (top) and cumulative (bottom) SFD of Run#2 (with $z = \times 300$).	193

B.15 Differential (top) and cumulative (bottom) SFD of Run#2 (with $z = \times 300$).	194
B.16 Differential (top) and cumulative (bottom) SFD of Run#3 (with $z = \times 150$).	195
B.17 Differential (top) and cumulative (bottom) SFD of Run#3 (with $z = \times 150$).	196
B.18 Differential (top) and cumulative (bottom) SFD of Run#3 (with $z = \times 150$).	197
B.19 Differential (top) and cumulative (bottom) SFD of Run#3 (with $z = \times 150$).	198
B.20 Differential (top) and cumulative (bottom) SFD of Run#3 (with $z = \times 150$).	199
B.21 Differential (top) and cumulative (bottom) SFD of Run#3 (with $z = \times 150$).	200
B.22 Raman spectra of olivine before and after the shot with $\Delta P_1 = 0.16$ and $\Delta P_2 = 0.2$.	201
B.23 Raman spectra of olivine before and after the shot with $\Delta P_1 = 0.53$ and $\Delta P_2 = 0.79$.	201
B.24 Raman spectra of olivine before and after the shot with $\Delta P_1 = 0.46$ and $\Delta P_2 = 0.16$.	202
B.25 Raman spectra of olivine before and after the shot with $\Delta P_1 = 0.88$ and $\Delta P_2 = 0.83$.	202
B.26 Raman spectra of olivine before and after the shot with $\Delta P_1 = 0.63$ and $\Delta P_2 = 0.61$.	203
B.27 Raman spectra of olivine before and after the shot with $\Delta P_1 = 1.0$ and $\Delta P_2 = 0.55$.	203
B.28 Raman spectra of olivine before and after the shot with $\Delta P_1 = 1.17$ and $\Delta P_2 = 0.65$.	204
B.29 Raman spectra of olivine before and after the shot with $\Delta P_1 = 1.44$ and $\Delta P_2 = 1.00$.	204
B.30 Raman spectra of olivine before and after the shot with $\Delta P_1 = 0.87$ and $\Delta P_2 = 0.52$.	205
B.31 Raman spectra of olivine before and after the shot with $\Delta P_1 = 0.04$ and $\Delta P_2 = 0.47$.	205
B.32 Raman spectra of olivine before and after the shot with $\Delta P_1 = 0.05$ and $\Delta P_2 = 0.37$.	206
B.33 Raman spectra of olivine before and after the shot with $\Delta P_1 = 0.64$ and $\Delta P_2 = 0.59$.	206
B.34 Raman spectra of olivine before and after the shot with $\Delta P_1 = 0.55$ and $\Delta P_2 = 0.64$.	207

B.35 Raman spectra of olivine before and after the shot with $\Delta P_1 = 0.25$ and $\Delta P_2 = 0.40$	207
B.36 Raman spectra of olivine before and after the shot with $\Delta P_1 = 0.16$ and $\Delta P_2 = 0.32$	208
B.37 Raman spectra of olivine before and after the shot with $\Delta P_1 = 0.30$ and $\Delta P_2 = 0.24$	208
B.38 Raman spectra of olivine before and after the shot with $\Delta P_1 = 0.54$ and $\Delta P_2 = 0.06$	209
B.39 Raman spectra of olivine before and after the shot with $\Delta P_1 = 0.40$ and $\Delta P_2 = 0.26$	209
B.40 Raman spectra of olivine before and after the shot with $\Delta P_1 = 1.27$ and $\Delta P_2 = 0.99$	210
B.41 Raman spectra of olivine before and after the shot with $\Delta P_1 = 1.49$ and $\Delta P_2 = 1.08$	210
B.42 Raman spectra of olivine before and after the shot with $\Delta P_1 = 0.15$ and $\Delta P_2 = 0.43$	211
B.43 Raman spectra of olivine before and after the shot with $\Delta P_1 = 0.11$ and $\Delta P_2 = 0.27$	211
B.44 Raman spectra of olivine before and after the shot with $\Delta P_1 = 0.02$ and $\Delta P_2 = 0.48$	212
B.45 Raman spectra of olivine before and after the shot with $\Delta P_1 = 0.01$ and $\Delta P_2 = 0$	213
B.46 Raman spectra of olivine before and after the shot with $\Delta P_1 = 0.10$ and $\Delta P_2 = 0.29$	213
B.47 Raman spectra of olivine before and after the shot with $\Delta P_1 = 0.57$ and $\Delta P_2 = 0.26$	214
B.48 Raman spectra of olivine before and after the shot with $\Delta P_1 = 0.25$ and $\Delta P_2 = 0.21$	214
B.49 Raman spectra of olivine before and after the shot with $\Delta P_1 = 0.24$ and $\Delta P_2 = 0.61$	215
B.50 Raman spectra of olivine before and after the shot with $\Delta P_1 = 0.23$ and $\Delta P_2 = 0.57$	215
B.51 Raman spectra of olivine before and after the shot with $\Delta P_1 = 0.28$ and $\Delta P_2 = 0.01$	216
B.52 Raman spectra of olivine before and after the shot with $\Delta P_1 = 0.28$ and $\Delta P_2 = 0$	216
B.53 Raman spectra of olivine before and after the shot with $\Delta P_1 = 0.06$ and $\Delta P_2 = 0.01$	217
B.54 Raman spectra of olivine before and after the shot with $\Delta P_1 = 0.25$ and $\Delta P_2 = 0.27$	217

B.55 Raman spectra of olivine before and after the shot with $\Delta P_1 = 0.02$ and $\Delta P_2 = 0.65$	218
B.56 Raman spectra of olivine before and after the shot with $\Delta P_1 = 0.03$ and $\Delta P_2 = 0.05$	218
B.57 Raman spectra of olivine before and after the shot with $\Delta P_1 = 0.40$ and $\Delta P_2 = 0.08$	219
B.58 Raman spectra of olivine before and after the shot with $\Delta P_1 = 0$ and $\Delta P_2 = 0.06$	219
B.59 Raman spectra of olivine before and after the shot with $\Delta P_1 = 0.45$ and $\Delta P_2 = 0.47$	220
B.60 Raman spectra of olivine before and after the shot with $\Delta P_1 = 0.18$ and $\Delta P_2 = 0.09$	220
B.61 Raman spectra of olivine before and after the shot with $\Delta P_1 = 0.28$ and $\Delta P_2 = 0.80$	221
B.62 Raman spectra of olivine before and after the shot with $\Delta P_1 = 0.50$ and $\Delta P_2 = 0.54$	221

List of Tables

1.1	Meteorite groups and their link with parent bodies. Table adapted and modified from Burbine et al. (2002).	30
3.1	The characteristics of the projectiles used for all shots (*data from Petrovic (2001) and Schultz (1993)).	56
3.2	Physical parameters for the targets. The density refers to the grains of each target. (*data from Petrovic (2001)).	62
4.1	Summary of successful experiments.	84
4.2	Summarised information of the analysis of the peridot ejecta and the fragments recovered from the targets. The parameters are summarised for each speed range as they remained constant for each Run.	85
4.3	Successful shots for olivine and basalt projectiles onto low porosity water-ice targets (<10%). $M_{1,f}/M_{im}$ represents the proportion of the largest fragment of the impactor of its initial mass. The S in naming correspond to impact speeds <1 km/s, while the G to >1 km/s. For the shots G031214 and G121214 we were not able to identify the largest fragment. For shots G260215 and G260515 the largest fragments were recovered from the bottom of the craters. The mass of the shot G180215 was estimated by measuring first the volume of the fragment. From the shots G031214 and G121214 no large fragment was recovered (Avdellidou et al. 2016).	89
4.4	Successful shots of Run#2 for olivine projectiles onto high porosity water-ice targets. $M_{1,f}/M_{im}$ represents the proportion of the largest fragment of the impactor of its initial mass. Data are included in Avdellidou et al. (in prep.).	93

4.5	Successful shots of Run#3 for olivine projectiles onto high porosity CaCO ₃ regolith-like targets. $M_{1,f}/M_{im}$ represents the proportion of the largest fragment of the impactor to its initial mass. After shot G191115 no large fragment was recovered. Data are included in Avdellidou et al. (in prep.).	93
4.6	The calculated energy density at catastrophic disruption limit, Q_p^* and Q_b^* for olivine and basalt respectively, after fitting Eq. 4.1 to the experimental data, where A and c the fitting parameters.	94
4.7	The mass fraction of the olivine projectile that was found embedded in the non-porous targets (Run#1) using two different detection thresholds, of 4 and 6 pixels respectively, for the minimum detected area. *Note, that for shot G260215 (1.6 km/s) the largest fragment was found in the crater with a mass of 31% of the initial mass, increasing the total amount implanted in the target from 53–55% (Avdellidou et al. 2016).	102
4.8	The projectile's mass that was identified by SExtractor, using two different configurations (Mode.1 and Mode.2), and was implanted in the porous (40%) water-ice targets (Run#2). *Note, there was no need to map the target filters of these two shots as the largest fragments were recovered had total mass 100% and 99.17% of the initial mass respectively (Avdellidou et al. in prep.).	103
4.9	The total mass, M_{total} , of the olivine projectile that was found embedded in the porous (40%) water-ice targets (Run#2). A fraction of this belongs to the mass that was in the big fragments and another part was estimated by SExtractor photometry (see Table 4.8) (Avdellidou et al. in prep.).	104
4.10	The mass fraction of the olivine projectile that was found embedded in the CaCO ₃ regolith-like targets (Run#3) (Avdellidou et al. in preparation). *Note that after the shot G191115 no large fragment was found.	105
4.11	The ranges of the P ₁ and P ₂ Raman peaks for each set of peridots that were used for each Run respectively.	108
4.12	The displacement of the P ₁ and P ₂ Raman lines of the largest peridot fragments that were recovered from all shots.	112
4.13	Peak pressure, P_{max} , peak temperature, T_{max} , and temperature at peak pressure, T_P , as calculated with Autodyn (see section 4.3.2), are shown for the range of shots at the time of the impact.	117
4.14	All the unsuccessful shots were during Run#1, mostly at 3.0 and 4.0 km/s.	120
4.15	Successful shots that were not used for further analysis.	121
5.1	Average probabilities of MBAs of different albedos to impact asteroid (142) Polana, measured in impacts/km ² /year.	150

1

Introduction

Understanding of Solar System's formation and evolution is at the forefront of many current scientific investigations, and is the primary context of several on-going, and future, space missions. Our view of planetary systems has changed tremendously over the past twenty years. In particular the discovery of the extrasolar planets around solar type (Mayor & Queloz 1995) and other types of stars (Perryman 2014) and the realisation of the enormous diversity of these bodies (Perryman 2014); the idea of planetary migration needed to explain features observed in our (Gomes et al. 2005; Tsiganis et al. 2005; Morbidelli et al. 2005; Minton & Malhotra 2009) and other exo-planetary systems (Udry et al. 2003). Additionally important was the realisation that impact mechanisms between bodies plays a major role in their formation and evolution. It is assumed, but not yet confirmed, that impacts at relatively low speed are constructive in the early Solar System (this assumption was made by Gayon-Markt et al. (2012) while trying to understand the formation of the multilithology asteroid 2008 TC₃). However, as the system evolved over time, impacts became disruptive due to higher impact velocities driven by the formation of planetary bodies with strong gravity fields. This idea is also based on the theory that all bodies

in the Solar System were formed on orbits with very low values for eccentricity and inclination, low enough for an accretion disk (Morbidelli & Brown 2004).

For the Solar System's small bodies, the physical characterisation of asteroids, comets, Transneptunian objects (e.g. Pluto) and satellites by remote sensing telescope observations and a multitude of space missions is bridging the gap between Astrophysics and Planetary Geophysics. Minor bodies are not just 'dots in space' but are now revealed to have a complex surface geology.

Small bodies played a protagonistic role in the evolution of our Solar System, as they built up planets by impact coalescence (Johansen et al. 2015). The minor bodies that we still observe today, 4.5 Gy after the birth of the Solar System, are the leftovers of those building blocks that formed the planets. Contrary to planets, many of the minor bodies have been subjected to lower temperatures and thus experienced little to no melting and igneous activity. For instance, chondritic meteorites (see Section 1.2.3), which are mostly believed to originate from asteroid parent bodies (CI1 type have also been proposed to originate from comets (e.g. Gounelle et al. (2006))), have compositions very similar to the Sun's photosphere. This suggests they were not subjected to differentiation and therefore preserve a record of the conditions that existed in the protoplanetary nebula.

In contrast, some minor bodes did progress further down the planet evolutionary path and did experience planetary processes, such as differentiation, as evidenced by achondritic meteorites.

Therefore the study of these minor bodies can also reveal details of the Solar Systems formation and evolutionary processes. Admittedly, at first glance, small bodies may not seem so fascinating, but in the last few decades the scientific interest in them has increased dramatically. Small bodies are located in several zones in the Solar System

and will be described in the first half of this Chapter, followed by an introduction to collisions which is the primary focus of this thesis.

1.1 Small Bodies in the Solar System

With the term ‘small body’ we mean, according to International Astronomical Union (IAU), any object in the Solar System that is not a planet or a satellite or a dwarf planet. Their minimum size or mass is not well defined. Therefore the main regions that small bodies are found in the Solar System are (see Fig. 1.1): i) the asteroid belt (labeled Main Belt), which lies between the orbits of Mars and Jupiter and the trojans asteroids, co-orbital with Jupiter, ii) the centaurs that exist between the orbits of the giant planets and the Kuiper belt beyond the orbit of Neptune and, iii) the comet Oort cloud which is believed to lie between 10,000 and 200,000 au from the Sun.

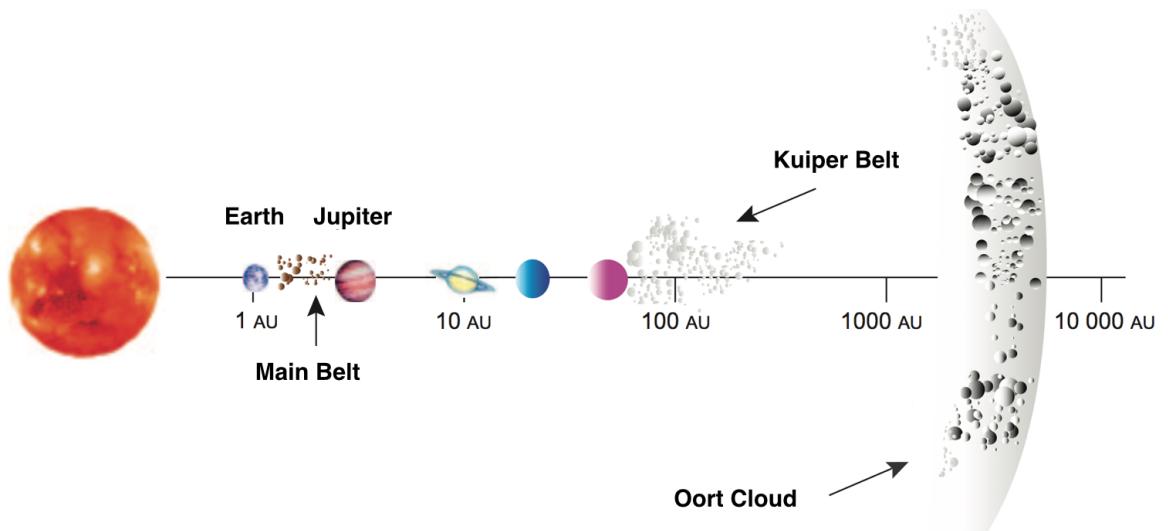


Figure 1.1: Main areas of small bodies in the Solar System. Due to the logarithmic scale of the diagram the orbits of the Mercury, Venus and Mars are not indicated. Modified image from Michele Serrano.

1.1.1 Main Belt Asteroids

The study of asteroids started relatively recently in history on January 1, 1801, when Giuseppe Piazzi, the Chair of Astronomy at the University of Palermo in Sicily, while working on his star catalogue, found a tiny moving object in the shoulder of Taurus, in an orbit with exactly the radius predicted by the Titius–Bode law. He dubbed it Ceres, after the Roman goddess of the harvest and patron of Sicily. Piazzi initially believed it to be a comet, but the absence of a coma suggested it was actually a planet.

Population

Asteroids are the building blocks of our planet, and their distribution, physical nature, formation and evolution are the fundamental aspects required to develop our understanding of planetary formation and the origins of life on Earth. To date, asteroid surveys have discovered approximately 700,000 small bodies that reside in orbits between 2.06 and 3.27 au distance from the Sun, and the total mass within this zone is approximately $\sim 5 \times 10^{-4} M_{\oplus}$, which is almost three times the mass of (1) Ceres. Mean motion resonances with Jupiter (i.e. their period of revolution around the Sun is an integer fraction of Jupiter’s orbital period), creates in the asteroid belt the so-called Kirkwood gaps, where asteroids were removed due to gravitational perturbations with the giant planet. These gravitational perturbations with Jupiter lead to several outcomes of their orbits: i) asteroids may be ejected from the Main Belt and collide with the Sun, ii) leave for ever the Solar System or, iii) migrate to planet-crossing orbits (e.g. Mars-crossers, Earth-crossers etc.). The latter scenario is responsible for the asteroid impacts onto the planetary surfaces of Mars and Earth and other inner Solar System bodies.

The story of asteroids begins in a very active Solar System: violent dynamical scenarios for its earlier stages (Morbidelli et al. 2015) are invoked by modern theories of planetary formation, such as the Grand Tack Hypothesis (Walsh et al. 2011) and the Nice Model (Gomes et al. 2005; Tsiganis et al. 2005; Morbidelli et al. 2005). These theories, which describe the early (~ 4.56 Ga) and the final (~ 4.1 Ga) phases of the giant planets' migration in our Solar System respectively, have to reproduce the distribution of the orbital and physical properties of the different classes of minor bodies, such as asteroids (Morbidelli et al. 2010; DeMeo & Carry 2014), comets, Jupiter Trojans (Morbidelli et al. 2005; Nesvorný et al. 2013), and Transneptunian objects (TNOs) (Gomes et al. 2005).

Physical Parameters

Another important goal of asteroid studies is to find the observational constraints to allow modelling of the collisional evolution of the Main Belt: from the epoch after the planetary migration and the end of the Late Heavy Bombardment (LHB) (Gomes et al. 2005), when the Solar System stabilised, up to now. Therefore, information is needed on several topics:

- What are the physical properties of the asteroids, such as their sizes, densities and mineralogy?
- How do their composition, mineralogy and other surface features (e.g. regolith particle sizes) change with their heliocentric distance?
- What does this tell us about the formation regions in the nebula of these bodies?
- What exactly are the processes that act on their surfaces and alter them?

S-complex



C-complex



X-complex



End Members

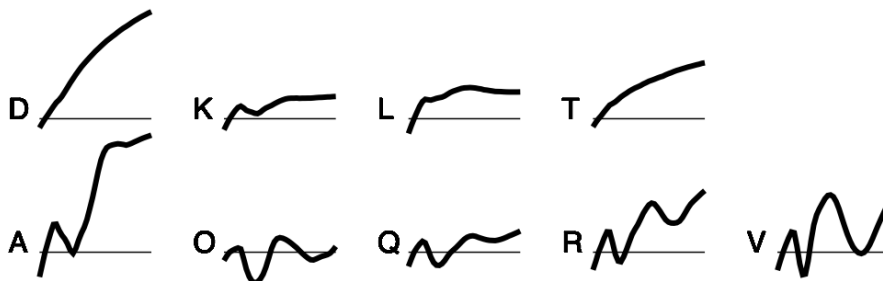


Figure 1.2: Spectra signatures of the three main complexes and End Members. Image modified from DeMeo et al. (2009).

- What do meteorites reveal about the formation and evolution of asteroids?

Asteroid spectral classes are thought to be diagnostic of the composition of these bodies. A spectral class is assigned to asteroids based on the shape of the object's surface reflectivity as a function of the wavelength. The surface reflectivity is typically determined by the ratio of the spectral energy distribution of the asteroid (SED) measured in visible and/or in the near-infrared light and the spectrum of the Sun. Figure 1.2 – adapted from DeMeo et al. (2009) – shows asteroid reflectivities in the visible and near-infrared.

Asteroid spectral classification was initiated by Chapman et al. (1975) with three main groups identified: the C-type for dark carbonaceous objects, S-type for stony (siliceous) objects, and U-type for those that did not fit into either C or S group. This classification has since been expanded by several works (Tholen 1989; Bus et al. 2002; DeMeo et al. 2009, see). Most recent visible spectroscopic classification schemes are based on spectra acquired by means of CCD spectrographs covering the wavelength range between 450 and 1000 nm. More recently, the growing availability of near-infrared (NIR) spectrographs at 3–4 m class and 8–10 m class telescopes allowed asteroid spectroscopy and their spectral classification to be extended in the near-infrared (DeMeo et al. 2009). The near-infrared spectral range is rich in silicate absorption bands diagnostic of the asteroid mineralogical composition. In addition, asteroid spectral classes have also been derived from multicolour spectro-photometry of asteroids (DeMeo & Carry 2014, 2013).

Currently, asteroids are divided into three large spectroscopic groups, also called complexes; the carbonaceous and the stony groups (C- and S-complexes respectively), which are broadly associated with carbonaceous and ordinary chondritic meteorites respectively and the third group, the X-complex. The X-complex was once considered to be constituted by metallic objects (the M-types), but we know today that it contains objects with very different mineralogy, ranging from carbonaceous (P-type), enstatite rich (E-type), to metallic (some of M-type). There are also several asteroids exhibiting spectra that do not fit into these complexes that are termed the End Members according to Bus-DeMeo taxonomy (DeMeo et al. 2015).

There is a taxonomic trend in the Main Belt which is clearer for the larger asteroids ($D > 100$ km), placing the S-complex closer to the Sun than the C-complex objects. However, at the smallest sizes there seems to be a blend of types. In particular it was

found that the relative abundance of the C-complex asteroids in the inner Main Belt is higher at smaller sizes (DeMeo & Carry 2014). This could be related to the fact that different compositional types may have different survival times (e.g. C-complex asteroids survive longer than other asteroid types due to their higher porosity) or asteroids with an icy composition may have shorter lifetimes (due to sublimation and collisions) (Rivkin et al. 2014).

Density is the fundamental property in order to estimate the composition and the internal structure of asteroids. The direct measurement of the bulk density, which is the sum of macro (m–km scale void spaces) and micro- (cm–submicron cracks/pores in the rocks fabric) porosity of the body, is made by obtaining independent measurements for the mass and volume of the bodies. Up to now, densities for only a few hundred of the small bodies have been calculated (Consolmagno et al. 2008; Carry 2012). However, apart from the direct methods, densities can be derived by using the effects of non-gravitational forces (such as the Yarkovsky effect (YE)) on the small bodies. So far this method has been used for the estimation of the density of cometary nuclei (Davidsson et al. 2007), but can be expanded to asteroids too. Densities and macroporosities (defined as the large voids in a body) can be measured with the use of the YE, a non-gravitational force that acts on a rotating asteroid caused by the emission of thermal photons that carry momentum. The main consequence of the YE is a drift of the orbital semi-major axis over time, da/dt .

As it is shown in Eq. 1.1, that drift depends on the asteroid’s density (ρ), radius (R), and the surface thermal inertia (Γ), via the thermal parameter (Θ) (Vokrouhlicky et al. 2015).

$$\frac{da}{dt} = \frac{(1-A)1}{\rho R} \frac{S_{\odot}}{3 c n r^2} \frac{0.5\Theta}{1 + \Theta + 0.5\Theta^2} \cos \gamma \quad \text{with } \Theta = \Gamma\sqrt{2\pi}/(\sqrt{P}\epsilon\sigma T_{\star}^3) \quad (1.1)$$

where S_{\odot} , c , n , r , A , γ , P , ϵ , T_{\star} , are the solar flux at 1 au, the speed of light, the mean orbital motion, the heliocentric distance (au), the bolometric Bond albedo, the spin axis obliquity (deg), the rotational period (h), the emissivity, and the sub-solar temperature, respectively. Equation 1.1 can be solved for ρ , provided Θ (i.e. Γ) is known. For example $da/dt \sim 10^{-4}$ au/My for an object at 2.5 au from the Sun with density $\rho \sim 3500$ kg/m³ (e.g. an S-type asteroid) and diameter of 1 km). This number is growing rapidly, and will grow even more after the ultra-precise astrometry data of the ESA space mission *Gaia* (Delbo' et al. 2008; Mouret & Mignard 2011) become available at the beginning of 2017. The application of these methods was limited, only to very few asteroids (Chesley et al. 2015; Rozitis et al. 2013, 2014; Rozitis & Green 2014), due to the lack of knowledge of Γ . Once the bulk density of a small body is derived, and compared to the microporosity (defined as the small scale voids and cracks in meteorites) of the relevant meteorites, the calculation of the macroporosity of the body is possible. Asteroid density increases with the size of the body, thus the very largest bodies (tens of km and therefore minor planets as well) have no macroporosity. Additionally the C-complex bodies have a higher macroporosity compared to the S-complex bodies, although there is a partial overlap (Carry 2012).

Water on Asteroids

One of the greatest quests in Solar System exploration is the discovery of water on other bodies, either directly, or by finding its traces on their surfaces. It is believed that Earth was formed dry, and thus water was delivered via impacts of small icy bodies or hydrated asteroids. While it was believed that the regions of origin of such icy bodies were located further than Neptune's orbit (see 1.1.2), about a decade ago, Hsieh & Jewitt (2006), reported the discovery of a new population of comets living in

the asteroid belt - the Main Belt Comets (MBC) - which may have formed there and are probably 'activated' by collisions. It was the spectroscopic detection of organics and water ice on asteroid (24) Themis (that belongs to the same dynamical family as the rest of the known MBCs) by Campins et al. (2010) and Rivkin & Emery (2010) that suggested ice is more common on asteroids than it was previously thought. The amount of ice water on Themis was a surprise, for how could it survive so long at 3.2 au. Several possible explanations could solve this problem, for example, if we assume that subsurface depositions of ice were revealed by e.g. impact gardening. The discoveries did not end there, as more and more asteroids were detected with water ice and/or organics, such as the large, primitive, outer main belt asteroid (65) Cybele (Licandro et al. 2011) and (90) Antiope, another member of the Themis family (Hargrove et al. 2015). These discoveries make the boundary between comets and asteroids less distinct and also make it more difficult to determine the position of the 'snowline', which actually divides dry from icy bodies. Küppers et al. (2014) have identified water vapour on two regions of Ceres' surface with infrared spectra obtained by ESA's Herschel Space Observatory, and suggested that it can be due to cryo-volcanism eruptions or to cometary-like sublimation. The water vapour observations were also verified by Perna et al. (2015), but on different regions. However, Li et al. (2016) suggested that this water vaporising on Ceres is not enough to cause a detectable global change of its albedo and also that the out-gassing is inconsistent with the body's heliocentric distance and so cometary-like activity, as Küppers et al. (2014) initially suggested, is not a possible mechanism. Additionally to these observations, the Dawn spacecraft, as it was approaching the dwarf planet, identified a mysterious bright dot, which, as the resolution improved, was proven to consist of two separate areas inside the Occator crater (Nathues et al. 2015) (see Fig. 1.3).

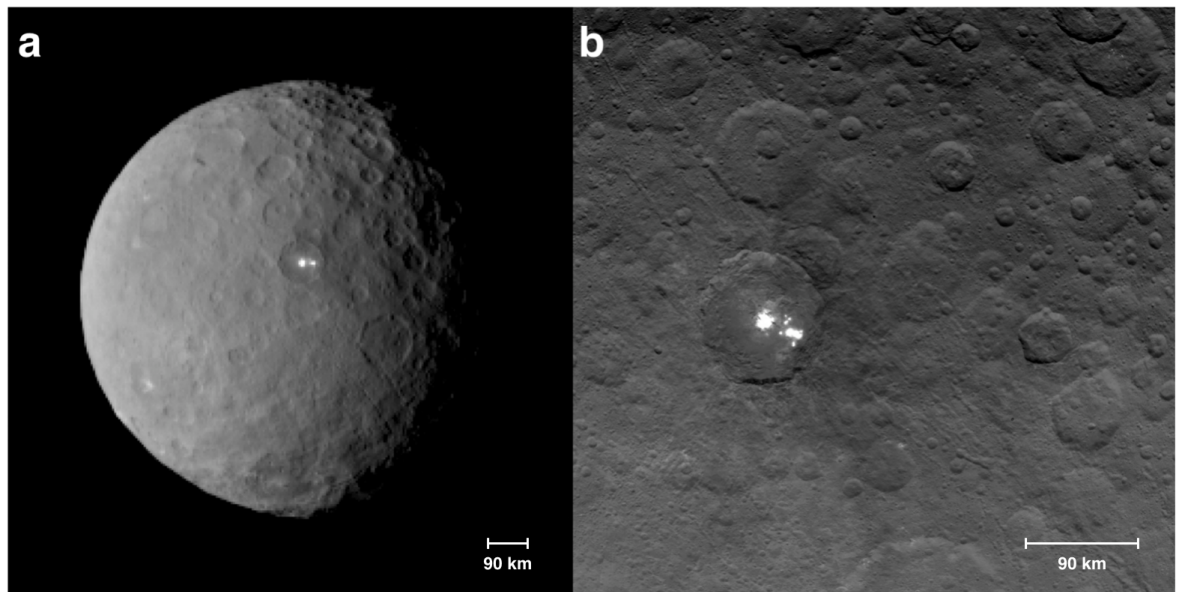


Figure 1.3: As NASA's Dawn spacecraft was approaching the asteroid (1) Ceres bright spots in the Occator crater were revealed. Images modified from NASA (2016).

1.1.2 Main Reservoirs of Icy Bodies

Small icy bodies are found in several places in the Solar System. The moons of the giant planets host ices along with comets, but the largest populations are located beyond the orbit of Neptune, where the Kuiper belt, the scattered disc and the Oort Cloud exist.

Trans-Neptunian Objects (TNOs), Centaurs and Oort Cloud

The main population of the TNOs reside in the so-called classical Kuiper belt. The very first TNO that was discovered was Pluto in 1930, which for a long period of time, was considered as the ninth planet of our Solar System. However, after the discoveries of larger objects in the same region of our Solar System (e.g. Eris has almost 30% more mass than Pluto), in 2006 Pluto was downgraded to a *dwarf planet* as it does not fulfil all the main criteria to be considered a planet according to the IAU, e.g. it has not cleared its neighbourhood of other bodies. The Kuiper belt Objects

(KBOs) are remnants of planetary formation and are located in a dynamically stable region between 30–50 au from the Sun. It is believed that this population consists of approximately 10^5 bodies with diameters larger than 100 km (Davies et al. 2008). The classical Kuiper belt appears to include two separate populations. The first, the ‘dynamically cold’ population, has nearly circular orbits, between 40 and 50 au (Levison & Morbidelli 2003), much like the planets, with an orbital eccentricity less than 0.1 and with relatively low inclinations up to about 10° (they lie close to the plane of the Solar System rather than at an angle). The second, the ‘dynamically hot’ population, have orbits much more inclined to the ecliptic plane, by up to 30° . The two populations have been given these names according to the ratio of the different gases (such as CH_4 , H_2O , CO , N_2 etc. (Stern & Trafton 2008; Doressoundiram et al. 2008)) they host on their surfaces, whose relative velocity increases as they are heated. The two populations not only possess different orbits, but different compositions. The cold population is markedly redder in spectra than the hot, suggesting it formed at a different heliocentric distance. The hot population is believed to have formed near Jupiter, and have been ejected out by movements among the gas giants (Nesvorný & Morbidelli 2012). The cold population, on the other hand, is believed to have formed more or less in its current position, although it may also have been later swept outwards by Neptune during its migration. Despite its vast extent, the collective mass of the Kuiper belt is relatively low. The total mass was estimated to be $0.1 M_\oplus$ according to Gladman et al. (2001). A more recent study by Fraser et al. (2014) estimates masses of 0.01 and $10^{-4} M_\oplus$ for the hot and the cold population respectively.

Initially the Kuiper belt was thought to be the reservoir of the progenitors of the Jupiter family comets (JFC), according to the results of the simulations by Duncan et al. (1995). However, later, when more accurate orbits were computed, it became

clear that this could not be the case, as many objects were found not to have close approaches with Neptune. It is now believed that short period comets originate from the scattered disc (Levison & Duncan 1997). This consists of planetesimals formed at smaller heliocentric distances, and are remnants of the icy giants' formation being scattered due to encounters with them during planetary migration. In recent years there has been a concerted effort to understand the origin, and the evolution, of the KBOs and link them dynamically with the short-period comets and via thermal evolution models.

Centaurs are called the minor planets whose orbits lie between those of the giant planets. It is believed that these objects were accrued there after perturbations with the planets, and collisions in the Kuiper belt. Interestingly it has been shown that approximately 6% of the Near Earth Asteroids (NEAs) come from the Kuiper belt (Morbidelli et al. 2002) and, further, that a Centaur may become an Earth-crosser every 880 yr (Horner et al. 2004). Their total population is estimated to 10^7 km-sized objects, but only about a hundred with diameter greater than 100 km. Therefore the calculated mass of this population is one order of magnitude less than the main asteroid belt.

Observations so far have shown that the surfaces of KBOs and Centaurs are fluffy, inhomogeneous and consists of μm – sub- μm size regolith. In particular the colours of the Centaurs show a bimodal distribution (Tegler et al. 2008). However, it is not clear if this diversity is due to processes such as weathering, collisions (and/or grain size), or reveals a more primitive composition gradient, as it is very possible that TNOs and Centaurs have kept some of their primordial composition. When the objects are observed in near-IR, their reflected spectrum may differ. Some objects may reflect more in longer wavelengths and have a 'red' slope (and thus at visible wavelengths

will seem redder). The spectra of some objects can be featureless (this flat spectra is usually called ‘gray’), while others can exhibit decreasing reflectance with increasing wavenumber (‘blue’ slope). For example, as KBOs are transferred inwards and become Centaurs they get redder. On the other hand, grey KBOs that have surfaces that suffered more from collisions become in turn grey Centaurs. Another possible scenario is that objects that formed up to 40 au from the Sun may have grey surfaces due to methane sublimation.

Concerning the densities is it assumed that the very large TNOs with sizes >200 km were not broken by collisions (e.g. the density of the large KBO 2003 EL₆₁ has been found to be 2600–3340 kg/m³, Rabinowitz 2006). Objects of smaller sizes (<100 km) may be monolithic fragments of larger bodies, or objects that were produced from the re-accumulation of impact ejecta. Trilling & Bernstein (2006) suggested that the mean density for the KBOs and Centaurs is in the range between 500–1500 kg/m³, a result that comes with a close agreement with Consolmagno et al. (2006). These values are very similar to the short-period comets and give porosities for such bodies in the range of 60–70% (see Fig. 1.4) indicating that there is a high abundance of volatiles.

The Oort cloud - named after the astronomer Jan Oort - is a spherical shell of cometary bodies surrounding our Solar System. The shell extends largely beyond 10,000 au from the Sun, likely up to 200,000 au. The Oort has never been imaged so far, but its presence can be deduced from the orbits of ‘nearly isotropic’ comets, which include new and returning long-period comets and Halley-type comets. The presence of a cloud of comets with orbital semi-major axis $a >10,000$ au can be deduced by a peak in the number of comets when planetary perturbations are ‘removed’ by calculating the comet’s orbit before it entered the planetary region (see Dones et al. (2004) and references therein). Because the observed orbital inclination of long-period comets is

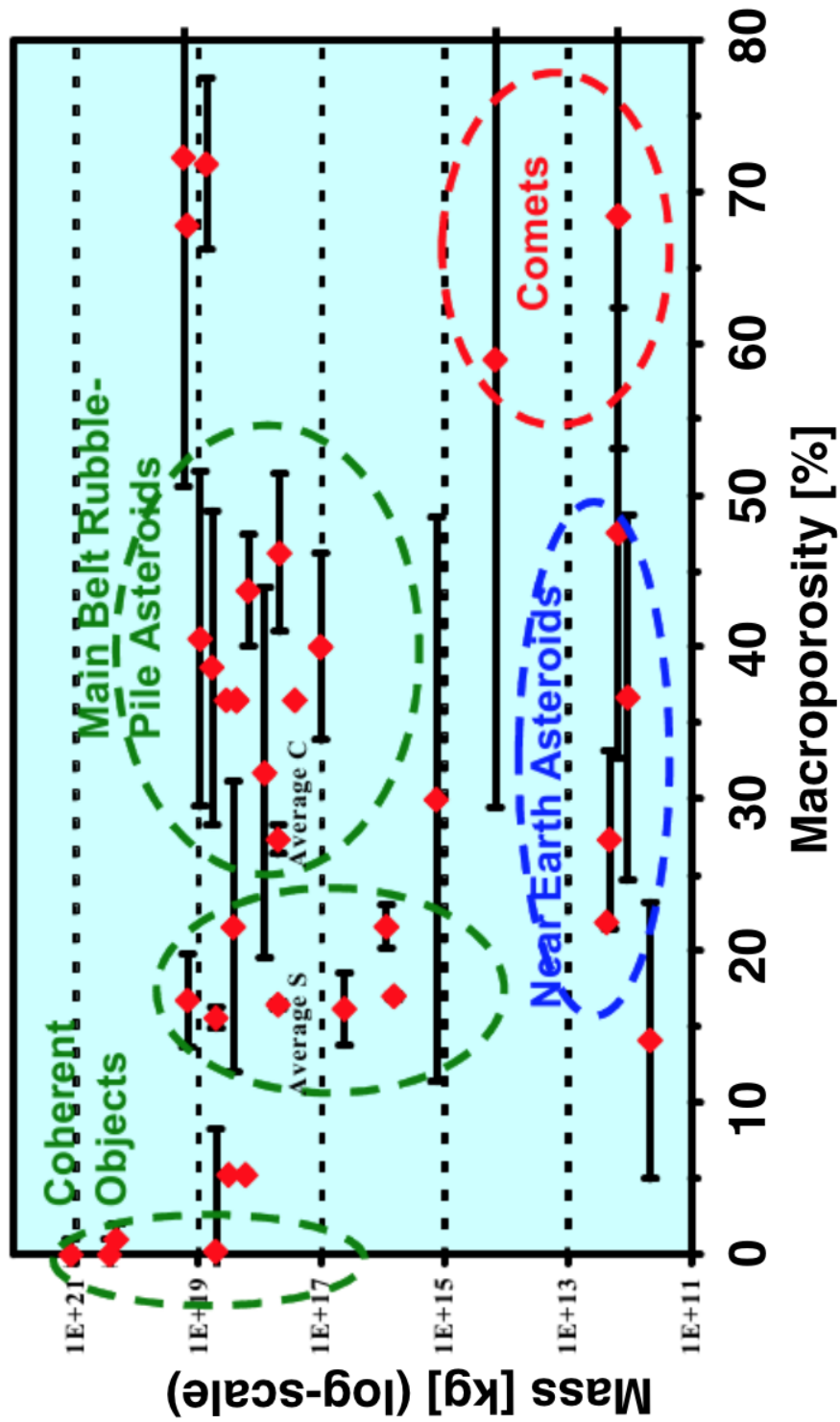


Figure 1.4: Estimated macroporosities of 32 small bodies according to studies by (Britt et al. 2006). It is a clear demonstration that the average macroporosity of the C-type asteroids is larger than S-types. Moreover, the most massive small bodies are more coherent, indicating that they were not fractured by impacts, but kept their primitive structure and survived the evolution of the Solar System.

quasi-uniform, we can deduce that these bodies come from a spherical shell. On the basis of his observations Oort (1950) estimated that the cloud contains about 2×10^{11} objects. More recent estimates revise up this number to 10^{12} comets, giving a total present-day Oort cloud mass of $38 M_{\oplus}$ (Dones et al. 2004). While the Jupiter-family comets coming from the Kuiper belt are thought to have formed in place, models of the primordial evolution of the Solar System show that comets of the Oort cloud formed in the region of the giant planets (Jupiter, Saturn, Neptune, and Uranus). These bodies were scattered in the Oort cloud by planetary encounters and by the stabilising effects of perturbations of stars passing near our Solar System (Dones et al. 2004).

Comets

Although observations of comets were first recorded almost 3,000 years ago by the Chinese, their origin was not clear for centuries. 500 years after the Chinese mentioned them, the first documents with suggestions to the comets' origin appear. During the Hellenistic period, philosophers proposed different ideas. Pythagoreans believed that comets were free floating planets, while Aristotle mentioned in his '*Meteorology*' that they are 'exhalations in the atmosphere'. The name '*comet*' comes from the greek word '*kometes*', which means 'long haired'.

Almost 1,000 years later, scientists tried to track the orbit of comets, and found that they could be parabolic. During the 19th century, having a larger sample for statistics, it was noticed that there was a large variety of periods, with comets with nearly parabolic orbits, hyperbolic orbits and elliptical, with some of them following orbits clearly inside the orbit of Jupiter. However, according to the existing sample, most of them had larger orbits than those of the known planets. A further classification of elliptical orbits was done by Lardner (1853), who divided them into three categories, which we now call

Jupiter Family Comets (JFCs), Halley-type comets (HTCs) and returning long-period comets (LPCs). One remarkable example of short-period comets is Halley's comet, which has an orbital period of 75–76 years. The first recorded observation was in 240 BC but it was in 1705 when the English astronomer Edmond Halley determined its orbit.

The proof that comets lose solid particles during their orbit around the Sun came a few decades later, when astronomers linked the Perseid and Leonid meteor showers on Earth with the orbits of 109P/Swift-Tuttle and 55P/Tempel-Tuttle respectively. Until the mid-twentieth century scientists were divided on whether comets come from interstellar space, or are members of our Solar System.

The breakthrough in modern cometary studies happened during 1950–1951, when Whipple (1950, 1951) and Oort (1950) proposed a cometary model from different perspectives. Oort suggested that comets should not have formed in their current orbits but in an outer region and eventually should collide with the Sun or a planetary body or be ejected from the Solar System. Whipple's suggestion was a solid nucleus with a mixture of ices. According to this model, as the comet approaches the Sun and the surface temperature rises, it produces gases by sublimation, as well as meteoritic dust. Whipple's new model gave an explanation of i) the observed gas production rates; ii) the observed jets in the coma and the irregular activity; iii) the observed non-gravitational forces, iv) the fact that many comets can survive close approaches with the Sun and v) the link between comets and meteor streams.

As people observed comets, they noticed a variety of tail forms between the different objects. Since the 19th century, scientists tried to connect tail behaviour with solar activity.

Apart from the physical structure of the nucleus, a great step was made in de-

termining their dynamical distribution. Whipple (1950) proposed the existence of a spherical cloud of comets whose aphelia lie far from the Sun in stable orbits, between 20,000–200,000 au. He reached this conclusion after he studied the distribution of the semi-major axes, a , of 19 known comets. From time to time, some of these comets leave the cloud due to perturbations of random passing stars close to the cloud.

There are many possible scenarios for the formation of cometary nuclei (Lamy et al. 2004). According to these, there should be a difference between nuclei of different populations, related to their formation mechanism. Even if it is assumed that the mechanism is the same for all the comets, the different physical and chemical conditions as a function of heliocentric distance cannot be ignored. Currently it is believed that there are at least two regions of cometary formation. One is the area beyond Neptune (the Kuiper belt and the scattered disk) and the other is the space between the giant planets, from which the majority of ecliptic comets and the long-period comets, that now reside in the Oort cloud, came from. The different groups of comets therefore come from different areas in the Solar System. It is helpful to understand whether they had originally different physical and chemical properties, or whether they are a result of a group of planetesimals with continuous characteristics. The second assumption will make them more similar, than different.

As with asteroids, the study of cometary nuclei helps to understand the Solar Systems evolution. As these bodies are among the first to accrete in the early solar nebula, they provide not only information about the conditions within the protoplanetary disk, but also the formation of the planetesimals from which the planets were built as a result of collisions. The composition of a comet's nucleus is a combination of rock, water ice, frozen CO_2 , CO , CH_4 and organic material. Although up to some years ago it was commonly said that comets are 'dirty snowballs', this came to change as evidence

showed that the dust content is higher. However their densities are very low, much less than the water-ice density, indicating that they are highly porous bodies (Weissman et al. 2004). Throughout the age of the Solar System, comets (through impacts) have played an important role in the formation and evolution of planetary atmospheres, and are believed to be a significant source of volatiles, water and organic materials (Morbidelli et al. 2000; Raymond et al. 2004). A common assumption was that the majority of the water on Earth was delivered via cometary impacts on our planet (Oró 1961; Anders & Owen 1977). This early assumption was later abandoned (Morbidelli et al. 2000) as the measured D/H ratio on bulk Earth and on studied comets is different, with comets having three times more D than earth water (Altwegg et al. 2015); so it is not possible that more than 0–10% of Earth’s water originated from them. On the other hand the D/H ratio of carbonaceous chondrites is in agreement with our planet’s, suggesting that its water could instead be of asteroidal origin (Robert 2003). However, the situation was later complicated by the discovery that comet 103P/Hartley 2 has a D/H ratio similar to that of the Earth (Hartogh et al. 2011) (Fig. 1.5).

The nuclei of all comets suffer erosion of their surface layers, because of sublimation, devolatilisation and alterations of their shape and structure, as they travel in the inner Solar System. In addition, the different lifetimes until their disruption imply different structures and properties. The most effective way to study cometary nuclei is with spacecraft flybys. After almost 40 years of successful flybys from space missions, such as Vega (I and II), Giotto, Deep Impact and Stardust, Rosetta, a comet rendezvous space mission, brought to light more cometary features.

The target body of Rosetta, comet 67P/Churyumov-Gerasimenko (67P/C-G), has a very complex bi-lobed shape, indicative of complex erosional processes. After the Rosetta approach, Massironi et al. (2015) showed that the two lobes could have been

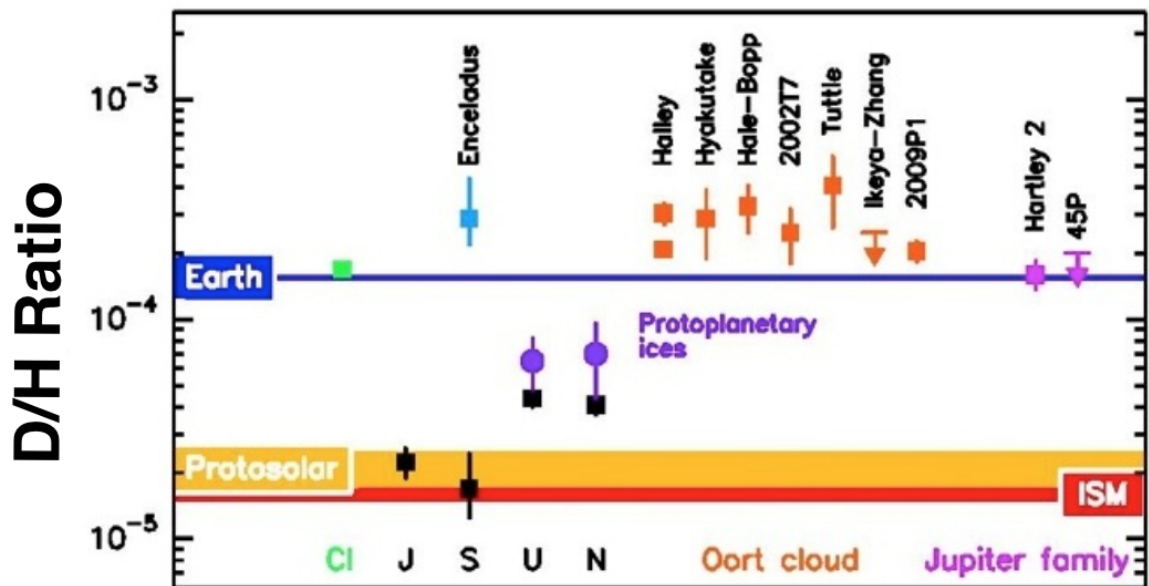


Figure 1.5: D/H ratio of several small bodies in comparison with Earth's ratio. Image adapted from Hartogh et al. (2011).

merged by a low velocity collision of two different parent bodies, while dynamical studies argue that a body of the size of 67P/C-G could not have survived intact for 4.5 Gy of collisions (Morbidelli & Rickman 2015). A further surprise was the rugged surface, the lack of a large amount of dust, but the existence of boulders, gravel (Mottola et al. 2015) and vertical cliffs and fractures (El-Maarry et al. 2015). The data show the importance of air-fall, surface dust transport, mass wasting, and insolation weathering for cometary surface evolution, and offers some support for subsurface fluidisation models and mass loss through the ejection of large chunks of material (Thomas et al. 2015). It is seen how activity arises from said fractures (Vincent et al. 2016) and pits (Vincent et al. 2015), offering a convincing explanation for the long-sought mechanism of cometary activity. Whilst years ago it was thought that comets are dirty snowballs, Rosetta's data, confirming previous findings, showed that the amount of water ice is

tiny compared to the organic rich dust (Capaccioni et al. 2015). However, water-ice was detected on 67P/C-G surface in a very few places (Filacchione et al. 2016), while in other regions ice is visible at the surface only when it condenses over night, but then it evaporates during the day (De Sanctis et al. 2015).

1.1.3 A quick overview

The small bodies played a key role in the evolution of our Solar System. They contain the most primitive material and its identification is one of the *Holy Grails* in Planetary Sciences, as from these materials we can constrain details of the conditions (e.g. temperature, pressure, reducing versus oxidizing conditions etc.) and location in which they were formed. Their current orbits, in combination with the explanation of their, sometimes confusing, composition, are going to clarify the picture. We also need to consider other processing they may have experienced, for example, how have catastrophic events, such as collisions, have affected them? By studying the outcome of these events, can we gain more insight on the initial form of the small bodies?

1.2 Collisions in the Solar System

1.2.1 Formation of Families of Small Bodies

The effect of impact evolution could have modified the surfaces of the different bodies in the Kuiper belt. For example, large impacts could have broken the largest bodies, producing families of objects that are genetically related, but possibly having different composition (for example if the parent body was already differentiated). Therefore, despite their low collisional velocities with each other, which are $<1\text{km/s}$ (Morbidelli & Brown 2004), this could be a possible scenario explaining the origin of some of the

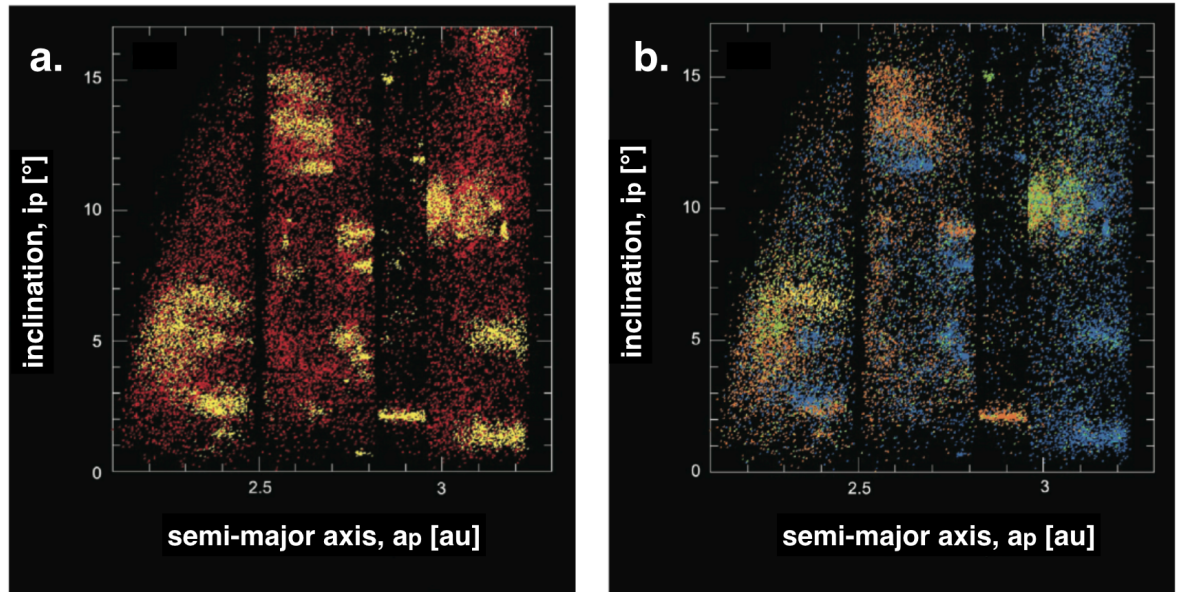


Figure 1.6: Left panel: In yellow are plotted the families in contrast to the background population in red. Right panel: A sample of 25,000 asteroids observed from SDSS and WISE are plotted in different colours indicating their albedo differences between the different families. Image from Nesvorný et al. (2015).

short-period comets. If this is the case, then the short-period comets can be a potential source of knowledge about the KBOs (Coradini et al. 2008).

Beside the orbital structure of asteroids, sculpted by the presence of the orbital resonances with the planets, there is another major dynamical feature in the asteroid belt manifesting itself at a smaller scale in orbital element space: the asteroid families (see Fig. 1.6). These can be identified as groupings of asteroids in orbital elements space, and are typically called dynamical families (Milani et al. 2014; Nesvorný et al. 2015). Some of these families play a fundamental role in the delivery of asteroids (larger than ~ 10 m) and meteoroids (< 10 m in diameter) from the Main Belt to near-Earth space (Bottke et al. 2007; Walsh et al. 2013; Reddy et al. 2014). The formation of a family is due to impacts between asteroids: this is referred to as a collisional family. These impacts can excavate giant craters such as Venenia and Reasilvia on (4)

Vesta, or catastrophically disrupt asteroids. The debris created by these impacts can re-accumulate and form new asteroids (Michel & Richardson 2013): these are rubble-pile asteroids and constitute members of the families (e.g. the Vesta's families, due to cratering events; the Themis family due to a catastrophic destruction of the parent asteroid). Therefore, families have a very important role in the compositional evolution of the Main Belt.

Collisions that happen today are generally disruptive, given the high velocity of asteroid-asteroid encounters (average is 5.3 km/s (Bottke et al. 1994)), but it has been investigated as to whether some low-speed collisions can still implant exogenous material onto asteroids (Gayon-Markt et al. 2012).

1.2.2 Cratering and Regolith Production

Impact cratering is an important geological process and craters are a dominant formation that affect the surfaces of the terrestrial planets, rocky and icy moons and, especially, asteroids because due to their small size and the lack of atmosphere are affected in a higher level. Despite their abundance, they were only first observed 400 years ago by Galileo when he pointed a telescope at the Moon. However, it was not until the last century when astronomers realised that these formations were the result of impacts. After the analysis of the Apollo lunar samples it became clear that the lunar craters were the result of impacts and not of other processes such as volcanism. Decades later the Galileo spacecraft identified, for the first time, craters on (951) Gaspra and (243) Ida asteroids (see Marchi et al. (2015) for a review). It has been found that even highly oblique (we refer to impact angles that start to produce elliptical crater, usually considered as $<10^\circ$) impacts produce identifiable craters. One significant result of impact cratering is that during the excavation, fresh material comes to the surface.

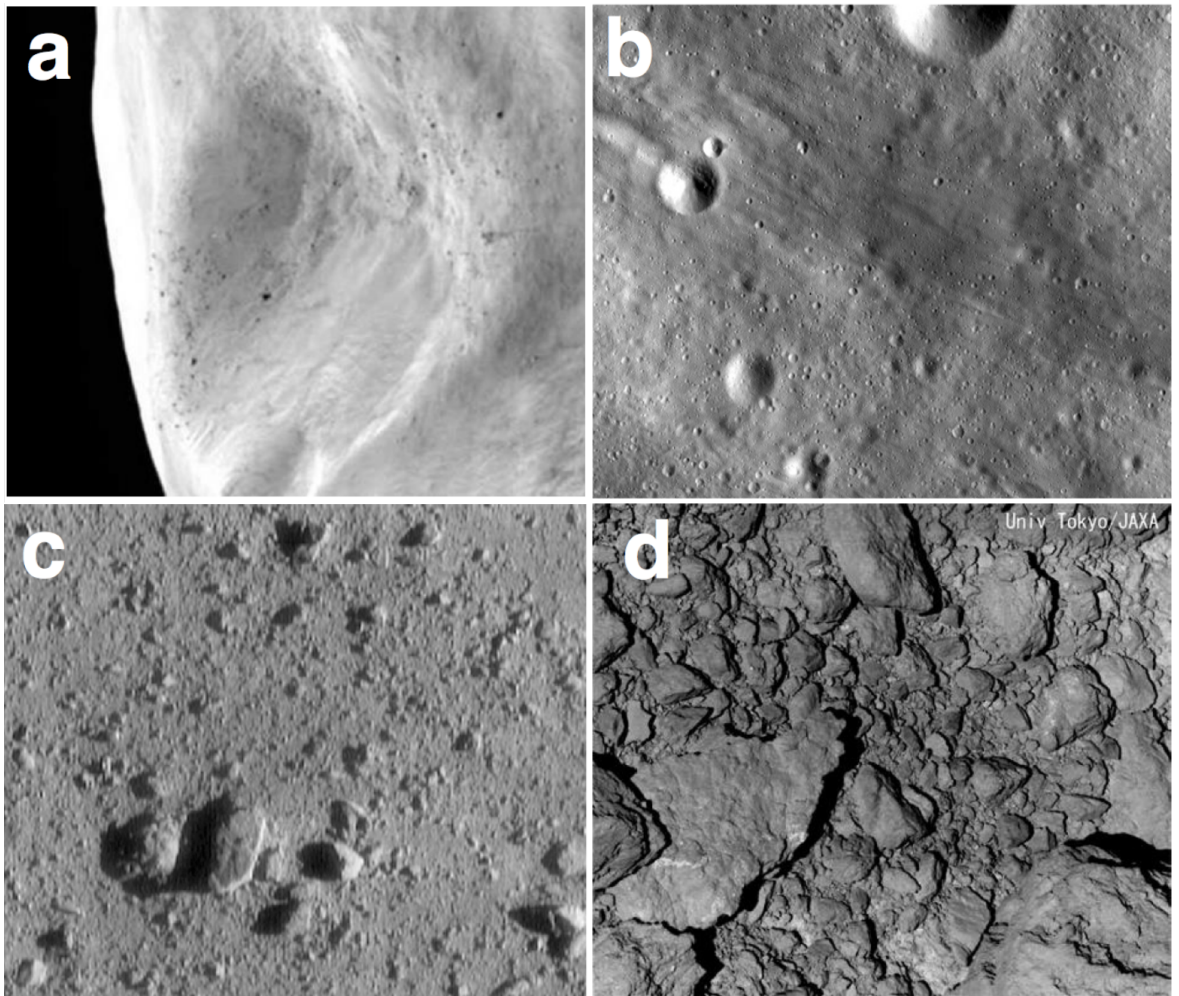


Figure 1.7: Images of regolith covered surfaces of several asteroids. (a) Image of asteroid (21) Lutetia taken from Rosetta spacecraft. (b) Image of asteroid (4) Vesta from the Dawn space mission. (c) Image of asteroid (433) Eros from NEAR-Shoemaker mission and (d) of asteroid (25143) Itokawa from Hayabusa mission.

Apart from the size and collisional speed, the target body's surface material plays an important role in the outcome of an impact. Porosity and strength of the material can lead to the formation of a crater with different topological and morphological characteristics (such as size, depth, size of ejecta blanket). Craters have been observed in a wide range of sizes, from $0.1 \mu\text{m}$, e.g. micro-craters on Apollo 15&16 samples (Schneider et al. 1973), up to more than 2,000 km (the Hellas basin on Mars).

The study of the cratering record on planetary surfaces can provide information on the age of the surface of that body. In order to achieve such a chronological model the knowledge of the population of the potential impactors and their impact probabilities (see Fig. 1.8 for the Earth) is required. From the total number of craters on a surface the age of the body can be estimated. However, so far, the only absolute chronology has been performed for the Moon, after the calibration using the Apollo samples for which radiometric dates are available.

As impact craters are accumulated on the surfaces of the small bodies more ejecta blankets are produced and they start to overlap with each other. When a rock is exposed on a body's surface it is also exposed to impacts which break it down to smaller pieces over time. This process leads therefore to regolith production. However, before the first thermal inertia, Γ , measurements of small asteroids and before the space missions that flew by several asteroids, the majority of researchers believed that the small asteroids were monolithic, with a bare surface. The main argument for this belief was that due to the low gravitational field, material produced from an impact could not survive on the surface, but got lost to space (Housen & Holsapple 2003, 2011). However space missions such as Galileo, NEAR-Shoemaker (Veveřka et al. 2001) and Hayabusa (Yano et al. 2006) revealed that asteroids are covered with a regolith layer (Fig. 1.7), in addition to thermal infrared observations from which the grain size of the regolith can be derived (Gundlach & Blum 2013). The regolith grain size differs on asteroids according to their size (Delbo et al. 2015). For example, on the largest asteroids, the grain sizes are in range 10–100 μm , on smaller asteroids (tens of km, such as Eros) it is a few mm, while on a few 100s-m bodies the grains are a few cm. The main regolith production mechanism was, up until very recently, traditionally considered to be the fall-back of impact ejecta and the comminution of boulders by micrometeorite

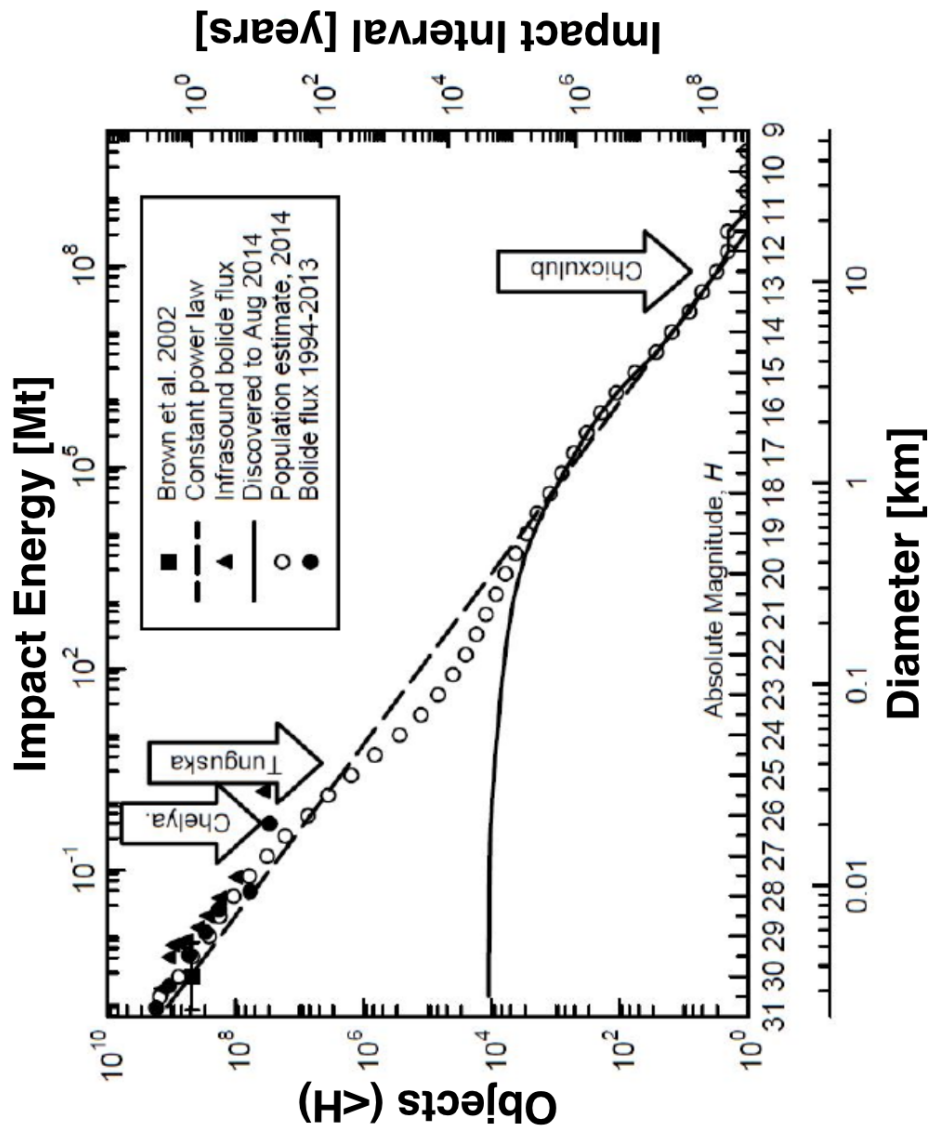


Figure 1.8: Size distribution of NEAs above a specific absolute magnitude. The line of circles represents the estimated total population, while the solid line is the observed one to 2014. The calculation of the size from the absolute magnitude is done by assuming an albedo of $p_v = 0.14$. For each size is calculated the impact energy along with the impact probability for an object with a given diameter and larger. Image adapted and modified from Harris et al. (2015).

impacts. However, very recently data by Delbo et al. (2014) show that the thermal fatigue, caused by surface diurnal temperature variations, is the dominant process, capable to break down in higher rate cm-size rocks than the meteoroid bombardment.

1.2.3 Linking meteorites with their parent asteroidal bodies

Meteorites are samples of extraterrestrial material (typically $>$ a few mm) arriving at the Earth's surface. Only in 1794, when Ernst F. Chladni combined all data from meteorite falls and proposed that meteorites consisted of rocks of an extraterrestrial origin did interest in these objects increase. As a meteoroid enters Earth's atmosphere, in order to produce a meteorite, it should be large and strong enough with a relatively low velocity. When a meteor (the radiation of the penetration of a meteoroid into the atmosphere) is brighter than -4 mag, it is called a 'bolide', and 'superbolide' when brighter than -17 mag (Borovička et al. 2015).

The sources of most meteorites are asteroids. Smaller micrometeorites and interplanetary dust particles in contrast are thought to be a mix of cometary and asteroidal material. In the last few decades it has been possible to link many meteorites with an asteroidal parent body (Lipschutz et al. 1989), as studies have shown that the majority of them were formed 4.56 Ga and originated from small bodies (sub-planetary). Exceptions do exist however, and consist of meteorites thought to originate from other major bodies (e.g. Mercury, Venus and Mars) or the Moon (Burbine et al. 2002).

Typically meteorites are divided according to their bulk composition into the stony, stony-iron, and iron types. Meteorites are also divided according to their 'primitiveness' into two large groups: those that are differentiated (which includes irons, stony-irons and the stony achondrites), and those which have not: this includes all of the unmelted stones. Together these different groups give us information about the early Solar

System and planetary evolution (Grady & Wright (2006)).

The differentiation of planetesimals into crust, mantle, and iron core is particularly poorly understood: it is estimated that asteroids larger than 100 km should have undergone partial or total differentiation. However, there is a lack of evidence of differentiated asteroids in the Main Belt (see e.g. DeMeo et al. 2015, for a review). On the basis of their mineralogical and petrographic characteristics and their whole-rock chemical and oxygen-isotopic compositions, meteorites are also divided into chondrites, primitive achondrites, and achondrites (Fig. 1.9). Chondrites are undifferentiated and are divided into 15 chondrite groups, including eight carbonaceous (CI, CM, CO, CV, CK, CR, CH, CB), three ordinary (H, L, LL), two enstatite (EH, EL), and R and K chondrites (Weisberg et al. 2006).

Establishing a link between asteroids and meteorites enables us to infer the composition of the first, the formation location of bodies appearing to have different compositions, and the alterations that happened to them during Solar System evolution (see Table 1.1). In other words, it will be possible to get a snapshot of the very early Solar System. So far, parent bodies have been identified for 100–150 meteorites (Burbine et al. 2002; DeMeo et al. 2015).

1.2.4 Impacts as Drivers for Life

The origin and the evolution of life on Earth is connected with small bodies in a violent way. It is believed that impacts on the early Earth could have delivered the essential components for the formation of life (e.g. complex organics and/or amino acids) providing that they could survive so energetic impacts. Several studies have been performed recently, in an attempt to demonstrate that this mechanism could work, using hyper-velocity laboratory experiments. For example Martins et al. (2013)

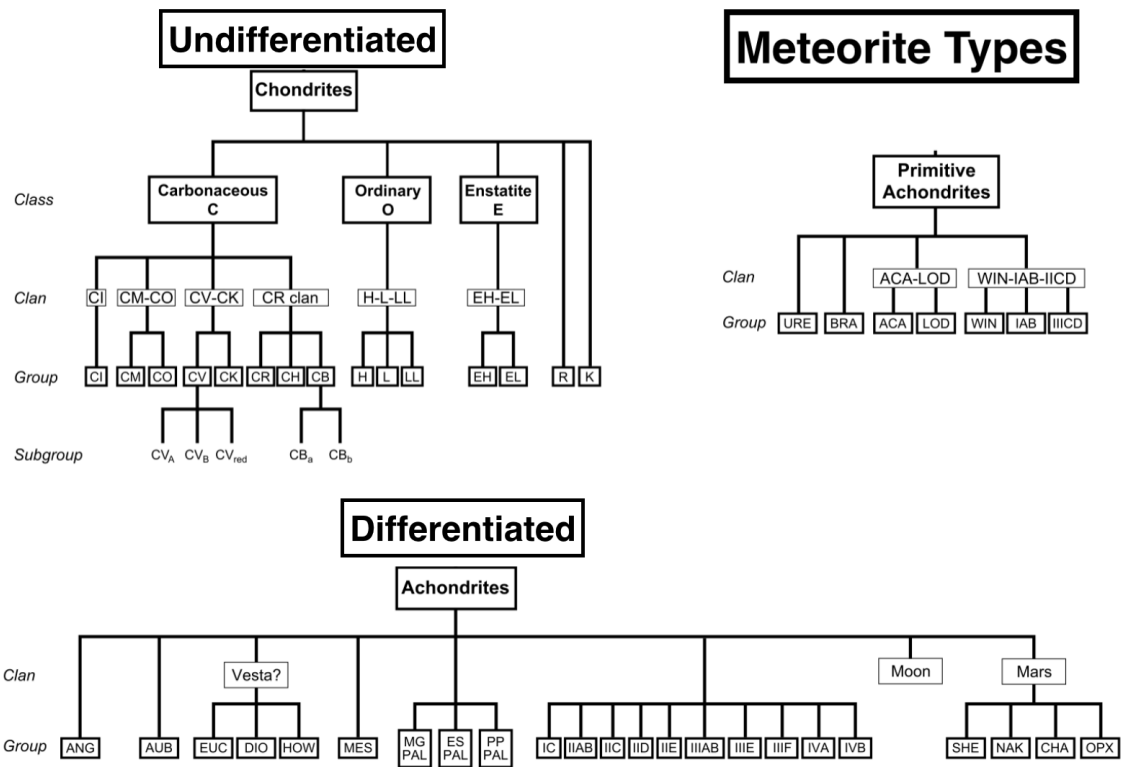


Figure 1.9: Classification of the meteorite types. Figure adapted and modified from Weisberg et al. (2006).

used the Light-Gas Gun at the University of Kent to shock simple ices, simulating cometary compositions, and produced several simple biologically significant amino acids. Therefore, this could be one possible way to produce the basis of proteins inside the Solar System. These results came as an experimental confirmation after the presence of glycine was found on samples from comet 81P/Wild-2 that returned by the Stardust mission. Moreover Pasini (2014) and Pasini & Price (2015) have shown that microanimals (e.g. tardigrades) kept in water-ice can survive impact shocks. This finding may apply to the scenario of the direct delivery of microbial life onto Earth (or conversely, the delivery of microbial life to Mars).

Table 1.1: Meteorite groups and their link with parent bodies. Table adapted and modified from Burbine et al. (2002).

Group	Fall [%]	Parent body/source
L	38.0	S(IV) asteroids
H	34.1	6 Hebe [S(IV)]
LL	7.9	S(IV) asteroids
Irons	4.2	M asteroids
Eucrites	2.7	4 Vesta (V)
Howardites	2.1	4 Vesta (V)
CM	1.7	19 Fortuna (G,Ch)
Diogenites	1.2	4 Vesta (V)
Aubrites	1.0	3103 Eger
EH	0.8	M asteroids
EL	0.7	M asteroids
Mesosiderites	0.7	M asteroids
CV	0.6	K asteroids
CI	0.5	C asteroids
CO	0.5	221 Eros
Pallasites	0.5	A asteroids
Ureilites	0.5	S asteroids
Martian	0.4	Mars
CR	0.3	C asteroids
CK	0.3	C asteroids
Acapulcoites	0.1	S asteroids
Angrites	0.1	S asteroids
Lodranites	0.1	S asteroids
R	0.1	A or S asteroids
Winonaites	0.1	S asteroids
Tagish Lake	0.1	D asteroids

1.2.5 Impacts as a Hazard for Life and Space Assets

Impacts, apart from potentially driving the wheels of life, may also have caused extinction events (e.g. the Chixculub impact event 66 My ago, Alvarez et al. (1980)).

Specifically NEAs pose a hazard to our planet's environment and human civilisation.

The awareness of the threat that the NEAs carry has grown rapidly in recent years.

Humanity has passed from the stage that an impact risk seemed distant and harmless, to the point where they are a very real possibility, making them very important targets for extensive investigation. The Chelyabinsk superbolide was a NEA that entered the Earth's atmosphere in 2013 with a speed of 19 km/s and exploded only 30 km above the ground (Popova et al. 2013). The result was 1,500 injured civilians and extensive ground damage across tens of km. Considering the shallow angle that the meteor entered the atmosphere, and the energy loss due to its long trajectory, the final damage was much less than could have occurred with different initial entry conditions. The Chelyabinsk superbolide was the biggest one since the Tunguska event in 1908 (Chyba et al. 1993), that destroyed 2,000 km² of forest land. The estimated carried kinetic energy of the Chelyabinsk meteor prior to its disruption was 20–30 times larger than the Hiroshima atomic bomb, while the Tunguska event was 1,000 times larger (Fig. 1.8)! However, if a meteor of a similar size had a different composition (e.g. metallic) it could reach the ground and form a km-size crater (e.g. Barringer crater, AZ), as the strength of its material would be higher, causing more severe damage of the surface. Another example is the multi-lithology asteroid 2008 TC₃ that lost almost its entire mass while travelling into the atmosphere, indicating that it was a highly porous body (Jenniskens et al. 2009).

These facts urged us to critically consider the notion of impact prevention. So far asteroid surveys have discovered more than 13,000 NEAs and 1,626 of them have been characterised as Potential Hazardous Asteroids (PHA) (HORIZONS System 2016). This number is expected to continuously increase, as new NEA discoveries will complete the catalogue of known sizes down to a few tens to hundreds of meters, which constitutes the population with the highest probability of impacting the Earth and causing significant damage.

To date, asteroid risk assessment has relied on several conclusions drawn from experiments, modelling, and space missions. It has been established that the damage caused by an impact (crater size) highly depends on the composition of the impactor: meteors with similar sizes and impact speeds, but higher densities/lower porosities cause greater damage on the target body. Now, very recent studies point out a mismatch between the impact simulations and observed crater/asteroid populations that indicates that impact damage may have been significantly underestimated (Bottke et al. 2015) and an asteroid of a given size can create a crater twice the size it was thought before. Several methods have been proposed and developed for asteroid deflection (Harris et al. 2015). Physical characterisation will be of paramount importance to decide the most effective deflection method to be used in case of an emergency. Any estimation of the size of a potential impactor has uncertainties which can be very large. Other important parameters that insert uncertainties from their estimation to the impact energy are the density and the albedo of the target body. It is then obvious that the knowledge of the composition and the porosity of the small asteroids is essential to estimate the fate of the meteor and the damage that will be caused by a potential impact. Asteroid observations, in combination with laboratory hypervelocity experimental results and hydrocode modelling continue to shed new light and redefine the importance of the impact hazard on our planet.

1.3 Approaches to Physics of Collisions

Although we are aware of the importance of impacts in the Solar System as it is one of the most important processes which drives surface evolution: simulations are needed in order to understand and interpret the large scale observations. The main ways to

approach this problem are via: (a) laboratory experiments, (b) computer simulations and scaling methods to finally predict the outcome of large-scale collisions and, (c) (in the last decade) direct, large scale, space experiments.

With laboratory experiments a direct investigation of the outcome of a collision can be performed. A large group of materials can be used for these purposes, however, there are significant constraints on the impact speed that can be produced with today's instrumentation, and also the size scale is limited to laboratory scales. When such experiments cannot be done due to the above limitations other approaches are used.

These techniques mainly include the use of so-called hydrocodes and particle codes and the target and projectile materials are represented differently according to the method used (Asphaug et al. 2015). In smooth particle hydrodynamics (SPH) for instance, the material is represented as a set of particles. The material properties of each of these particles are averaged with its neighbours, but also are weighted according to their distance from the 'studied' one. On the other hand, in classical hydrocodes a fixed grid is used, which represents the colliding body. So, at each time-step, the material properties, momentum and energy are propagated from cell to cell.

However the major drawback of all these methods is the lack of exact knowledge of the type of materials (and material models) and the surface and internal structure of the small bodies in the Solar System. Even when this knowledge exists, the reproduction in the laboratory or in computer simulations, is not that precise to draw definite conclusions, as porosities, material strengths etc. are not known. Despite these uncertainties, the outcome can be used to obtain a better overview of the *big picture* of collisions in the Solar System.

1.3.1 Laboratory Impact Experiments

Laboratory impact experiments, involving both low (<1 km/s) and high collisional speeds (>1 km/s) have been performed for many decades, using a variety of accelerating methods such as single and two-stage gas guns, powder guns, electromagnetic dust accelerators, free-fall apparatus or even field explosives. A range of materials have also been used both for targets and projectiles, including rocks (e.g. basalt, granite or even real meteorites), glass, cement, sand, ice, metals (e.g. aluminum and steel), nylon, Pyrex etc. (Holsapple et al. 2002). Impacts are performed with either horizontal or vertical apparatus, simulating collisions at different impact angles with respect to the horizontal. The quantities that are commonly studied are the energy required for a specific combination of materials to achieve catastrophic disruption of the target, the sizes and shapes of the target's fragments along with the ejecta velocities and the crater characteristics.

So far it has been demonstrated that the properties of the materials used, and the collisional speeds play a significant role in the outcome of the experiments. For example it is shown that:

- i the larger the target body, the easier is to fragment compared with smaller ones (Housen & Holsapple 1999);
- ii porous targets are more difficult to break and need higher energies to disrupt, although they are theoretically more fragile with their low compressive and tensile strengths (see Holsapple et al. (2002) for a review and references therein). For example, porous ice can be seen, to be as hard as silicate targets;
- iii crater formation on porous targets is different compared to non-porous materials

due to the compaction mechanisms (Housen et al. 1999);

iv ejecta velocities can be up to 80% lower for highly porous targets compared to non-porous;

v the size-frequency distributions of the target's fragments follow a power law consisting usually of several segments, each corresponds to a different population of fragments originating from a different area of the target (di Martino et al. 1990);

vi the shapes of the target's fragments after a cratering or catastrophic impact may differ substantially (Michikami et al. 2016).

1.3.2 Relevance of Space Missions and Large Scale Experiments to Impacts

As the value of studying the small bodies increases, more space missions are being dedicated to their exploration. So far, many successful missions have been operated to both asteroids and comets, all of them trying to answer, through their discoveries, the fundamental questions of how these planetary formation leftovers were formed, and what and where is hidden the primitive material of the Solar System. There were or going to be 'flyby' missions (Giotto, Rosseta, Dawn etc), sample return missions (Hayabusa I and II, Stardust, Osiris-REx) and large scale laboratory missions (i.e. Deep Impact, AIDA Asteroid Impact and Deflection Assessment).

A future promising mission, ARM (Asteroid Redirect Mission) is being developed by NASA with the aim to actually bring a primitive small body closer to us, into a stable orbit around the Moon for more detailed human examination in the 2020s. Therefore, simultaneously with laboratory experiments and computer simulations, large scale tests can give the crucial information required in order to validate extrapolation of the laboratory-scale studies.

Deep Impact

The first space mission, attempting to simulate a large scale collision, was NASA's Deep Impact: A mission to a comet whose aim was the exploration of the interior of the 6 km diameter comet 9P/Tempel 1. It was a unique opportunity to excavate and reveal the pristine material that exists under the surface of a small body. The probe of the mission, had a mass of 364 kg and was ~ 1 m in diameter. It collided with the cometary nucleus in 2005 (Blume 2005). The impact speed was 10.2 km/s and the angle was between 25° and 35° with respect to the horizontal plane on the illuminated side of the comet (Fig. 1.10).

A few years later, in February of 2011, the second mission of the Stardust spacecraft, the Stardust-NeXT mission studied in detail the outcome of the Deep Impact mission. Up to that time the calculation of the crater sizes were based upon the estimated ejecta mass that was observed straight after the impact. With data from Stardust-NeXT it was estimated that the diameter of the crater produced is approximately 49 m with an ejecta blanket up to 120 m in diameter around the crater (Richardson & Melosh 2013).

AIDA

The most reasonable approach in the case a deflection will be required, albeit very dependent on the porosity and composition of the target, is the deflection by a hyper-velocity kinetic impact using a spacecraft (see Fig. 1.11), such as the AIDA (Asteroid Impact & Deflection Assessment) project (ESA/NASA) (Michel et al. 2015; Cheng 2013). The mission will consist of two different parts: the Asteroid Impact Mission (AIM, ESA) and Double Asteroid Redirection Test (DART, NASA), that will fly to

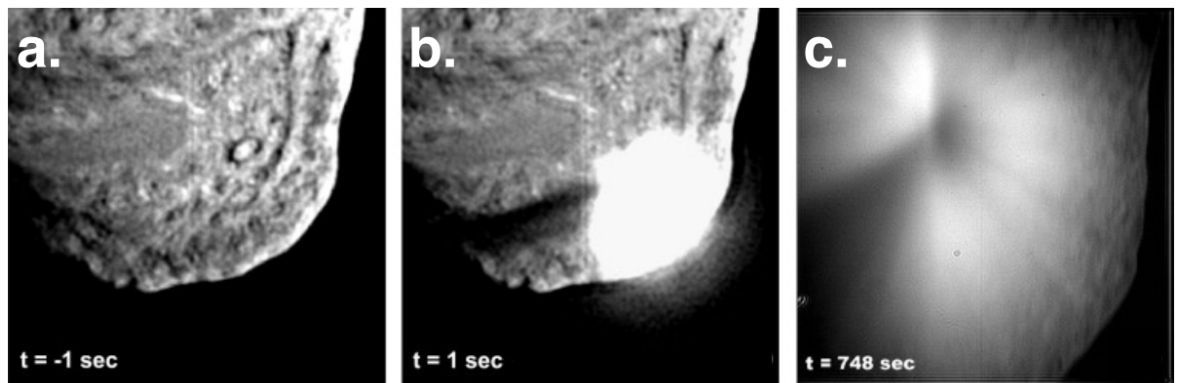


Figure 1.10: Images from the Deep Impact spacecraft flyby to the comet 9P/Tempel 1 at different times: a) prior to the impact, b) soon after and, c) later showing the impact ejecta plume development Richardson & Melosh (2013).

the binary NEA (65803) Didimos in 2022. The idea for modifying the trajectory of a potential impactor started with the study for the ESA project Don Quijote in 2005–2007. The AIM (Asteroid Impact Monitoring) mission is going to determine accurately the orbital and rotation state of the binary, deriving the shape, mass, and size for both components. In addition it will analyse the surface characteristics of the bodies, will observe the crater and derive the impact properties. In turn the DART mission will impact into the companion of Didimos with a single >300 kg spacecraft at 6.25 km/s, changing the mutual orbit of the binary components. It is estimated that the DART impact will change the period by 0.5 – 1% and this change is going to be determined with ground-based observations. Up to now, no other small body deflection experiment has been performed, so it is not possible to make an accurate prediction of the outcome. If funded, AIDA is going to be the first large scale experiment to demonstrate of the feasibility of asteroid deflection and characterisation of the impact effects.

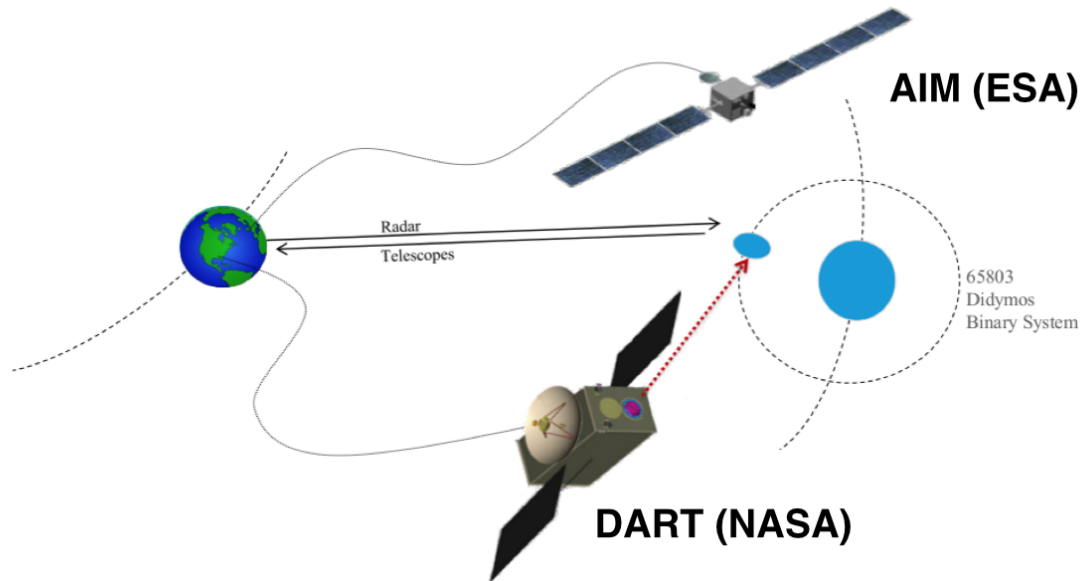


Figure 1.11: The concept of the AIDA space mission from ESA (2016).

1.4 Thesis Overview

In light of the above, the author set out to investigate the behaviour of impactors into different types of regolith material. Many impact studies have been performed looking at the fate of the target, but very few have been devoted to looking at the fate of the impactor. This is important in trying to understand such processes as impact regolith formation as well as the origin of multi-lithological asteroid bodies.

Considering the current knowledge of small body populations, the importance of the impact processes and the experimental work that has been done so far, initially are stated some important questions that remain unanswered. According to the recent findings from the spectral variability of some asteroids, the images of space missions and the diverse compositions of meteorites, we address the problem that arises: **how are the multi-lithology bodies formed?** Considering this problem we experimentally

simulate collisions in the laboratory using the University of Kent's Light-Gas Gun (LGG). Simple materials were used, such as water-ice and fine CaCO_3 powder as the targets and olivine, a common material in the Solar System, as the projectile. The research was focused on the fate of the impactor. Following the experiments a novel method was used to count and measure automatically and accurately the projectile's fragments. Their size-frequency distributions, the implanted mass and a crude Raman spectral analysis are presented from the experiments using different target material, but in the same collisional speed range that overlapped with the low-speed part of the main asteroid belt collisional speeds. Towards the end of this thesis, a discussion is given along with the implications of this work. Finally a summary of conclusions together with thoughts for future work on this topic are also given. In the supplementary material, that is divided in two appendices, are given all the algorithms that the author developed for the analysis of the experiments and the total set of graphs that are included in the main body of the manuscript. The third appendix contains both papers that were published during the PhD along with a list of all publications in international conferences.

2

The State of the Impactor after Hypervelocity Collisions

EVIDENCE is growing for the presence of small bodies with variation in composition, e.g. the multi-lithology asteroid 2008 TC₃ (Jenniskens et al. 2009). Although progress has been made towards a better classification of the physical properties of asteroids, with the results of asteroid surveys and the attempt to link meteorites with their parent asteroidal bodies; recent meteorite findings, imaging of asteroid surfaces from spacecraft and spectroscopic observations, point to the fact that the surfaces and the interior of these bodies might not be mineralogically as homogeneous as was previously thought. Therefore the main question that arises is: **how were small bodies with heterogenous composition formed, where are they in the Main Belt and how abundant are these bodies?**

2.1 Introduction to the Problem

One of the biggest problems that is awaiting a solution is a way to determine the surface compositions of asteroids. The contents of asteroids are currently investigated

by studying meteorites and the samples returned by space missions (e.g. Hayabusa). Through this research it has been found that asteroids are formed mainly of the minerals pyroxene, olivine and plagioclase, and iron rich metals, oxides and sulphides.

Another way to identify the asteroidal surface material is by observing their spectra. However, the majority of the materials on an asteroidal surface do not produce distinct features in reflectance spectra (as the compounds may have no absorption features in the infra-red). In addition, the asteroid spectra are not only affected by the composition, but also of the grain size of the regolith and the effects of space weathering. This last process (Clark et al. 2002), in the case of S-type asteroids, reddens their surfaces in less than $\sim 10^6$ years (Vernazza et al. 2009).

2.1.1 Exogenous Material on Asteroids

(4) Vesta

The surface heterogeneity of asteroids has been detected from ground-based and spacecraft spectroscopic observations, as well as direct imaging of their surfaces. For example, the main composition of asteroid (4) Vesta has been determined since 1970 when McCord et al. (1970), using metre-class telescopes and narrow band filters, reported a strong feature in the 0.9-micron band and associated it with basaltic achondrites, by comparing their telescope data with Nuevo Laredo HED meteorite samples. The link between the HED meteorites and Vesta indicated that the body is differentiated. It was melted early in its evolutionary history, likely due to ^{26}Al and ^{60}Fe decay. This happened about 3 My after the formation of CAIs (calcium–aluminum-rich inclusions) that dated to 4.567 Gy ago (Amelin et al. 2002). A core was formed, surrounded by several layers, which consisted of an olivine mantle, a lower crust with diogenites and

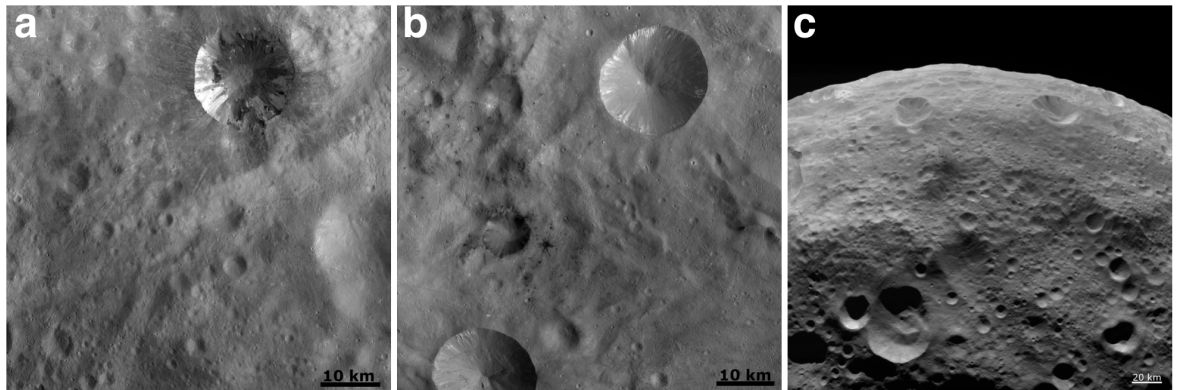


Figure 2.1: Images taken from NASA's Dawn space mission to asteroid (4) Vesta (2011–2012), revealing dark material inside (a) and around (b) impact craters as well as on the top of 'hills' (c). Images from NASA (2016).

an upper crust with eucrites.

NASA's Dawn mission observations revealed a big basin on the surface of Vesta, capable of producing the Vestoids and also the HED meteorites that we have received on Earth (Russell et al. 2012). Spectroscopic data from Dawn of Vesta confirmed also that the surface composition of the asteroids is compatible with the HED meteorites (De Sanctis et al. 2012). Moreover, a compositional variability at both small and large scales, has been also observed, but especially a variability with height (Fig. 2.1). This variability, indicates that the impact bombardment happened after the differentiation of the body (De Sanctis et al. 2012; Russell et al. 2012). With these findings one can assume that this variability is due to a mix of endogenous materials from different layers of the body. Although the largest part of the vestan surface has a grey colour, dark and bright regions have also been found and are associated with impact craters (Reddy et al. 2012a). There has been a debate about the origin of the material of these regions, whether they are endogenic or exogenic material. McCord et al. (2012) reports that although the bright material is freshly exposed after impacts, the dark material can be an implanted material from impacts by low-albedo impactors. Slowly,

via impacts, the mixture of this exogenic dark material with the local brighter material forms the grey background. According to Reddy et al. (2012b) the spectrum of this dark material is similar to that of carbonaceous chondrites mixed with local material, after low-velocity impacts during the formation of the Veneneia basin. The study of Palomba et al. (2014), who analysed 123 dark areas on the vestan surface, came to strengthen their formation explanation via primitive carbonaceous asteroids. But where these impactors came from, when did they hit Vesta, and how was the material deposited on the surface?

(25143) Itokawa

Asteroid Itokawa is an S-type, Mars-crossing asteroid (its orbit crosses the orbit of Mars) that belongs to the Apollo group. It was set as the target body for the JAXA's space mission Hayabusa, which revealed that there is a lack of craters on its surface but there is an abundance of boulders. One of the most interesting features found on the surface of Itokawa was undoubtedly the so-called 'Black Boulder' (Fujiwara et al. 2006), a unique rock with an unusually low brightness (Fig. 2.2). It has a triangular shape and is located at the 'head' of the asteroid, where the gravitational potential is strongest (Hirata & Ishiguro 2011). This indicates that the boulder, after its deposition on the surface, has not migrated since then. One possible scenario to explain the presence of this peculiar rock, different from the background, is that it could have been implanted by a collision event. Space weathering processes are global and would not affect only a selected rock. As a result they could not construct a possible mechanism for the alteration of only this particular boulder, other than an impact origin.

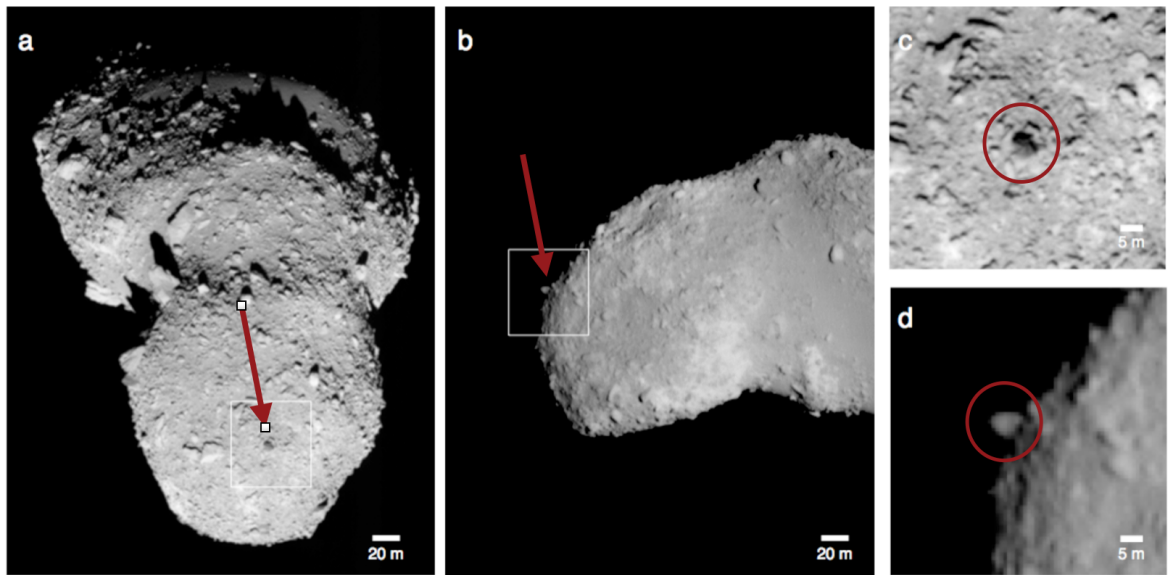


Figure 2.2: Images of the so-called ‘Black Boulder’ on asteroid (25143) Itokawa, taken from JAXA’s Hayabusa space mission (Hirata & Ishiguro 2011).

(21) Lutetia

Asteroid (21) Lutetia is a puzzling small body, as ground-based observations have shown different spectral properties, leading to the speculation that it has heterogeneous surface properties (Belskaya et al. 2010). Later studies performed, after the release of Rosetta data during its fly-by of the asteroid, confirmed compositional and morphological variations over surface (Barucci et al. 2012). Specifically, it varies from carbonaceous to enstatite chondrite-like spectra, and could be due to impacts contaminating Lutetia’s surface with exogenic material. Schröder et al. (2015), after analysing the surface colours and finding large variations in the Baetica crater cluster (Fig. 2.3), also stated that the craters were too small and, therefore, the impacts that formed them could not be energetic enough to excavate and reveal hidden material under the surface layer. So a possible mechanism could be similar to the formation of the dark areas on Vesta (Reddy et al. 2012b).

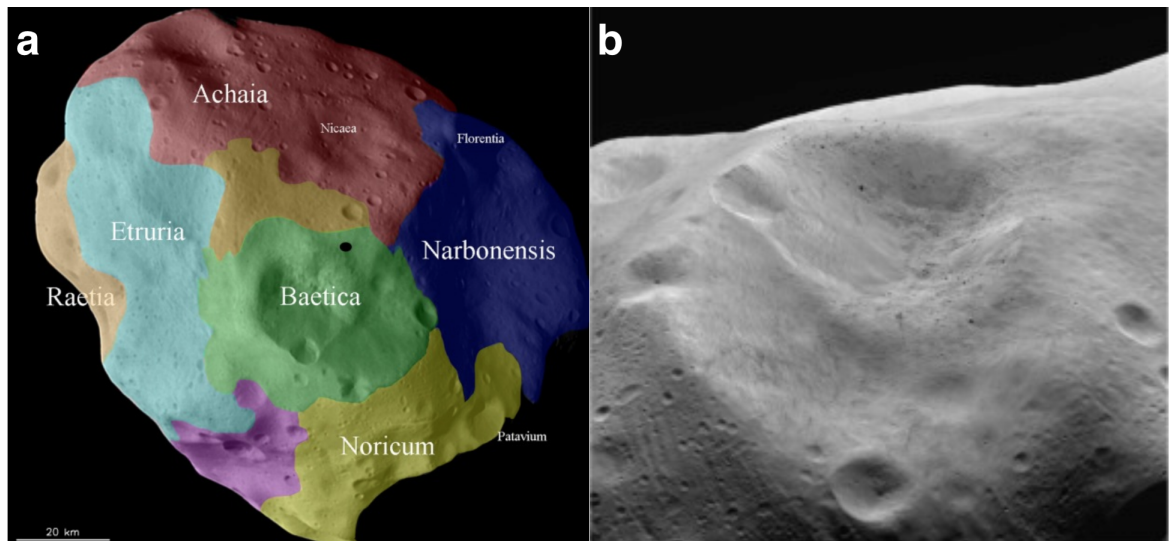


Figure 2.3: Images taken by the Rosetta space mission during the fly-by to asteroid (21) Lutetia, showing (a) the geological variability map of the asteroid's surface and (b) the Baetica crater cluster. The black dot in (a) denotes the north pole of the asteroid. The Baetica region is the youngest area on the asteroid's surface. Images taken from Thomas et al. (2012) and Schröder et al. (2015).

2.1.2 Multi-lithology Meteorites from Multi-Lithology Asteroids?

2008 TC3

Asteroid 2008 TC₃, was a NEA (Jenniskens et al. 2009; Bischoff et al. 2010) that impacted Earth's atmosphere on October 7, 2008 and it is estimated that it exploded approximately 37 km above the Nubian Desert in Sudan. It was the first meteorite fall that was predicted in advance. A large number (~600) of small (0.2–379 g) meteorites were recovered from 2008 TC₃, and are collectively called Almahata Sitta. The big surprise was that those meteorites were of various mineralogical types: analyses of 110 meteorites revealed 75 ureilites, 28 enstatite chondrites (both EH and EL), five ordinary chondrites (H, L, LL), one carbonaceous chondrite (CB) and one which is a previously unknown type of chondrite related to R-chondrites. So summarising the main lithologies are three consisting of (i) pyroxene-dominated, porous lithology,

(ii) a pyroxene dominated, compact lithology and (iii) an olivine-dominated, compact lithology. These various lithologies give clues about the complex evolutionary history of the parent body changing completely our paradigm that one meteorite fall produces meteorites of only one particular type. But how were these different types of meteorite put together into a single body? A recent study by Gayon-Markt et al. (2012) reported that the parent body of TC₃ was located in the Nysa-Polana family region in the Main Belt, and there is only a very small probability that foreign material remained on the surface of a body after low speed collisions with asteroids whose orbits lay in a limited area in a-e space in the Nysa-Polana region and which have different compositions. However, their results were based on the assumption that, in order to preserve the impactor, an impact velocity ≤ 0.5 km/s is required, which is much smaller than the typical impact velocity (about 5 km/s) among random asteroids in the Main Belt (Bottke et al. 1994; O'Brien & Sykes 2011).

Benesov

The second confirmed case of a heterogeneous meteorite is Benesov (Spurný et al. 2014) whose multi-lithology was discovered twenty years after its fall. Surprisingly, one meteorite was an H chondrite, one was LL chondrite and one was LL chondrite with embedded achondritic clasts. The bolide entered Earth's atmosphere with an initial velocity of 21 km/s. Its fragmentation started at high altitude (38–31 km) where it started to produce meteorites; catastrophic disruption occurred at 24 km altitude. The calculations of the dynamical and photometric mass of the Benesov bolide resulted into a huge discrepancy. This discrepancy was overcome by assuming a low density for the body (Borovicka et al. 1998).

2.2 Open questions

All these findings of multi-lithology meteorites, and the identified exogenic material on asteroids, raises some fundamental questions that require an answer in order to shed light on the collisional evolution of small bodies in the Solar System:

- If this formation mechanism via impacts of bodies with diverse compositions is effective, the discovery of impactor residues on a target could reveal details about the impact history of the body and/or the impactor populations? For example, it is now known for the Moon that remnants of impactors do exist, and these exogenous materials can give information of the type and sources of the impactor bodies, and also how the impactors changed during the collisional evolution of our natural satellite (Joy et al. 2012).
- Is there a bias against the meteorites similar to Almahata Sitta and Benesov? i.e. are they so loosely held together that they cannot survive the passage through the Earth's atmosphere and therefore they break apart at even higher altitude than the parent body of Almahata Sitta? These findings shed new light on some old meteorite finds, such as the Galim meteorite fall (LL+EH), Hajmah (ureilite+L), Gao-Guenie (H+CR), and Markovka (H+L) (Borovička et al. 2015). Therefore, asteroids with mixed mineralogies might be more abundant than previously thought, but their formation mechanism(s) remain mysterious (Horstmann & Bischoff 2014).
- Why there is a lack of carbonaceous meteorites found on Earth? If we consider that between one quarter and one third of the NEAs belong to the complex of asteroids with a C-type taxonomy, why are only 1.5% of the meteorite falls

linked to C-type asteroid parent bodies (Burbine et al. 2002, see Table 1.1)? The obvious explanation could be that these meteorite types are more fragile and therefore they fail to survive their passage through the Earth's atmosphere (Borovička et al. 2015).

- If this heterogeneity of bodies is more common than we now think, the theories about asteroid families and their compositions may need to be revised in the future.
- Low velocity (e.g. <0.5 km/s) impacts between asteroids are invoked to explain this mixing, but in the Main Belt the occurrence of such impacts is too low to explain substantial asteroid mixing. One possible solution is that the heterogeneous composition of some asteroids was inherited from a time when the asteroid belt was in a different dynamical state, most likely in the very early Solar System (Gayon-Markt et al. 2012).
- When considering the implantation of exogenic material on an asteroid, we currently assume low-speed collisions. However is it possible to have effective implantation with higher speeds? What is the probability of such higher speed collisions and that they involve different types of bodies?

2.3 Current Status of Experimental Research

Over the last four decades, a plethora of laboratory experiments and computer simulations have provided insights into collisional processes that constitute the foundation of our current understanding of large-scale asteroid collisions and are summarised by Holsapple et al. (2002). The majority of these studies focused on the fate of the target

after an impact (e.g. degree of fragmentation, catastrophic disruption of different materials, crater sizes etc.). They have provided data on the speed and size distributions of the target fragments using several target materials, mostly cement mortar, basalt or ice, while the projectiles are mostly iron, copper, pyrex or basalt. Additional efforts have been devoted to the study of the mass and the velocities of the ejecta (Housen & Holsapple 2011; Michikami et al. 2007).

A very interesting study was performed by Ryan et al. (1999), where they experimented at low impact velocities using the AMES airgun, on the fragmentation of porous ice targets using several projectiles, such as aluminum, solid and fractured ice. These experiments showed that even as the target's porosity increases, it still behaves as a solid material. Assuming that the icy KBOs consist of a mixture of ice and silicates with a high bulk porosity, the collisional outcome can be similar to the one of asteroids. Additionally Flynn (2014) used meteorites as targets, comparing ordinary chondrite samples (with $\sim 9\%$ porosity for the specific sample) with carbonaceous chondrites (with $\sim 23\%$ porosity for the specific sample). He found that porosity plays an important role for the longer survival of the target body compared to the non-porous target bodies due to the quicker attenuation of the impact shock - using the same projectile materials.

However, the fate of the impactor at impact speeds of a few km/s is still very poorly understood. The investigation of the projectile, and projectile debris, during hypervelocity impacts is crucial to explain the observations of mixed mineralogies on the surface of asteroids. Such phenomena, which have been observed only relatively recently (see 2.1.1 and 2.1.2), are the possible source of the olivine and dark material deposits observed on Vesta (McCord et al. 2012; Reddy et al. 2012b) and possibly of the 'Black Boulder' on (25143) Itokawa (Hirata & Ishiguro 2011). Mixing of asteroid

material with different lithology through impacts is also necessary to explain the nature of NEA 2008 TC₃, a multi-lithology body whose formation mechanism is still not completely understood (Jenniskens et al. 2009; Bischoff et al. 2010).

These findings call for new experiments devoted to ascertaining what is the highest velocity that projectile material can be preserved and/or implanted onto asteroids via impacts. Pioneering experiments by Schultz & Gault (1984) and Schultz & Gault (1990) demonstrated a change in projectile fragmentation and cratering efficiency as a function of impact velocity. Recently, Nagaoka et al. (2014) performed several laboratory experiments using pyrophyllite and basalt projectiles fired onto regolith-like sand and aluminum targets. They found that projectile material survived the impacts, although the degree of fragmentation of the projectile depended on the impact energy (Q) and the strength of the projectile, along with the strength and the porosity of the target. However, considering an average impact speed of $v = 5.3$ km/s for collisions in the main asteroid belt (Bottke et al. 1994), the collisional speed range that was tested (<1 km/s) in the experiments of Nagaoka et al. (2014) was at the lower end of the inter-asteroid collisional velocity distribution.

Moreover, Daly & Schultz (2015, 2016) used aluminum and basalt projectiles which were fired onto pumice and highly porous water-ice targets, trying to explain the implantation of an impactor's material onto the vestan regolith, and the possibility of a similar process onto Ceres' surface. They found that material can be deposited via impacts, but the amount decreased with impact angle. However Daly & Schultz (2016) presented results on several impact angles but used impact speeds only in a very narrow regime between 4.4 and 4.9 km/s. McDermott et al. (2016) used copper projectiles impacting porous ($\sim 50\%$) water-ice targets at a wide range of speeds (1.00–7.05 km/s). Their results show that the projectile can be recovered completely intact at speeds up

to 1.50 km/s, whereas it started to break into smaller fragments at speeds above 1.50 km/s. Increasing the impact velocity was found to produce an increasing number of projectile fragments of decreasing size.

2.4 Aim of the Study

All of these recent investigations try to shed light onto the fate of the impactor. The main question that is addressed is how much of the impactor's material is embedded on/into the target by using different combinations of materials, trying to simulate collisions in the Main Belt and on the surface of icy bodies. While the experiments of Nagaoka et al. (2014) were limited to speeds $<1\text{km/s}$, the McDermott et al. (2016) study used only porous water-ice and a copper projectile - which is an atypical type of impactor material in the Solar System.

In this work we advance on the investigation of the fate of the projectile during hypervelocity impacts by firing lithological projectiles, specifically olivine and basalt, onto low and high-porosity water-ice and high-porosity CaCO_3 powder targets, at a range of speeds between 0.30–3.50 km/s. During the analysis we developed novel methods to detect and measure sizes of thousands of impactor fragments down to a size-scale of a few microns. This technique enables us to obtain excellent statistics on the size distribution of fragments of the projectile, which has not been done in any previous work.

3

Survival of the Impactor in Hypervelocity Impacts: An Experimental Approach

IN this thesis we carried out hypervelocity (0.3–3.5 km/s) impact experiments where olivine (peridot) and synthetic basalts projectiles are fired by means of a Light Gus Gun (LGG) onto pure water-ice and CaCO_3 regolith-like targets (schematics in Fig. 3.1). Description of the projectiles and targets are presented in 3.1, the LGG and the experimental protocol in 3.2, and the methods for the data analysis in 3.3.

The experimental campaign was performed over 13 months in total, including the shots, analysis and interpretation of the results. During this campaign a standard procedure for each individual target type was developed and carefully followed in order to secure to a maximum level the reproducibility of each shot. The scientific interest is motivated by recent discoveries in planetary sciences, such as multi-lithology meteorites and dark material on the surfaces of non-dark asteroids. All these features can be explained by impacts between asteroids of different types, which call for detailed studies of the fate of the impactor after a hyper-velocity impact. Therefore, we used materials

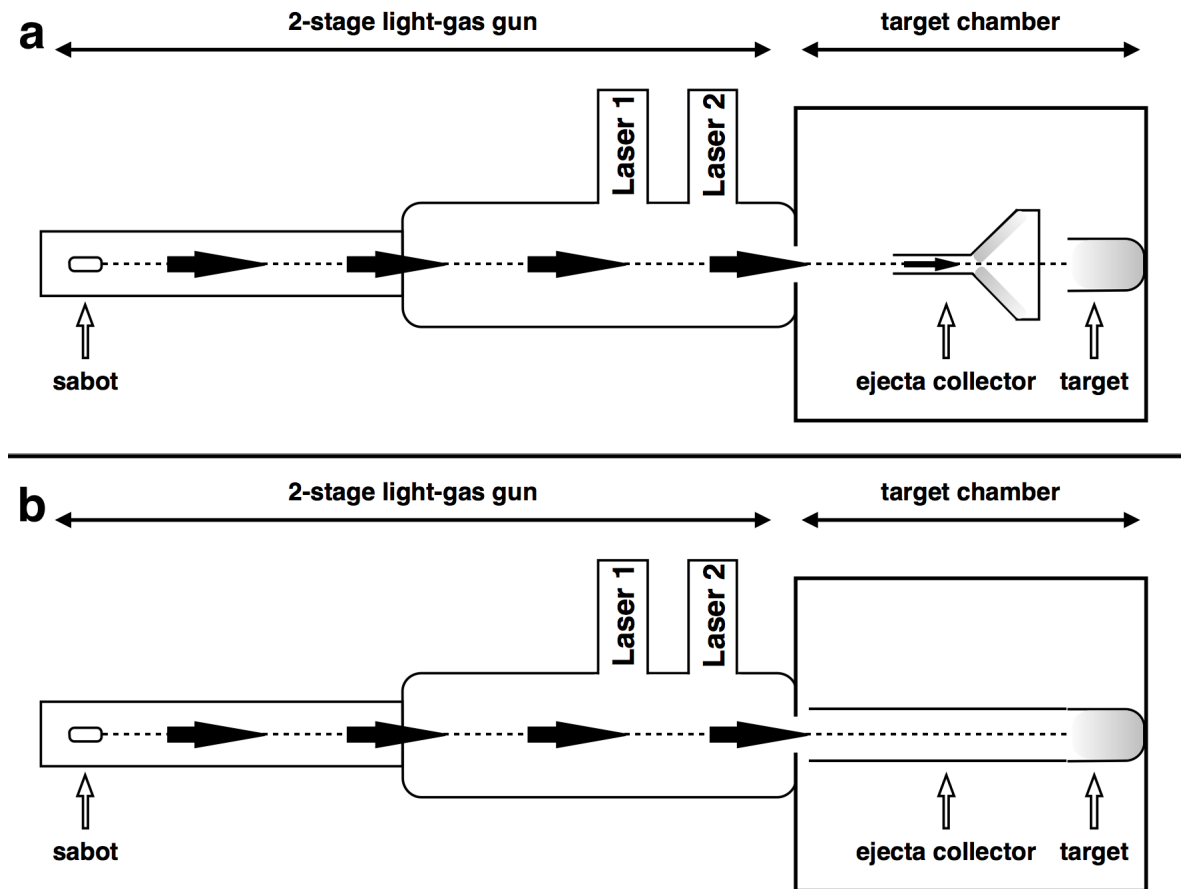


Figure 3.1: The experimental set-up, used for the icy (a) and regolith-like (b) targets, showing the projectile, which was placed inside a sabot (isoplast cylinder to hold the projectile at the beginning of the launch), inside the two-stage LGG, and the configuration of the target chamber (Avdellidou et al. 2016). The projectile impacts the target at 0° with respect to its trajectory (dashed line). The ejecta collection funnel (a) was aligned with the flight path of the projectile and the centre of the target. It contained water-ice layers in order to collect the projectile's debris after the impact. For the regolith shots a plastic tube was used to capture all the ejecta with no extra coating (b).

and speeds that could be encountered in small bodies populations but also allowed us to analyse the outcomes from these experiments. The physical parameters that we tried to measure were both macroscopic, such as the energy density at the impact and the impactor's embedded mass in the target, and microscopic, such as the change in material structure due to impact shock.

3.1 Projectile and Target Materials

The main goal of this thesis is to go beyond the previous experiments. This study is devoted to the fate of the projectile, and makes use of materials that are more representative of the mineralogy of small bodies. In order to unambiguously separate projectile fragments from those of the targets and gun contamination, we used a high purity, Mg-rich olivine - in the form of a gem quality peridot (Fig. 3.2 a, b) - and synthetic basalt glass spheres (Fig. 3.2 c) as projectiles. The targets were prepared with high-purity water-ice or CaCO_3 powder.

3.1.1 Projectiles

These materials were also chosen as:

- (a) olivine is one of the most common minerals in the Solar System. Olivine and pyroxenes are the primary silicate minerals in stony and stony-iron meteorites, 75% of chondritic meteorites and 50% of pallasites (Petrovic 2001; Gaffey et al. 2002);
- (b) Mg-rich olivine (fosterite) has been detected in the spectra of several cometary tails and is present in the majority of comet Wild 2 samples returned by NASA's *Stardust Mission* (Zolensky et al. 2006);
- (c) parallel studies of the spectral features of the dust particles, observed in exoplanetary system β Pictoris (de Vries et al. 2012), confirm similar abundance of Mg-rich olivine in areas far from the host star, as similarly happens to our Solar System (Mg-rich olivine mostly found in large heliocentric distances). However, it has been reported (Sanchez et al. 2014) the existence of olivine-dominant aster-

oids in the Main Belt (A-types), which consist fragments from differentiated large parent bodies. Comparing their spectra with meteoritic spectra (from R chondrite meteorites) which were obtained in the laboratories (Reddy et al. 2011), was found that some of these asteroids (such as 354 Eleonora and 1951 Lick) appear to have Mg-rich olivine.

- (d) Fe-rich olivine (i.e. fayalitic pyroxene) is mostly encountered in asteroid mineralogies (Nakamura et al. 2011) and, therefore, in the warmer, inner parts, of planetary space (Olofsson et al. 2012). Possible explanations for this distribution of the different types of olivine are: (1) the presence of water on comets which leads to aqueous alteration, as the fayalite may not survive in the presence of water (Olofsson et al. 2012) and, (2) the higher abundance of heavier elements, such as Fe, in the inner Solar System;
- (e) basalt is considered to be the main material on the surface of the differentiated asteroids and planets. Differentiation, which leads to a multi-layered body with core, mantle and crust and the production of basalt, is thought to have occurred in the early Solar System. It is found in the basaltic eucrites and howardites of the HED meteorites (McSween et al. 2011) which are linked with asteroid Vesta (Russell et al. 2012). As the most likely heat source for differentiation is the decay of radioactive isotopes (e.g. ^{26}Al , ^{60}Fe) and the accretion time to form a planetesimal increases with increasing distance from the Sun, it is more plausible that differentiated asteroids existed mainly in the inner Solar System ($a < 2$ au) (Bottke et al. 2006);
- (f) although initially it was commonly thought that basalt is associated only with asteroids which have similar spectrum, and are dynamically connected with Vesta,

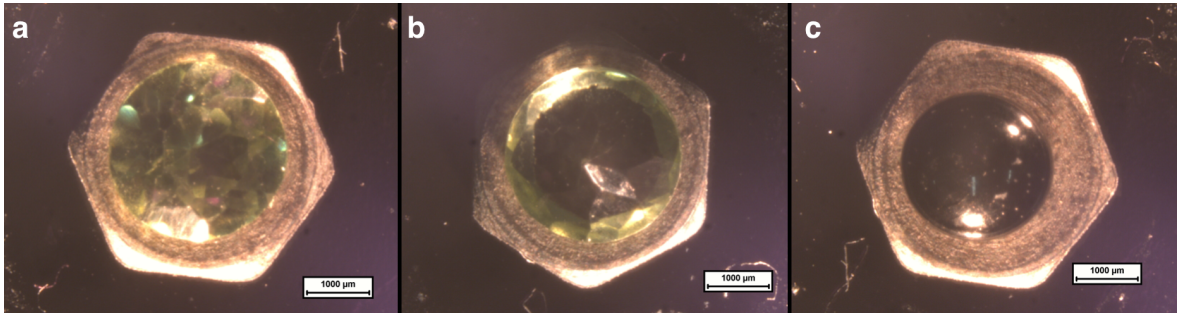


Figure 3.2: Front (a) and back (b) side of peridots and spherical (c) basalt projectiles that were used for this work. (Image credit: Taken by author.)

Table 3.1: The characteristics of the projectiles used for all shots (*data from Petrovic (2001) and Schultz (1993)).

Projectile	shape	size	avg. mass	strength*	density
forsterite olivine	gem	3 mm	23.6 mg	80 MPa	3.217 g/cm ³
synthetic basalt	sphere	2.0–2.4 mm	15.55 mg	100–262 MPa	not available

observations have shown that V-type asteroids do also exist in other locations in the Main Belt (Moskovitz et al. 2008).

The peridots are high quality gemstone olivine with a brilliant cut, with no visible inclusions or cracks. Additionally their composition was very uniform (measured using Raman spectroscopy and verified by quantitative Energy-dispersive X-ray spectroscopy) and found to be $\text{Mg}_{82}\text{Fe}_{18}\text{SiO}_4$ using the simplified equations of Foster et al. (2013) with a compositional variance across the surface of 1% (Fig. 3.2).

The basalt projectiles were not a natural basalt rock but synthetic spheres, sourced from ‘Whitehouse Scientific’ with a composition of SiO_2 (43%), Al_2O_3 (14%), CaO (13%), Fe_2O_3 (14%), MgO (8.5%), $\text{Na}_2\text{O}/\text{K}_2\text{O}$ (3.5%) and others (4%). These projectiles are homogeneous and compositionally identical and thus we maximise the reproducibility of the shots.

3.1.2 Targets

For the purposes of our work, simulating collisions at laboratory scales, it is essential to know the mechanical properties (strengths and micro/macro-porosity) of small Solar System bodies. Several literature sources give the compressive and tensile strength for a series of meteorites (analogues of asteroid surfaces), however the number that has been studied is very limited. Popova et al. (2011) summarises data from several meteorites, giving the ranges of compressive and tensile strengths to be 20–450 MPa and 2–62 MPa respectively for L ordinary chondrites, and 77–327 MPa and 26–42 MPa for H ordinary chondrites. However, the calculated bulk strengths during entry of similar type meteoroids into the Earth’s atmosphere are much lower than the above-quoted strengths. The average meteorite microporosity for the different types of ordinary and carbonaceous chondrites ranges between 6–16%. However, only the largest asteroids seem to have comparable bulk porosity with their equivalent meteorite microporosity. The average bulk porosity for the S-type asteroids is $\sim 30\%$, while for C-types is around $\sim 40\%$ (Britt et al. 2002). As the porosity of a body increases, the strength decreases, which could be an explanation for the big difference between the calculated, and observed, strength of bolides. This may explain the high altitude where some meteoroids start to disrupt and also the greater abundance of ordinary chondrites compared to carbonaceous chondrites among the meteorite samples.

In order to start this study and investigate a range of porosities and strengths, we used for the first run (Run#1) of experiments a high purity water-ice target of low porosity ($<10\%$), comparable to the microporosities of the examined meteorites. For the second run (Run#2) of experiments high purity water-ice targets were also used but with higher porosity ($\sim 40\%$), comparable to the bulk porosities of C-type asteroids. In

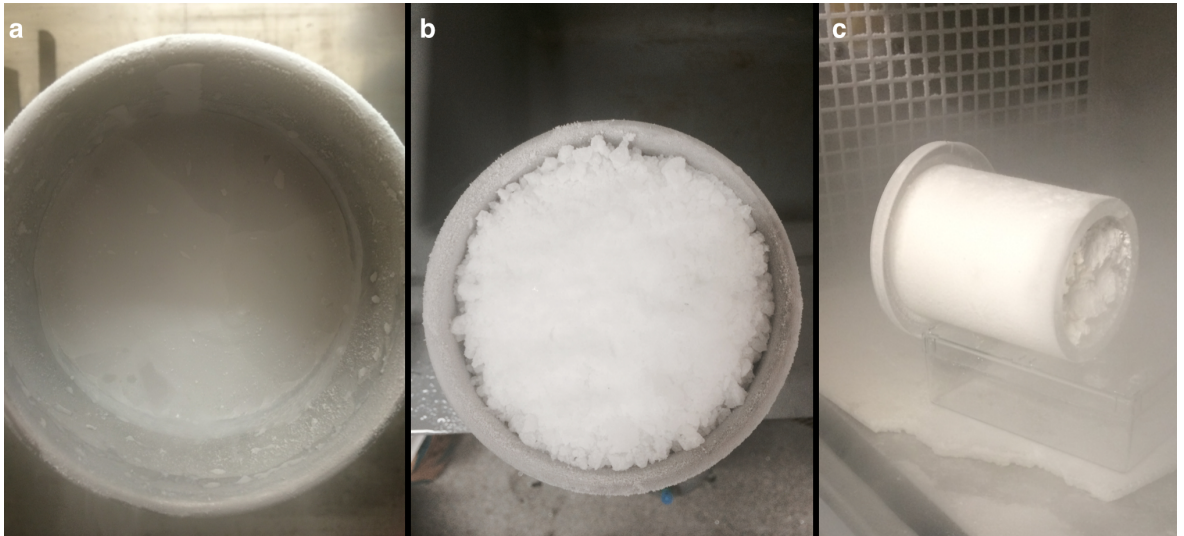


Figure 3.3: The three different targets that were used in the experiments we made of a) solid water ice with porosity $<10\%$, b) crushed water ice with porosity $\sim 40\%$ and c) CaCO_3 powder with porosity $\sim 70\%$. (Image credit: Taken by author.)

the third run (Run#3) the projectiles were fired on to very fine CaCO_3 powder with very high porosity ($\sim 70\%$) therefore examining an extreme range of porosities. This was also chosen because one of the main aims of this study was to attempt to recover projectile fragments within the target. By using a water-ice, the targets of Run#1 and Run#2 only had to melt and the resulting water filtered through clean, $0.1 \mu\text{m}$ pore-size filters to recover the projectile fragments. The target material of Run#3 was dissolved in nitric acid leaving behind the projectiles fragments that were unaffected by acid.

Prior to this target selection, several tests were performed to verify the procedure. Big peridot fragments (a few mm) and finer (peridot powder of μm) were placed inside nitric acid for several days and showed no damage under the microscope due to dissolution. The CaCO_3 powder was almost completely dissolved leaving residues $\sim 1\%$ according to supplier (Sigma-Aldrich/Part #: 310034). Below we detail the prepara-



Figure 3.4: The liquid nitrogen freezer in the Impact Lab where the targets were frozen down to -130°C before each shot. Image credit: Taken by author.

tion method for each target:

- Run#1: Each water-ice target was prepared and frozen following an identical procedure for each shot. A stainless-steel cylinder was filled with high purity water. It was first frozen down to -20°C and then placed into a liquid nitrogen freezer (Fig. 3.4), which decreased and held the target's temperature down to -130°C (Fig.3.3a). The elapsed time from the time that the target was removed from the liquid nitrogen freezer and placed into the LGG's target chamber until the shot was approximately 10 minutes. Tests that were performed prior to



Figure 3.5: For Run#2 the icy target was prepared by spraying high purity water into liquid nitrogen. Image credit: Taken by author.

experiments showed that when the target was exposed to room temperature (same part of the laboratory) its temperature increased up to -50°C in the same amount of time. This is important to note, as the strengths of the ice (both tensile and compressive, but to different degrees) increase with decreasing temperature. The porosity of our targets was measured to be $<10\%$ and was determined by making a test sample of ice in an identical way to the targets in a cubical plastic box. The box was slightly under-filled with water so that a void remained at the top of the box after freezing. To measure this volume, a small amount of chilled ethanol (at -30°C) was injected into the box. Since the mass and volume of the box are known, as well as the volume of injected ethanol and the temperature of pure water-ice (and hence density), the porosity was calculated.

- Run#2: For these targets the same ice as for Run#1 was used but with increased porosity. The School of Physical Sciences owns an ice-cube production machine.

However, there were two major drawbacks of the use of this ice: 1) the crushed ice was kept at relatively high temperature (between $+2$ and -2°C), thus it was wet. When it was then frozen down to -130°C it formed a solid mass, not appropriate for the shots; 2) after filtering, the melt of this crushed ice left a large amount of residues indicating that it was not pure enough to be used for these experiments. As a result the targets had to be made using a new procedure developed for these experiments.

The most effective way to produce small ‘grains’ of ice (a few microns to a few mm, comparable with the projectile size), giving the desired final porosity, was to spray high purity water, the same that used for Run#1, directly into liquid nitrogen (Fig. 3.5). The water droplets were frozen instantly down to 77 K. When the metal cylinders were filled with the crushed ice (Fig. 3.3b), they were put into the liquid nitrogen freezer to be kept at -130°C until ready to be shot at. The same procedure as for the targets in Run#1 was kept because we wanted to make sure that the icy targets were at the same temperature in both Runs.

- Run#3: CaCO_3 powder was placed inside a plastic cylinder compressed in such a way to give porosities of $\sim 70\%$. Then the target was placed as before inside the liquid nitrogen freezer (Fig.3.3c). The unavoidable condensation of water vapour onto the target during its time inside the freezer helped to stabilise the surface of the target. However, we assume that the water condensation was not extended, as the target’s surface was not wet a few minutes after the shot, when we were able to inspect. That was a very crucial point as shots onto surfaces consisted of small grains are difficult with the horizontal firing Light Gas Gun of the Impact Laboratory.

Table 3.2: Physical parameters for the targets. The density refers to the grains of each target. (*data from Petrovic (2001)).

Target	material	strength		density	porosity
		compressive	tensile		
Run#1 LPI	water-ice	35 MPa*	3 MPa*	0.934 g/cm ³	<10 %
Run#2 HPI	water-ice			0.934 g/cm ³	35–40%
Run#3 HPR	CaCO ₃			2.71 g/cm ³	70%

3.2 Experimental Protocol

The methodology consists of seven steps:

1. Initially physical characterisation of the pre-impact projectiles was carried out; measurement were made of their sizes and masses, and Raman analyses were performed. Raman spectroscopy (see 3.3.4) was used for peridot projectiles to identify possible Raman line shifts due to deformation of the projectile's crystal structure induced by the impact shock. This was not the main aim of this thesis, however provided complementary data for other ongoing programmes within the laboratory.
2. The projectiles are fired onto the targets. The formation of impact craters was observed, although, due to the ephemeral nature of the target, they were not measured. The projectile and target material, along with contaminating residues from the gun, were collected by our set up (ejecta collectors – see Fig. 3.1).
3. All projectile fragments were collected and visually inspected to identify the largest ones. The ratio between the mass of the largest fragment to the initial mass of the projectile, gives information about the degree of fragmentation of the latter (see 3.3.2).

4. The target material from the target container and the ejecta collector are removed, after melting or dissolution in acid, and the projectile fragments, plus contaminating gun debris, are filtered through two different types of filters with different pores sizes ($0.1 \mu\text{m}$ for the target (Sigma-Aldrich part # P9825) and $5 \mu\text{m}$ for the ejecta (Sigma-Aldrich part # P9074)).
5. Additional, post-impact Raman spectra provided indication of any crystallographic alteration or deformation of the recovered fragments (see 3.3.4).
6. The filters were then mapped using a Scanning Electron Microscope (SEM – see 3.2.2).
7. The final phase consists of analysing the data from the SEM, discriminating projectile fragments from gun detritus and allowing us to build the size frequency distributions (SFDs) of the fragments and quantify the amount of projectile embedded in the target (see 3.3.2 and 3.3.3).

3.2.1 The Light-Gas Gun

The gun used to perform the experiments was the horizontal two-stage Light Gas Gun (LGG) at the University of Kent (Burchell et al. 1999). It fires a shotgun cartridge in the first stage, which drives a piston to further compress a pressurised light gas in the pump tube. This gas is then suddenly released from its high pressure when a retaining disc of aluminium ruptures. This releases the gas into the second stage, where it accelerates the projectile. The projectile, which is placed in a sabot made of isoplast, is launched and travels down the gun range. The four independent parts of the sabot are removed during launch, letting the projectile to fly alone down the range and enter the target chamber.

Two laser light screens are placed downrange and record the time of flight. The known separation of the two lasers, plus the time taken for the projectile to cross between the two laser screens, gives the speed (to within $\pm 0.2\%$) of the projectile before it enters the target chamber and impacts the target. It should be noted that since the publication of Burchell et al. (1999), the Impact Group has developed the ability to fire non-spherical projectiles such as, for example, gem-stones (as used here) and icy projectiles (Price et al. 2013).

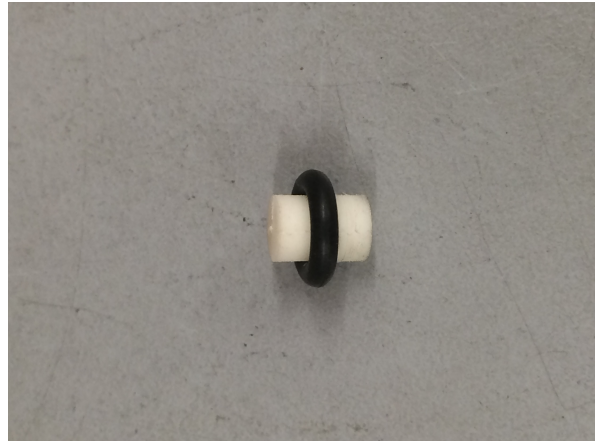


Figure 3.6: The projectile is placed inside a sabot. During flight, the four quarters of the sabot are removed by centripetal forces and only the projectile reaches the target.

The pressure measured in the target chamber was no less than 50 mbar, due to the continuous sublimation of the ice target during the experiments. The impact angle was always 0° . Here zero degrees is defined as impacting parallel to the impactor's trajectory, and 90 degrees to the target's ambient plane. According to numerical simulations, which were applied to craters on the Moon's surface (Bland et al. 2008), the biggest proportion of the impactor's material remained in the crater for impacts occurring at 0° angles (see Fig. 3.1). A decreasing amount of projectile material is expected to be embedded in the target with increasing impact speed and impact angle, as has been demonstrated for the Moon's surface by Bland et al. (2008) and, more recently, by Daly & Schultz (2016) and, Daly & Schultz (2015) for asteroid surfaces.



Figure 3.7: The two-stage Light Gas Gun of the Impact Group, University of Kent. Image credit: Impact Lab.

3.2.2 Experimental Setup

As one of the aims of this project was to measure the size frequency distribution of the projectile's fragments after impact at different speeds, two different setups were developed and constructed to collect the ejecta (see Fig. 3.1). As the projectile entered the target chamber it flew through the ejecta collector, and hit the centre of the target. Ejecta from the target was ejected and captured by the interior surface of the collector. The effect of the Earth's gravity is an important extra factor in these experiments, as the gun is fired horizontally, as such loosened material that might otherwise remain in

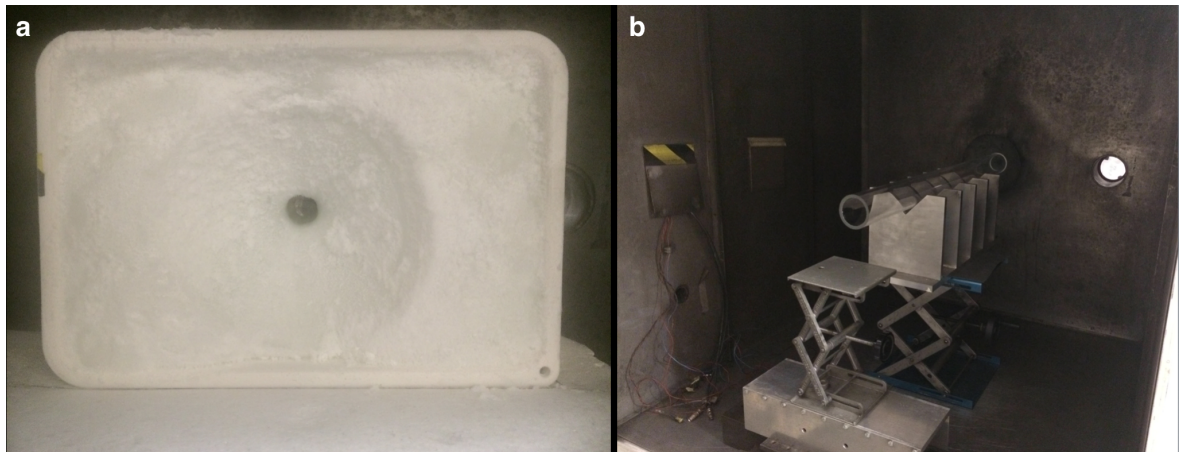


Figure 3.8: For Run#1 and Run#2 a plastic funnel with an internal water-ice internal coating was used to capture the ejecta, for Run#3 the funnel was replaced with a plastic transparent tube that covered the whole length of the chamber.

a crater in a minor body impact, will here be lost as the Earth's gravity acts to pull it out of the crater. This indicates that our results for the implantation of the impactors material, as described in section 4.2, correspond to a minimum value.

- Ejecta collector for Run#1 and Run#2: For the icy targets a funnel with an internal water-ice layer (high purity water) of a few cm (2–5 cm) was developed (Fig. 3.8a). After each shot, the funnel was removed and the ice allowed to melt. In an identical way to the target, the melt ice was filtered and the majority of the projectile fragments were collected on a filter. Any ejecta that travelled backwards at small ejection angles ($4.7^\circ \pm 0.3$) as measured from the projectile's trajectory, was able to escape the funnel, but was collected directly from the target chamber floor which had been covered before the shot with sheets of clean aluminum foil.
- Ejecta collector for Run#3: For the regolith (CaCO_3) targets a slightly different collection system was tested which consisted of a plastic tube (Fig. 3.8b) placed

between the target and the entrance to the chamber from the gun range, aligned also with the trajectory of the projectile as shown in Fig. 3.1. After each shot all the ejecta was collected, dissolved in nitric acid and filtered. Thus, all the fragments were also collected on a filter. The advantage of this setup was that no fragments exited the collecting system and fell on the chamber's floor. In that way the loss of projectile fragments was minimised.

The use of a water-ice collection system led to a simple recovery technique of the ejecta fragments. However, secondary fragmentation is possible as the ejected projectile fragments can hit the ejecta collection system and break again to smaller pieces introducing a bias to the size frequency distributions (SFDs) of the ejected fragments. This is an unavoidable process, using any sort of practical collection technique we can employ. In these experiments the secondary fragmentation is deemed minimal, as the speed of ejecta is only a small fraction of the impact speed (Holsapple et al. 2002; Burchell et al. 2012). Additionally the ejecta fragment size is smaller than the projectile's size, and therefore less prone to fragmentation due to its smaller size - although we do acknowledge that these fragments have been shocked and weakened during the primary impact process.

3.3 Data Analysis Methods and Tools

3.3.1 Analysis Devices

Scanning Electron Microscope (SEM)

In order to count the number, and measure the sizes, of projectile fragments we used a Scanning Electron Microscope (SEM) in the School of Physical Sciences. This SEM (a

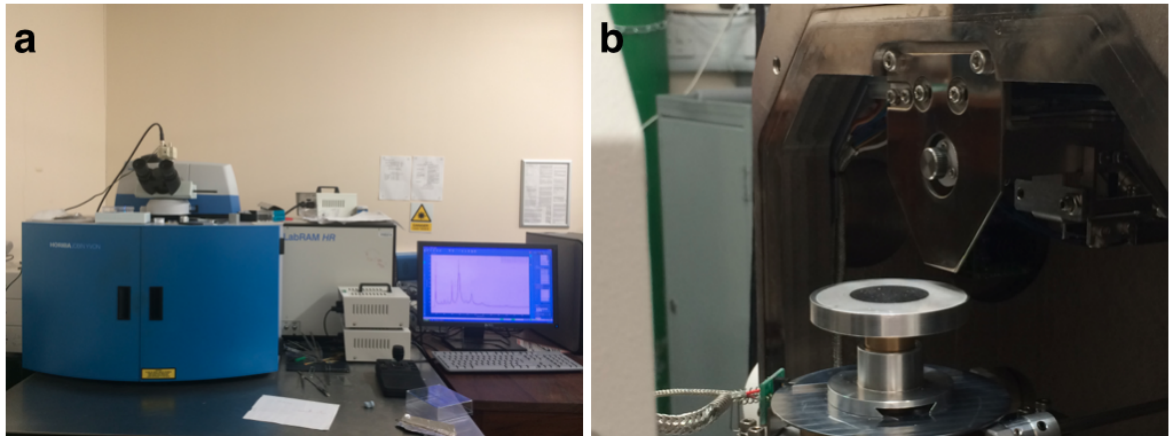


Figure 3.9: (a) The Raman spectrometer and (b) the SEM of the University of Kent. Image credit: Impact Lab

Hitachi S-3400N) has the ability to run long scans (upto 24 hours) with high magnifications, mapping the surface of the filters (see Fig.3.9b). For each one of the images obtained with the microscope, the on-board Energy Dispersive X-ray (EDX) spectrometer (Oxford Instruments ‘Xmax-80’) was used to generate elemental maps. As the composition of the projectiles is well defined, the EDX maps enabled the identification of their fragments and distinguish them from contaminating gun residues. The procedure will be described analytically in section 3.3.2. As a result the datasets include, for each field of every filter, SEM BSE images and EDX maps. Due to the limitations of the performance of this instrument, it was not able to run maps longer than 24 continuous hours, due to degradation (or failure) in the tungsten filament of the instrument. This led to darker SEM images and fainter EDX images, or even be burnt. Another drawback of the instrument was that it could drift out-of-focus during long maps, something that affected mostly the quality of the SEM images. However, because this study was based on the EDX maps, the result of the work was not affected.

Raman Spectrometer

The final part of the investigation includes a brief study of the projectiles' fragments that were recovered after the collision. For this purpose the Raman spectrometer (a Horiba 'LabRam-HR') within the School of Physical Sciences (Fig. 3.9a) was used to observe any change in the Raman spectra of the fragments after impact shock. The Raman spectrometer is equipped with lasers in four different wavelengths, IR at 784 nm, Red at 633 nm, Green at 532 nm and Blue at 468 nm. The monochromatic laser beam interacts with the sample resulting in an inelastic scattering of photons. The incident photons interact with the molecules and either lower or excite their rotational and vibrational energy levels. The IR laser beam is more dispersed on the diffraction grating (1800 lines per mm) of the spectrometer than the other lasers. As a result, the light on the CCD detector has higher resolution, which means more wavenumbers (cm^{-1}) per pixel. Because the IR laser gives the highest spectral resolution the fragments were examined using this laser wavelength in order to try and constrain any possible change in the Raman spectra. Measurements were consistently made with a $\times 50$ objective, giving a spot size on the sample of approximately 2 microns in diameter. Prior to any measurements, the spectrometer was calibrated with a pure silicon sample, which has a high-intensity Raman line at 620.1 cm^{-1} which is widely used as a calibration standard (and as recommended by the manufacture). Mineralogical standards (i.e. San Carlos olivine) obtained from the Natural History Museum (London) were additionally used as a secondary check of the quality of the spectra obtained as well as library spectra from the 'Ruff' database (Ruff 2016) provided by the Dept. of Geosciences, University of Arizona. The spectrometer was also located in a temperature stabilised room to minimise calibration drift during the measurements.

3.3.2 Analysis 1: Projectile Fragmentation–Largest recovered fragment and SFDs of ejecta

The first step after each shot was to search for the largest surviving fragment of the impactor. This was done by visually examining the crater in the target before it was dissolved, as well as the floor of the target chamber and the ejecta collector.

In Run#2 the vast majority of large fragments were recovered from the target while in Run#3 all of the fragments were recovered from the target. Interestingly, in Run#1 for all but one of the peridot shots the largest fragment was found on the target chamber's floor, implying that this largest fragment must have 'bounced' backwards along its original flight path after impacting the target. For the spherical synthetic basalt projectiles all the largest fragments were found in the ejecta funnel, except for one shot where the largest fragment was recovered from the crater in the target. For each shot, the mass ($M_{1,f}$) of the largest recovered fragment was measured with a high precision scale (AND BM-20) at the University of Kent, with a precision of $0.1 \mu\text{g}$.

An important quantity to derive for the projectile fragments is their size fre-



Figure 3.10: After each shot the melt water (Run#1) or the solution (Run#3) was filtered through PTFE filters with hole sizes $0.1\text{--}5 \mu\text{m}$. Image credit: Taken by the author.

quency distribution (SFD): for instance, steep cumulative SFDs are indicative of projectiles being pulverised by the impact, whereas shallow cumulative SFDs indicate that large fragments coexist with small ones. Moreover, the size at which the differential SFD has peaks (or a peak) indicates the typical dimension of the fragments. These peaks are also called fragmentation modes. SFD calculations were made by measuring the sizes of the impactor fragments stopped by, and accumulated on, the ejecta collector or picked directly by hand from the target chamber floor.

In order to identify the fragments which could not be identified optically, we melted the ice of the ejecta apparatus or dissolved the CaCO_3 powder and filtered the resulting water through polytetrafluoroethylene (PTFE) disk filters (Fig. 3.10), to separate and expose the projectile fragments it contained ready for study (identification and measurement) in the SEM. These filters contained the projectile fragments mixed with contaminating material from the gun. These were fragments from the burst-disc, sabot, shotgun cartridge and any particulates picked up from the range during repressurisation of the target chamber. The majority of this material is C, Fe, Al and Si-rich (see Fig. 3.13a), but is of a size (a few - 100s of microns) comparable to the projectile fragments we were interested in. This, currently unavoidable, contamination led us to develop a novel way to discriminate, count and measure the peridot fragments in the ejecta (described below) and later in the target (see section 3.3.3).

The effective area of each filter that contained the particles was a circle with a diameter of 35 mm (for Run#1 and Run#2) and 16 mm (Run#3), with hole sizes $5\ \mu\text{m}$ (for all Runs) to collect the ejecta fragments. We initially used a large in area filter for the ejecta of the first two Runs, as we assumed that the majority of projectile fragments would escape in ejecta. For Run#3 we noticed that less ejecta fragments were produced, and so we reduced the filter area. In that way they would be more

concentrated on the filter surface and each frame (in BSE imaging) would include enough number of fragments for our statistics. However the result was not affected by the choice of the filter size as the selection of filter size was constant for all Runs.

Images of the projectile's fragments were obtained by scanning the filters using a Back-Scattered Electron detector (BSE) on the department's SEM. The accelerating voltage that was used was always 30 kV, as more energetic electron beam was needed to get a strong signal back from the samples and have well distinguished fragments from the background. EDX maps of the same fields were taken simultaneously in order to distinguish projectile fragments from any contaminating material. We thus recorded information about the elemental composition of the sample. Considering that: (i) the peridot projectiles are rich in Mg and, (ii) there is no Mg contamination from gun debris, we used the EDX maps of Mg to discriminate the projectile fragments (see Fig. 3.13b) from contaminating gun debris.

For Run#1 we acquired BSE image and EDX maps consisting of 50 frames (each BSE image and EDX map had the same resolution), this was acquired for 30 minutes per frame, which translates to 18-20 EDX scans per frame. Each frame contained hundreds of fragments (see Fig. 3.13b) and was taken with a magnification of $\times 300$, giving a pixel scale of $0.4 \mu\text{m}/\text{pxl}$ (in both BSE images and EDX maps), thus enabling us to detect the smallest fragments. Run#2 and Run#3 produced much less ejecta, thus we reduced the magnification and the acquisition time per frame (16-18 EDX scans per frame). We acquired maps for Run#2 with magnification $\times 150$ and $\times 300$ and for Run#3 $\times 100$.

For EDX spectra the X-ray intensity is usually plotted against energy. They consist of several, approximately Gaussian-shaped, peaks being characteristic of the elements present in the interaction volume (Fig. 3.11). Most of the chemical elements can be

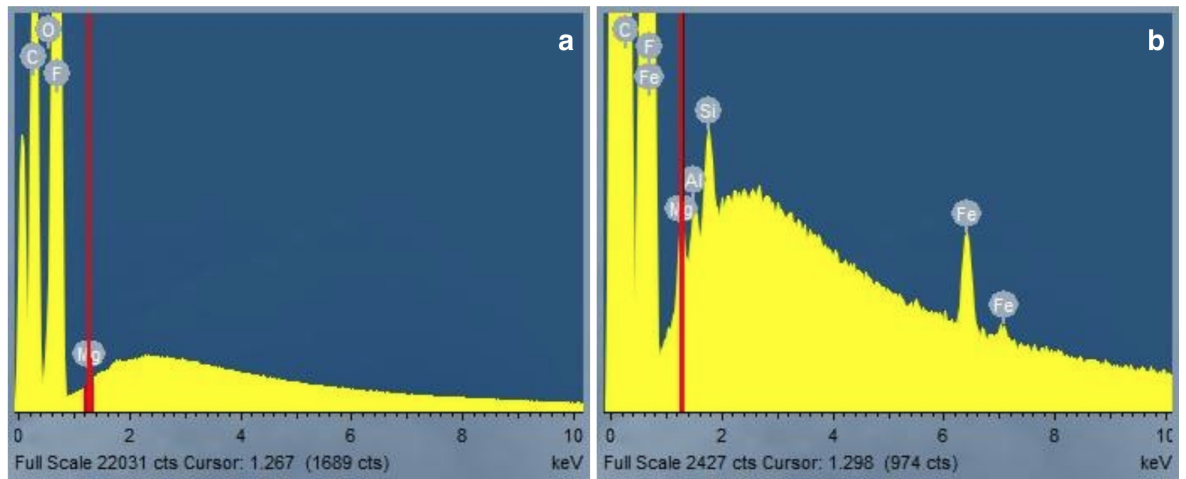


Figure 3.11: (a) The background Bremsstrahlung radiation measured using a blank filter and the (b) superimposed X-ray lines using a filter with material from ejecta and gun debris. The red solid line indicates the area of Mg in the energy spectrum. The X-ray lines of C and F correspond to the PTFE filter that was used in both cases. Both were point spectra.

identified by EDX spectroscopy. In an electron-excited X-ray spectrum the discrete X-ray lines are superimposed on a continuous background. This is the Bremsstrahlung continuum ranging from zero to the primary energy E of the electrons. The reason for this continuum due to electrons emitting X-rays when they are decelerated in the Coulomb field of an atom. As a result, the upper energy limit of X-ray quanta is identical to the primary electron energy.

Many researchers within this field so far use very simple, or inaccurate, methods to collect, identify and measure the ejecta (or fragments embedded in the targets). For example they use paper filters where the smallest fragments become mixed with the paper's fibres, making the separation/identification extremely difficult. Also, in many works, the SFDs that are presented are based only on the largest fragments that can be collected and measured with the naked eye. Another example of inaccurate identification of the fragments and separation of the gun contamination is the subtraction of the total SFD from a statistical one that corresponds only to the gun debris (obtained

by firing an empty sabot). However, our experience has shown that there is not a constant debris amount for each shot (so the ‘blank’ SFD will be different for each shot) and that this is related also to the impact speed as the sabot will accelerate a different amount and different gas pressures are used to obtain different speeds. This means the rupture of the burst disc and the amount of contaminating dust picked up along the range will be a function of the speed and thus the SFD of a ‘blank’ shot will not be constant. Manually counting the fragments and measuring their dimensions is, therefore, extremely time consuming and prone to observer bias.

Here we developed a new, novel method to solve this problem. All the post-analysis was based on the EDX datasets, as using the elementary maps the identification of the projectile’s fragments and discrimination from gun debris was easy and accurate. The INCA software of Oxford Instruments, which is used to control the SEM and record data, did not include a routine for the fast extraction of the EDX maps in individual frames. This work had to be done manually ‘by hand’, a task that could have taken weeks to be completed. After requests to Oxford Instruments’ software engineers, they kindly provided experimental software as an extension to INCA. With this extension the extraction of hundreds of frames was done in only a few minutes. It was possible to extract the raw data, which were actually data cubes by selecting specific channels in the whole channel. We carefully selected 15 channels according to the Gaussian of the Mg signal. In this way we avoided any interference with the counts of other nearby elements. This help of Oxford Instruments greatly increased the efficiency of the analysis and the outcome of the final results.

However, even working with EDX maps the identified fragments (many 10s of thousands) were too many to be counted manually. To tackle this, a fast and automated way to process the data was developed by the author using her experience in astro-

nomical data reduction. An astronomical photometry technique was applied to each frame using the Source Extractor ('SExtractor') open source software for astronomical photometry (Bertin & Arnouts 1996). SExtractor is a program that builds a catalogue of objects from an astronomical image. The software was specifically written to automatically identify and measure extended light sources, such as galaxies, within astronomical images. To prepare the SEM-EDX images to be suitable for use by SExtractor, the raw data images were first converted to 16-bit Flexible Image Transport System (FITS) files, making sure that there was no loss of information through the transformation.

Unlike stars and most galaxies, which are well defined circular or elliptical sources, mineral fragments are irregular in shape. In addition the fragments give illuminated pixels on a frame which correspond to their real 2D area. Stars, on the contrary are point sources and they get their multi-pixel area on the CCD detector due to the effect of the turbulence of the atmosphere (photometric 'seeing') and due to the telescope optics which are diffraction limited. Therefore, to measure the total X-ray emission from a fragment, we did not use the usual aperture method for photometry. By using the normal aperture for photometry, illuminated pixels are left out of the circle and thus are not measured. By increasing the aperture in order to include all the illuminated pixels, due to irregular shapes, many non-illuminated pixels would now be taken into account. Instead the ISO photometry setting within SExtractor was used, which is able to identify the irregularity of the shape of each fragment (see Fig. 3.12). The background of the frames was not at exactly zero-level. The value measured at each pixel is a function of the sum of a background signal (Bremsstrahlung) and light coming from the objects of interest. To be able to detect the faintest of these objects, and also to measure accurately their fluxes, one needs to have an accurate estimate of

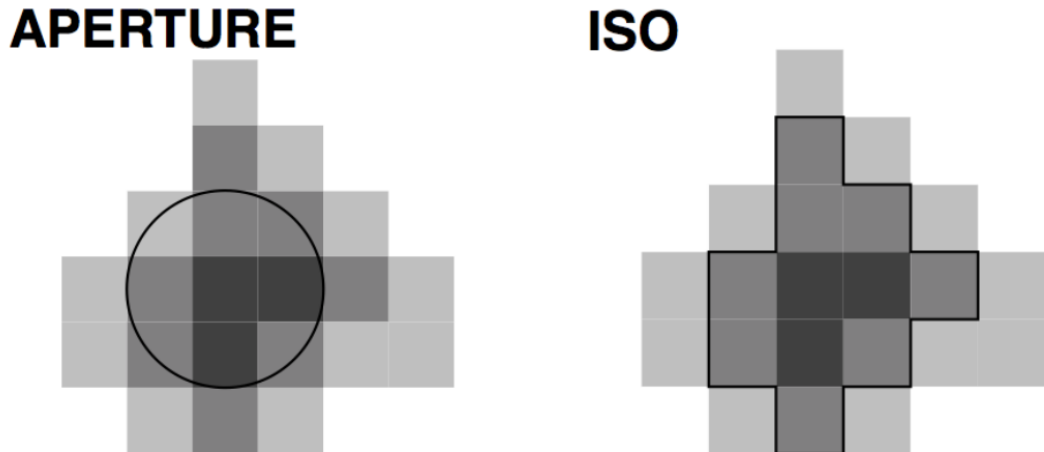


Figure 3.12: Comparison between aperture and ISO photometry method with SExtractor. In the first case it identifies the centre of the light source analysing the pixels which are enclosed in the circle, product of the FWHM of the source. In the second case it analyses all the illuminated pixels of the light source according to area and pixel value thresholds that the user sets (e.g. in this example ISO leaves out the light grey pixels as their value is lower than the set threshold) (Bertin & Arnouts 1996).

the background level in any place of the image (a background map). There are three ways of setting a threshold for the background signal from which two were used:

- `DETECT_THRESH` sets the threshold value. If one single value is given, it is interpreted as a threshold in units of the background's standard deviation. As the background noise from the EDX images was very close to zero counts, we were able to set this to a very low detection threshold in units of the background's standard deviation (based on the Bremsstrahlung). By selecting pixels with counts at least three times above the mean background noise, we were able to identify the vast majority of the fragments per field (as some extremely small may have comparable size with the background noise and be missed from the detection technique, however, we cannot quantify how much percentage of the initial mass is lost to the smallest fragments). The whole dataset was reduced by setting the threshold value at 3σ .

- `DETECT_MINAREA` sets the minimum number of pixels a group should have to trigger a positive detection of an object. Obviously this parameter can be used just like `DETECT_THRESH` to detect only bright and big sources, or to increase detection reliability. It is however more tricky to manipulate at low detection thresholds because of the complex interplay of object topology and noise correlations. Generally this threshold should be as low as possible. The extraction of the fragments was run multiple times, each time slightly increasing this threshold, from 4 pixels up to 8 pixels, in order to check the behaviour of `SExtractor` on the light sources (see section 4).

The third threshold is to set a maximum detected area, however this was not necessary for this study as the fragments could be of any size and the nature of the background signal could not create large artefacts on the frame.

`SExtractor` also has the ability to discern objects even in highly dense fields, giving good statistics by automatically counting thousands of fragments. Each time an object extraction is completed, the connected set of pixels passes through a 'filter' that tries to split it into individual overlapping components. If the field is very crowded with fragments, there is the possibility of blending the X-ray emission of several fragments. `SExtractor` comes with a sophisticated de-blending algorithm which flags the initially blended fragments. `SExtractor` also has an edge detection algorithm and ignores fragments that lay on the edge of an image. The basic flags with their warning are listed in Appendix A.

To ensure that the de-blending algorithm worked with the dataset, we performed a test. Running `SExtractor` on a specific dataset of Mg images (from our results) we extracted two different normalised SFDs, based on two different fragment populations:

(i) measuring only the well defined and isolated fragments (the identified fragment in the output file is returned with a flag=0) and (ii) measuring the population from (i) plus the fragments which were initially flagged as blended (flag=0 and flag=2 the latter being those that were blended, which the software then managed to separate and size). The result of this experiment was the production of two SFDs with extremely similar characteristics. This outcome indicated that, after the end of the fragments' extraction, for further analysis, we were able to use every fragment reported with 'flag 0' and 'flag 2' (for more details on possible flags see Appendix A). This selection process increased the number of positively identified fragments from the sample significantly, giving reliable statistics.

SExtractor measures the half semi-major (A) and semi-minor (B) axes allowing each object to be described as an ellipse. It gives other potentially useful values, such as the elongation (A/B), ellipticity (1-A/B) and the angle THETA that is measured anticlockwise in respect to the image's x-axis. According to the setting of the threshold which constrains the size of the minimum area identified as a fragment, SExtractor reproduces another image containing only the identified fragments with area equal or greater than the DETECT_MINAREA threshold, as shown in Fig. 3.13, not measuring anything smaller. By examining the new images we verified that there were no false detections due to background noise.

Apart from the study of the SFDs of the ejecta fragments, another significant parameter for the projectile's fragmentation was to calculate its catastrophic disruption limit. The energy density has long been used to assess disruption of projectiles (Davis et al. 1979; Schultz & Gault 1990). In this work, following Nagaoka et al. (2014), the energy density at the time of the impact is Q (J/kg), and its form for the impactor is

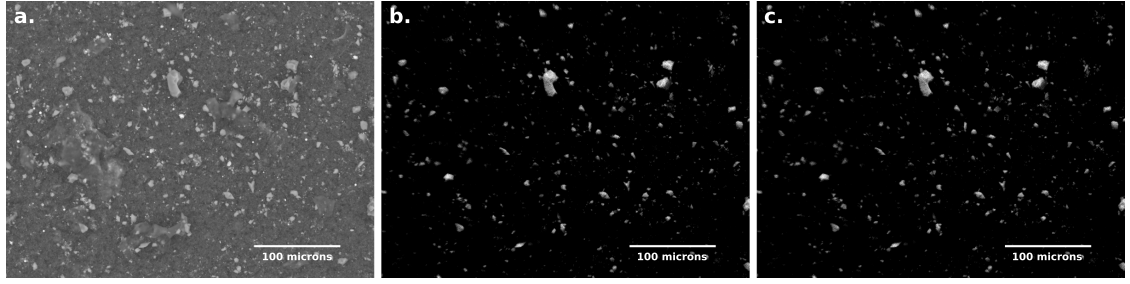


Figure 3.13: BSE image showing that the fragments of the projectile are mixed with other material from the gun (a). As the projectile is Mg-rich it gives a strong signal in Mg X-ray maps (b). Considering also that there are no other sources of Mg contamination, these maps are used as the main dataset for the analysis. SExtractor identifies each fragment and reproduces another image containing only the pixels which contain information according to the given threshold (c). Images taken from Avdellidou et al. (2016).

given by:

$$Q_{\text{im}} = \frac{1}{2} \frac{M_{\text{im}}}{M_{\text{t}} + M_{\text{im}}} v^2 \quad (3.1)$$

where M_{im} (kg) is the mass of the impactor, M_{t} (kg) the mass of the target and v (m/s) the impact speed. It represents the kinetic energy of the impactor divided by the total mass of the system.

The mass of the largest fragment was determined after weighing each fragment several times with the high precision scale. In our case, the mass of the target can be considered as $M_{\text{t}} \gg M_{\text{im}}$ compared to the impactor, therefore, neglecting the target's mass, Q_{im} can be calculated simply as :

$$Q_{\text{im}} = \frac{1}{2} v^2 \quad (3.2)$$

where v (m/s) is the impact speed. Traditionally, it is assumed that catastrophic disruption occurs when $M_{\text{l,f}}/M_{\text{im}} \leq 0.5$, with the energy threshold of Q^* . Plots of $M_{\text{l,f}}/M_{\text{im}}$ vs. Q_{im} are used to give an estimate of the projectile fragmentation as a function of the impact velocity (energy).

3.3.3 Analysis 2: Implantation on Target

The same analytical approach was used, as described in Section 3.3.2, to analyse the filters of the target's melt water and solution of the water ice and CaCO_3 respectively. These filters collected projectile material once the target was filtered away. At the start of these experiments it was decided the target melt would be filtered through PTFE filters with a pore-size of $5\ \mu\text{m}$. However, upon inspection under the SEM it was observed that a large percentage of fragments were present between the pores that were significantly smaller than $5\ \mu\text{m}$. It was then decided to use filters with a much smaller pore size to capture this smaller population. We used filters of 16 mm in diameter with pore size $0.1\ \mu\text{m}$. We used a smaller pore-size filters (compared to ejecta, see section 3.3.2) to collect the projectile fragments that remained in the target, as we wanted to quantify the mass as accurate as possible. While mapping the target filters, in contrast with the mapping of the ejecta filters, we used low magnification ($\times 50$) in the SEM. This is because it was noticed that there was some spatial variability in the number of fragments on the filter and we choose to map the entire surface of the filter to detect all possible impactor fragments. The chosen resolution enabled us to scan a whole filter in approximately 24 hours with pixel scales between $4.4\text{--}4.9\ \mu\text{m}/\text{pixel}$ and thus create a mosaic of the whole filter area. This means that if the fragments that remained in the target follow a similar size-frequency distribution with the ejecta fragments, then we should expect to have a number of fragments smaller than a pixel. The significant factor to consider in choosing a detection threshold in SExtractor is the background noise of the images, which is due to the Bremsstrahlung radiation as the electron beam decelerates within the sample. The level of this background noise is different for each different element. Ideally, if there was no Bremsstrahlung background, we could use

an extremely low threshold for the minimum detected fragment area as every pixel with a value greater than 0 would correspond to a real Mg signal. That way we could measure fragments with sizes as small as the pixel scale. However this was not possible and, in order to overcome the problem, we performed the analysis of the maps using SExtractor choosing several different thresholds (e.g. 3, 4, 6 and 8 pxl area) for the minimum detected area (Avdellidou et al. 2016).

After having extracted the 2D area of each fragment, as projected by the X-ray detector, an extra step was performed in order to estimate a z-length that corresponds to the fragment's height. As there was not a preferable rest position of the fragments, we were therefore able to adopt simple estimations of the z-axis which was assumed to follow the same distribution of x and y axes. As an estimation of a volume was demanded, we used simple formulae to estimate the z-axis dimension; such as a simple average of the x and y dimensions (Avdellidou et al. 2016).

Assuming that the produced fragments are cubioid, the estimation of the total mass of the projectile was done by using the Eq. 3.3:

$$M_p = \sum_{i=0}^N x_i \times y_i \times \frac{(x_i + y_i)}{2} \times \rho \quad (3.3)$$

where x_i and y_i are the big and small axis of each fragment respectively, and ρ , the density of the projectile's material.

3.3.4 Analysis 3: Final State of the Projectile

Although the primary goal of this study was not the structural and compositional alteration of the projectile, Raman spectra were obtained for the peridots before each shot. These initial spectra were compared against spectra obtained after the shot

from the largest fragment in order to examine the state of the largest fragment after the impact. Previous impact experiments have shown shifts in Raman spectra of the shocked target - and the magnitude of this shift has the potential to be used as a shock 'barometer' (Kuebler et al. 2006). However, as the basalt has a glassy matrix it does not give well-defined, distinguishable, peaks in the Raman spectrum and no further spectra of the synthetic basalt projectiles were undertaken.

All spectra were taken using the IR Raman laser at 784 nm as described in 3.3.1. The intensity was normalised and the spectrum of each large fragment was plotted with its reference spectrum taken before the shot.

4

Experimental Results: Fragmentation, Implantation and Final State of the Projectile

IN this Chapter are presented all the results of the series of experiments investigating the fragmentation, implantation and final state of the projectile. This study is based on the results of 39 successful shots - that were used for the analysis - out of 47 in total that were performed. In the Table 4.1 are summarised the number of experiments performed for every different combination of target and projectile materials and in Table 4.2 the analysis parameters, as were described in 3.1. This Chapter is divided into four parts. In the first three parts are presented all the results that came out from the analysis of the projectile's fragmentation, implantation and a brief examination of its final state. In section 4.4.3, the last part of this Chapter, are described the experimental complications that were faced during the experiments and the solutions found to overcome them. We found that a) there is a difference in the fragmentation of the projectile, b) the degree of implantation in the target significantly increases with increasing target porosity, c) but the final state of the produced fragments show no melt or alteration in their Raman spectra with increasing collisional speed or target porosity,

Table 4.1: Summary of successful experiments.

Run (type of target)	peridot	basalt
Run#1 (solid water-ice)	13	7
Run#2 (porous water-ice)	11	-
Run#3 (CaCO ₃ powder)	7	-

as the olivine spectral features remained unaltered after impact with no change. The main result is that, contrary to previous assumptions (Gayon-Markt et al. 2012), the projectile can be preserved at impact speeds significantly higher than 0.5 km/s (up to 3.5 km/s).

4.1 Projectile Fragmentation

For the projectile's fragmentation we derived the SFDs of the fragments found in the ejecta. Ejecta were captured by designing and building custom collection systems (for details see 3.2.2 and Fig. 3.1) and the fragments were extracted and mapped with an SEM (see 3.3.2). During the last step, by using the SExtractor routine (3.3.2), the dimensions of the fragments were obtained and the SFDs were produced. One of the main goals was the comparison of the SFDs of the fragments from the same type of projectile, as they impacted into different porosity targets. Another purpose was to ascertain if there is a difference (and how much) in the value of the energy density Q_{im}^* of the projectile when catastrophic disruption occurs.

4.1.1 Low porosity targets

Here will be discussed the results of Run#1, which includes the impact of olivine and synthetic basalt projectiles onto pure water-ice with low porosity $\sim 6\%$, as described in 3.1. In the same range of speeds, 13 shots were devoted to olivine projectiles and

Table 4.2: Summarised information of the analysis of the peridot ejecta and the fragments recovered from the targets. The parameters are summarised for each speed range as they remained constant for each Run.

EJECTA	porosity	v_{col} range	filter size	magn.	SEx thres.	detection limit
Run#1 (solid water-ice)	< 10%	0.38–3.50	5 μm	$\times 300$	5 pxl	1–1.2 μm
Run#2 (porous water-ice)	40%	0.30–3.08	5 μm	$\times 150$	5 pxl	4.1–4.9 μm
Run#2 (porous water-ice)	40%	0.30–3.08	5 μm	$\times 300$	5 pxl	2.2–2.7 μm
Run#3 (CaCO ₃ powder)	70%	0.92–2.98	5 μm	$\times 100$	5 pxl	6.2–7.4 μm
TARGET						
Run#1 (solid water-ice)	< 10%	0.38–3.50	0.1 μm	$\times 50$	4 & 6 pxl	8.3–10.4 μm
Run#2 (porous water-ice)	40%	0.30–3.08	0.1 μm	$\times 50$	4 & 6 pxl	8.3–10.4 μm
Run#3 (CaCO ₃ powder)	70%	0.92–2.98	0.1 μm	-	-	-

7 to basalt projectile shots. The threshold of speeds was determined according to the probability of the gun successfully accelerating gemstones at higher speeds than 3.5 km/s. Another guiding consideration was the ability to retrieve relatively large fragments from the target, and/or the ejecta, in order to study the fragmentation of the impacting material. At the end of this Chapter, a summary of the unsuccessful shots will be described (see 4.4). The analysis was based mostly on the results of the shots that used the peridot projectiles, although we also carried out experiments using the synthetic basalt projectiles in order to compare the catastrophic disruption.

Following the procedures described in 3.3.2, we measured the SFDs of the fragments for all the peridot shots. After filtering the melted ice of the ejecta collecting funnel through a 35 mm diameter filter with 0.1 μm diameter pores, a noticeable number of fragments smaller than 0.1 μm remained on the filter, lying between the holes. After this detection it was realised that the projectiles were producing fragments so small that in order to identify them, and include in our statistics the smallest possible fraction of the fragments population, we would have to scan the filters using a magnification of at least $\times 300$. However the resolution of the SEM-EDX images that were taken in order to produce the Mg maps, was 0.4 $\mu\text{m}/\text{pxl}$. Thus, it was not possible to measure fragments smaller than this resolution limit using our automated image analysis routines of SExtractor and therefore $\sim 0.4 \mu\text{m}$ was, effectively, the limiting spatial resolution of our SEM using this specific magnification ($\times 300$). Although the limiting resolution of the maps with this magnification is 0.4 $\mu\text{m}/\text{pxl}$, we present results obtained when the minimum detection threshold for a fragments area in SExtractor was 5 pixels. This means that, according to the configuration of these 5 pixels, the smallest fragments detected, by averaging the dimensions, would have a size in the range $\sim 1\text{--}1.2 \mu\text{m}$.

The SFDs of the size of the fragments appears to have a power-law tail, as shown

in Fig. 4.1. There is a shift of approximately $3 \mu\text{m}$ of the principal mode of the distribution when the velocity was increased from 0.608 to 1.33 km/s, but above this speed the mode remains constant at approximately $1.5 \mu\text{m}$. Considering the pore size of the filters used for these experiments, the detection threshold of the EDX maps ($0.4 \mu\text{m}$) and the SExtractor detection limit ($1.0\text{--}1.2 \mu\text{m}$) the turnover of the curves $\sim 1.5 \mu\text{m}$ could be statistically significant. It was expected that as the impact speed increased the number of smaller fragments would increase. However, as can be seen from Fig.4.1, although there are differences of even an order of magnitude in the number of fragments, there is no clear trend in the fragmentation behaviour with increasing impact speed. Similarly the slopes of the cumulative distributions in Fig. 4.1b show no clear trend with increasing speed, which also seems to be counter-intuitive.

We found that the slopes of all size frequency distributions lie in a range between -1.04 and -1.68 . Here it should be pointed out that due to possible secondary fragmentation occurring on the ejecta collecting system the observed slopes of the SFDs would be steeper. However, as described in section 3.2.2, it is expected that this phenomenon would be limited.

Figure 4.2 shows the mass of the largest fragment retrieved as a fraction of the initial impactor's mass, in relation to the energy density Q_{im} . Analytically the data are presented in Table 4.3. Note that for the shot G180215 the largest fragment was also found in ejecta. Due to its very small size, the mass was estimated by calculating first the dimensions of the fragment. The x and y axes were measured directly from an SEM image of the fragment, while the z axis was measured using the Raman spectrometer by determining the height where the laser was on focus. In order to calculate the values of the energy density at the catastrophic disruption threshold, Q_{im}^* , we fit the parameters

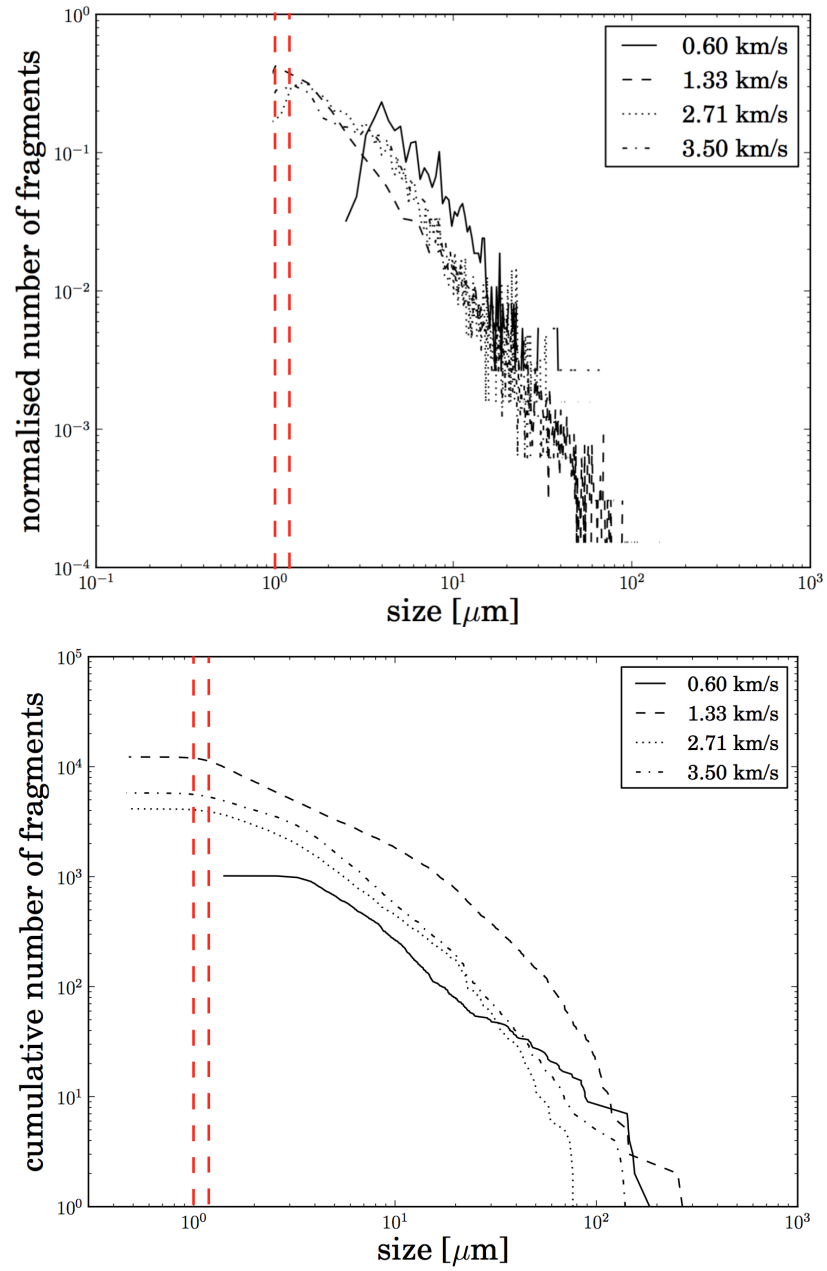


Figure 4.1: Differential (top) and cumulative (bottom) SFD of ejecta fragments of indicative shots in Run#1 (magnification $\times 300$), showing no significant change, apart from the 0.60 km/s shot, with increasing speed (Avdellidou et al. 2016). The red dashed lines indicate the threshold range of the detection limit.

Table 4.3: Successful shots for olivine and basalt projectiles onto low porosity water-ice targets (<10%). M_{1f}/M_{im} represents the proportion of the largest fragment of the impactor of its initial mass. The S in naming correspond to impact speeds <1 km/s, while the G to >1 km/s. For the shots G031214 and G121214 we were not able to identify the largest fragment. For shots G260215 and G260515 the largest fragments were recovered from the bottom of the craters. The mass of the shot G180215 was estimated by measuring first the volume of the fragment. From the shots G031214 and G121214 no large fragment was recovered (Avdellidou et al. 2016).

Run#1	Peridot	impact speed [km/s]	M_{im} [mg]	M_{1f}/M_{im} [%]	Run#1	Basalt	impact speed [km/s]	initial mass [mg]	M_{1f}/M_{im} [%]
	S141114	0.38	26.20	100		G010415	1.49	17.07	77.42
	S180315	0.60	22.55	86.25		G260515	1.68	14.72	70.93
	S211114	0.92	21.40	65.50		G240415	2.07	16.07	63.20
	G060315	1.33	20.97	29.46		G050615	2.14	14.73	66.32
	G260215	1.60	24.90	19.30		G260515	2.17	14.35	77.00
	G230115	1.95	20.50	7.80		G070515	2.70	14.74	5.36
	G250315	2.00	21.60	13.42		G270415	3.03	17.22	1.30
	G220515	2.04	24.33	10.05					
	G261114	2.05	26.80	3.21					
	G130315	2.16	25.16	2.92					
	G180215	2.71	25.70	0.02					
	G031214	2.97	21.80	-					
	G121214	3.50	26.00	-					

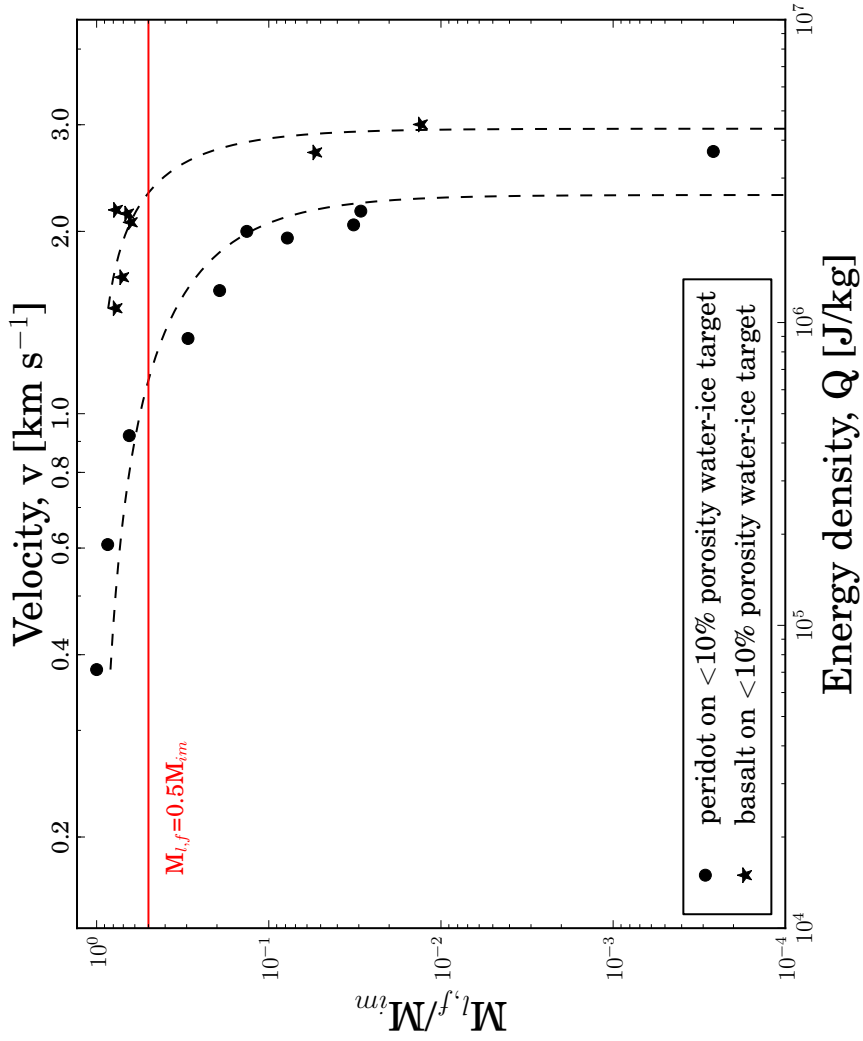


Figure 4.2: Mass ratio of the largest surviving fragment of the impactor versus the energy density, Q_{im} , for speed ranges 0.38–2.71 km/s and 1.49–3.03 km/s for olivine and basalt respectively in Run#1. The dashed lines correspond to the best-fitting curves using Eq.4.1 (Avdelidou et al. 2016).

of Eq.4.1 to the data:

$$\frac{M_{1,f}}{M_{im}} = 1 - AQ_{im}^c \quad (4.1)$$

We found that $c_p = 0.49$, $A_p = 6.89 \times 10^{-4}$ for peridot and $c_b = 1.42$, $A_b = 3.63 \times 10^{-10}$ for basalt fragments, indicating that basalt needs higher speeds to fragment in a similar way to the olivine projectile. The derived values of the catastrophic disruption threshold, Q_{im}^* , were estimated at 6.46×10^5 J/Kg and 2.71×10^6 J/Kg for peridot and basalt respectively.

4.1.2 High porosity targets

A procedure based on the same principles as described above was followed also for the analysis of the projectile's fragmentation in the subsequent two Runs using higher porosity targets. In Run#2 we initially scanned the filters containing the ejecta with lower magnification ($\times 150$) (and pixel scale $1.65 \mu\text{m}/\text{pxl}$) compared to Run#1 ($\times 300$) producing the SDFs (see Fig. 4.3). The magnification decreased as we noticed during the first inspection of the filters that the produced fragments were bigger than in Run#1. However, later, we repeated the X-ray maps using higher magnification, the same with Run#1 ($\times 300$), for a direct comparison. Images were taken with lower resolution than before, having dimensions 512×384 pixels, instead of 1024×768 that was in Run#1. This was to try and reduced the SEM time required to map the filters; a map with a resolution of 1024×768 took approximately 24 hours of SEM time. The analysis of this later images of Run#2 ($\times 300$) were used for the discussion of this work.

As it can be seen when the peaks of the SFDs from Run#1 and Run#2 (using the same magnification) are compared (Fig. 4.1 and Fig. 4.4) there is a small shift in the modes from ~ 1.5 to $\sim 2.5\text{--}3 \mu\text{m}$. However during this run the pixel scale was 0.9

$\mu\text{m}/\text{pxl}$, implying a rough cut-off of the detection at approximately 2.2–2.7 μm , that is actually on the observed turnover.

The SDFs of the fragments of the shots in Run#3 are shown in Fig. 4.5. After recovery, the largest fragments were weighed (Table 4.5) and it was noticed that the majority of the initial mass was retained in a single fragment. This was an indication that not as many fragments were going to be recovered from the ejecta, compared to the previous Runs with a lower porosity target. In order to visualise this we examined very quickly some filters in the SEM and then the mapping magnification was adjusted to $\times 100$. The lack of many very small fragments enabled the scanning of larger fields with this lower magnification and also greater sampling of area on these filters. The pixel scale here was 2.47 $\mu\text{m}/\text{pxl}$, implying a fragment detection cut-off at approximately 6.2–7.4 μm . From Fig. 4.5 the turnovers of the majority of shots are $\sim 7\text{--}8 \mu\text{m}$. This means that also here, as in Run#1, the observed turnovers in the SDFs is debatable whether can be considered as real.

A more robust comparison of the three different SDFs is the calculation of the slopes of the cumulative distributions in order to detect any differences in steepness. Moreover, the slopes can reveal any changes of fragmentation with increasing impact speed. As we saw in Run#1 the steepness fluctuates in a relatively small range without giving any consistent change with speed. The slopes were calculated in ranges between -2.5 and -4.0 for Run#2 and -3.0 and -4.8 for Run#3, these values are consistently higher compared to Run#1.

Another way to compare the fragmentation of the peridot projectiles during the three Runs was to look for differences in the largest fragments which survived after each shot, and also what speed required for its catastrophic disruption to occur (3.3.2). In Tables 4.4 and 4.5 are given the absolute masses and the mass fractions of the largest

Table 4.4: Successful shots of Run#2 for olivine projectiles onto high porosity water-ice targets. $M_{l,f}/M_{im}$ represents the proportion of the largest fragment of the impactor of its initial mass. Data are included in Avdellidou et al. (in prep.).

Run#2	impact speed	M_{im}	$M_{l,f}$	$M_{l,f}/M_{im}$
Peridot	[km/s]	[mg]	[mg]	[%]
S230915	0.30	25.00	25.00	100
S160715	0.60	22.75	13.04	57.30
S160715	0.97	24.27	8.26	34.02
G190615	1.33	21.47	3.05	14.19
G120615	1.58	24.54	0.557	2.27
G080715	1.99	20.90	1.08	5.18
G130815	2.00	27.30	0.36	1.32
G250915	2.01	27.31	0.93	3.4
G080715	2.19	21.97	0.59	2.70
G070815	2.60	28.33	0.29	1.03
G130815	3.08	29.33	0.083	0.28

Table 4.5: Successful shots of Run#3 for olivine projectiles onto high porosity CaCO_3 regolith-like targets. $M_{l,f}/M_{im}$ represents the proportion of the largest fragment of the impactor to its initial mass. After shot G191115 no large fragment was recovered. Data are included in Avdellidou et al. (in prep.).

Run#3	impact speed	M_{im}	$M_{l,f}$	$M_{l,f}/M_{im}$
Peridot	[km/s]	[mg]	[mg]	[%]
S151015	0.92	22.72	22.72	100
G151015	1.25	23.71	21.51	90.7
G211015	1.58	22.35	19.36	86.6
G121115	1.95	23.46	16.38	71.5
G291015	2.23	21.76	12.12	55.7
G051115	2.67	23.54	2.45	10.4
G191115	2.98	24.99	-	-

pieces that were recovered mostly from the target. In all Runs (including Run#1, described earlier) the mass of the large fragment constantly decreases with increasing collisional speed, a fact that was expected and has been seen in previous studies (e.g. Nagaoka et al. (2014)).

In Figure 4.6 are presented the mass fractions of the largest fragments with in-

Table 4.6: The calculated energy density at catastrophic disruption limit, Q_p^* and Q_b^* for olivine and basalt respectively, after fitting Eq. 4.1 to the experimental data, where A and c the fitting parameters.

Run	Peridot			Basalt		
	Q_p^* [J/Kg]	A	c	Q_b^* [J/Kg]	A	c
Run#1	6.46×10^5	6.89×10^{-4}	0.49	2.71×10^6	3.63×10^{-10}	1.42
Run#2	2.40×10^5	1.4×10^{-2}	0.28	-		
Run#3	2.58×10^6	1.8×10^{-12}	1.78	-		

creasing speed and the energy density for each collision. The tail of the points for the peridot projectile when impacted onto porous water-ice targets seems less steep than the equivalent when the same type of projectile impacted the non-porous water-ice targets. Unfortunately it was not possible to do a similar comparison for the outcome of Run#3, as the last shot at 2.95 km/s did not give any large fragments, and thus we could not continue the shot programme due to the speed limit when firing 3 mm peridots (see discussion in 4.4.1).

The fitting of the data was done using the Eq. 4.1 as described earlier, enabling the determination of the Q_{im}^* . The results are summarised in Table 4.6 along with their fitting parameters A and c.

4.1.3 Summary

In this section we showed the results on the fragmentation of the projectiles in the range of speeds we could successfully achieve with the LGG. To begin with, we notice a difference in the steepness of the SFDs for all Runs, with impacts on the non-porous targets seeming to have less steep distributions. However we did not notice a change in steepness with increasing collisional speed within the same Run. Another important result is that the basalt projectiles, in the same range of speeds, needed higher speeds to fragment compared to the peridot projectiles, needing an order of magnitude

higher energy for catastrophic disruption to occur. Moreover we report a change in the disruption energy required for the same projectile, but on a different target. Further comparison of the results of the different Runs will be presented in the next Chapter.

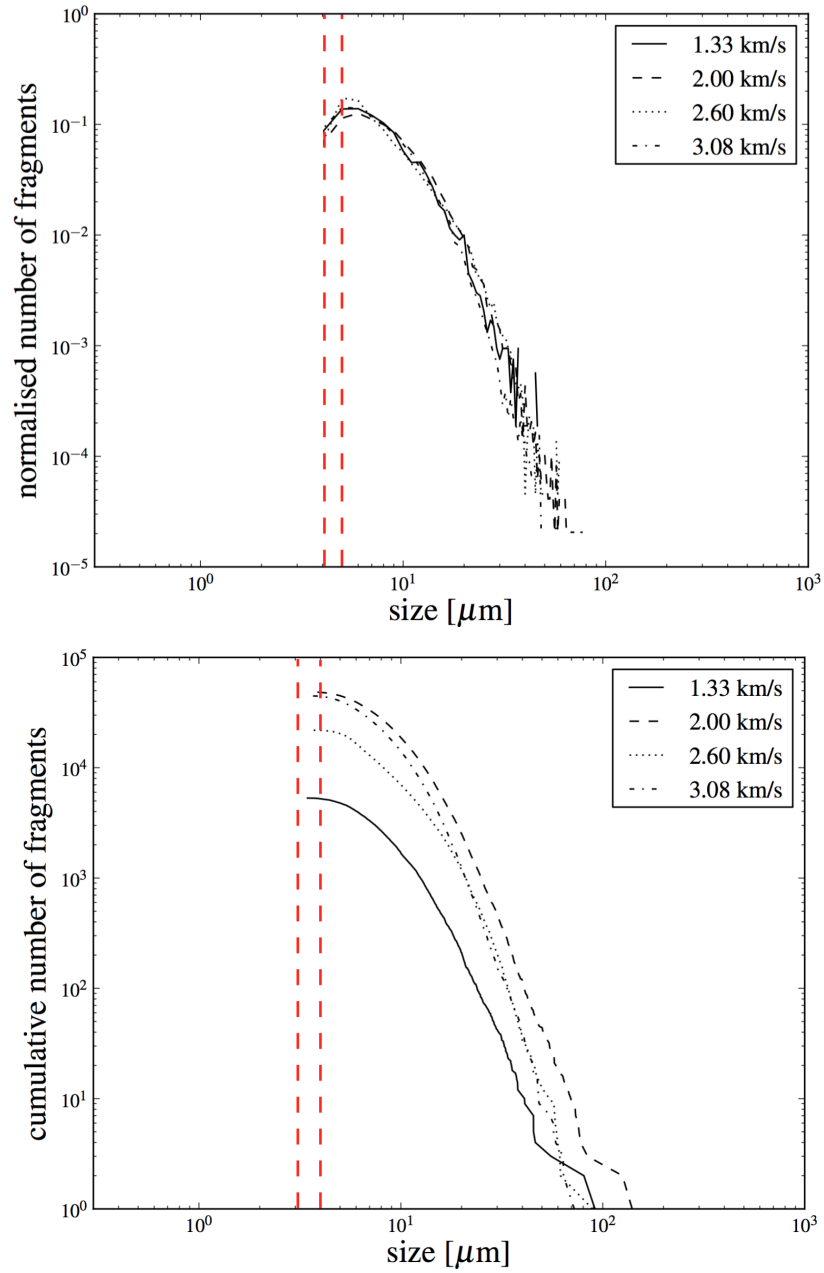


Figure 4.3: Differential (top) and cumulative (bottom) SFD of the ejecta fragments of indicative shots in Run#2 (magnification $\times 150$), showing no significant change with increasing speed, apart from the impact speed at 1.33 km/s that appears shallower (Avdellidou et al. in prep.). The red dashed lines indicate the threshold range of the detection limit.

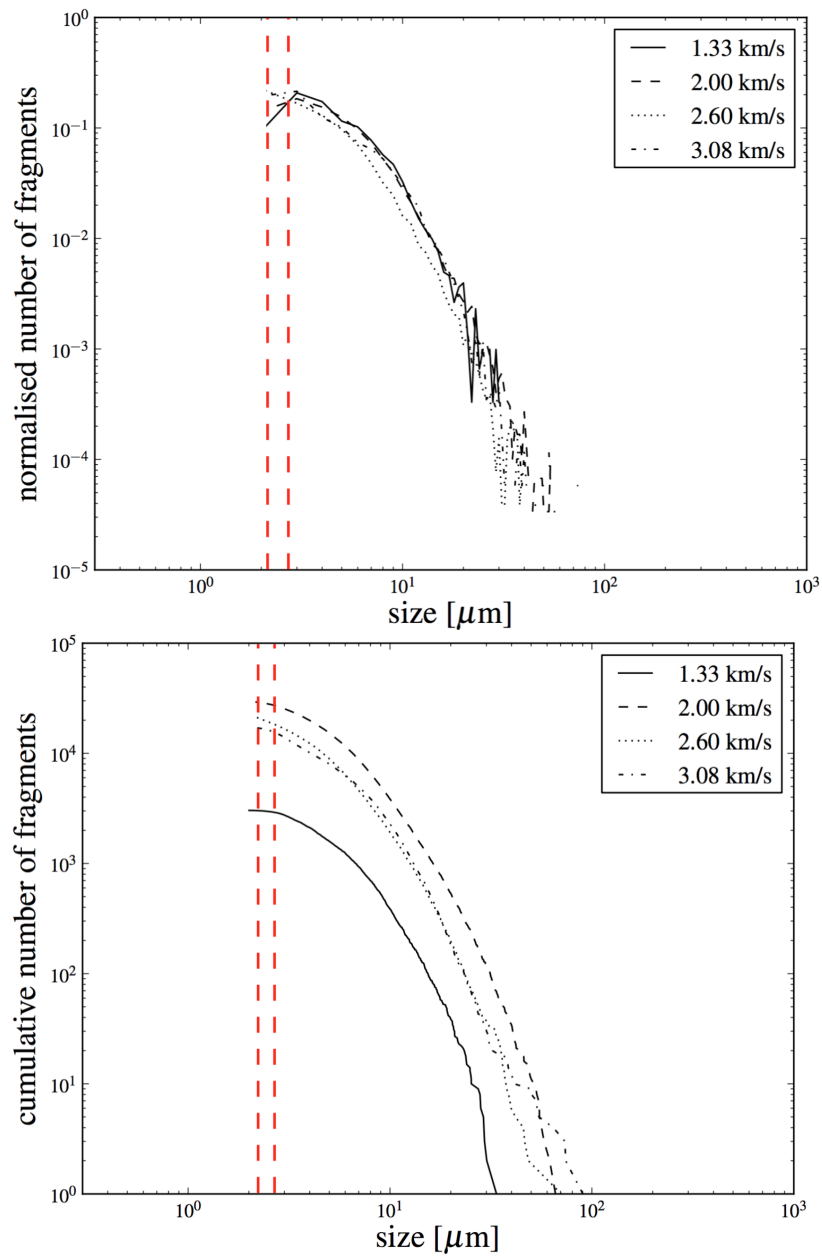


Figure 4.4: Differential (top) and cumulative (bottom) SFD of the ejecta fragments of indicative shots in Run#2 (magnification $\times 300$), showing no significant change with increasing speed (Avdellidou et al. in prep.). The red dashed lines indicate the threshold range of the detection limit.

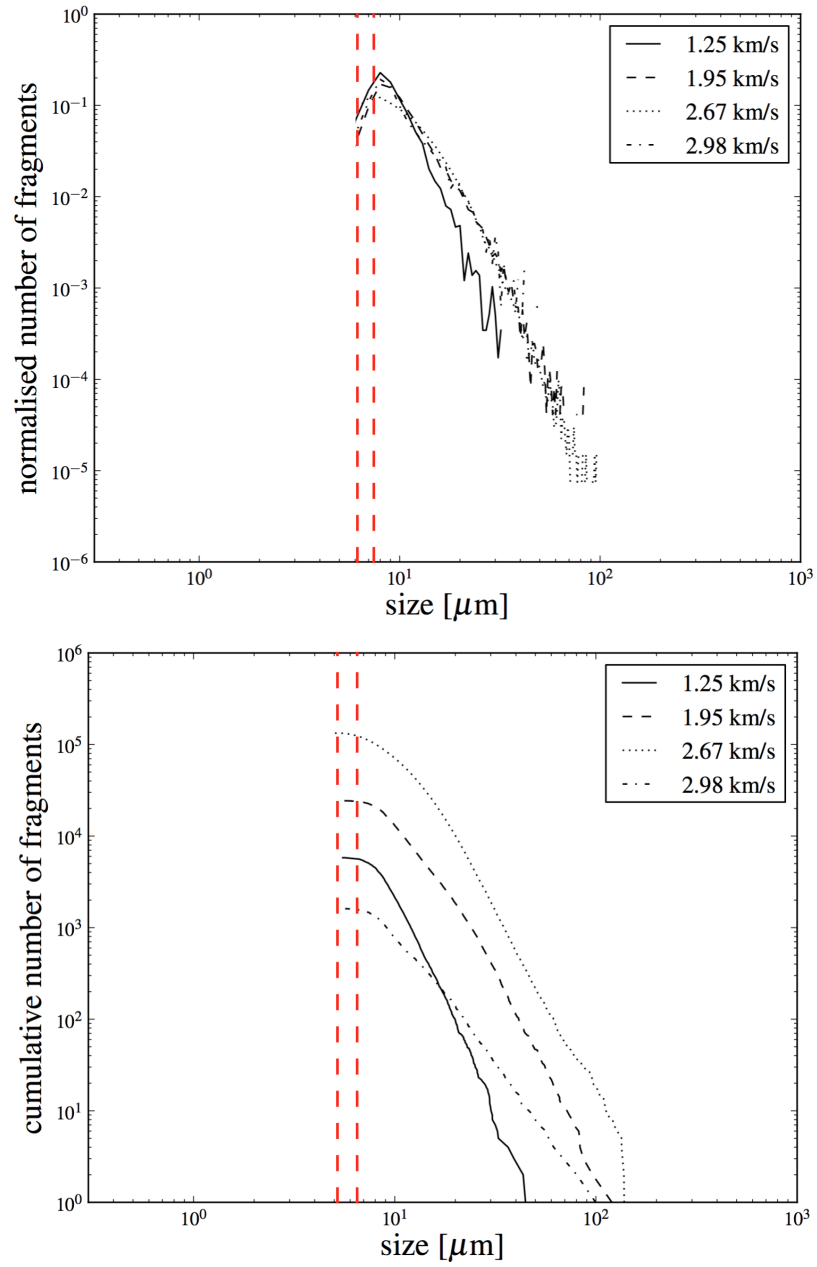


Figure 4.5: Differential (top) and cumulative (bottom) SFD of the ejecta fragments of indicative shots of Run#3 (magnification $\times 100$), showing no significant change with increasing speed, except the distribution at 1.25 km/s that appears to be steeper (Avdellidou et al. in prep.). The red dashed lines indicate the threshold range of the detection limit.

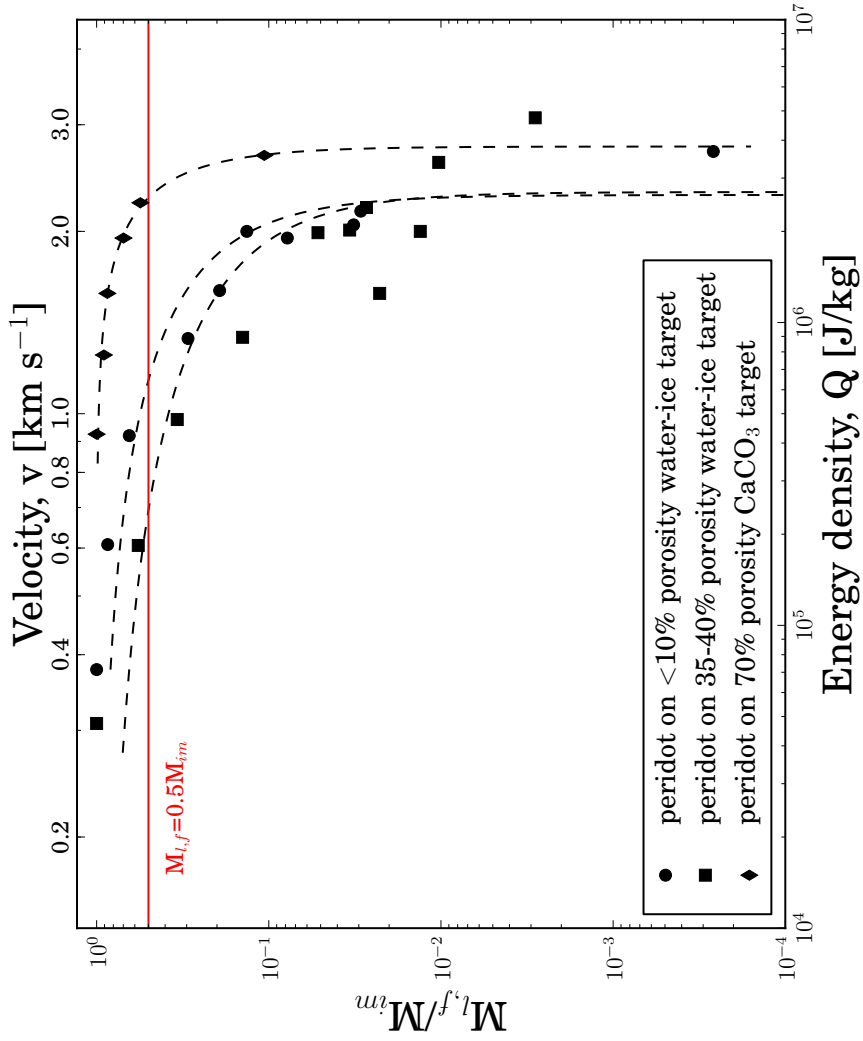


Figure 4.6: Mass ratio of the largest surviving peridot fragment of the impactor versus the energy density, Q_{im} and the impact velocity, v , using data from Run#2 and Run#3 (Avdellidou et al. in prep.). The dashed lines correspond to the best-fitting curves using Eq.4.1 ((Avdellidou et al. 2016)).

4.2 Projectile Implantation in the Target

An important goal of the experiments was to discover whether any, and how much, of the impactor's mass was implanted into targets with increasing porosity. Using two different methods we obtained an estimation of the total implanted projectile mass in each target.

The first approach was to find instantly (by visual inspection) any large fragments (mm to sub-mm) that stayed in the target immediately after the impact and weigh them using a high precision balance (with precision $0.1 \mu\text{g}$). With this method we had a measurement of part of the implanted mass with good accuracy, as any smaller fragments not found would have a very small mass relative to the original mass of the projectile.

The second approach was more complicated. Independently, regardless of whether any large fragments were recovered or not, the target material was filtered out and the filters were mapped by the SEM (see for details 3.3.2 and 3.3.3). In turn the Mg maps obtained from the X-ray scanning (EDX-maps) all across the filter's area were analysed by SExtractor routines, giving the amount of small μm -size fragments. In the next step, by knowing the density of the peridot and having estimated 3D sizes for all the identified fragments, we calculated the total mass recovered per shot. This procedure was repeated four different times, each time changing the minimum detection threshold of SExtractor. This means that every time the calculation of the mass of the very same filter was based on a different number of identified fragments by giving a constraint for the smallest 2-D projected area (in pixels) that a fragment could occupy in a maps frame. We calculated masses using three, four, six and eight pixel area threshold per fragment. Here are presented the results using the four (SEx-Mode.1) and six pixels

(SEx-Mode_1) area threshold as we thought these are the most reliable: we avoided including results using the three-pixel area threshold, as it was too small and confusion with background noise could happen, on the other hand we did not use the results from the analysis of 8 pixel area identification threshold, as we realised we would miss out the very small identifiable fragments.

Both methods were used for the water-ice targets (Run#1 and Run#2), but only the direct weighing method for Run#3 due to the larger amount of CaCO_3 residues found on the filters. These procedures will be discussed analytically in 4.2.1 and 4.2.2.

4.2.1 Low porosity targets

In low porosity targets, Run#1, we did not recover any large (mm to sub-mm) fragments from the target, apart from shot G260215 (1.6 km/s). In this shot the largest fragment was found in the crater with a mass of 31% of the initial mass. The lack of identification of large fragments for direct and accurate weighing led us to the development of the second approach as described in 3.3.2 using the SEM and SExtractor software.

In Table 4.7 we present the overall masses of the fragments which were found in the target filters as a fraction of the initial projectile mass. For the identification of the fragments we used two different photometric thresholds for the minimum detected area (4 and 6 pixel area respectively, as described above).

4.2.2 High porosity targets

The mass estimation in Run#2 was performed using the same method as described previously for the low-porosity targets in 4.2.1. However, during this set of experiments, we recovered large projectile fragments from the target and this enabled us to directly

Table 4.7: The mass fraction of the olivine projectile that was found embedded in the non-porous targets (Run#1) using two different detection thresholds, of 4 and 6 pixels respectively, for the minimum detected area. *Note, that for shot G260215 (1.6 km/s) the largest fragment was found in the crater with a mass of 31% of the initial mass, increasing the total amount implanted in the target from 53–55% (Avdellidou et al. 2016).

Run#1	speed	SEx-Mode_1 (4 pxl)	SEx-Mode_2 (6 pxl)
Peridot	[km/s]	mass [%]	mass [%]
S180315	0.60	0.20	0.18
S211114	0.92	0.43	0.37
G060315	1.33	1.40	1.17
G260215*	1.60	24.0	22.40
G230115	1.95	8.29	0.58
G250315	2.00	1.71	0.55
G220515	2.04	1.15	0.48
G130315	2.16	3.50	2.60
G180215	2.71	0.17	0.12

weigh them. In this Run the largest fragments, in 10 out of 11 shots, were found in the target and not in the ejecta. That was another reason that we continued the investigation to recover the majority of the mass. The targets were left to melt and were then filtered and these filters were mapped in SEM as before. The results of this additional mass existing in the tiniest projectile fragments are given in Table 4.8.

For two out of three low-speed shots, S230915 (0.3 km/s) and S160715 (0.6 km/s), there was no need to search for small fragments, as specifically in S230915 the whole projectile was found in the target, with no cracks and missing chips. In S160715 EDX scanning was also not necessary as the projectile was found broken in two pieces, one found in the target and the other in the ejecta and their total mass was $\sim 99.17\%$ of the projectile's original mass.

The total mass per shot was estimated by the simple addition of the masses identified by the two methods (Table 4.9). As can be seen, the masses found in Run#2 are much greater than in Run#1 clearly indicating that high porosity targets retain the

Table 4.8: The projectile’s mass that was identified by SExtractor, using two different configurations (Mode_1 and Mode_2), and was implanted in the porous (40%) water-ice targets (Run#2). *Note, there was no need to map the target filters of these two shots as the largest fragments were recovered had total mass 100% and 99.17% of the initial mass respectively (Avdellidou et al. in prep.).

Run#2	speed	SEx-Mode_1 (4 pxl)	SEx-Mode_2 (6 pxl)
Peridot	[km/s]	mass [%]	mass [%]
S230915*	0.30	-	-
S160715*	0.60	-	-
S160715	0.97	39.4	39.16
G190615	1.33	8.08	7.71
G120615	1.58	3.02	2.67
G080715	1.99	20.26	19.54
G130815	2.00	27.43	25.48
G250915	2.01	0.08	0.06
G080715	2.19	56.17	55.07
G070815	2.60	1.23	1.06
G130815	3.08	22.56	20.38

projectile more easily. That prompted us to continue the experiments with the same projectile in a similar range of impact speeds. The discovery of the largest fragments in the targets was one additional factor to test higher porosities and compare the results again.

For the analysis of the targets of Run#3, it was initially intended to follow the same steps as in the previous two Runs. Again, the majority of the largest fragments were found inside the target and only a few in the ejecta. After shot S151015 the peridot projectile was recovered intact, retaining the 100% of its initial mass. Very large fragments were found for all the subsequent shots, apart from the very last one, G191115 (2.98 km/s), where no large fragments could be recovered either in the target or in the ejecta. That was an unexpected outcome, considering that for the exact previous shot, G051115 (2.67 km/s), the total recovered mass was 17% of the initial and the difference in impact speeds was only 0.31 km/s. We would have a better

Table 4.9: The total mass, M_{total} , of the olivine projectile that was found embedded in the porous (40%) water-ice targets (Run#2). A fraction of this belongs to the mass that was in the big fragments and another part was estimated by SExtractor photometry (see Table 4.8) (Avdellidou et al. in prep.).

Run#2	speed	M_{total} (incl. SEx-Mode.1)	M_{total} (incl. SEx-Mode.2)
Peridot	[km/s]	[%]	[%]
S230915	0.30	100	100
S160715	0.60	57.3	57.3
S160715	0.97	92.5	92.3
G190615	1.33	22.3	21.9
G120615	1.58	6.40	6.10
G080715	1.99	25.4	24.7
G130815	2.00	30.58	28.63
G250915	2.01	18.22	18.20
G080715	2.19	59.8	58.7
G070815	2.60	1.23	1.06
G130815	3.08	23.08	20.9

idea of the fate of this projectile, e.g. if it was completely pulverised, however the further analysis of these targets was not possible. The amount of CaCO_3 powder that we had to dissolve was much more than expected and thus the filters were covered by an insoluble residue layer that effectively hid any small projectile fragments (the residue is due to the CaCO_3 powder being only 99% pure, the other 1% is a by-product of the production process, that cannot be dissolved and removed). This did not allow further investigation, such as EDX mapping, as it would be fruitless. Any small peridot fragments would be buried inside the residue and the Mg signal was not detectable. Analytically the problem is described in 4.4.3.

As a result, the total masses, M_{total} , that are presented in Table 4.10, are only of the manually recovered large fragments. Still the embedded masses are extremely high compared to the previous Runs and in this Run the implanted masses decreased constantly with increasing impact speed. In the first two Runs, unfortunately, we do not see this behaviour, but a fluctuation, possibly due to the affect of the target's grain

Table 4.10: The mass fraction of the olivine projectile that was found embedded in the CaCO_3 regolith-like targets (Run#3) (Avdellidou et al. in preparation). *Note that after the shot G191115 no large fragment was found.

Run#3	speed	M_{total}	M_{total}
Peridot	[km/s]	[mg]	[%]
S151015	0.92	22.72	100
G151015	1.25	23.71	90.7
G211015	1.58	22.35	86.6
G121115	1.95	19.70	84.0
G291015	2.23	12.12	55.7
G051115	2.67	4.00	17.0
G191115*	2.98	-	-

sizes that was comparable to the projectile's.

4.2.3 Summary

Implanted masses are calculated for all three Runs of the experimental campaign. In Run#1, no big fragments were found in the target, so the M_{total} was calculated only from the results of SExtractor routine. In Run#2 both big fragments and small ones (identified after EDX mapping) contributed to the M_{total} , while in Run#3, due to obscuration by the thick residue layer, the mass contribution from any small fragments could not be measured. The masses estimated by SExtractor in the first two Runs were slightly but not significantly different in the two modes presented here (SEx-Mode_1 and SEx-Mode_2). That indicates that the SExctactor routine worked well, returning a slightly smaller mass as the pixel number threshold for the minimum detected area was increased. We report increasing implanted mass in the targets as the target porosity increased, which is in agreement with our initial speculations.

4.3 The Final State of the Projectile

Although the primary goals of this work were the study of the fragmentation of the projectile (see 3.3.2 and 4.1) and its degree of implantation in the targets (see 3.3.3 and 4.2), we continued to study the final state of the recovered projectile fragments (3.3.4). In Fig. 4.7 are shown some large peridot fragments that recovered after the shots and were examined for any changes primarily with the Raman spectrometer within the School of Physical Sciences (see description in 3.3.1). It was examined whether the impact shock was strong enough to shift the characteristic olivine peaks in respect to the reference ones. An additional hydrocode simulation was undertaken for the shots of Run#1, in order to have an estimation of the temperatures and pressures at the time of the impact.

4.3.1 Raman Spectra

Raman spectra of the recovered fragments, using a near-IR laser at 785 nm, were obtained to ascertain whether the impact shock caused a shift in the main olivine lines, referred to as P_1 and P_2 . The P_1 and P_2 reference spectra lines of the peridot projectiles were measured before each shot (Hibbert et al. 2014) and were found to be in a very narrow range (indicating a very consistent composition) and are given in Table 4.11. By comparing the spectra we obtained before and after each shot we wanted to look for possible shock induced shifts.

Although the resolution of the instrument is $0.6\text{--}1.0\text{ cm}^{-1}$, if we make the assumption that the Raman peaks are Gaussian, we can fit more accurate peak positions on our spectra data. With this way the peak values for the reference and post-impact spectra were generated and compared.

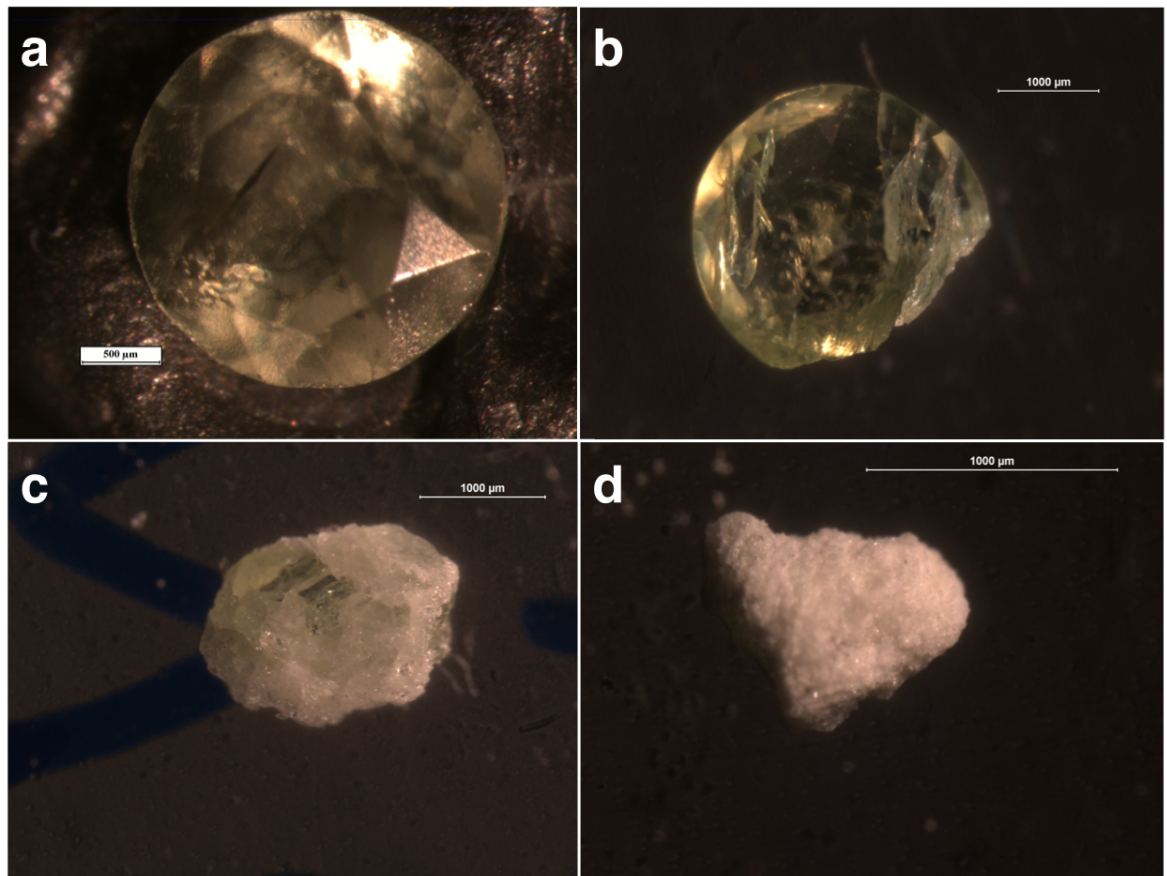


Figure 4.7: Some of the largest recovered fragments from the experiments on the non-porous water-ice target (speeds: (a) before shot, (b) 0.6 km/s, (c) 1.3 km/s and (d) 2.1 km/s). As the collisional speed was increased the recovered fragments were more white, indication that were more fractured.

After the examination of the Raman spectra of the fragments recovered during Run#1, no significant changes in the Raman spectra were observed. The greatest shifts were slightly greater than the measurement accuracy of the machine ($0.6\text{--}1.0\text{ cm}^{-1}$), and were 1.49 and 1.08 cm^{-1} for the P_1 and P_2 respectively after an impact at 2.16 km/s (see Appendix B.41), and 1.44 and 1.00 cm^{-1} for the 1.95 km/s shot (see Appendix B.29). If the projectile melted, then there would be no features in Raman spectra.

However, we cannot actually know from which part of the projectile the recovered

Table 4.11: The ranges of the P_1 and P_2 Raman peaks for each set of peridot that were used for each Run respectively.

	P_1 [cm^{-1}]	P_2 [cm^{-1}]
Run#1	822.64–824.20	854.15–855.63
Run#2	822.91–823.49	854.62–855.46
Run#3	823.09–823.44	854.20–855.29

fragments came from, and so we were not able to reveal the shock history of the projectile. It is possible that for the medium speed shots the recovered fragments were from a more heavily shocked part of the projectile, than the fragments from the higher speed shot. According to Mouri & Enami (2008) (and references therein) the pressure derivatives of fosterite are $2.85\text{--}3.27 \text{ cm}^{-1}\text{GPa}^{-1}$ and $3.07\text{--}3.12 \text{ cm}^{-1}\text{GPa}^{-1}$ for the two peaks respectively and therefore we can infer a crystalline stress of $\sim 418 \text{ MPa}$ for the impact at 2.16 km/s . Although it is impossible to tell where the fragments originated from with respect to the front face of the peridot, the inferred pressure seems to be only a fraction of the AUTODYN calculated peak pressure (see Table 4.13).

The same comparison was done for the other two Runs that involved the higher porosity targets. Again all the measured shifts are below the accuracy level of the instrument. In particular the shifts that calculated in Run#2 and Run#3 are generally lower than the ones measured for Run#1.

Figures 4.8, 4.9 and 4.10, present the spectra of the recovered fragments from the lowest and highest speed shots for every Run. The Raman peaks displacement for the large recovered fragments for all impact speeds tested are presented in Table 4.12 and all the individual Raman plots in Appendix B.

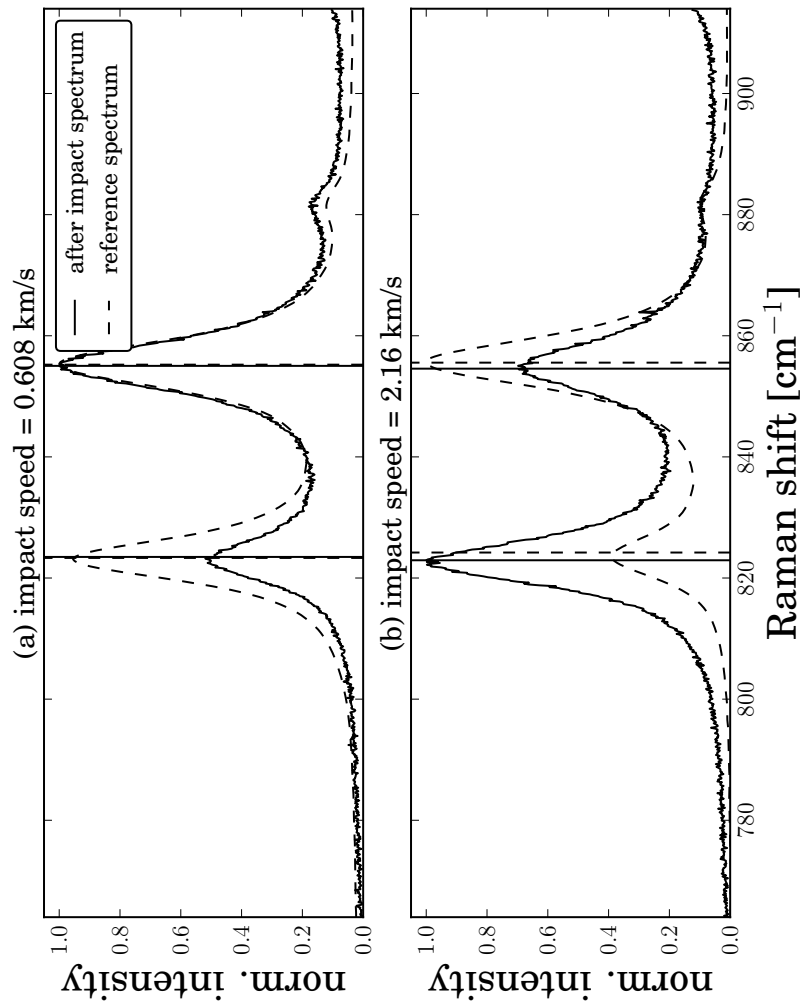


Figure 4.8: At 0.608 km/s none of the shifts exceed the precision of the instrument, whilst for the 2.16 km/s shot a shift in P₁ and P₂ olivine lines was observed to be 1.49 cm⁻¹ and 1.08 cm⁻¹ respectively.

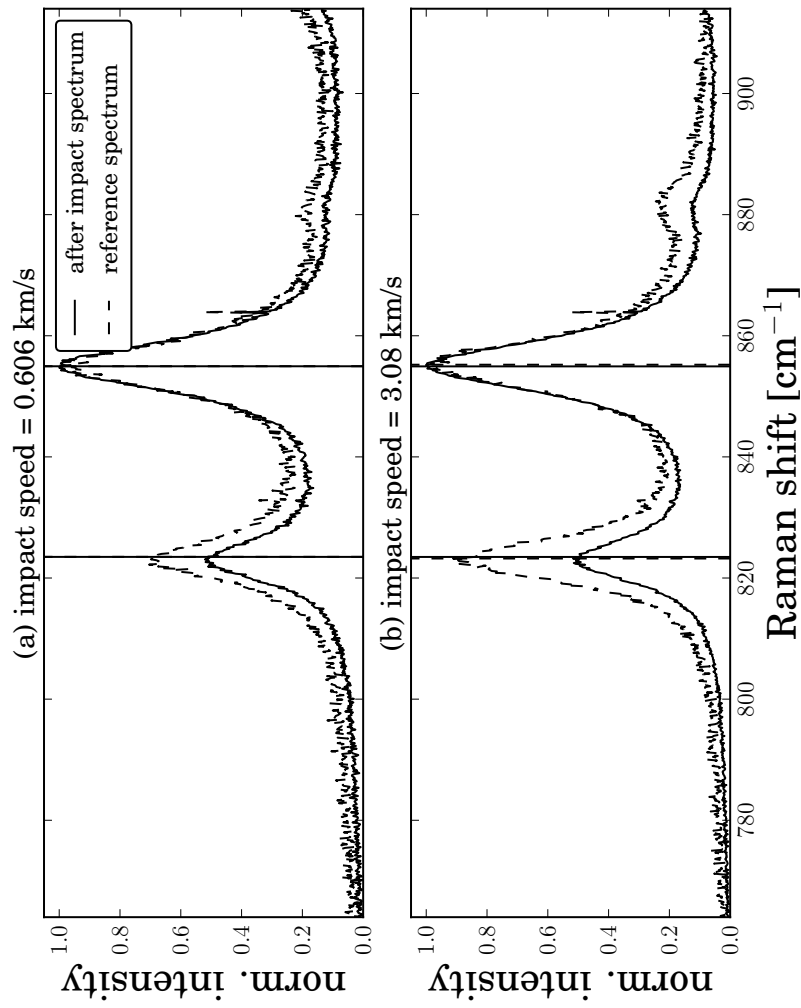


Figure 4.9: Raman spectra of large fragment that recovered after shots (solid line) during Run#2, in comparison with the reference (dashed line). No significant change above the instrument precision was observed in the P_1 and P_2 olivine lines.

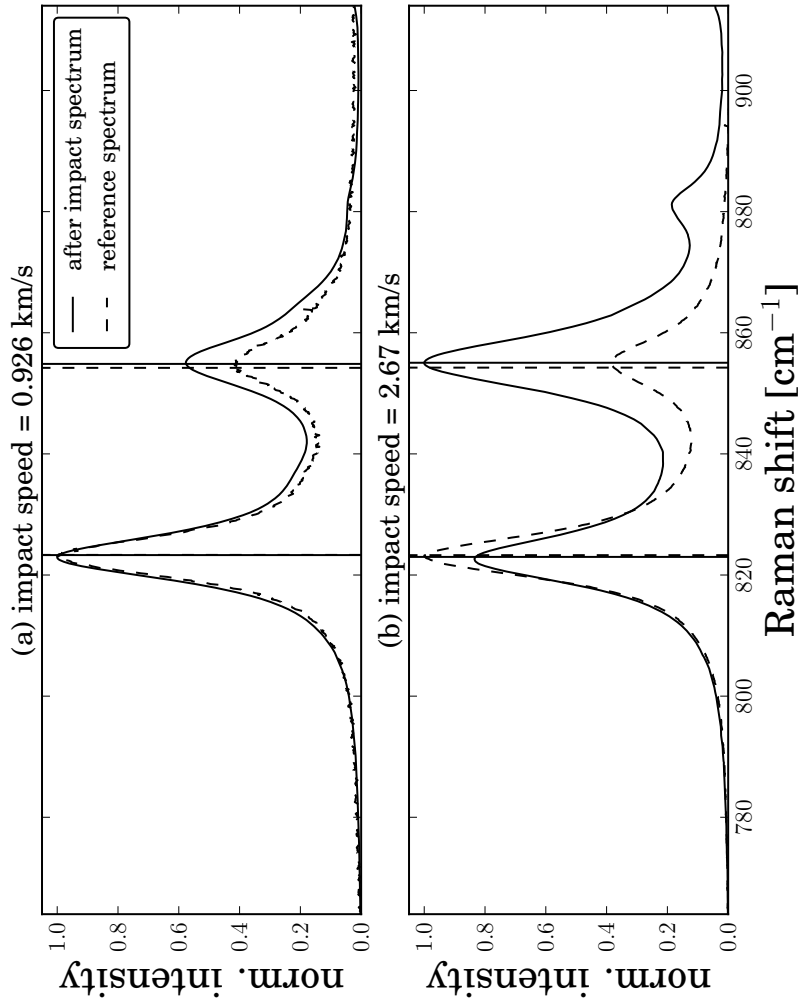


Figure 4.10: Raman spectra of large fragment that recovered after shots (solid line) during Run #3, in comparison with the reference (dashed line). No significant change above the instrument precision was observed in the P_1 and P_2 olivine lines.

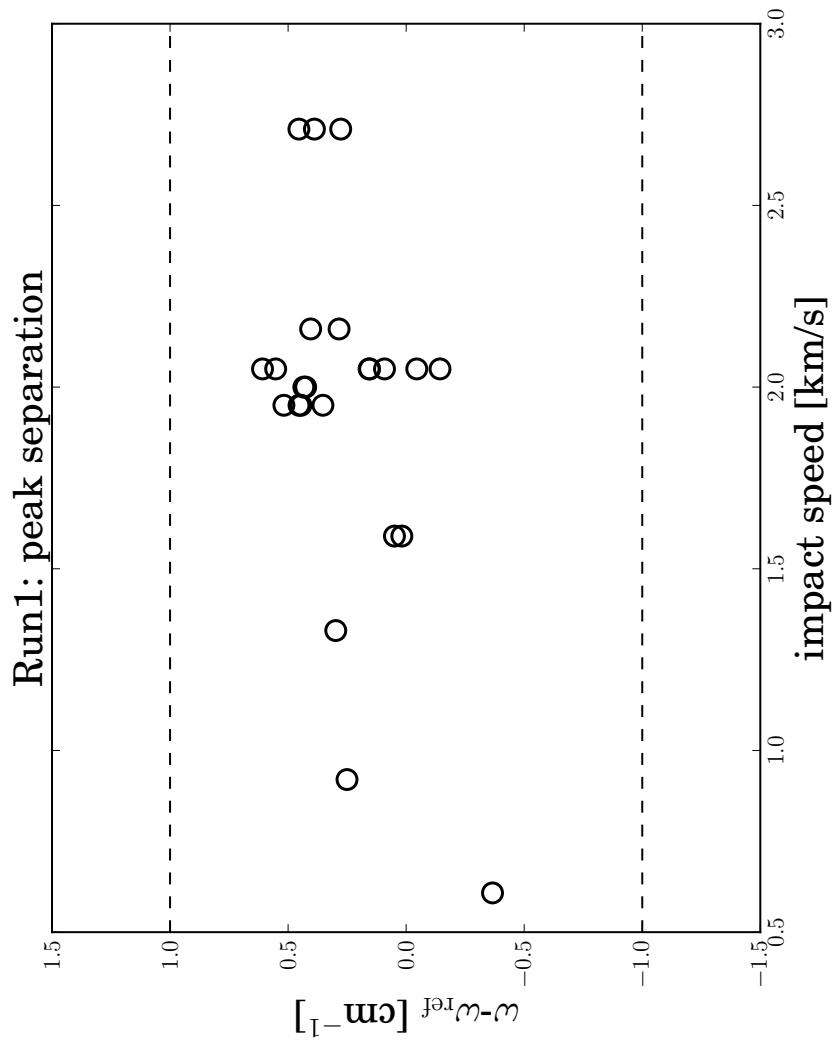


Figure 4.11: The change in separation, ω , of the P_1 and P_2 olivine lines was calculated for all the big surviving fragments in the range of impact speeds 0.608–2.71 km/s.

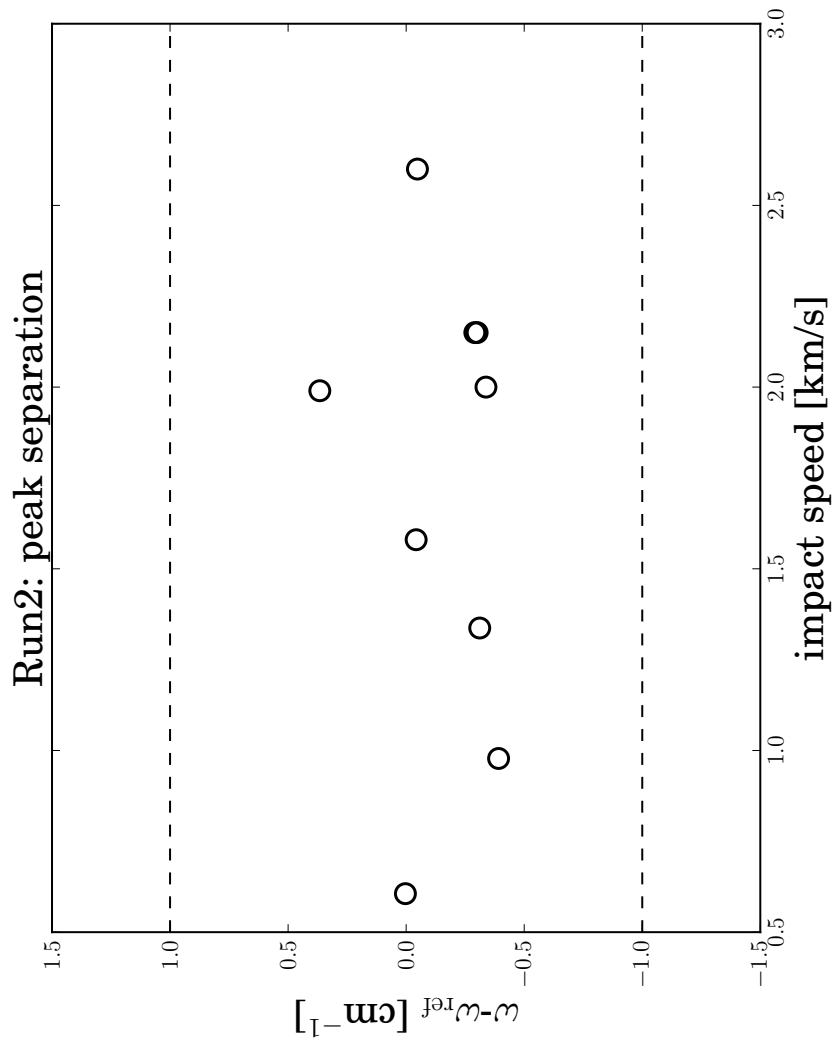


Figure 4.12: The change in separation, ω , of the P_1 and P_2 olivine lines was calculated for all the big surviving fragments in the range of impact speeds 0.61–3.08 km/s.

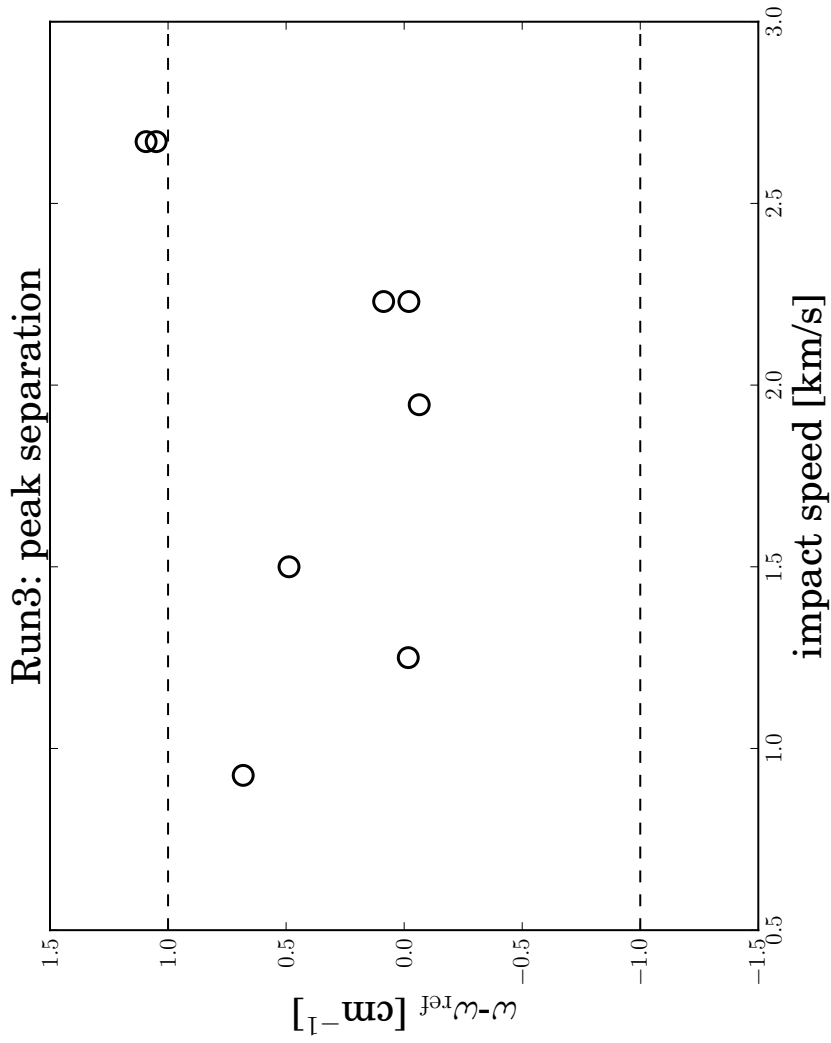


Figure 4.13: The change in separation, ω , of the P_1 and P_2 olivine lines was calculated for all the big surviving fragments in the range of impact speeds 0.93–2.67 km/s. Notice that at the highest speed shot at 2.67 km/s, the separation slightly exceeds the resolution limit for both fragments.

Another interesting application of Raman spectra would be the identification of any change in the separation (ω) of the two characteristic peaks of forsterite which, together with elemental quantification of Mg and Fe, could show possible shock induced change to the crystallisation and/or the elemental composition of the olivine (Kuebler et al. 2006; Foster et al. 2013). These two prominent peaks are the result of the fundamental vibration of the chemical bonds (here of Si-O bonds). Peak positions and shifts are generally used to calculate the ratio of Mg/(Mg+Fe) in olivine. The positions of the P_1 and P_2 are strongly related to Fe and Mg compositions of the olivine. For example according to Kuebler et al. (2006) the separation of the P_1 can be up to 10 cm^{-1} from fayalite to forsterite while the separation of the P_2 can be up to 20 cm^{-1} . However, up to our maximum collision speed (3.08 km/sec), no change in ω was detected above the lower limit of the spectral resolution of the spectrometer ($\sim 1 \text{ cm}^{-1}$) (Fig.4.11).

4.3.2 Additional Hydro-Code Simulations

In order to investigate the peak pressures and temperatures experienced by the projectile during impact, a complementary program of hydrocode modelling was undertaken by Dr. Mark Price, and was included in a joint publication with the author (Avdellidou et al. 2016). Simulations were performed with the AUTODYN hydro-code (Hayhurst & Clegg 1997). A simple Lagrangian, 2-D half-space model was set up, using 20 cells across the projectile's radius. The total number of cells in the model was approximately 500,000. Material models for ice were taken from Fendyke et al. (2013) using a 5-Phase Equation-of-state (EoS) from Senft & Stewart (2011). Strength and EoS data were taken from Ranjith et al. (2012) and Marsh (1980) respectively. Gauges (or tracers) were placed along the axis of the projectile so that pressure and temperature could be determined during the impact. In Table 4.13 we present the peak pressures, P_{max} , the

Table 4.13: Peak pressure, P_{\max} , peak temperature, T_{\max} , and temperature at peak pressure, T_P , as calculated with Autodyn (see section 4.3.2), are shown for the range of shots at the time of the impact.

Run#1	speed	P_{\max}	T_{\max}	T_P	Run#1	speed	P_{\max}	T_{\max}	T_P
Peridot	[km/s]	[GPa]	[K]	[K]	Basalt	[km/s]	[GPa]	[K]	[K]
S141114	0.38	0.54	301	293	G010415	1.49	0.80	360	307
S180315	0.60	1.21	298	293	G260515	1.68	1.02	401	302
S211114	0.92	1.64	297	294	G240415	2.07	1.29	433	303
G060315	1.33	2.84	302	295	G050615	2.14	1.32	436	303
G260215	1.60	3.75	312	296	G260515	2.17	1.33	440	303
G230115	1.95	4.83	330	297	G070515	2.70	2.97	463	308
G250315	2.00	4.94	331	297	G270415	3.03	4.58	522	317
G261114	2.05	5.06	342	297					
G130315	2.16	5.59	335	298					
G180215	2.71	7.13	397	299					
G031214	2.97	8.04	407	305					
G121214	3.50	10.2	513	353					

temperatures at the time of the peak pressures, T_P , was experienced and the maximum temperature, T_{\max} , 1 μm below the front surface of the projectile. Note, that for the lowest speed shot (0.38 km/s) the peak pressure as modelled does not exceed the yield strength of olivine (1.5 GPa) (Table 4.13). This agrees with the observed state of the recovered projectile, that retained 100% of its initial mass and showed no signs of damage.

4.3.3 Summary

In order to examine the final state of the large surviving peridot fragments after each shot, we obtained and analysed their Raman spectra. From the samples we recovered we report that for the majority of them, no displacement of the two main peaks P_1 and P_2 above the precision limit of the instrument (see Table 4.12) could be observed. Even in the spectra that exhibit shifts above the detection limit, we consider it as

marginal for any conclusion stating change in the material to be drawn. In addition, the mutual differences of these peaks are also inside the range of the precision limits (see Figures 4.11, 4.12 and 4.13).

4.4 Complications encountered in the experimental programme

During the experiments we faced two different types of problems that led to not completing the shot programmes as originally intended. Both of these complications were caused by unforeseen external reasons, and not by the developed methodology. The first complication (which became a constraint), was the limitation in impact speed. This was unavoidable and being aware of that we continued the experiments, but at a lower range of speeds that we would have liked. The second problem had to do: i) with contamination of the high purity water used to prepare the ice targets, after a lot of investigation which carried on for several weeks, the problem was overcome and ii) with the residues that CaCO_3 powder left after filtering.

4.4.1 Impact speed limit

The initial idea of the project was to impact onto different targets using primarily peridot projectiles. The speed range would cover the lowest limit that the LGG operates (this happens at ~ 0.3 km/s) up to the maximum speed that the LGG can reach (~ 7.5 km/s). The majority of the shots up to 3.5 km/s were successful, however increase of the speed caused constant failures. The unsuccessful shots were due to the combination of high velocity and the symmetry of peridots. During the experiments we experienced several outcomes:

- The projectile was unable to exit the gun. It crashed on the gun's walls between the two laser curtains.
- Several times the projectile crashed onto the back of the gas diverter located just before entry to the target chamber (see Fig. 4.14).

- Finally, the projectile reached the chamber but missed the target.



Figure 4.14: The gas diverter is a metallic funnel that is placed in between the target chamber and the gun. Several projectiles hit the back of the funnel leaving traces of damage.

After several failures during Run#1 to repeatedly achieve speeds >3.0 km/s, we stopped the attempts due to lack of allocated time on the LGG. Therefore in the following two Runs, with the porous targets (Run#2 and Run#3), the impact speed range was limited up to 3.0 km/s, in order to have a direct comparison of the data in the same speed range with Run#1. The unsuccessful trials are summarised in Table 4.14. From the total number of the performed shots, apart from the unsuccessful ones that are described above, two more were not included in the analysis and are given in

Table 4.15. In Run#2, data from shot G070815 (3.0 km/s) was not used as we realised that the target was not frozen properly. The target that was prepared was a solid and not granular, dissimilar to the previous ones of the same experimental Run. Specifically the ice grains were more wet than usual when the container was put into the liquid nitrogen freezer. In Run#3 data from shot

Table 4.14: All the unsuccessful shots were during Run#1, mostly at 3.0 and 4.0 km/s.

Run#	Shot No	speed	outcome
Run#1	G081214#1	4.0	crashed in the gun
Run#1	G081214#2	4.0	crashed on gas diverter
Run#1	G290115#1	0.64	crashed in the gun
Run#1	G290115#2	3.07	crashed on the ejecta collector
Run#1	G110315#1	3.0	crashed on gas diverter
Run#1	G130515#2	2.1	crashed on gas diverter

Table 4.15: Successful shots that were not used for further analysis.

Run#	Shot No	speed	reason
Run#2	G070815#2	3.0	target too hard
Run#3	G230915#1	2.0	higher porosity

G230915 (2.0 km/s) were not used as the porosity of the target was higher than the desired one. In the whole of Run#3 the porosity of the target was constantly 70%. In this particular shot, the porosity was calculated to be 78.5%.

4.4.2 Missing Basalt Shots

The intention for these experiments was not only to test the outcome by changing the porosity (or material) of the target, but also to test the behaviour of two different projectiles, peridots and basalt spheres, in the same speed range and on the same target. During Run#1 we used the synthetic basalt projectiles to impact the non-porous water-ice targets and we retrieved the largest fragments. However this was not possible to happen for the second Run, on the higher porosity water-ice target. Due to the nature of the projectile and target, the initially identified large pieces, fell apart inside the water droplets, and this made their recovery and measure impossible. Indeed two basalt shots were performed during the Run#2, G180915#1 (1.58 km/s) and G180915#2 (1.65 km/s). Due to this very brittle behaviour we proceeded directly to Run#3. Due to capillary action, water from the molten target is sucked up into the cracks and disrupts the basalt fragments. This was not observed to happen with the peridot fragments, which further implies the cracking/fragmentation of the two materials is significantly different.

4.4.3 Contamination of the targets

Water-ice targets

As described in 3.3, water-ice targets were used to allow for an easy separation from the projectile material, as they had only to melt and be filtered. For that purpose we used high purity HPLC water (which, according to manufacturer, had 3 ppm residue). Prior to its use, we filtered an amount of water similar to the one we used to prepare each target through the same type of filters. The result of this filtering left clean filters with no residues collected, and thus the water was deemed pure enough to be used for the targets. After the freezing and subsequent filtering of the target of the first shot of Run#1, we realised that there was left a white residue, the quantity of which was enough to obscure the projectile fragments. However the initial thought was that this powder consisted of the pulverised projectile. After examining the filters under the SEM to identify the composition of the white residues, we found that it was a Si-rich material. Since then there was a struggle to identify the source of contamination. There were several possibilities for contamination and therefore several tests were made.

- Initially we thought that our target containers were not well washed or rinsed. In order to test this, we got two different containers, one metallic and one plastic, washed and rinsed them well. Then we filled them with the very same water and filtered. The resultant filters were clean and no residues were found.
- As a second step we filled the containers with RO water containing a special cleaning solution (Decon 90), as we still believed the contamination was caused by the cleaning products. Again the filtering showed nothing. We repeated the same test, using the same liquid, but this time we froze them following the same

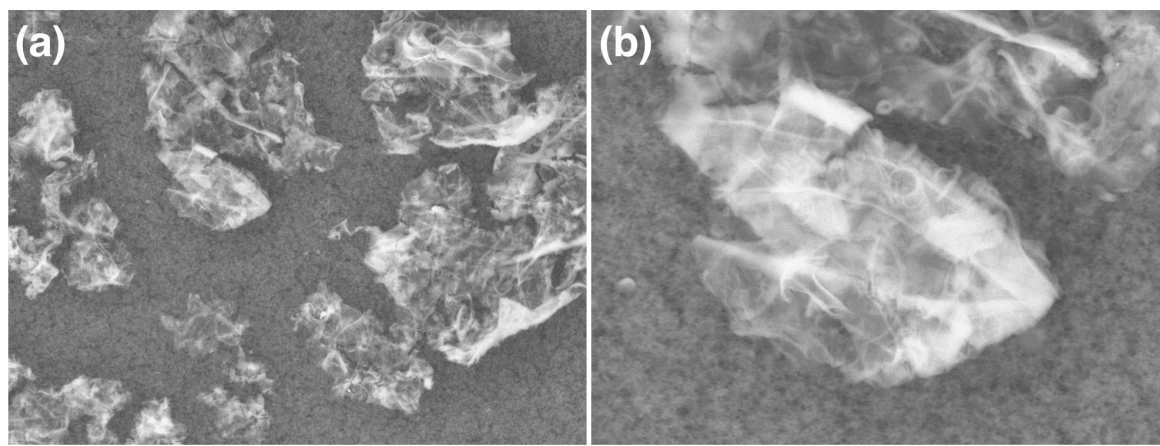


Figure 4.15: Images using different magnifications of the residue layer found after filtering the HPLC water that was previously frozen down to -130°C .

procedure used for the shot samples. The following day we let them melt and repeated the filtering. The result with the same, no residues were found.

- Another test was to compare the two types of water. For this reason we got four containers and we filled two of them with HPLC water and two with RO water. One of each was placed in the freezer to stay overnight while the rest remained in room temperature. Next day all were filtered and the contaminating powder was found only in the filter of the HPLC frozen water.
- In order to verify the result, as a last trial, we used only the HPLC water in four different containers. Two of them were plastic and two metallic. We froze one of a kind and the next day we repeated the filtering. Both filters that came from the frozen water showed the same type of contamination.

This led us to the conclusion that when the HPLC water was frozen, a silicon-rich contaminant dropped out of solution. The silicon-rich contaminant is possibly part of the purification process used by Sigma to produce the HPLC water. We made repeated

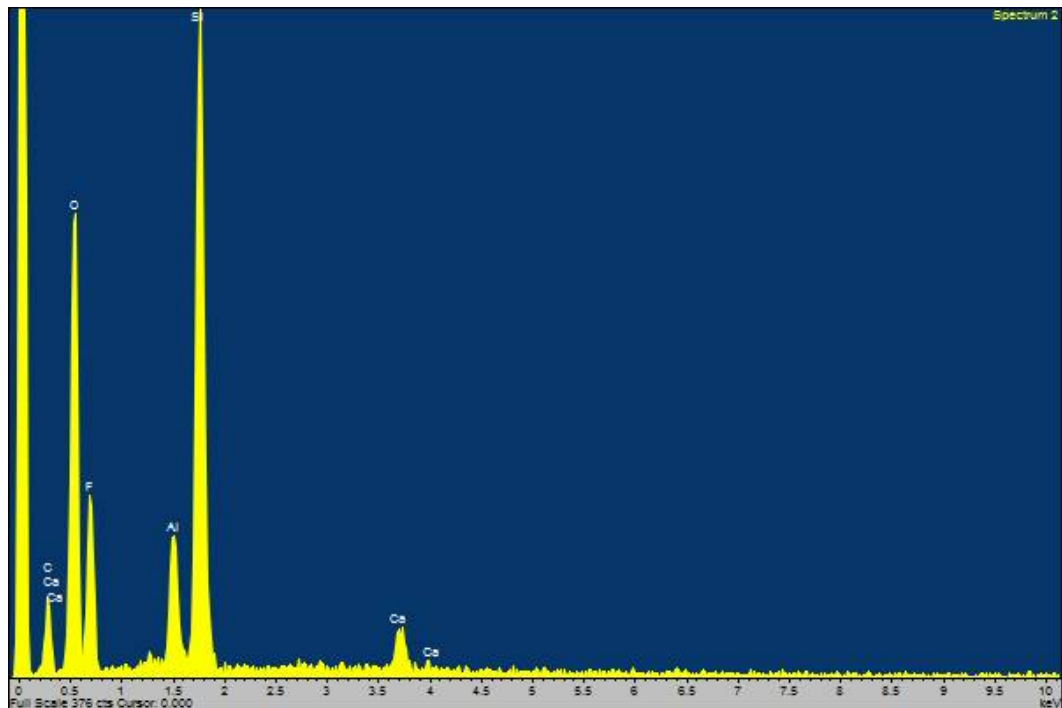


Figure 4.16: The composition of the residue layer. Spectrum taken from the same region as the SEM image in Fig. 4.15.

attempts to contact Sigma to ask about this issue but received no response.

Regolith-like targets

As described in 3.1, the targets were chosen with the basic condition to be made of a material that can be completely removed from the projectile and, as a result after filtering, to keep only the projectile's fragments. In order to use a target with high porosity ($\sim 70\%$), we selected high purity CaCO_3 powder. Before we finalised the decision to use this material, we tried to check that the material could successfully and totally be dissolved. Several experiments were performed where a few grams were put into nitric acid and, in turn, the resultant solution was filtered through the same type of PTFE filters, that were used in the actual experiments. No significant residues were

found on the filter. The product provider, states that the CaCO_3 , should be at least 99% pure.

However, during the actual experiments the amount of material that had to be dissolved (several 10s of grams) was significantly more than the amount initially tested. As a result, after the filtering processes, the whole filter surface was covered by a grey-transparent, residue layer (Fig. 4.17). After examining the layer in the SEM, we found that this residue was Si-rich and we were not able to dissolve more, in order to eliminate the residue (Fig. 4.18) and extract the projectile fragments. This layer was produced independently of the type of filter used (pore size and total filtering area, see 3.3.2) and it was thick enough (a few microns) to obscure the impactors fragments and it remains of unknown origin.

Therefore, further investigation into small projectile fragments for the CaCO_3 target was not possible. However due to the nature of the target (see 4.1), the peridots fragmented less, and large fragments were embedded and easily discovered in the powder. The main reason for this unwanted situation, was our ignorance of the depth of the craters that were going to be produced, and so the total volume that had to be excavated and removed from the target for dissolving and filtering, in order to be sure it would include the majority of impactor's fragments.

4.4.4 Summary

During the experimental procedure we faced several difficulties due to limitations of the instrumentation, and also due to unforeseen imperfections in the materials used. However, we managed to overcome some of these problems, e.g. after several tests we identified the source of contamination as the HPLC water. Unfortunately the limitation of the gun, firing projectiles with complex shapes at higher speeds, was not something

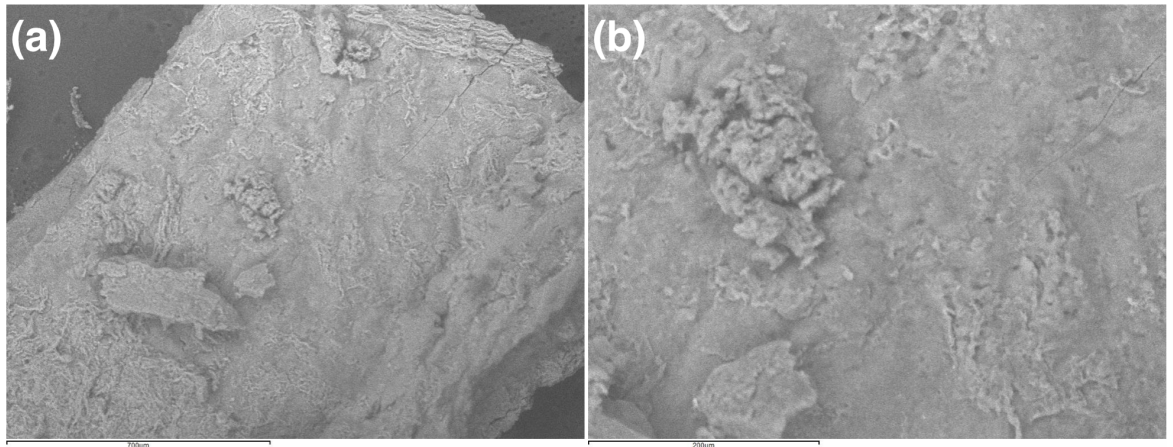


Figure 4.17: BSE Images of different magnifications of the residue layer found after filtering the dissolved CaCO_3 targets.

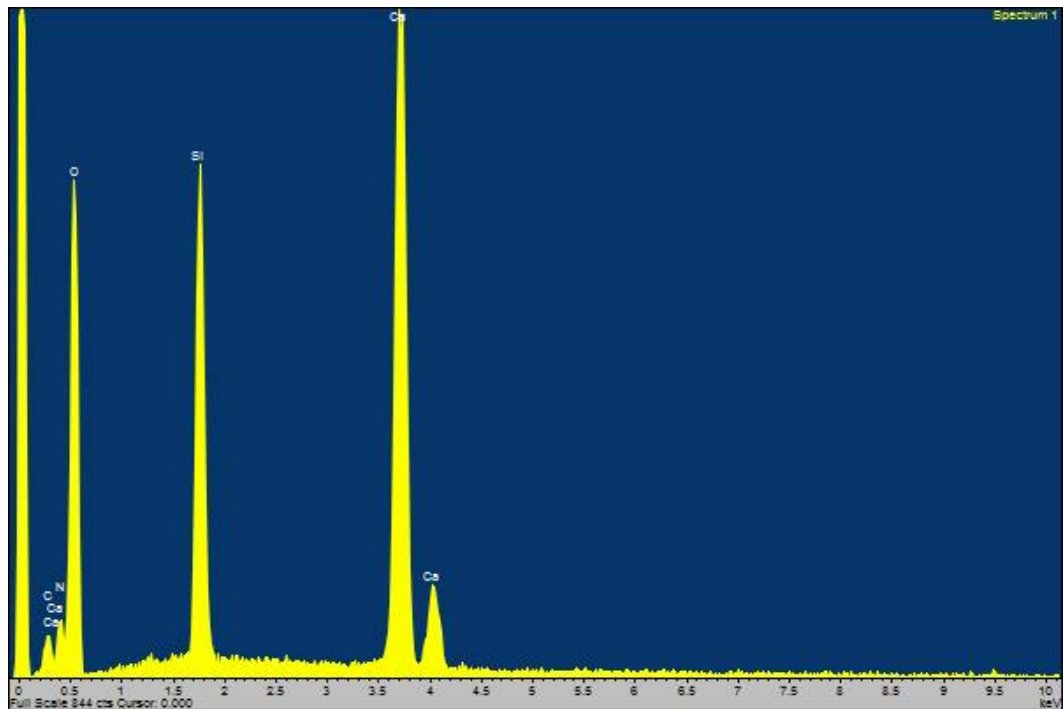


Figure 4.18: The composition of the residue layer. EDX spectrum taken from the same region as the SEM image in Fig. 4.17.

that could be worked around for this specific work. Neither was the brittle behaviour of the synthetic basalt projectiles impacting the porous ice, which ultimately forced us

to quit the experiments using that as projectile (although this was an interesting result in itself).

5

Contextual Overview

IN this Chapter are discussed the results of the experimental campaign that was analysed in the methods Chapter 3 and results Chapter 4. There is an attempt to interpret these results with small body observations, as mentioned in the introductory Chapters 1 and 2. Moreover are presented some preliminary simulations of asteroid collisions in the Main Belt, using part of our experimental results.

5.1 Discussion of the Results

The first experimental data obtained were the masses of the largest recovered fragments of the projectile after each shot. We are confident that the recovered fragment is the largest for each shot, as we painstakingly searched the ejecta, target and target chamber for projectile pieces. More specifically, for the Run#3, the ejecta collection system was built in such a way that no fragment escape could occur, unless it bounced off the target and travelled straight back down the gun. However, such an assumption is counter to the observation that the ejecta after the shots on high porosity targets had a very low speed and would not travel all this distance. From observation of the ejecta collection system we had an estimation up to where the ejecta flew within the collection system

and thus we knew the ejecta was not very energetic. By plotting the mass of the largest projectile fragment against the energy density, Q_{im} , we can see the behaviour of the projectile on a specific target. In our experiments the largest fragments create smooth plots, with little scatter, revealing a clear trend of the decrease of the mass of the largest fragment with increasing collisional speed. The data points were fitted with a power law, as described in 3.3.2 and 4.1, which is a straight forward way to obtain the value for the energy density at the catastrophic disruption limit, Q_{im}^* .

Figure 5.1 compared the fragmentation behaviour of the peridot and basalt projectiles when impacted onto several types of targets. Specifically:

1. The synthetic basalt projectiles, which have a comparable size to the peridots, require an order of magnitude higher energy to retain 50% of their initial mass ($Q_{p}^*=6.46 \times 10^5$ J/kg versus $Q_{b}^*=2.71 \times 10^6$ J/kg). So catastrophic disruption for peridot projectiles occurs at 1.14 km/s, whereas for synthetic basalt this happens at 2.33 km/s, indicating that peridots are more fragile than basalt. This is in agreement with the comparison of the compressive strengths of both materials; which are 80 MPa and 100–250 MPa for basalt respectively (Petrovic 2001; Schultz 1993).
2. There is a small shift of the data points towards smaller energies when peridot projectiles impacted the porous water-ice targets (Run#2), in comparison with the same projectiles onto the non-porous water-ice targets (Run#1), and this difference is more obvious at lower speeds. Moreover the tail of the plot for the porous target appears to be less steep: the 50% of the initial impactor mass is preserved at collisional speeds of 1.14 km/s and 0.60 km/s respectively, giving a reduction of the energy density of ~ 3 .

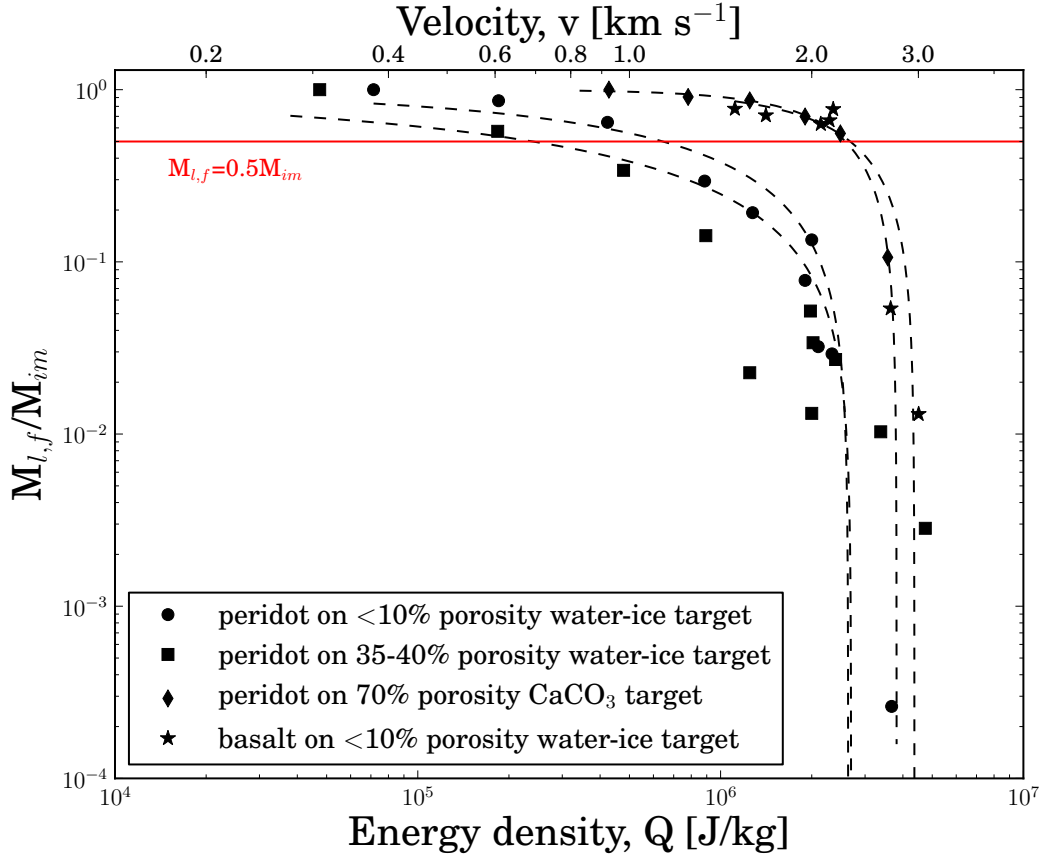


Figure 5.1: The largest recovered fragments from all Runs. The dashed lines correspond to the best fitting of a power law as shown in Eq. 4.1. The red solid line shows the limit for the catastrophic disruption of the projectile, when $M_{l,f}/M_{im}=0.5$.

3. Upon increasing the porosity of the target (to 70%), we expected to see a further shift of the energies towards lower values, following the same behaviour as stated earlier. However this is not observed for the CaCO $_3$ regolith target (Run#3). Indeed on the contrary, the whole dataset shifts to the right (relative to the data from the non-porous water-ice targets) with the collision speed for catastrophic disruption occurring at 2.27 km/s, where we find the large fragments of the synthetic basalt, giving an increase in the energy density of an order of magnitude ($Q_{p}^*=6.46 \times 10^5$ J/Kg and $Q_{p,r}^*=2.58 \times 10^6$ J/Kg for the non-porous and regolith

target respectively, where the subscript ‘p’ refers to ‘peridot’ projectile and ‘r’ the regolith target).

From the above three results it is clear that the target’s porosity does play a role in the fragmentation of the projectile. However it is also clear that this is not the only parameter. From the shift towards higher energies for the regolith targets, it is understood that the target material and possibly the target’s material grain size also contribute to the result. In Run#2, where peridots impacted onto $\sim 40\%$ porosity water-ice targets, the ice grain sizes were in the size range from a few mm (similar to the impactor’s size: 3 mm) down to 10s of microns. While in Run#3, where peridots hit the regolith CaCO_3 powder, the average grain size dropped significantly to microns, similar to the finest water-ice ‘grains’.

Further investigation of all the large fragments that could be collected separately and weighed, using the Raman spectrometer as described in 4.3, showed no indication of impact melting, as the Raman spectra did not lose its original features. The temperatures that were calculated from the hydrocode (see Table 4.13) at the time of the impact are significantly lower than the melting point of olivine which is ~ 2100 K at 101 kPa. By placing the calculated temperature and pressure into the phase diagram of forsterite (Fig. 5.2) we see that the values we calculated for the maximum tested impact speed (3.50 km/s) are outside this range and, therefore, we should expect no phase change of the projectile. Additionally, the obtained spectra showed no measurable shift of the two characteristic olivine peaks, indicating no significant alteration to the material. In some fragments spectra were obtained from two different locations with similar results (i.e. no measurable shift). One would expect that the shift of peaks would gradually increase as the impact speed increases, as the induced impact

shock would have been greater. Although this is something we do not observe in the results, for a couple of shots (at 1.95 km/s of Run#2 and 2.16 km/s of Run#1) we see a marginal shift of the peaks. The impact speed of these two shots was not the highest used.

One possible explanation is that, up to the tested impact speeds (that gave large identified fragments), the speed is too low to produce any significant change to the peridot impactor material. The other explanation is that the origin of the material examined under Raman spectrometer was ‘far’ from the impact point (i.e. originated at the middle or back of the projectile) and, thus, was not affected strongly by the impact shock. Inspection of the recovered fragments gave no indication where they were originally located within the projectile.

We subsequently moved on to study the ejecta size frequency distributions by obtaining EDX maps over the filtered ejecta samples. The ejecta filter areas that were mapped and examined were the same for each shot. From the recorded elemental frames we statistically handled the following results, some of which were not expected:

1. There is not a clear trend in the statistical modes of the differential ejecta SFDs in the same Run with increasing impact speed. For example, the modes are approximately around 1.5, 2.7 and 7.5 μm for each of the three Runs. A small shift towards larger sizes exists in the ejecta SFD for shots with the very lowest impact speed, that produced fragments (usually for the shot with the lowest speed the projectile was recovered completely intact) for both Run#1 and Run#2. Especially in Run#1 the shot at 0.60 km/s has the size peak at $\sim 4 \mu\text{m}$.
2. A similar result is also observed for the slopes of the cumulative ejecta SFDs. The slopes per Run have values in narrow ranges, but they do not appear to

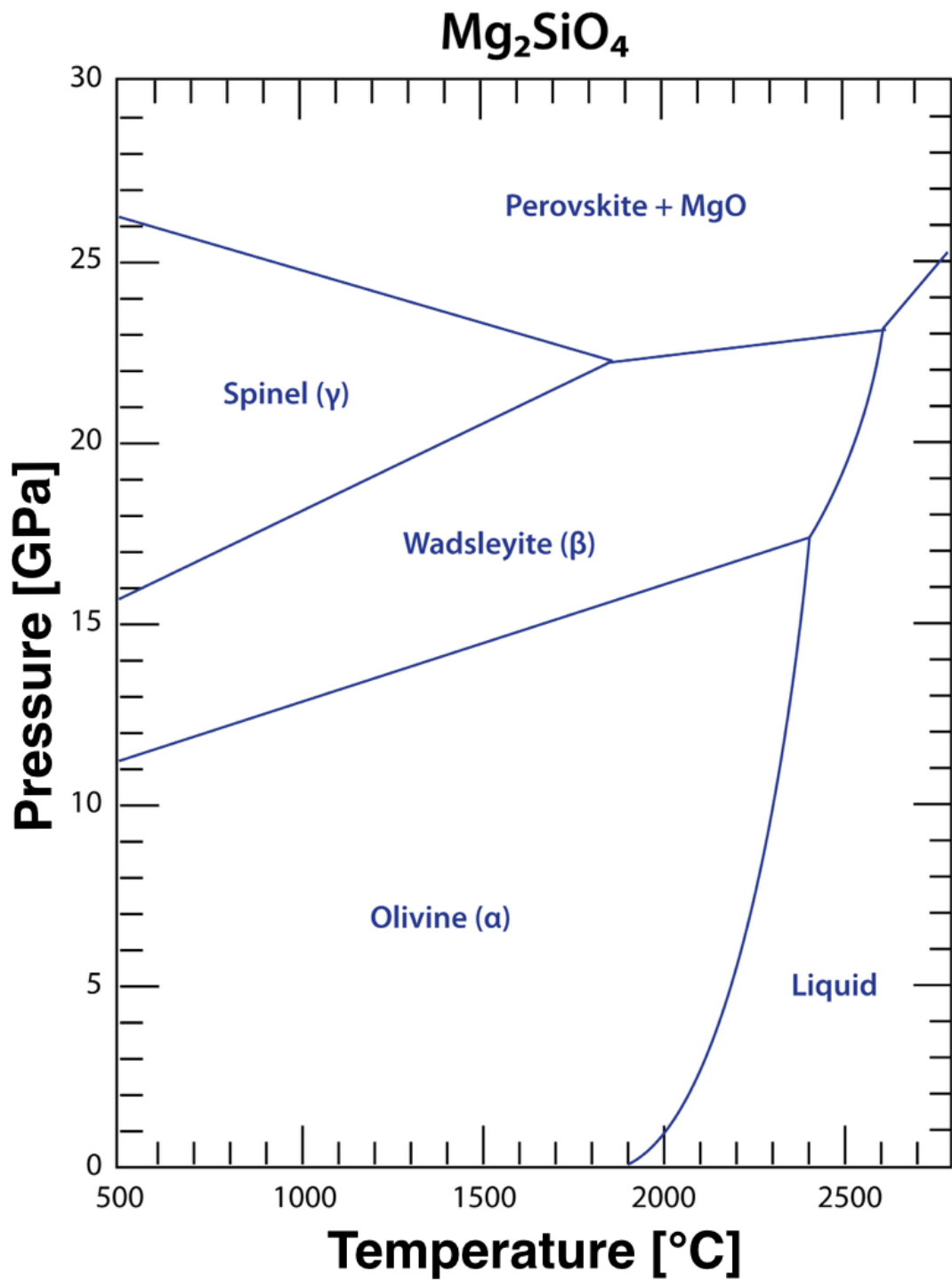


Figure 5.2: Phase diagram of forsterite olivine (Fei & Bertka 1999). AUTODYN simulations (see Table 4.13) gave for the 3.50 km/s impact speed of peridot onto non-porous water-ice target $P_{\max}=10.2$ GPa and $T_P=80^\circ\text{C}$. The temperatures we calculated are below the range of the phase diagram, indicating that the recovered fragments were still in the olivine phase (a).

have a clear trend with increasing impact speed. Again the lowest speed shots in Run#1 have shallower SFDs, but surprisingly, the lowest at Run#3 is steeper than the rest of the same Run.

3. Another interesting outcome is that, although for each scanned ejecta filter the same area was scanned with EDX spectroscopy, there is also no increase in the number of fragments with increasing speed, apart again from the shots with the minimum impact speed.
4. As it can be seen in Figures 4.3 and 4.4 the scanning with lower magnification of the same filter misses the smallest fragments and shifts the mode slightly to larger sizes. Also the analysis of the images taken with lower magnification gives steeper average slope value. This implies that care has to be taken comparing results taken at different magnifications, as they could introduce biases.

Surprisingly from the above results it is understood that the impact speed (up to the maximum speed used here) does not substantially affect the fragmentation behaviour of the peridot projectiles. This result is in contrast to our initial speculations that the impactor should produce more numerous and smaller ejecta fragments - and thus steeper ejecta SFDs - when it hits the same target at higher speeds. One explanation for this observation can be that there is secondary fragmentation on the ejecta collecting systems. However, as was mentioned in 3.2.2, we expect this secondary fragmentation to be limited due to the low ejecta speeds, which are only a small fraction of the incident speed. The other explanation is that indeed the peridot projectiles have this fragmentation behaviour, which differs from more ductile (i.e. metal) projectiles (Hernandez et al. 2006; Kenkmann et al. 2013; McDermott et al. 2016), and is independent of the collisional speed, when these collisions happen onto the same type of

target.

From the comparison of the modes and slopes of the ejecta SFDs between the three Runs we reach some general conclusions that verify the initial speculations. In Run#1, according to the pixel scale of the images and the pore size of the PTFE filters, there is identification cut-off between 1 and 1.2 μm , and fan average turnover of the fragment size at 1.5 μm as real. In Run#2, where the same type of projectile impacted the $\sim 40\%$ porosity water-ice targets, the observed turnover at $\sim 2.5\text{--}3.0$ μm is very close to the cut-off limit of the fragment detection at $\sim 2.2\text{--}2.7$ μm (see 4.1). In Run#3, the fragment identification cut-off is around 6.2–7.4 μm , according to the pixel scale, and the SFD turnovers are between $\sim 7\text{--}8$ μm . This Run was mapped with lower magnification compared with the previous two, but despite this fact the cut-off is further than the peak of the distribution and so the result is not biased. This implies that the same type of projectile does not produce so small fragments when impacting on a very porous material at the same speed. These are very marginal results and thus we should be more reluctant to state that a clear shift of the modes is observed between the Runs.

By comparing the average slopes of the cumulative SFDs between the three Runs, there is a clear trend of increasing steepness of the slopes with increasing target porosity. This means that the fraction of the small fragments produced is greater than the larger ones. As the target's porosity increases, the target itself become weaker and thus is easier to break. But, on the other hand, the increased porosity makes the target to 'be seen' harder from the projectile's perspective. The increased macroporosity, means larger voids inside the target that dissipate the energy that is delivered by the impact. As both porous targets consisted of grains, we can assume that the impact procedure was not the same as on a non-porous target. During an impact on a solid material, a

shock-wave is produced and penetrates the target as well as the projectile. At higher speed impacts, a stronger shock-wave will be produced and (depending on the projectile size) will totally penetrate it backwards and when the shock-wave reaches the rear to move again forward and so forth: this causes the fragmentation of the projectile. Whilst impacts on non-porous materials will only ‘see’ one target, in porous targets comprised of grains with size comparable to, or smaller than the projectile, multiple impacts may occur as the impactor penetrates the target material. Each of these impacts will cause the production of a new shock-wave. Therefore, in this example, the projectile will suffer stronger shock due to multiple shock-events, something that will lead to higher fragmentation. Additionally, on entering a porous target, the projectile might fragment, and each of these fragments could travel through void space before impacting another target grain. This would result in multiple shock events and further fragmentation of the projectile.

Finally we moved onto investigate the projectile material implanted in the targets. Based on materials and porosities, we reported several findings:

1. There exists a large increase of implanted material with increasing porosity of the target material. In Run#1 the projectile leaves a few per cent of its initial mass in the targets even at impact speeds >2.0 km/s. In the next following Runs, where the porosity is a lot higher, the amount of implanted material increased dramatically. It should be mentioned though that only in Run#3 did the embedded mass decrease consistently with increasing impact speed, as it was expected. In Run#1 and Run#2, where water-ice targets were used, there is no clear trend observed but the implanted mass fluctuates in the range of tested speeds. This result may be biased up to some extent, as from Run#3 there is

no mass estimation of the very small fragments that remained in the target, as due to the residue left after dissolving CaCO_3 , it was not possible to perform the EDX mapping. Because of this missing mass fraction we cannot have an absolute result. However, the recovered mass of the large fragments found in targets, consisted of a very large fraction of the initial impacting mass.

It should be commented that after two shots of Run#2 (for impact speeds 1.58 km/s and 2.60 km/s) it was found that only a tiny amount of mass was embedded (total mass from large fragments and outcome of SExtractor calculations), compared to the shots prior and after. A possible explanation could be that the target's surface was not as even as in the other shots and the slight variation in angle with which the projectile may have hit the grains changed the outcome of the collision.

2. The ejecta velocities became smaller as the target's porosity increased. Although the investigation of the ejecta velocities was outside of the scope of this project, it was noticed that ejecta material (both target and projectile) was flying up to shorter distances from the target. We were able to understand also the target material in ejecta either from the water droplets found or from the presence of the CaCO_3 powder. When the transparent plastic tube was used for ejecta collection, this phenomenon became very clear. During Run#1 ejecta could fly backwards (~ 50 cm), through the ejecta collection setup and exit almost at the end of the chamber. In Run#3, no ejecta was recovered further more than a few cm (~ 5 cm) from the impact point.

From the above it is clear that the target porosity plays a definite role on the implantation of the impactor's material on the target after a collision. The low ejection

velocities also contribute to the non-escape of the projectile's material from the target. For a porous material the ejecta velocities have been measured to be up to two orders of magnitude less than the ejecta speeds measured for rocks. This means that for the impact speeds tested in a laboratory the ejecta cannot fly with a speed beyond a few m/s (Holsapple et al. 2002). Another contributing factor could be that the largest fragments of the ejecta travel with lower velocities compared to the small ones, a phenomenon that is also not affected by the impact angle (Benz & Asphaug 1999). Also, this last factor was partly responsible for the majority of the largest fragments of Runs#2&3 being recovered directly from the target as described in 4.1.

Considering also the results of the ejecta SFDs mentioned earlier, target porosity is not the only factor that determines the impact outcome. Although it dominates for the implantation of exogenous material on a target, the type of the target material (e.g. composition, hardness etc.) itself contributes too. As it was shown in Figure 5.1, when the CaCO_3 powder was used (highest porosity, finest grained), even with the highest porosity in this series of experiments, the data points are shifted to higher energies in order for similar level of impactor fragmentation to occur, compared with the non-porous targets. So, although increasing porosity for water-ice target produced harder targets for the projectile, the higher porosity CaCO_3 target behaved as a softer target to the same projectile. In the next section we try to cement all these experimental results into context for observations of collisions onto asteroids.

5.2 Implications for Asteroid Collisions

5.2.1 Porosity of Asteroids

One of the fundamental physical properties of asteroids is their density. When the total mass of an object and its volume are known, the calculation of density is straight forward and if the mineralogy of an asteroid is also known then the *grain density* of the solid parts of the object can be inferred. However, spacecraft missions give a different value for many small bodies, which is lower than the estimated one using only meteorite analogues. This happens because for the calculation of this *bulk density* the internal voids of the body contribute to this reduction. *Bulk porosity* is the derivative quantity when these two densities are divided. However, some porosity has been found at very small scales in meteorite samples, the so-called *microporosity*, and corresponds to the small voids and fractures and has scales $\sim\mu\text{m}$ sizes, while the large scale voids inside the bodies create the component of *macroporosity*. The sum of *microporosity* and *macroporosity* gives the *bulk porosity*.

In order to have estimations of an asteroid's bulk porosity it is essential to link the parent body with meteorite samples (to know the mineralogy and microporosity) and also the bulk density. Figure 5.3, Britt et al. (2002), provides values for macroporosity and the bulk porosity of individual asteroids, for which we have data. When the bulk densities are very close to the meteoritic analogues, this implies that the porosity is close to zero. This is observed for the very large asteroids (10^{20} kg), that are believed to have survived the 4.5×10^9 Gyr of evolution and belong to the 'coherent group' of bodies. At the other end of the scale, asteroids with estimated very high bulk porosity (60–70%) are believed to be re-accumulations of fragments produced by large scale impacts forming the 'rubble-pile group'. Densities for >260 bodies (see Fig. 5.4) have

been estimated to date using several methods so far (see for a review Carry (2012)), such as: a) orbit detection during close encounters with another asteroid, b) spacecraft tracking and c) the orbit of their satellite when they are a binary system.

Asteroids with intermediate porosities (15–25%) are the so-called ‘fractured group’, with bodies that suffered from collisions, but which were not strong enough to be disrupted. As it is shown from the study of Carry (2012), the C-type bodies tend to have higher porosities compared to S-types, and also the most massive asteroids of all types are coherent (see Fig. 5.4).

The general conclusions from asteroid porosity studies are that the darker, and more primitive, asteroids appear to have higher porosities than the S-types that populate more the fractured group. Through the determination of an asteroid’s porosity one can infer the body’s collisional history.

Apart from the general estimation of the overall porosity of an asteroid, studies have been done to determine the variation of porosity near the surface. Estimations of the thermal inertia and radar observations, have shown that large asteroids have up to 50% porosity in the first metre from the surface and approximately 90% within the first few millimetres (Vernazza et al. 2012). Figure 5.5 is a graphical representation of the first layers of an asteroid’s surface and the difference in porosity with increasing depth.

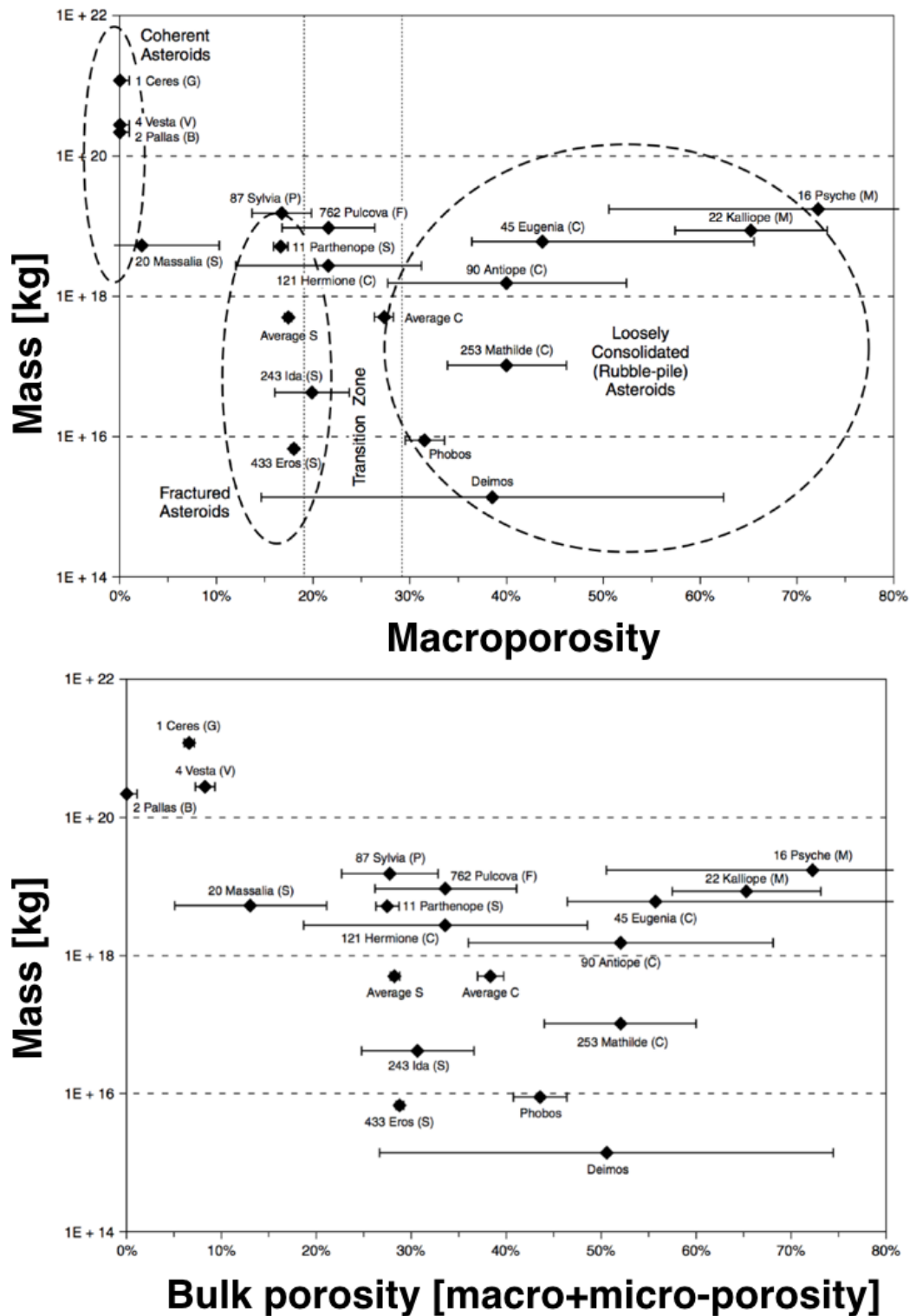


Figure 5.3: Macroporosities and bulk porosities of individual asteroids of the different types. Top: Are defined the three groups of objects according to their porosity values. Bottom: The average porosity for C-types is larger than the S-types, with $\sim 30\%$ and $\sim 40\%$ respectively (Britt et al. 2002).

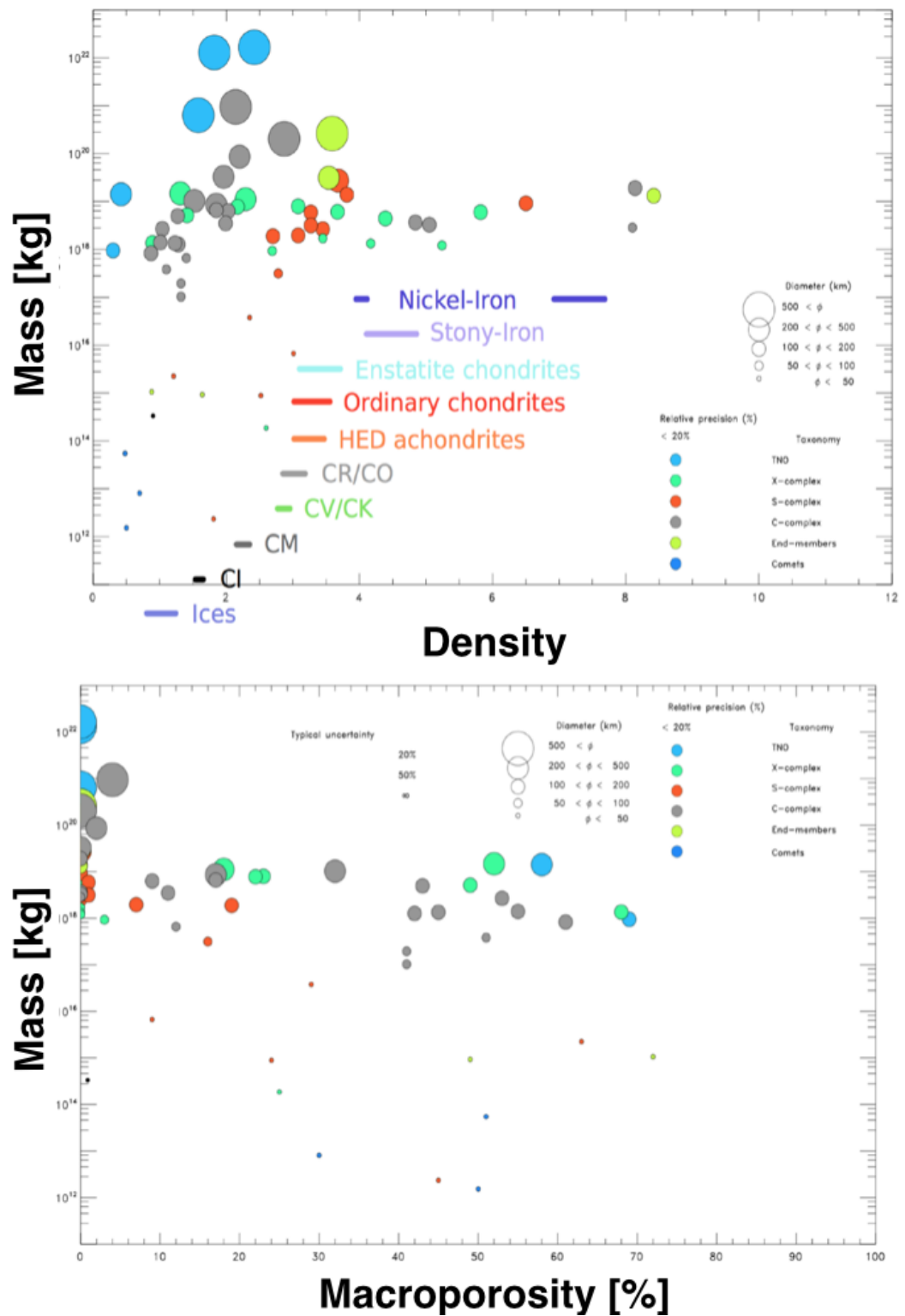


Figure 5.4: Densities (top) and macroporosities (bottom) of six groups of small bodies including TNOs, comets and the four types of asteroids vs. their mass. The size of the markers correspond to the objects' diameters (Carry 2012).

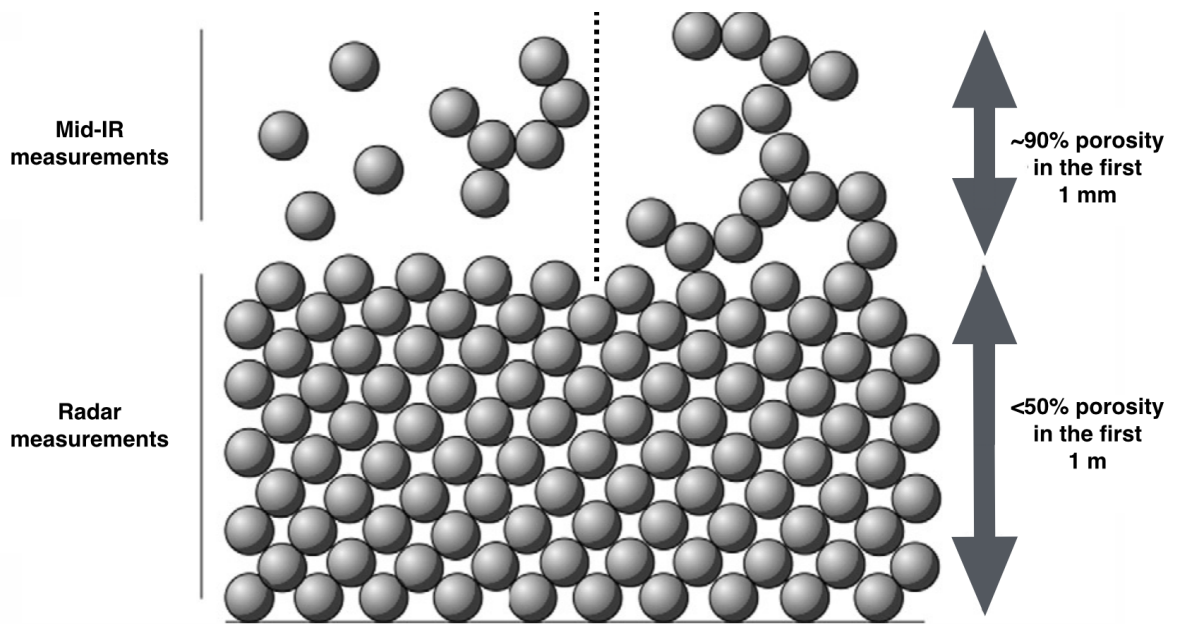


Figure 5.5: Structure of the asteroids surfaces, showing a very high porosity in the first mm which can be explained either by cohesive forces (right side) or by small particles floating (left side). Model adapted and modified from Vernazza et al. (2012).

5.2.2 How Does Porosity Affect the Outcome of Asteroid Collisions?

When collisions happen on porous targets the outcome is different than for collisions on non-porous materials, as has been shown by several studies so far (Holsapple et al. 2002) and within this thesis. Compaction mechanisms dominate the processes: during an impact onto a porous material, the shock propagates causing the empty spaces to collapse, compacting the material. Also the transfer of the shock-wave is blocked and terminated more quickly due to pore spaces (as the shock-wave effectively loses energy collapsing the pores), which leads to the attenuation of the shock pressure. This mechanism makes the highly porous asteroids, that are mechanically weak bodies, more resistant to collisions. Flynn (2014) concluded that the asteroid porosity, which leads the porous weak bodies to behave as strong bodies, is the possible cause of their survival and abundance. A highly porous asteroid was either formed as a rubble-pile

or it resulted in this form after disruptive collisions. Such collisions would reduce its bulk porosity with increasing number of impacts on its surface, as the compaction waves close the pores as they propagate and damp out. Also, when a collision is sub-catastrophic, then the shaking of the fragments can rearrange them in a more compact form.

Target porosity is very important, not only for the overall fate and disruption of the colliding body, but also for the crater formation and ejected material. As the shock waves are absorbed more efficiently on porous targets, craters can be formed very close to each other, without overlapping. As the gravity increases on the porous asteroids, the radius remains almost constant (Housen & Holsapple 2003). This phenomenon was also observed on the surface of the C-type asteroid (253) Mathilde, which has a low density and an estimated bulk porosity of $\sim 50\%$.

The reason for this observation of the craters being well-defined in diameter, is the lack of visible ejecta. As was mentioned earlier, porous targets create ejecta with much lower velocities compared to ejecta produced from non-porous bodies, and it decreases as the porosity increases. Several experimental studies have been done to calculate the ejecta velocities, and give the result that, for example, ejecta can have a velocity of two orders of magnitude less than the collisional speed, when target has porosity $\sim 60\%$. Especially in large bodies, the ejecta speeds can be much lower than the escape velocity of the target body. This behaviour shows a dependence of the escaping ejecta on the target's size, enabling the re-accumulation of the fragments (Ryan & Melosh 1998). As a result, the amount of ejecta mass that escapes from the parent body, decreases with the increase of the porosity and total mass of the target (see Fig. 5.6). Also it has been shown by Housen & Holsapple (2003) that while small craters on porous bodies indeed can produce an ejecta blanket, this is not the case for the larger craters. In

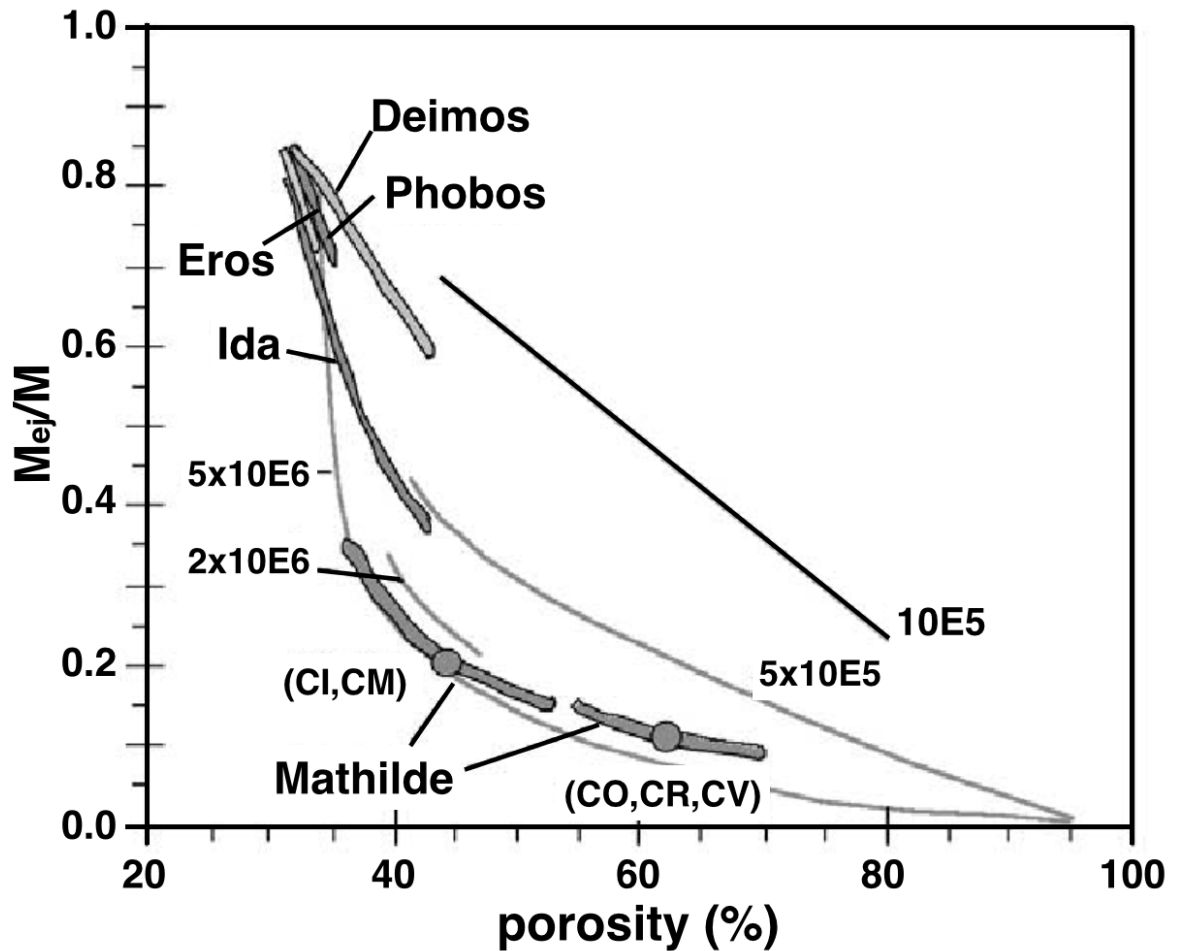


Figure 5.6: Mass ratio of the escaped ejecta material from the large craters from asteroids Mathilde, Eros, Ida and the martian satellites Phobos and Deimos as a function of the body's porosity. Image adapted and modified from Housen & Holsapple (2003).

large craters the majority of the material never escapes the crater.

All these facts (e.g. low ejection speed of the material after impacts on porous targets) could give an explanation behind the small number of carbonaceous chondrite meteorites that have been found on Earth (not observed falling and therefore biased by weathering effects on Earth causing a difficulty to identify them as extraterrestrial), according to the statistics of the Meteoritical Bulletin Database (see Figure 5.7). More specifically the carbonaceous chondrites comprise 3.7% of the chondrites found, which

makes them the 3.5% of the overall meteorite population.

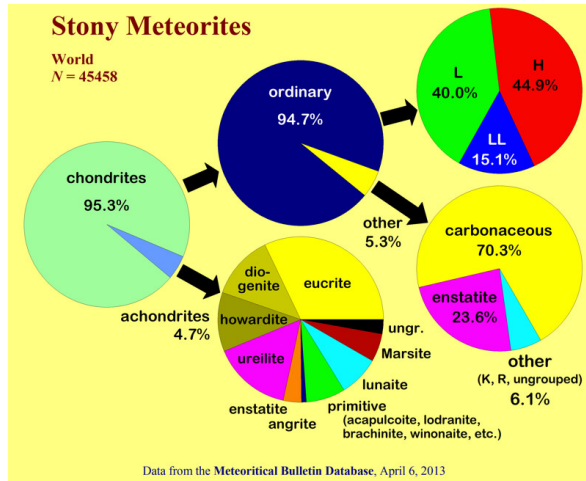


Figure 5.7: Meteorites that have been found worldwide until 2013. The vast majority belongs to the ordinary chondrites, while the carbonaceous chondrites are only a small fraction of the chondrite population, with the vast majority being ordinary chondrites (http://meteorites.wustl.edu/meteorite_types.htm).

However if we consider only the meteorite falls (those observed to reach the Earth and collected soon after the event), then the carbonaceous chondrites comprise an even smaller fraction of all meteorites collected ($\sim 1\%$) according to statistics gathered and presented by Burbine et al. (2002) (see Table 1.1). This could be due to their less frequent production via impacts in the Main Belt and, thus, delivery into near Earth space. So, one could consider that there is a preference on the production of small fragments

after asteroid collisions, relevant to the target's physical parameters. For example higher porosity asteroids produce less ejecta, which then could be delivered to the near Earth space and impact our planet.

Another possibility is that due to their higher porosity, they are more fragile and destroyed during their passage through the Earth's atmosphere (e.g. break-up at higher altitudes). It is discussed by Borovička et al. (2015) that the carbonaceous chondrites (three falls recorded so far, Tagish Lake, Maribo and Sutter's Mill) are the most fragile meteorites (large impactors, early fragmentation in the atmosphere). The later scenario is something that has been already witnessed with the break up at higher atmospheric altitudes of bolides with high porosity, such as the multi-lithology objects (2008 TC₃ and Benesov).

Both the observations of the ejected mass dependence on the crater size and the largest ejecta fragments having slower speeds, strengthens the idea that porous objects can retain a larger amount of the implanted exogenous mass from a projectile. This is in agreement with findings presented here that the projectile's mass, recovered from targets during the experiments, increases as the target's porosity increases.

5.3 Can we Make a Multi-Lithology Body?

Considering the experimental results presented in Chapter 4 and the discussion above, for the study of the mechanism to implant exogenous material into a target body, we can imagine two approaches. For the first approach, the impactor has a very small size (e.g. micrometeorites, \sim mm-size meteorites) compared to the impacted body and, therefore, there is no need to scale to the impact velocities as the range that was tested is inside the velocity distribution of the main asteroid belt (Bottke et al. 1994). Also there is no need to scale the sizes of the impactors as it is known that micrometeorite bombardment occurs on asteroid surfaces, and is one of the processes responsible for producing the regolith. As was shown by Vernazza et al. (2012) the first mm of an asteroid surface can have porosity up to 90% and the first metre approximately 50%, so the results from this thesis can be directly applied to this approach. For the second approach we consider collisions of km-size asteroids (a few 10s km up to 100 km) by smaller ones (100s-m to km sizes). In this case, although there is also no need for scaling the impact speeds, what is needed however, is a size-scaling of the impactor body as it is orders of magnitude larger than any projectile can be used in an impact laboratory.

However, even by concluding that the porous asteroids are the best population

that can retain exogenous material after impacts, there is a great need to understand how frequent were these collisions throughout the lifetime of the Solar System. This is especially true when we try to trace the formation of a body that includes several lithologies; it is important to know whether (on a specific target) impacts of bodies that carry different mineralogies can occur.

There is an effort to link recovered meteorites with their parent bodies in the asteroid belt. The big question is how can we bring the different lithologies on a single parent body from which a multi-lithology meteorite was produced? Gayon-Markt et al. (2012) suggested that it is very difficult to form a parent body with different lithologies via asteroid-asteroid collisions. Their work, however, was not conclusive as they used a very low impact speeds (0.5 km/s). They arbitrarily assumed that, in order for a target body to retain exogenous material, very low impact speeds are needed. In their study, the target was placed in the Nysa-Polana asteroid family region and the upper impact speed limit was set to 0.5 km/s. This random selection was done as it was argued that at higher impact speeds the impactor would be pulverised and thus no material would be embedded on the target. At average impact speeds in the belt between 4.4–5.3 km/s (Bottke et al. 1994), if the mixing was effective, then meteorites with several different lithologies would be more frequent as this is something that is not observed, knowing that the population of main belt asteroids that can hit any target in the belt increase with increasing impact speed limit.

But Gayon-Markt et al. (2012) did not consider some fundamental aspects, such as the very low ejecta speeds after impacts on porous materials, the small fraction of mass that can escape and also the ability of a porous target to retain a relatively larger amount of exogenous material. In addition to the above, regardless of any possible formation mechanism of the type of body (or part of a body), a multi-lithology small

body has loosely bound pieces of different mineralogies, and during its entry in the Earth's atmosphere would fragment earlier on its path (high altitude) and probably break into its diverse components.

Another assumption that was made was that all the possible impactors with different mineralogies would impact on a limited surface area on the parent body of 2008 TC₃, as its size was approximately 8 m. They calculated that the impact probability for this target is $P_i=3\times 10^{-19}$ impacts/km²/yr and when corrected for the estimated collisional lifetime of 2008 TC₃ ($\tau_{coll}=16.2$ Myr) and the estimated number of impactors with a given size, they obtained only 10^{-6} impacts. In order to get a positive probability they needed a large population of impactors down to cm-size, which do not expect to produce such extended contamination of exogenous material.

Here are presented similar calculations, but with updated initial conditions and assumptions, based on the results of the experimental work and the above discussion. The C-type asteroid (142) Polana, with diameter $d=54.8$ km, was selected as the target of the collisions. To begin with, the probability of MBAs impact with Polana was calculated. To estimate the flux of impactors, a catalogue of approximately 1.23×10^5 MBAs with known albedo and diameter was used. This catalogue was prepared at the Observatoire de la Côte d'Azur for the purposes of this work. The resultant list of potential impactors (several thousands), was then divided in three different groups according to their albedo value. Group#1 included dark asteroids with albedo $pV<0.1$, group#2 asteroids with albedos in range $0.1<pV<0.3$ and group#3, the brightest ones, with $pV>0.3$. The first restriction applied was the cut-off of the maximum collisional speed this was set to 0.5, 1.0 and 2.0 km/s, as observed from the laboratory impact experiments herein that material is implanted at speeds <2.0 km/s. In Figures 5.8, 5.9 and 5.10 are presented the current population of the Main Belt that has non-

Table 5.1: Average probabilities of MBAs of different albedos to impact asteroid (142) Polana, measured in impacts/km²/year.

	0.5 km/s	1.0 km/s	2.0 km/s
P_i (group#1)	2.8×10^{-19}	6.0×10^{-19}	1.5×10^{-18}
P_i (group#2)	2.2×10^{-19}	5.0×10^{-19}	1.6×10^{-18}
P_i (group#3)	2.1×10^{-1}	5.0×10^{-19}	1.5×10^{-18}

zero impact probability on Polana. It is clear that by increasing the collisional speed limit from 0.5 to 2.0 km/s, the potential impactor population increases dramatically, enclosing objects from a very large fraction of the belt.

The average probability, P_i , of asteroids from each albedo group to hit Polana with a range of speeds are presented in Table 5.1. Because these results are for a km² of Polana per year, we calculated the probability of an impactor to hit Polana in a cross section ($A=r^2$), for $\tau_{coll}=10^9$ years, as the estimated collisional lifetimes for the asteroids is a function of their size according to Bottke et al. (2005). In order to obtain the number of impacts on Polana, the SFDs of the asteroids with non-zero impact probabilities were calculated and, from the fitting, was estimated the number of impactors down to 100 m. We started with this estimation for the number of the impactors using a simple extrapolation, assuming that the Main Belt has not undergone a dramatic change after the Late Heave Bombardment (Bottke et al. 2005). This was repeated for all selected impact speeds for each albedo population, as is shown in Fig. 5.11. Therefore, the number of impacts (n), on the cross section of Polana (A) from the estimated impactors' population (N_{im}) through its collisional lifetime (τ_{coll}) is given by:

$$n = P_i A \tau_{coll} N_{im} \quad (5.1)$$

This simple calculation has shown that with increasing collisional speed there is a

larger population of potential impactors with differing albedos that could participate in the collisional history of the target. We found that the number of collisions on Polana starts from only a few tens of impacts at the lowest speed (up to 0.5 km/s), and can be up to 10^2 through its lifetime for all the albedo groups at higher speeds (up to 2.0 km/s). This implies that it is indeed possible to mix material on its surface and could, thus, explain multi-lithology asteroid parent bodies and derivative meteorites and the spectral variability observed on individual asteroids.

5.4 Summary

We confirm that porosity plays a significant role in the fragmentation of the impactor but, more importantly, on the amount of the implanted mass on the target. This result has implications for studies on large-scale collisions between asteroids in Main Belt. Although it was initially believed that the impactor after a high-speed collision is pulverised (and/or vaporised) and not able to embed material into the target body, it is shown herein that such studies should be revised, thus altering the big picture of collisions in the Main Belt, providing formation scenarios for the observed spectral variability of some asteroids or even the formation of multi-lithology objects. Future spacecraft observations of asteroid surfaces and sample-return missions, such as Hayabusa II and Osiris-REx, will provide invaluable information also for the collisional history of such bodies. Can we find exogenous material on C-type asteroids? It is hoped that the work presented here will help to interpret the data from such space missions.

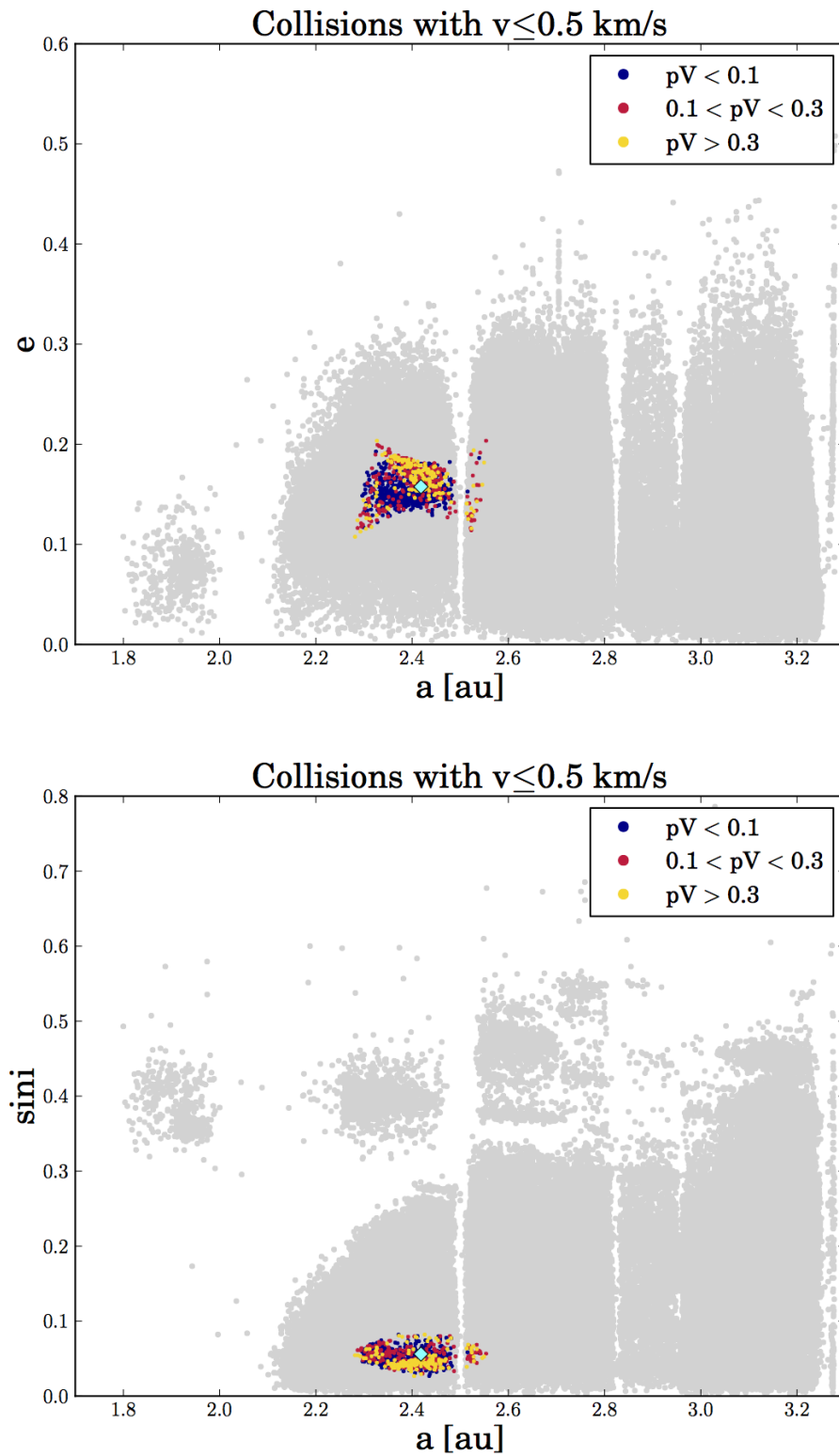


Figure 5.8: Semi-major axis (a) vs. eccentricity (e): Main Belt asteroids with different albedos that have non-zero impact probability on asteroid Polana, with collisional speed up to 0.5 km/s. The grey dots correspond to all the Main Belt population with known albedos and diameters, while the cyan square represents Polana.

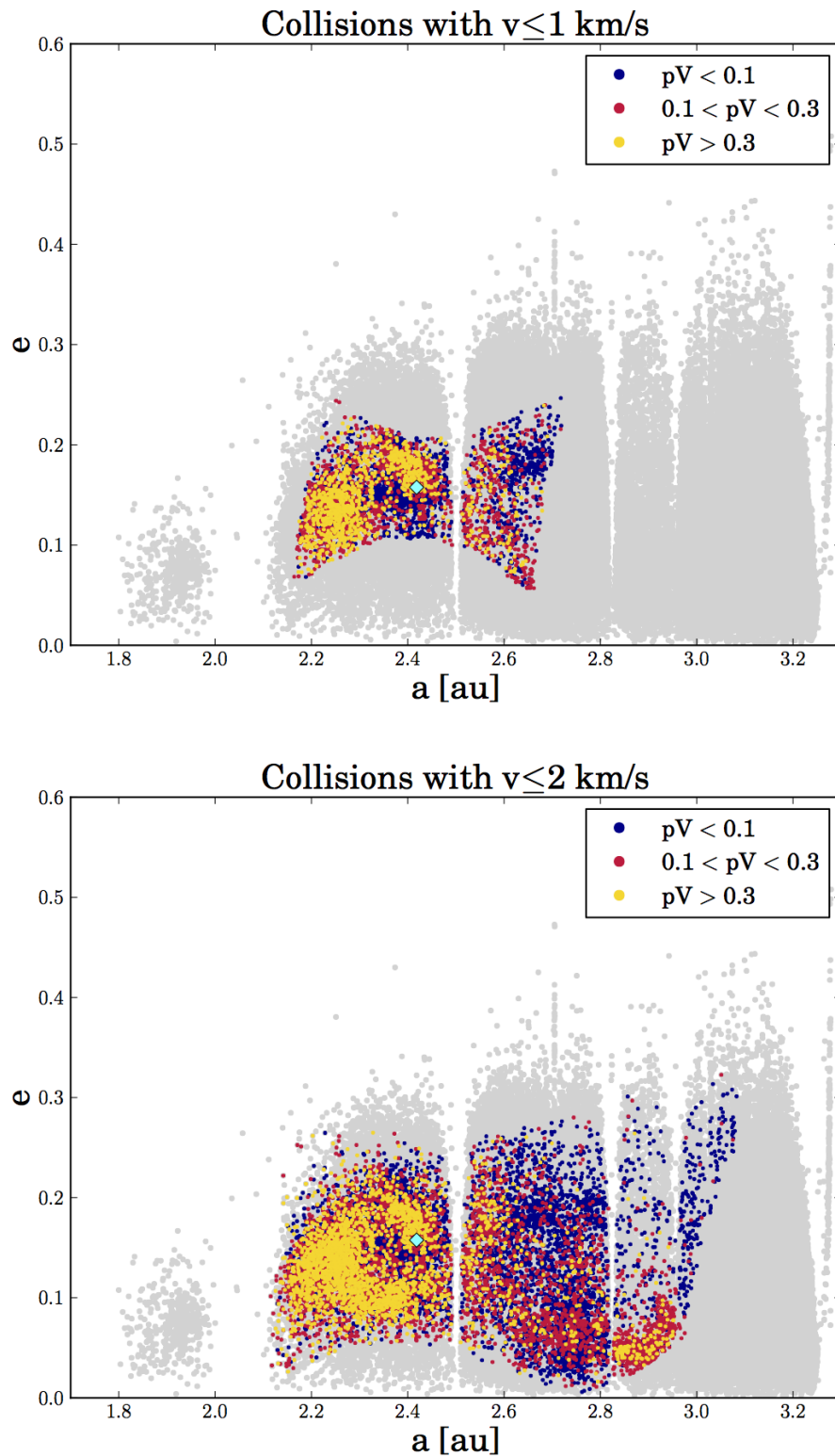


Figure 5.9: Semi-major axis (a) vs. eccentricity (e): Main Belt asteroids with different albedos that have non-zero impact probability on Polana, with collisional speeds up to 1.0 and 2.0 km/s respectively. The grey dots correspond to all the Main Belt population with known albedos and diameters, while the cyan square represents Polana. As the impact speed threshold increases, the population of potential impactors in the current Main Belt increases too.

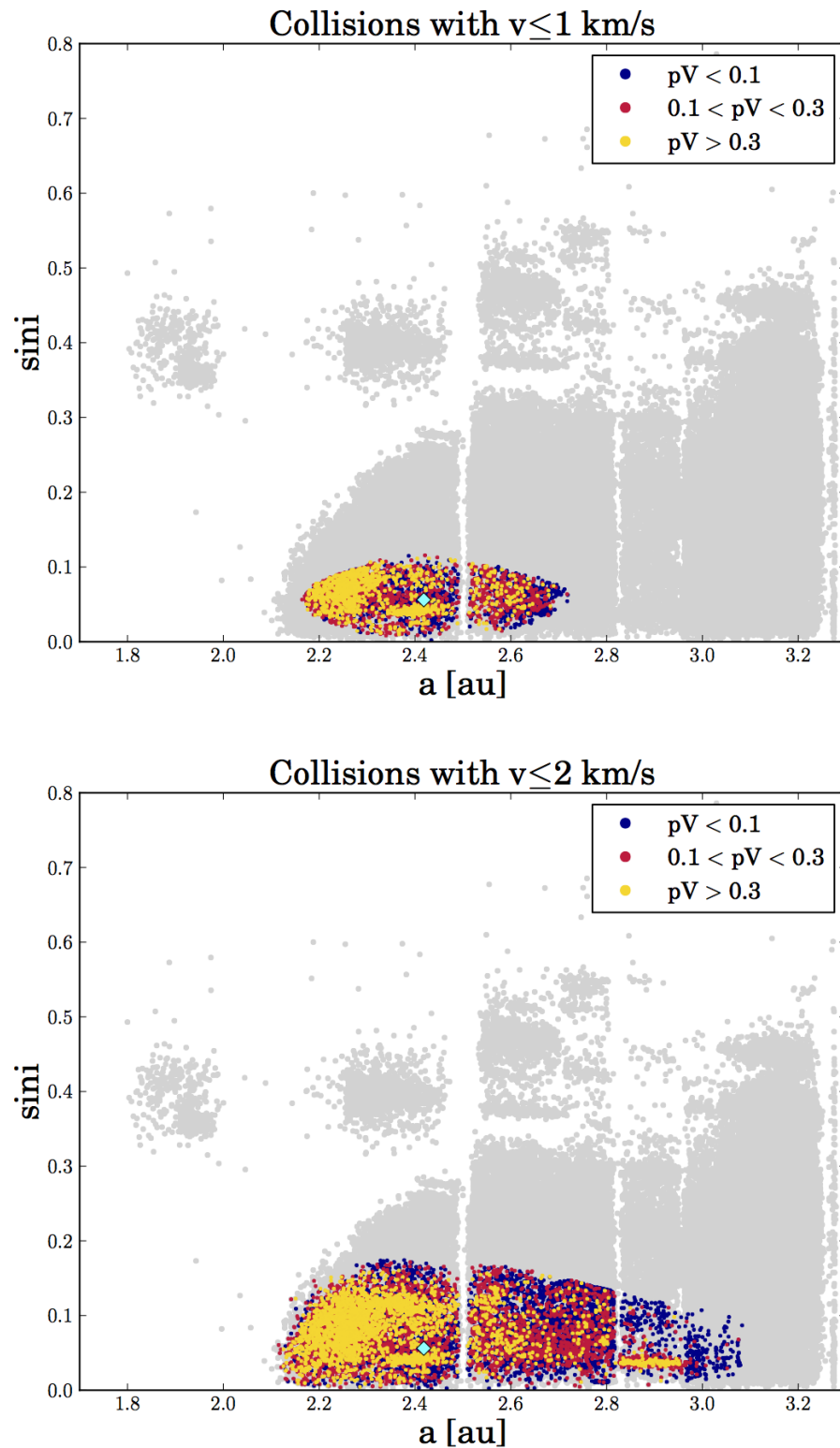


Figure 5.10: Semi-major axis (a) vs. \sin of inclination ($sini$): Main Belt asteroids with different albedos that have non-zero impact probability on Polana, with collisional speeds up to 1.0 and 2.0 km/s respectively. The grey dots correspond to all the Main Belt population with known albedos and diameters, while the cyan square represents Polana. As the impact speed threshold increases, the population of potential impactors in the current Main Belt increases too.

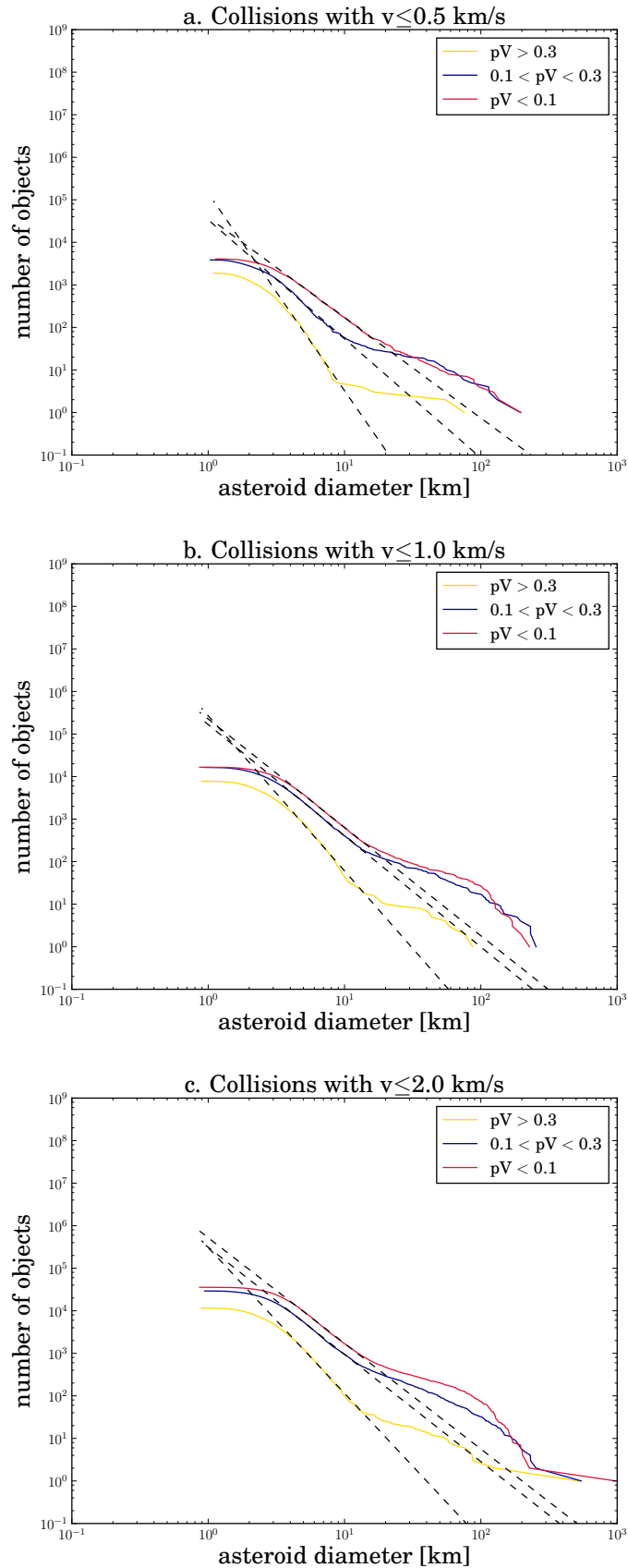


Figure 5.11: SFDs of the current MB population that could impact Polana at 0.5, 1.0 and 2.0 km/s. By extrapolating linearly the slopes, we obtained the impactors' population down to 100 m in diameter. The dashed lines correspond to the fitting of the slope for the estimation of the impactors population down to 100 m in size.

6

Conclusions

THE outcome of this thesis hopefully adds a brick to the enormous developing building of Planetary Sciences. The original idea of the experiments, presented here, was triggered after long interaction with astronomers who specialise in studying small bodies. The recent findings of multi-lithology meteorites (Jenniskens et al. 2009; Spurný et al. 2014), the dark material (Reddy et al. 2012a; Hirata & Ishiguro 2011) and the compositional variegations (Barucci et al. 2012; Schröder et al. 2015) on asteroid surfaces, indicate that collisions could be a common mechanism for material mixing. The idea for such a research study, using the facilities of the Kent Impact Lab, was inspired by the lack of relevant experimental work from other groups worldwide, focusing on the fate of the impactor and the subsequent contamination of the target body. At the beginning of this study only one work could be found by Nagaoka et al. (2014) dedicated to the impactor. However the speed regime that was tested was very low ($<1\text{km/s}$). The team of Nagaoka et al. (2014) used the facilities of the Kobe University including a vertical powder gun and a He gas gun. Although it was thought that material mixing is more effective at lower impact speeds, collisions at this speed regime are not very frequent in the Main Belt. By the end of this thesis

(March 2016) a couple more relevant works were published by Daly & Schultz (2015, 2016), who used the NASA Ames Vertical Gas Gun in the USA firing basalt and aluminium projectiles on pumice and porous water-ice targets, but impact speeds at ~ 5 km/s. Therefore, we were interested in testing how the impactor behaves at higher speeds and a larger range, using materials that could be separated, enabling the more accurate study of the impactor after the collision. Is material still implanted in the target? Additionally, apart from the collisional speed, does the porosity of the target affect the result? Can we embed more material on porous bodies compared to solid bodies?

6.1 Summary of the work

This study was based on the outcome of three experiments of low to hyper-velocity collisions using the University of Kent LGG. Simultaneously a new automated technique was developed by the author to count and measure thousands of projectile fragments.

During the first pioneering experiment we used water-ice cylinders as targets, representing solid materials with zero (or almost zero) bulk porosity. We fired olivine and synthetic basalt projectiles in a range of speeds, representative of the lower end of impact speeds that occur in the Main Belt, between 0.3 and 3.5 km/s. The results enabled us to compare the behaviour of these two different projectiles, when they impact onto the same type of body. In the second and third set of experiments, we again used peridot projectiles, in a similar range of speeds, but fired onto porous water-ice and calcium carbonate powder, simulating a regolith surface.

The selection of this specific type of materials enabled the separation of the projectile fragments from the target's material, and from the ejecta collection setups. The

identification and analysis of the impactor's fragments was done by using a new technique, based on a combination of SEM-EDX imaging and an astronomical photometry routine (Avdellidou et al. 2016).

During this research we recorded the behaviour of the projectiles and compared the results for each set of experiments. It is discovered that:

- I. a difference in the fragmentation of the forsterite olivine and synthetic basalt projectiles exists when they are fired onto low porosity water-ice targets, giving catastrophic disruption energy densities, Q^* , that differ by an order of magnitude, implying that synthetic basalt requires higher impact velocities to fragment than the peridot projectile.
- II. the energy at the catastrophic disruption limit decreases by a factor of 2.7 when a peridot impacts the same material (water-ice) but with higher porosity (from 6% to 40%). Although we would expect that the energy when it hits an even higher porosity target (70%), would decrease more, we record instead an increase of an order of magnitude as the material changes from water-ice to calcium carbonate.
- III. there is no change in modes and slopes of the SFDs for the peridot projectile fragments in each of the three Runs. This means that by increasing the collisional speed the size distribution does not change as we initially expected, by comparison with the behaviour of ductile materials. In addition we did not record any melt or vaporisation of the projectile for the range of impact speeds 0.30–3.50 km/s (range that covers all shots from all Runs). Therefore, we suggest that, for such velocities that represent the lower end of the distribution of impact velocities in the main asteroid belt (about 5 km/s), there should be significant survival of the impactor's material.

-
- IV. there is a change in the mean slope value for olivine fragments found in ejecta between the different Runs. The SFD become steeper when the porosity of the target significantly increases. This means that the projectile fragments are more numerous, small fragments. Safer conclusions can be made measuring the fragments, using the same magnification of the EDX maps.
- V. the implanted projectile's mass in the target increases dramatically as the porosity of the target increases. However for the same set of materials (target and impactor) the implanted mass decreases with increasing speed. This was a very clear conclusion for the Run#3, but for the first two Runs the mass fluctuated, without a clear trend.
- VI. by examining the Raman spectra of the largest peridot fragments, we saw no change in the position of the two characteristic olivine mineral peaks, greater than the resolution of the instrument. Moreover, we measured no change in the mutual distance of these two peaks. This means that the impact shock was not strong enough to change the material in using this method.

In this work we also present a novel way to measure thousands of fragments autonomously and accurately, in order to study the fragmentation properties of the projectile during a hypervelocity impact with unprecedented statistical significance. Applying astronomical photometry techniques enabled us to measure fragments down to the sizes of a few microns, and adequately define the 2D area (and thus inferred volume) of each fragment. This analysis method is essential to estimate SFD and masses of very small fragments, as the LGG cannot fire bigger projectiles, which would produce larger fragments suitable for weighing.

6.2 Thoughts for future work

After the end of the mentioned experiments, the results gave birth to a few ideas for further studies, both experimental and computational, that are summarised below.

- In order to verify further the result of III, a possible test could be the study of the SFD that result from the fragments that stayed in the target and thus did not suffer from any further (even minimal) fragmentation on the ejecta collection setup.
- It was very important that we test the fate of the projectile by using the same target material (water-ice) but with different porosities. Although we learnt that for implantation, the porosity of the target material is important, we saw with the CaCO_3 regolith shots that the type of porous material may also play a more significant role. A further study could include a set of shots, in the same collisional speed range and using the same type of projectile, on a CaCO_3 grit target with porosity similar to the one of the water-ice targets in the Run#2 ($\sim 40\%$). Moreover, this material will have also similar grain size with the larger parts of the crushed water-ice used.
- The initial idea for our experiments was to use real meteorites as target and projectiles (e.g. fire ordinary chondrites onto carbonaceous chondrites). However the problem that we were going to face was the effective separation of projectile from target for further analysis. One possible start could be to use meteorites only for the projectile material, keeping the target's material more simple for separation as described in Chapter 3.

-
- Further studies can be done by examining the shapes of the fragments that resulted from different projectile materials.
 - During discussions with astronomers at several meetings, it was pointed out the idea to perform the reverse experiments. For example to keep the target material and porosity fixed, but increase the porosity of the projectile in order to examine its behaviour and the results of its implantation.
 - Finally, having basic results for the implantation of material on the target, which show that material can be embedded at higher speeds than previous works have shown, we can calculate the impact probabilities that asteroids of different types have to hit an asteroid of a specific type (e.g. a C-type). Using the experimental results and modelling we can test how effective this procedure is to create multi-lithology bodies in the Main Belt. A further study like this could explain the formation of the asteroid 2008 TC₃ or even to understand whether the observed spectral variability of C-type asteroids could be due to exogenous material inclusions.

Bibliography

- Altwegg, K., Balsiger, H., Bar-Nun, A., et al. 2015, *Science*, 347, 1261952
- Alvarez, L. W., Alvarez, W., Asaro, F., & Michel, H. V. 1980, *Science*, 208, 1095
- Amelin, Y., Krot, A. N., Hutcheon, I. D., & Ulyanov, A. A. 2002, *Science*, 297, 1678
- Anders, E., & Owen, T. 1977, *Science*, 198, 453
- Asphaug, E., Collins, G., & Jutzi, M. 2015, ArXiv e-prints, arXiv:1504.02389
- Avdellidou, C., Price, M. C., Delbo, M., Ioannidis, P., & Cole, M. J. 2016, *MNRAS*, 456, 2957
- Barucci, M. A., Belskaya, I. N., Fornasier, S., et al. 2012, *Planet. Space Sci.*, 66, 23
- Belskaya, I. N., Fornasier, S., Krugly, Y. N., et al. 2010, *A&A*, 515, A29
- Benz, W., & Asphaug, E. 1999, *Icarus*, 142, 5
- Bertin, E., & Arnouts, S. 1996, *A&A*, 117, 393
- Bischoff, A., Horstmann, M., Pack, A., Laubenstein, M., & Haberer, S. 2010, *Meteoritics and Planetary Science*, 45, 1638
- Bland, P. A., Artemieva, N. A., Collins, G. S., et al. 2008, in *Lunar and Planetary Science Conference*, Vol. 39, 2045
- Blume, W. H. 2005, *Space Sci. Rev.*, 117, 23
- Borovicka, J., Popova, O. P., Nemtchinov, I. V., Spurn'ý, P., & Ceplecha, Z. 1998, *A&A*, 334, 713
- Borovička, J., Spurný, P., & Brown, P. 2015, ArXiv e-prints, arXiv:1502.03307

- Bottke, W., Ghent, R., Mazrouei, S., Robbins, S., & Vokrouhlicky, D. 2015, in AAS/Division for Planetary Sciences Meeting Abstracts, Vol. 47, AAS/Division for Planetary Sciences Meeting Abstracts, 201.07
- Bottke, W. F., Durda, D. D., Nesvorný, D., et al. 2005, *Icarus*, 179, 63
- Bottke, W. F., Nesvorný, D., Grimm, R. E., Morbidelli, A., & O'Brien, D. P. 2006, *Nature*, 439, 821
- Bottke, W. F., Nolan, M. C., Greenberg, R., & Kolvoord, R. A. 1994, *Icarus*, 107, 255
- Bottke, W. F., Vokrouhlický, D., & Nesvorný, D. 2007, *Nature*, 449, 48
- Britt, D. T., Consolmagno, G. J., & Merline, W. J. 2006, in Lunar and Planetary Science Conference, Vol. 37, 37th Annual Lunar and Planetary Science Conference, ed. S. Mackwell & E. Stansbery
- Britt, D. T., Yeomans, D., Housen, K., & Consolmagno, G. 2002, *Asteroids III*, 485
- Burbine, T. H., McCoy, T. J., Meibom, A., Gladman, B., & Keil, K. 2002, *Meteoritic Parent Bodies: Their Number and Identification*, ed. W. F. Bottke, Jr., A. Cellino, P. Paolicchi, & R. P. Binzel, 653
- Burchell, M. J., Cole, M. J., McDonnell, J. A. M., & Zarnecki, J. C. 1999, *Measurement Science and Technology*, 10, 41
- Burchell, M. J., Cole, M. J., Price, M. C., & Kearsley, A. T. 2012, *Meteoritics and Planetary Science*, 47, 671
- Bus, S. J., Binzel, R. P., Sunshine, J., Burbine, T. H., & McCoy, T. J. 2002, in *Bulletin of the American Astronomical Society*, Vol. 34, AAS/Division for Planetary Sciences Meeting Abstracts #34, 859
- Campins, H., Hargrove, K., Pinilla-Alonso, N., et al. 2010, *Nature*, 464, 1320
- Capaccioni, F., Coradini, A., Filacchione, G., et al. 2015, *Science*, 347, aaa0628
- Carry, B. 2012, *Planet. Space Sci.*, 73, 98
- Chapman, C. R., Morrison, D., & Zellner, B. 1975, *Icarus*, 25, 104
- Cheng, A. F. 2013, in Lunar and Planetary Science Conference, Vol. 44, Lunar and Planetary Science Conference, 2985
- Chesley, S., Farnocchia, D., Pravec, P., & Vokrouhlicky, D. 2015, *IAU General Assembly*, 22, 2248872

- Chyba, C. F., Thomas, P. J., & Zahnle, K. J. 1993, *Nature*, 361, 40
- Clark, B. E., Hapke, B., Pieters, C., & Britt, D. 2002, *Asteroids III*, 585
- Consolmagno, G., Britt, D., & Macke, R. 2008, *Chemie der Erde / Geochemistry*, 68, 1
- Consolmagno, G. J., Tegler, S. C., Romanishin, W., & Britt, D. T. 2006, in *Lunar and Planetary Science Conference, Vol. 37, 37th Annual Lunar and Planetary Science Conference*, ed. S. Mackwell & E. Stansbery
- Coradini, A., Capria, M. T., de Sanctis, M. C., & McKinnon, W. B. 2008, *The Structure of Kuiper Belt Bodies: Link with Comets*, ed. M. A. Barucci, H. Boehnhardt, D. P. Cruikshank, A. Morbidelli, & R. Dotson, 243
- Daly, R. T., & Schultz, P. H. 2015, *GRL*, 42, 7890
- . 2016, *Icarus*, 264, 9
- Davidsson, B. J. R., Gutiérrez, P. J., & Rickman, H. 2007, *Icarus*, 187, 306
- Davies, J. K., McFarland, J., Bailey, M. E., Marsden, B. G., & Ip, W.-H. 2008, *The Early Development of Ideas Concerning the Transneptunian Region*, ed. M. A. Barucci, H. Boehnhardt, D. P. Cruikshank, A. Morbidelli, & R. Dotson, 11
- Davis, D. R., Chapman, C. R., Greenberg, R., Weidenschilling, S. J., & Harris, A. W. 1979, *Collisional evolution of asteroids - Populations, rotations, and velocities*, ed. T. Gehrels, 528
- De Sanctis, M. C., Ammannito, E., Capria, M. T., et al. 2012, *Science*, 336, 697
- De Sanctis, M. C., Capaccioni, F., Ciarniello, M., et al. 2015, *Nature*, 525, 500
- de Vries, B. L., Acke, B., Blommaert, J. A. D. L., et al. 2012, *Nature*, 490, 74
- Delbo, M., Mueller, M., Emery, J. P., Rozitis, B., & Capria, M. T. 2015, *ArXiv e-prints*, arXiv:1508.05575
- Delbo', M., Tanga, P., & Mignard, F. 2008, *Planet. Space Sci.*, 56, 1823
- Delbo, M., Libourel, G., Wilkerson, J., et al. 2014, *Nature*, 508, 233
- DeMeo, F. E., Alexander, C. M. O., Walsh, K. J., Chapman, C. R., & Binzel, R. P. 2015, *The Compositional Structure of the Asteroid Belt*, ed. P. Michel, F. DeMeo, & W. F. Bottke

- DeMeo, F. E., Binzel, R. P., Slivan, S. M., & Bus, S. J. 2009, *Icarus*, 202, 160
- DeMeo, F. E., & Carry, B. 2013, *Icarus*, 226, 723
- . 2014, *Nature*, 505, 629
- di Martino, M., Martelli, G., Smith, P. N., & Woodward, A. W. 1990, *Icarus*, 83, 126
- Dones, L., Weissman, P. R., Levison, H. F., & Duncan, M. J. 2004, Oort cloud formation and dynamics, ed. G. W. Kronk, 153
- Doressoundiram, A., Boehnhardt, H., Tegler, S. C., & Trujillo, C. 2008, Color Properties and Trends of the Transneptunian Objects, ed. M. A. Barucci, H. Boehnhardt, D. P. Cruikshank, A. Morbidelli, & R. Dotson, 91–104
- Duncan, M. J., Levison, H. F., & Budd, S. M. 1995, *AJ*, 110, 3073
- El-Maarry, M. R., Thomas, N., Gracia-Berná, A., et al. 2015, *Geophys. Res. Lett.*, 42, 5170
- ESA. 2016, AIDA Study
- Fei, Y., & Bertka, C. M. 1999, Mantle petrology: field observations and high pressure experimentation, 6, 189
- Fendyke, S., Price, M. C., & Burchell, M. J. 2013, *Advances in Space Research*, 52, 705
- Filacchione, G., de Sanctis, M. C., Capaccioni, F., et al. 2016, *Nature*, 529, 368
- Flynn, G. J. 2014, in *Asteroids, Comets, Meteors 2014*, ed. K. Muinonen, A. Penttilä, M. Granvik, A. Virkki, G. Fedorets, O. Wilkman, & T. Kohout
- Foster, N., Wozniakiewicz, P., Price, M., Kearsley, A., & Burchell, M. 2013, *Geochimica et Cosmochimica Acta*, 121, 1
- Fraser, W. C., Brown, M. E., Morbidelli, A., Parker, A., & Batygin, K. 2014, *ApJ*, 782, 100
- Fujiwara, A., Kawaguchi, J., Yeomans, D. K., et al. 2006, *Science*, 312, 1330
- Gaffey, M. J., Cloutis, E. A., Kelley, M. S., & Reed, K. L. 2002, *Asteroids III*, 183
- Gayon-Markt, J., Delbo, M., Morbidelli, A., & Marchi, S. 2012, *MNRAS*, 424, 508
- Gladman, B., Kavelaars, J. J., Petit, J.-M., et al. 2001, *AJ*, 122, 1051

- Gomes, R., Levison, H. F., Tsiganis, K., & Morbidelli, A. 2005, *Nature*, 435, 466
- Gounelle, M., Spurný, P., & Bland, P. A. 2006, *Meteoritics and Planetary Science*, 41, 135
- Grady, M. M., & Wright, I. 2006, *Types of extraterrestrial material available for study*, ed. D. S. Lauretta & H. Y. McSween, 3
- Gundlach, B., & Blum, J. 2013, *Icarus*, 223, 479
- Hargrove, K. D., Emery, J. P., Campins, H., & Kelley, M. S. P. 2015, *Icarus*, 254, 150
- Harris, A. W., Boslough, M., Chapman, C. R., et al. 2015, *Asteroid impacts and modern civilisation: Can we prevent a catastrophe?*, ed. P. Michel, F. DeMeo, & W. F. Bottke
- Hartogh, P., Lis, D. C., Bockelée-Morvan, D., et al. 2011, *Nature*, 478, 218
- Hayhurst, C. J., & Clegg, R. A. 1997, *International Journal of Impact Engineering*, 20, 337, *hypervelocity Impact Proceedings of the 1996 Symposium*
- Hernandez, V., Murr, L., & Anchondo, I. 2006, *International Journal of Impact Engineering*, 32, 1981
- Hibbert, R., Price, M. C., Burchell, M. J., & Cole, M. J. 2014, *European Planetary Science Congress 2014*, 9, 295
- Hirata, N., & Ishiguro, M. 2011, in *Lunar and Planetary Science Conference*, Vol. 42, 1821
- Holsapple, K., Giblin, I., Housen, K., Nakamura, A., & Ryan, E. 2002, *Asteroids III*, 443
- HORIZONS System. 2016, JPL
- Horner, J., Evans, N. W., & Bailey, M. E. 2004, *MNRAS*, 354, 798
- Horstmann, M., & Bischoff, A. 2014, *Chemie der Erde / Geochemistry*, 74, 149
- Housen, K. R., & Holsapple, K. A. 1999, *Icarus*, 142, 21
- . 2003, *Icarus*, 163, 102
- . 2011, *Icarus*, 211, 856
- Housen, K. R., Holsapple, K. A., & Voss, M. E. 1999, *Nature*, 402, 155

- Hsieh, H. H., & Jewitt, D. 2006, *Science*, 312, 561
- Jenniskens, P., Shaddad, M. H., Numan, D., et al. 2009, *Nature*, 458, 485
- Johansen, A., Jacquet, E., Cuzzi, J. N., Morbidelli, A., & Gounelle, M. 2015, ArXiv e-prints, arXiv:1505.02941
- Joy, K. H., Zolensky, M. E., Nagashima, K., et al. 2012, *Science*, 336, 1426
- Kenkmann, T., Trullenque, G., Deutsch, A., et al. 2013, *Meteoritics and Planetary Science*, 48, 150
- Kuebler, K. E., Jolliff, B. L., Wang, A., & Haskin, L. A. 2006, *GCA*, 70, 6201
- Küppers, M., O'Rourke, L., Bockelée-Morvan, D., et al. 2014, *Nature*, 505, 525
- Lamy, P. L., Toth, I., Fernandez, Y. R., & Weaver, H. A. 2004, *The sizes, shapes, albedos, and colors of cometary nuclei*, ed. G. W. Kronk, 223
- Lardner, D. 1853, *MNRAS*, 13, 188
- Levison, H. F., & Duncan, M. J. 1997, *Icarus*, 127, 13
- Levison, H. F., & Morbidelli, A. 2003, *Nature*, 426, 419
- Li, J.-Y., Reddy, V., Nathues, A., et al. 2016, ArXiv e-prints, arXiv:1601.03713
- Licandro, J., Campins, H., Kelley, M., et al. 2011, *A&A*, 525, A34
- Lipschutz, M. E., Gaffey, M. J., & Pellas, P. 1989, in *Asteroids II*, ed. R. P. Binzel, T. Gehrels, & M. S. Matthews, 740
- Marchi, S., Chapman, C. R., Barnouin, O. S., Richardson, J. E., & Vincent, J. B. 2015, *Cratering on Asteroids*, ed. P. Michel, F. DeMeo, & W. F. Bottke
- Marsh, S. P. 1980, *Los Alamos series on dynamic material properties* (London: University of California Press)
- Martins, Z., Price, M. C., Goldman, N., Sephton, M. A., & Burchell, M. J. 2013, *Nature Geoscience*, 6, 1045
- Massironi, M., Simioni, E., Marzari, F., et al. 2015, *Nature*, 526, 402
- Mayor, M., & Queloz, D. 1995, *Nature*, 378, 355
- McCord, T. B., Adams, J. B., & Johnson, T. V. 1970, *Science*, 168, 1445

- McCord, T. B., Li, J.-Y., Combe, J.-P., et al. 2012, *Nature*, 491, 83
- McDermott, K. H., Price, M. C., Cole, M., & Burchell, M. J. 2016, *Icarus*, 268, 102
- McSween, H. Y., Mittlefehldt, D. W., Beck, A. W., Mayne, R. G., & McCoy, T. J. 2011, *Space Science Reviews*, 163, 141
- Michel, P., & Richardson, D. C. 2013, *A&A*, 554, L1
- Michel, P., Cheng, A., Galvez, A., et al. 2015, *Highlights of Astronomy*, 16, 480
- Michikami, T., Hagermann, A., Kadokawa, T., et al. 2016, *Icarus*, 264, 316
- Michikami, T., Moriguchi, K., Hasegawa, S., & Fujiwara, A. 2007, *P&SS*, 55, 70
- Milani, A., Cellino, A., Knežević, Z., et al. 2014, *Icarus*, 239, 46
- Minton, D. A., & Malhotra, R. 2009, *Nature*, 457, 1109
- Morbidelli, A., Brasser, R., Gomes, R., Levison, H. F., & Tsiganis, K. 2010, *AJ*, 140, 1391
- Morbidelli, A., & Brown, M. E. 2004, *The Kuiper belt and the primordial evolution of the solar system*, ed. G. W. Kronk, 175
- Morbidelli, A., Chambers, J., Lunine, J. I., et al. 2000, *Meteoritics and Planetary Science*, 35, 1309
- Morbidelli, A., Jedicke, R., Bottke, W. F., Michel, P., & Tedesco, E. F. 2002, *Icarus*, 158, 329
- Morbidelli, A., Levison, H. F., Tsiganis, K., & Gomes, R. 2005, *Nature*, 435, 462
- Morbidelli, A., & Rickman, H. 2015, *A&A*, 583, A43
- Morbidelli, A., Walsh, K. J., O'Brien, D. P., Minton, D. A., & Bottke, W. F. 2015, *ArXiv e-prints*, arXiv:1501.06204
- Moskovitz, N. A., Jedicke, R., Gaidos, E., et al. 2008, *Icarus*, 198, 77
- Mottola, S., Arnold, G., Grothues, H.-G., et al. 2015, *Science*, 349, doi:10.1126/science.aab0232
- Mouret, S., & Mignard, F. 2011, *MNRAS*, 413, 741
- Mouri, T., & Enami, M. 2008, *Journal of Mineralogical and Petrological Sciences*, 103, 100

- Nagaoka, H., Takasawa, S., Nakamura, A. M., & Sangen, K. 2014, *Meteoritics and Planetary Science*, 49, 69
- Nakamura, T., Noguchi, T., Tanaka, M., et al. 2011, *Science*, 333, 1113
- NASA. 2016, DAWN mission
- Nathues, A., Hoffmann, M., Schaefer, M., et al. 2015, *Nature*, 528, 237
- Nesvorný, D., Broz, M., & Carruba, V. 2015, ArXiv e-prints, arXiv:1502.01628
- Nesvorný, D., & Morbidelli, A. 2012, *AJ*, 144, 117
- Nesvorný, D., Vokrouhlický, D., & Morbidelli, A. 2013, *ApJ*, 768, 45
- O'Brien, D. P., & Sykes, M. V. 2011, *SSR*, 163, 41
- Olofsson, J., Juhász, A., Henning, T., et al. 2012, *A&A*, 542, A90
- Oort, J. H. 1950, *Bull. Astron. Inst. Netherlands*, 11, 91
- Oró, J. 1961, *Nature*, 190, 389
- Palomba, E., Longobardo, A., De Sanctis, M. C., et al. 2014, *Icarus*, 240, 58
- Pasini, D. 2014, *European Planetary Science Congress 2014, EPSC Abstracts*, Vol. 9, id. EPSC2014-67, 9, EPSC2014
- Pasini, J. L. S., & Price, M. C. 2015, in *Lunar and Planetary Science Conference*, Vol. 46, *Lunar and Planetary Science Conference*, 2725
- Perna, D., Kaňuchová, Z., Ieva, S., et al. 2015, *A&A*, 575, L1
- Perryman, M. 2014, *The Exoplanet Handbook*
- Petrovic, J. 2001, *Journal of Materials Science*, 36, 1579
- Popova, O., Borovička, J., Hartmann, W. K., et al. 2011, *Meteoritics and Planetary Science*, 46, 1525
- Popova, O. P., Jenniskens, P., Emel'yanenko, V., et al. 2013, *Science*, 342, 1069
- Price, M., Solscheid, C., Burchell, M., et al. 2013, *Icarus*, 222, 263
- Ranjith, P. G., Viète, D. R., Chen, B. J., & Perera, M. S. A. 2012, *Engineering Geology*, 151, 120

- Raymond, S. N., Quinn, T., & Lunine, J. I. 2004, *Icarus*, 168, 1
- Reddy, V., Nathues, A., Gaffey, M. J., & Schaeff, S. 2011, *Planet. Space Sci.*, 59, 772
- Reddy, V., Nathues, A., Le Corre, L., et al. 2012a, *Science*, 336, 700
- Reddy, V., Le Corre, L., O'Brien, D. P., et al. 2012b, *Icarus*, 221, 544
- Reddy, V., Sanchez, J. A., Bottke, W. F., et al. 2014, *Icarus*, 237, 116
- Richardson, J. E., & Melosh, H. J. 2013, *Icarus*, 222, 492, stardust/EPOXI
- Rivkin, A. S., Asphaug, E., & Bottke, W. F. 2014, *Icarus*, 243, 429
- Rivkin, A. S., & Emery, J. P. 2010, *Nature*, 464, 1322
- Robert, F. 2003, *Space Science Reviews*
- Rozitis, B., Duddy, S. R., Green, S. F., & Lowry, S. C. 2013, *A&A*, 555, A20
- Rozitis, B., & Green, S. F. 2014, *A&A*, 568, A43
- Rozitis, B., MacLennan, E., & Emery, J. P. 2014, *Nature*, 512, 174
- Ruff. 2016, *Ruff Database*
- Russell, C. T., Raymond, C. A., Coradini, A., et al. 2012, *Science*, 336, 684
- Ryan, E. V., Davis, D. R., & GIBLIN, I. 1999, *Icarus*, 142, 56
- Ryan, E. V., & Melosh, H. J. 1998, *Icarus*, 133, 1
- Sanchez, J. A., Reddy, V., Kelley, M. S., et al. 2014, *Icarus*, 228, 288
- Schneider, E., Storzer, D., Hartung, J. B., Fechtig, H., & Gentner, W. 1973, in *Lunar and Planetary Science Conference Proceedings, Vol. 4, Lunar and Planetary Science Conference Proceedings*, 3277
- Schröder, S. E., Keller, H. U., Mottola, S., et al. 2015, *Planet. Space Sci.*, 117, 236
- Schultz, P. H., & Gault, D. E. 1984, in *Lunar and Planetary Science Conference, Vol. 15, Lunar and Planetary Science Conference*, 730
- Schultz, P. H., & Gault, D. E. 1990, *GSA*, 247, 239
- Schultz, R. A. 1993, *Journal of Geophysical Research: Planets*, 98, 10883
- Senft, L. E., & Stewart, S. T. 2011, *Icarus*, 214, 67

- Spurný, P., Haloda, J., Borovička, J., Shrubený, L., & Halodová, P. 2014, *A&A*, 570, A39
- Stern, S. A., & Trafton, L. M. 2008, On the Atmospheres of Objects in the Kuiper Belt, ed. M. A. Barucci, H. Boehnhardt, D. P. Cruikshank, A. Morbidelli, & R. Dotson, 365–380
- Tegler, S. C., Bauer, J. M., Romanishin, W., & Peixinho, N. 2008, Colors of Centaurs, ed. M. A. Barucci, H. Boehnhardt, D. P. Cruikshank, A. Morbidelli, & R. Dotson, 105
- Tholen, D. J. 1989, Asteroid taxonomic classifications, ed. R. P. Binzel, T. Gehrels, & M. S. Matthews, 1139
- Thomas, N., Barbieri, C., Keller, H. U., et al. 2012, *Planet. Space Sci.*, 66, 96
- Thomas, N., Sierks, H., Barbieri, C., et al. 2015, *Science*, 347, aaa0440
- Trilling, D. E., & Bernstein, G. M. 2006, *AJ*, 131, 1149
- Tsiganis, K., Gomes, R., Morbidelli, A., & Levison, H. F. 2005, *Nature*, 435, 459
- Udry, S., Mayor, M., & Santos, N. C. 2003, *A&A*, 407, 369
- Vernazza, P., Binzel, R. P., Rossi, A., Fulchignoni, M., & Birlan, M. 2009, *Nature*, 458, 993
- Vernazza, P., Delbo, M., King, P. L., et al. 2012, *Icarus*, 221, 1162
- Veverka, J., Thomas, P. C., Robinson, M., et al. 2001, *Science*, 292, 484
- Vincent, J.-B., Bodewits, D., Besse, S., et al. 2015, *Nature*, 523, 63
- Vincent, J.-B., Oklay, N., Pajola, M., et al. 2016, *A&A*, 587, A14
- Vokrouhlický, D., Bottke, W. F., Chesley, S. R., Scheeres, D. J., & Statler, T. S. 2015, ArXiv e-prints, arXiv:1502.01249
- Walsh, K. J., Delbó, M., Bottke, W. F., Vokrouhlický, D., & Lauretta, D. S. 2013, *Icarus*, 225, 283
- Walsh, K. J., Morbidelli, A., Raymond, S. N., O’Brien, D. P., & Mandell, A. M. 2011, *Nature*, 475, 206
- Weisberg, M. K., McCoy, T. J., & Krot, A. N. 2006, Systematics and Evaluation of Meteorite Classification, ed. D. S. Lauretta & H. Y. McSween, 19

-
- Weissman, P. R., Asphaug, E., & Lowry, S. C. 2004, Structure and density of cometary nuclei, ed. G. W. Kronk, 337
- Whipple, F. L. 1950, *ApJ*, 111, 375
- . 1951, *ApJ*, 113, 464
- Yano, H., Kubota, T., Miyamoto, H., et al. 2006, *Science*, 312, 1350
- Zolensky, M. E., Zega, T. J., Yano, H., et al. 2006, *Science*, 314, 1735

A

Appendix

A.0.1 Conversion of BTM to FITS files

```
for i in glob.glob('*.bmp'):  
    name = i.split('.')[0]  
    print name  
    frame = im.open(i)  
    frame_array = array(frame)  
    im_gr = sum(frame_array, axis = 2)  
    im_gr = array(im_gr, dtype = int16)  
    pf.writeto('\%s.fits'\%(name), im_gr)
```

A.0.2 Photometry routine of fragments

```

#create the conf.sex using sextractor:
os.system("rm *.cat")
os.system("rm *check.fits")
os.system("./sex -d > conf.sex")

#define the sextractor parameters to be changed
sexparams = "-DETECT_THRESH 3 \
-ANALYSIS_THRESH 3 \
-FILTER N \
-DETECT_MINAREA 5 \
-CHECKIMAGE_TYPE OBJECTS \
-CHECKIMAGE_NAME check.fits \
-MEMORY_OBJSTACK 30000 \
-MEMORY_PIXSTACK 3000000 \
-MEMORY_BUFSIZE 2048"

#create the default.param using sextractor:
defparam = "NUMBER\n\
X_IMAGE\n\
Y_IMAGE\n\
FLUX_ISO\n\
FLUXERR_ISO\n\
ISOAREA_IMAGE\n\
A_IMAGE\n\
B_IMAGE\n\
ELONGATION\n\
ELLIPTICITY\n\
FLAGS\n"

open('default.param', 'w').write(defparam)

#run the sextractor for all frames and calculate the median fwhm:
for frame in glob.glob('*.fits'):
    os.system("./sex -c conf.sex \\\%s \\\%s > junk" \\\%(frame, sexparams))
    #time.sleep(2)
    newframe = frame.replace('.fits', '.cat')
    fname = frame.replace('.fits', 'check.fits')
    os.rename("test.cat", newframe)

```

```
os.rename("check.fits",fname)
```

A.0.3 Flags of Source Extractor (SExtractor v2.13 User's Manual)

The numbers indicate the type of FLAG was risen during the extraction. FLAGS may also have indication numbers which consist the sum of the following basic:

- 1 The object has neighbours, bright and close enough to significantly bias the MAG AUTO photometry, or bad pixels (more than 10% of the integrated area affected)
- 2 The object was originally blended with another one
- 4 At least one pixel of the object is saturated or very close to saturation level
- 8 The object is too close to the image boundary and thus is truncated
- 16 Object's aperture data are incomplete or corrupted
- 32 Object's isophotal data are incomplete or corrupted
- 64 A memory overflow occurred during de-blending
- 128 A memory overflow occurred during extraction

A.0.4 Identification of Raman spectra peaks P_1 and P_2

```

def gauss_full(gauss , xs ):
    ys = []
    for x in xs:
        y = gauss_point(gauss , x)
        ys.append(y)
    ys = numpy.array(ys)
    return ys

def gauss_point(gauss , x):
    return gauss [0]*numpy.e**(-(x-gauss [1])**2/(2* gauss [2]**2))

def gauss_doublet(x, Aa, Ma, Sa , Ab, Mb, Sb):
    return gauss_point([Aa, Ma, Sa] , x)+gauss_point([Ab, Mb, Sb] , x)

def gauss_singlet(x, A, M, S):
    return gauss_point([A, M, S] , x)

def error_point(gauss , x, y):
    return gauss_point(gauss , x) - y

def error_doublet(gausses , x, y):
    return gauss_point(gausses [0:3] , x)+gauss_point(gausses [3:6] , x)-y

def error_singlet(gausses , x, y):
    return gauss_point(gausses [0:3] , x)-y

#input file; as 'xs' and 'ys'
xs, ys = loadtxt('reffile.txt', unpack = True)
ys = ys - numpy.median(ys)
gauss_1_mean = 822.0
gauss_1_sigma = 6.0 # gauss 1 width
x1 = numpy.argmin(numpy.abs(xs - gauss_1_mean))
gauss_1_int = ys[x1] # gauss 1 intensity estimate

gauss_2_mean = 854.0 # gauss 1 position
gauss_2_sigma = 6.0 # gauss 1 width
x2 = numpy.argmin(numpy.abs(xs - gauss_2_mean))
gauss_2_int = ys[x2] # gauss 1 intensity estimate

```

```
parameters_guess = [gauss_1_int, gauss_1_mean, gauss_1_sigma,  
gauss_2_int, gauss_2_mean, gauss_2_sigma]
```

```
fit_function = error_doublet
```

```
parameters_opt, success = optimize.leastsq(fit_function,  
parameters_guess, args = (xs,ys), maxfev = 1000)
```

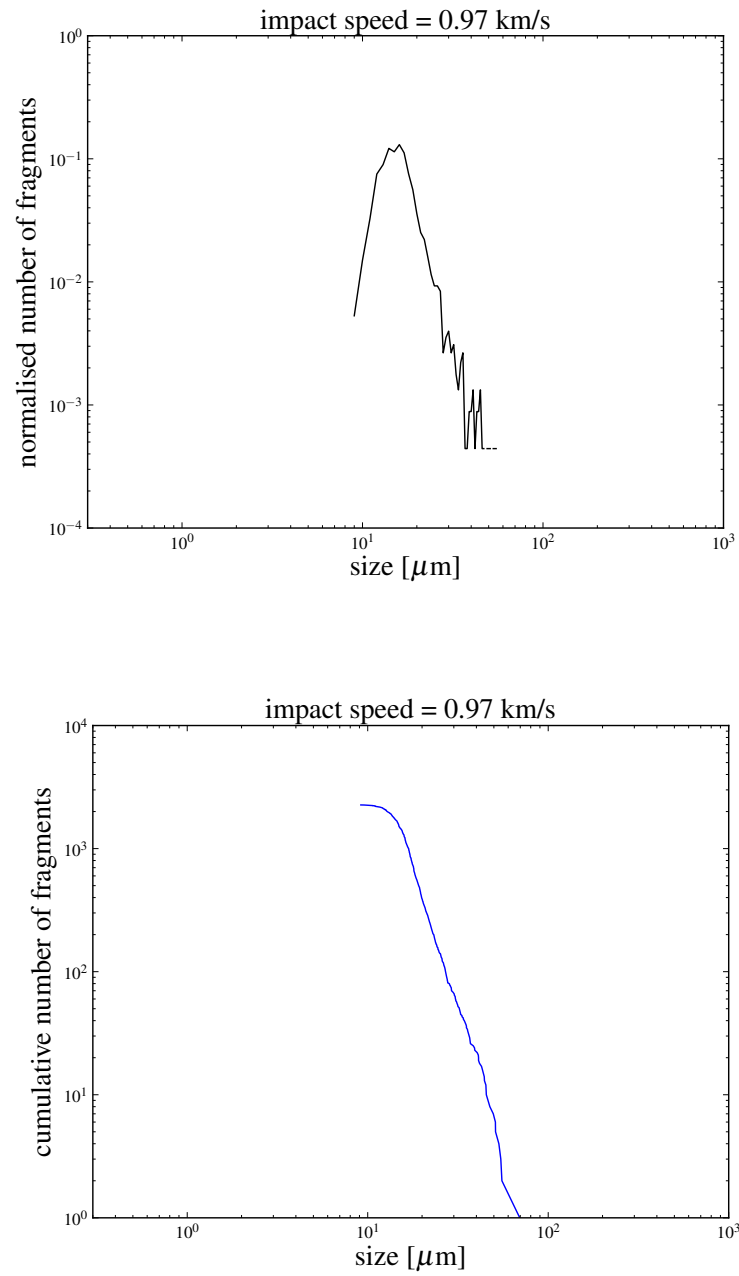
```
print parameters_opt
```

B

Appendix

Here are presented:

- the differential and cumulative SFDs of the the shots.
- the Raman spectra of the largest fragments from all shots in comparison to the reference projectile spectra pre-shot.

B.0.5 Fragmentation: Run#2 (with $z = \times 150$)Figure B.1: Differential (top) and cumulative (bottom) SFD of Run#2 (with $z = \times 150$).

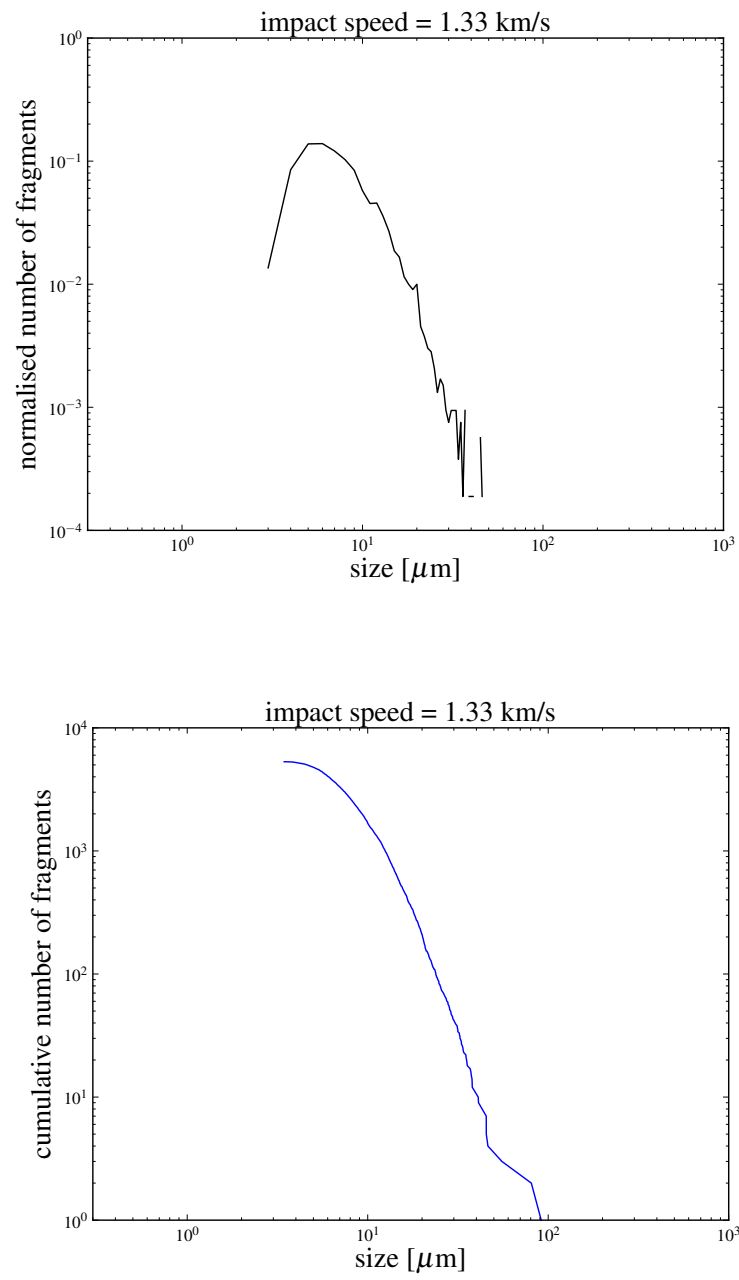


Figure B.2: Differential (top) and cumulative (bottom) SFD of Run#2 (with $z = \times 150$).

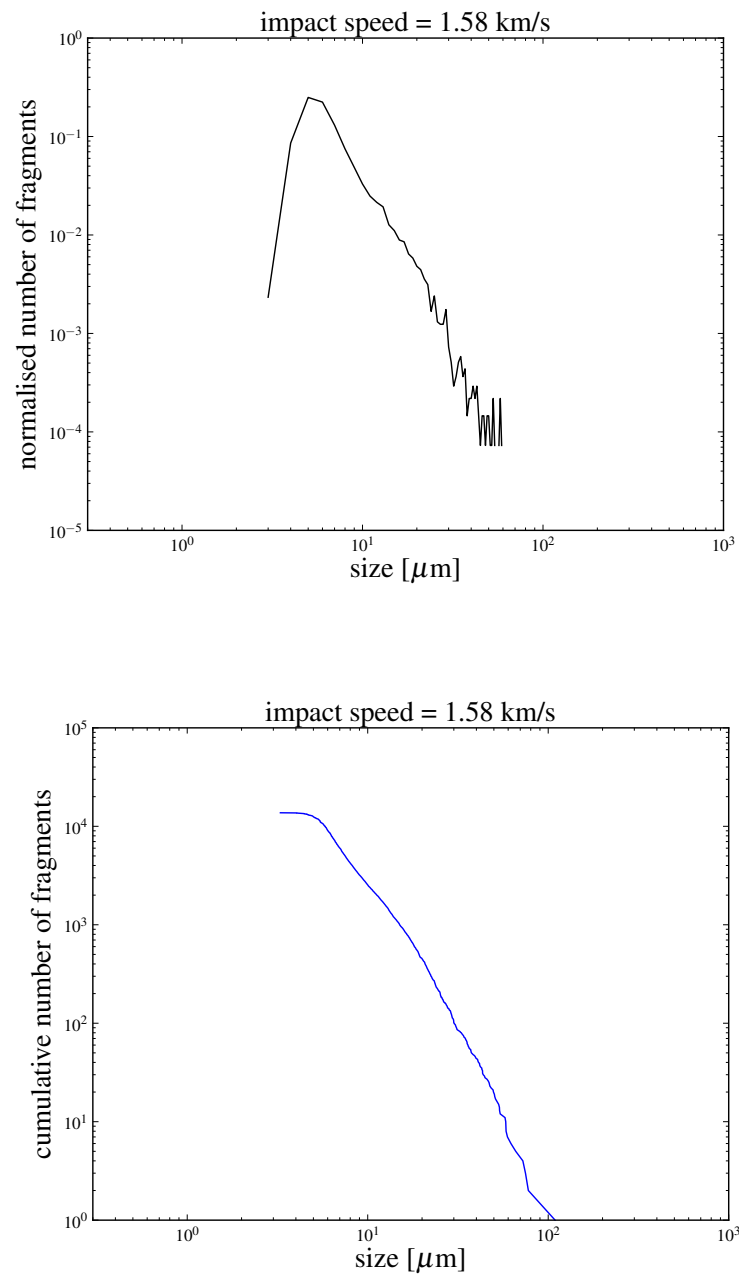


Figure B.3: Differential (top) and cumulative (bottom) SFD of Run#2 (with $z = \times 150$).

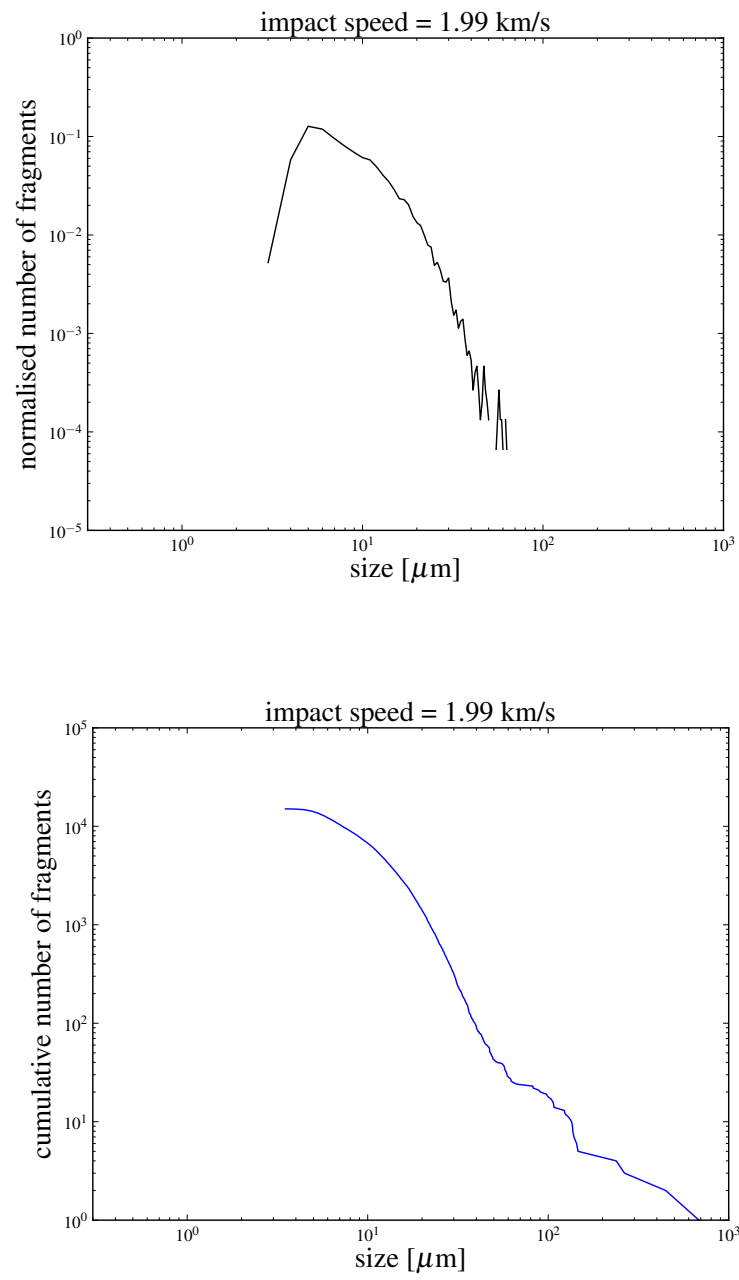


Figure B.4: Differential (top) and cumulative (bottom) SFD of Run#2 (with $z = \times 150$).

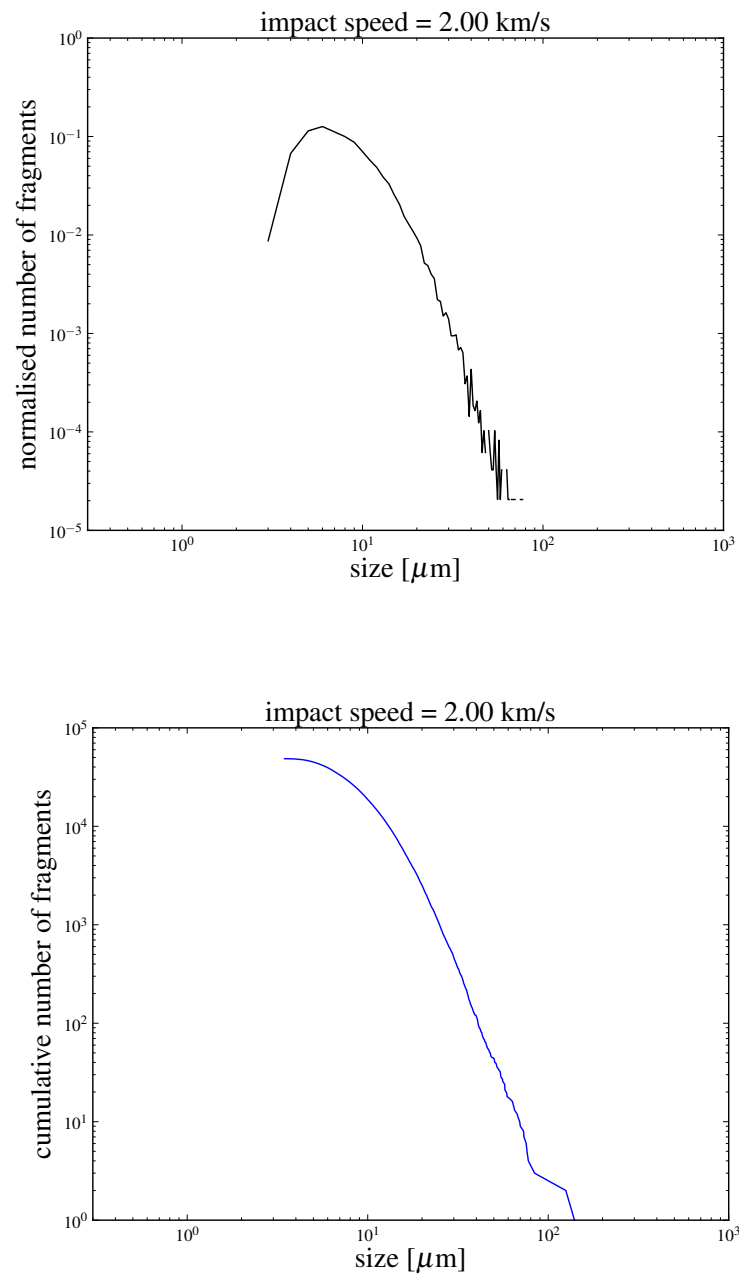


Figure B.5: Differential (top) and cumulative (bottom) SFD of Run#2 (with $z = \times 150$).

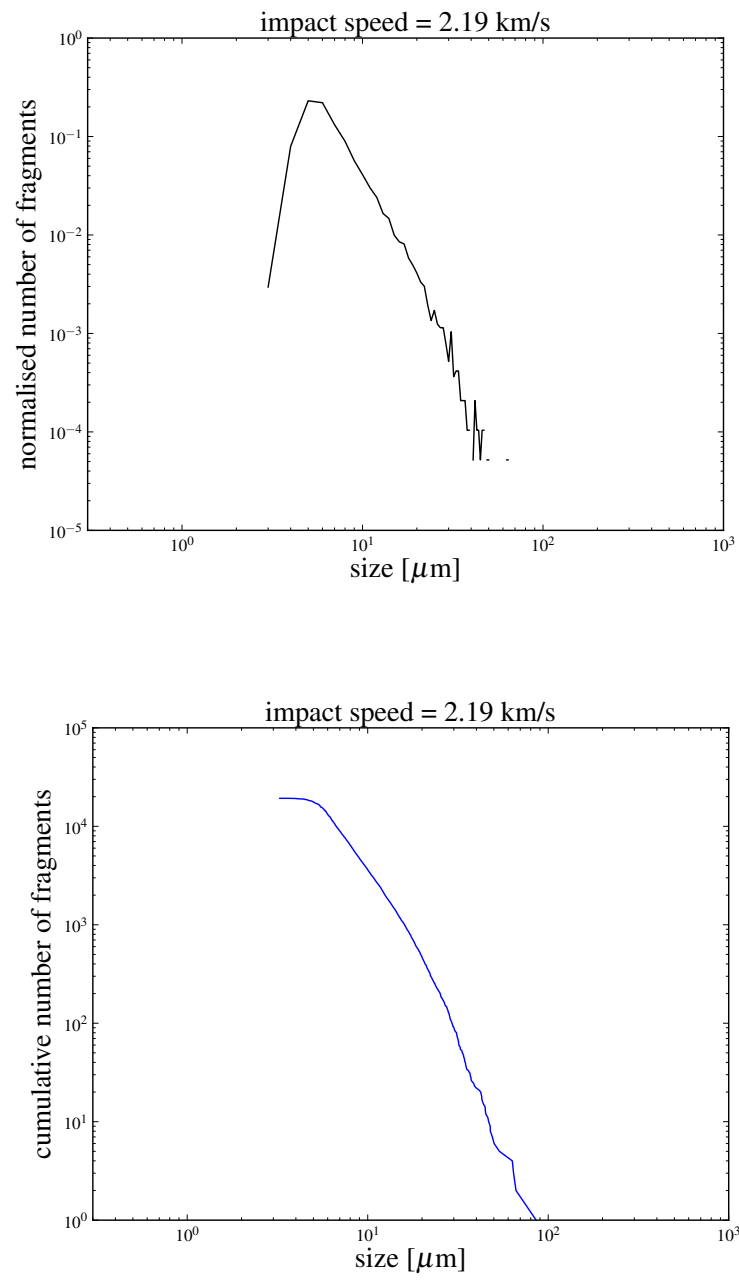


Figure B.6: Differential (top) and cumulative (bottom) SFD of Run#2 (with $z = \times 150$).

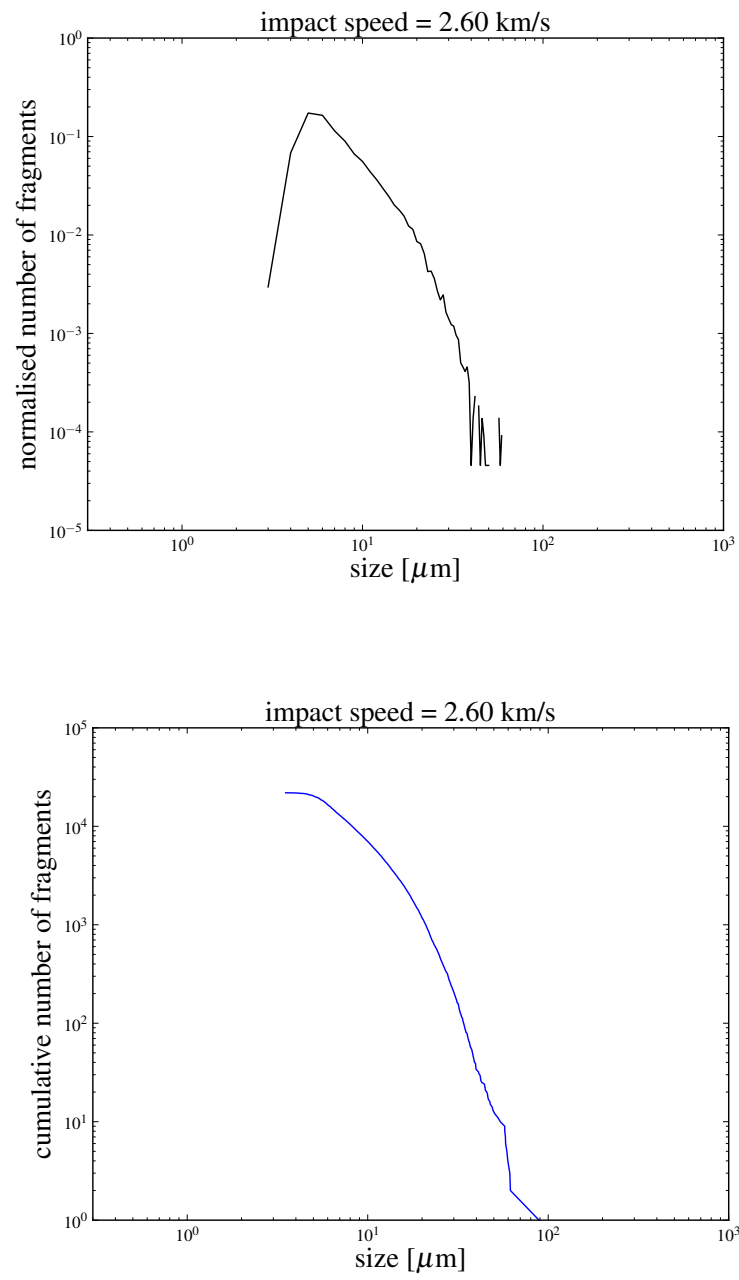


Figure B.7: Differential (top) and cumulative (bottom) SFD of Run#2 (with $z = \times 150$).

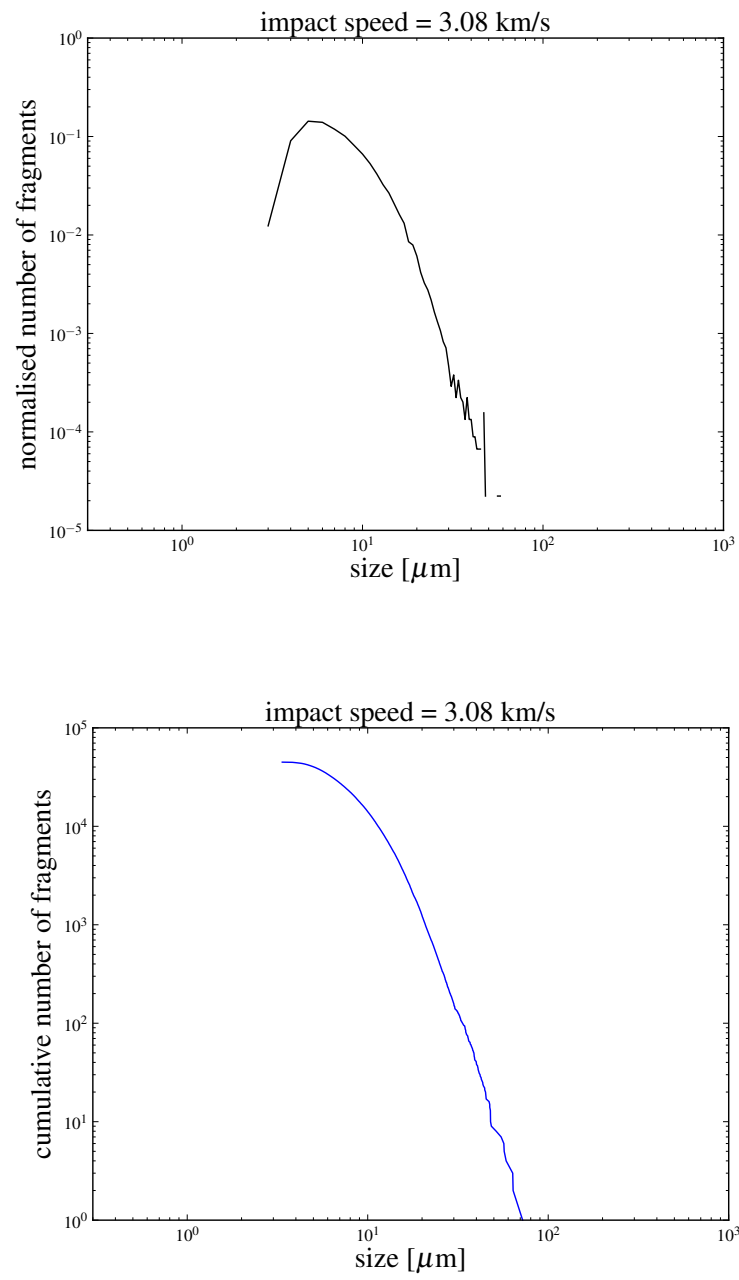
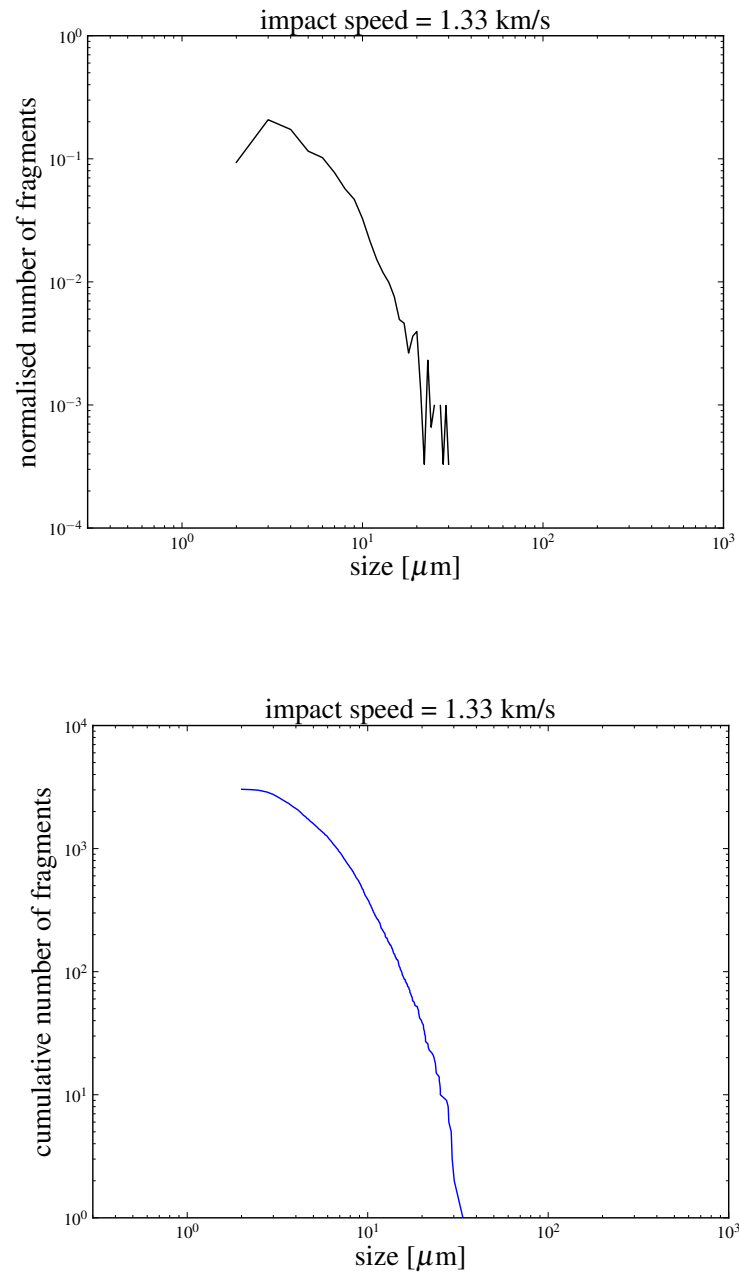


Figure B.8: Differential (top) and cumulative (bottom) SFD of Run#2 (with $z = \times 150$).

B.0.6 Fragmentation: Run#2 (with $z = \times 300$)Figure B.9: Differential (top) and cumulative (bottom) SFD of Run#2 (with $z = \times 300$).

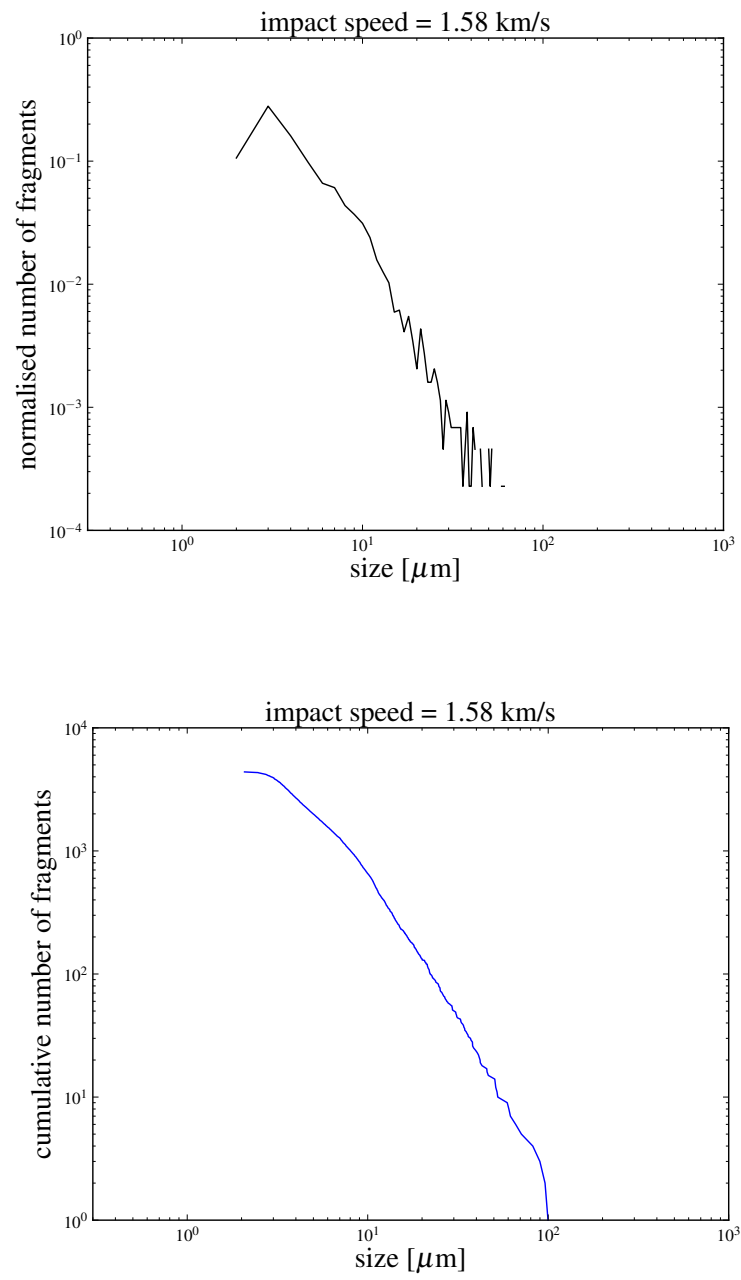


Figure B.10: Differential (top) and cumulative (bottom) SFD of Run#2 (with $z = \times 300$).

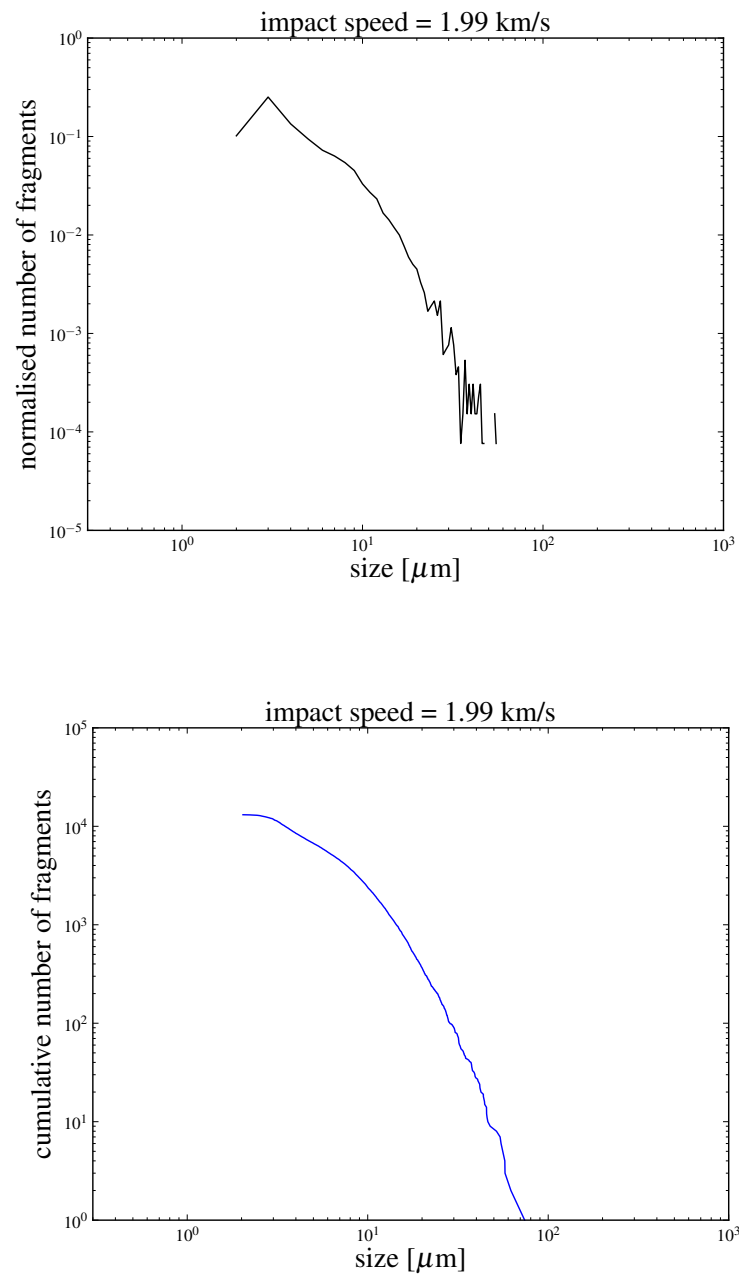


Figure B.11: Differential (top) and cumulative (bottom) SFD of Run#2 (with $z = \times 300$).

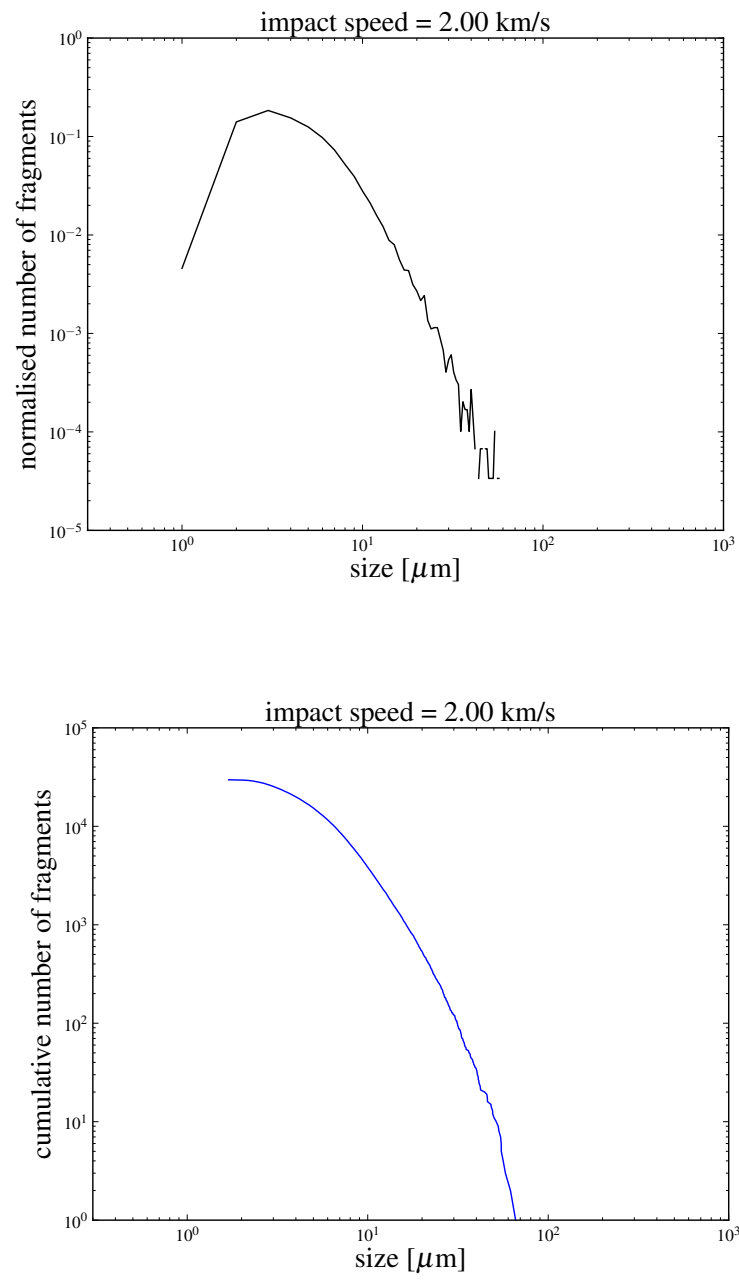


Figure B.12: Differential (top) and cumulative (bottom) SFD of Run#2 (with $z = \times 300$).

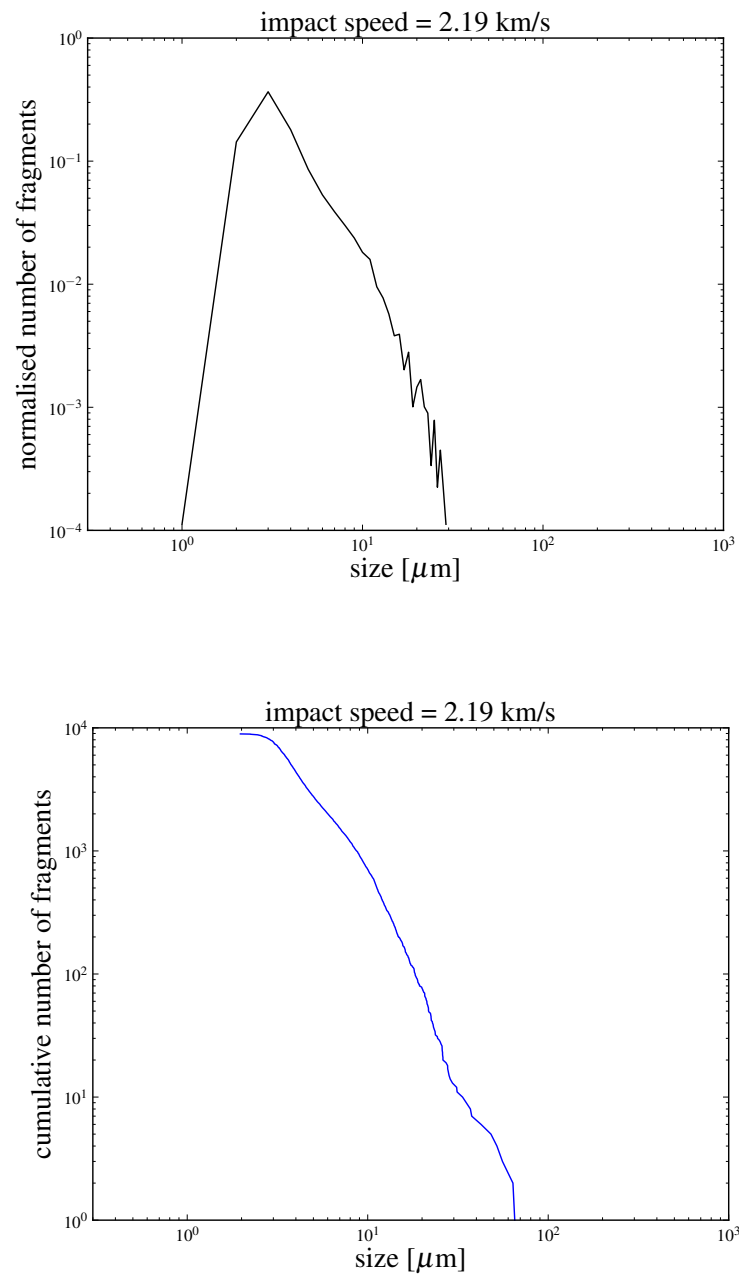


Figure B.13: Differential (top) and cumulative (bottom) SFD of Run#2 (with $z = \times 300$).

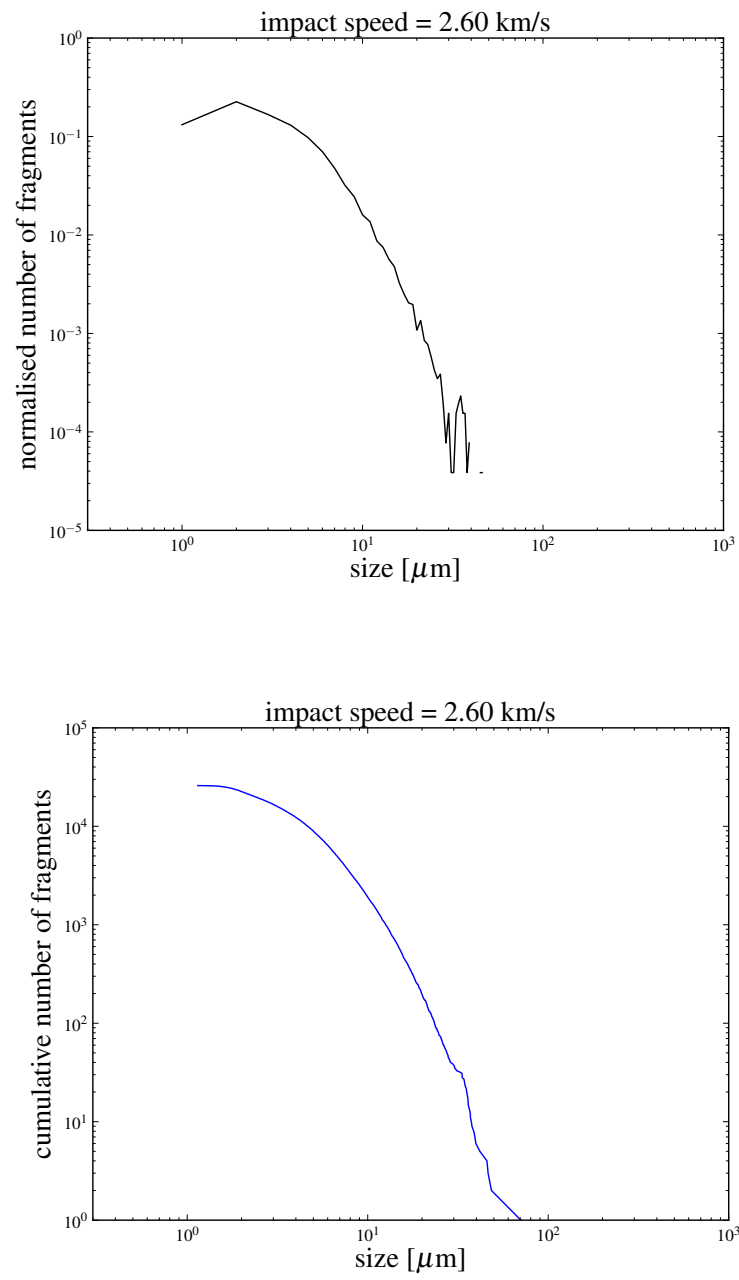


Figure B.14: Differential (top) and cumulative (bottom) SFD of Run#2 (with $z = \times 300$).

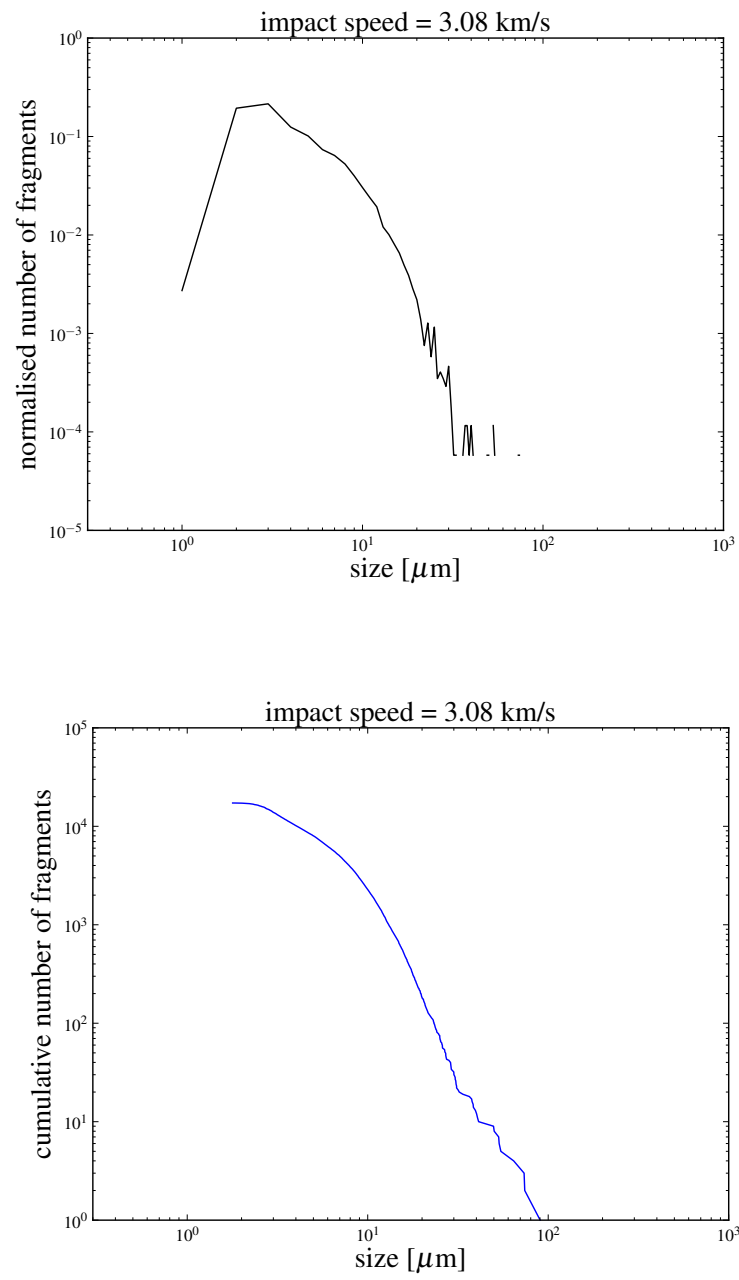


Figure B.15: Differential (top) and cumulative (bottom) SFD of Run#2 (with $z = \times 300$).

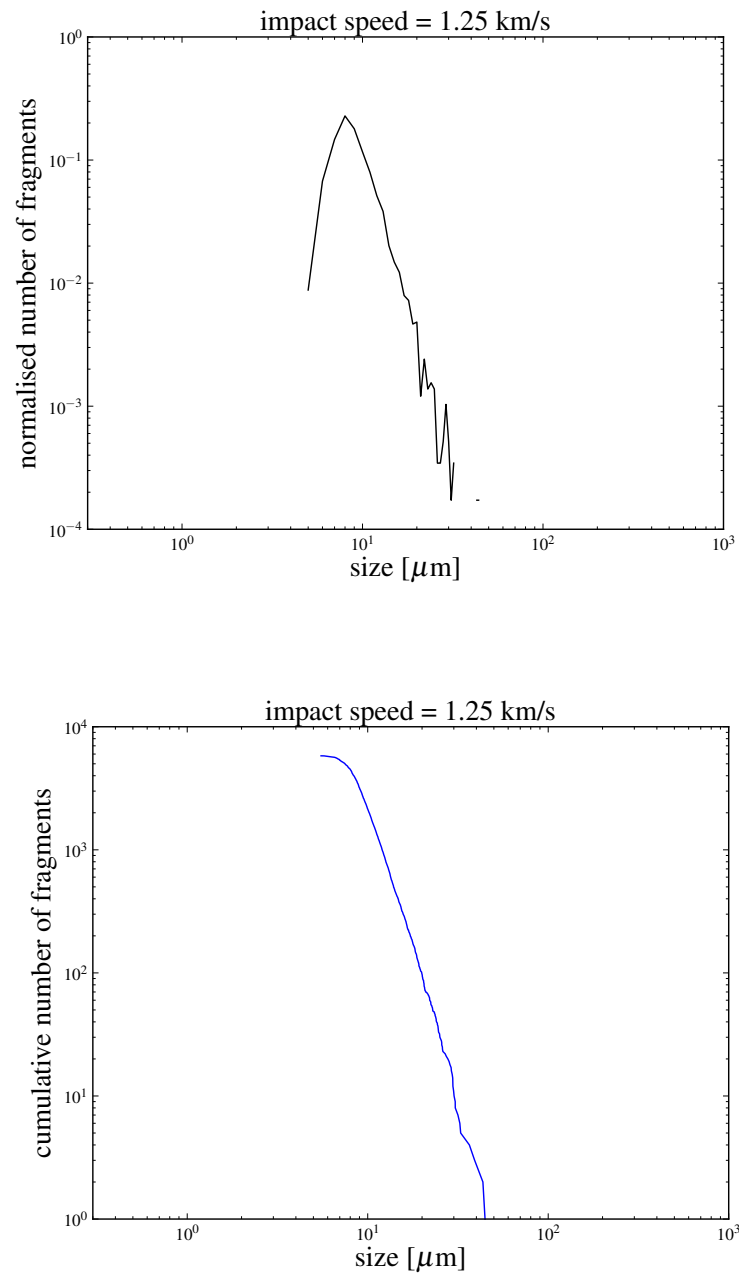
B.0.7 Fragmentation: Run#3

Figure B.16: Differential (top) and cumulative (bottom) SFD of Run#3 (with $z = \times 150$).

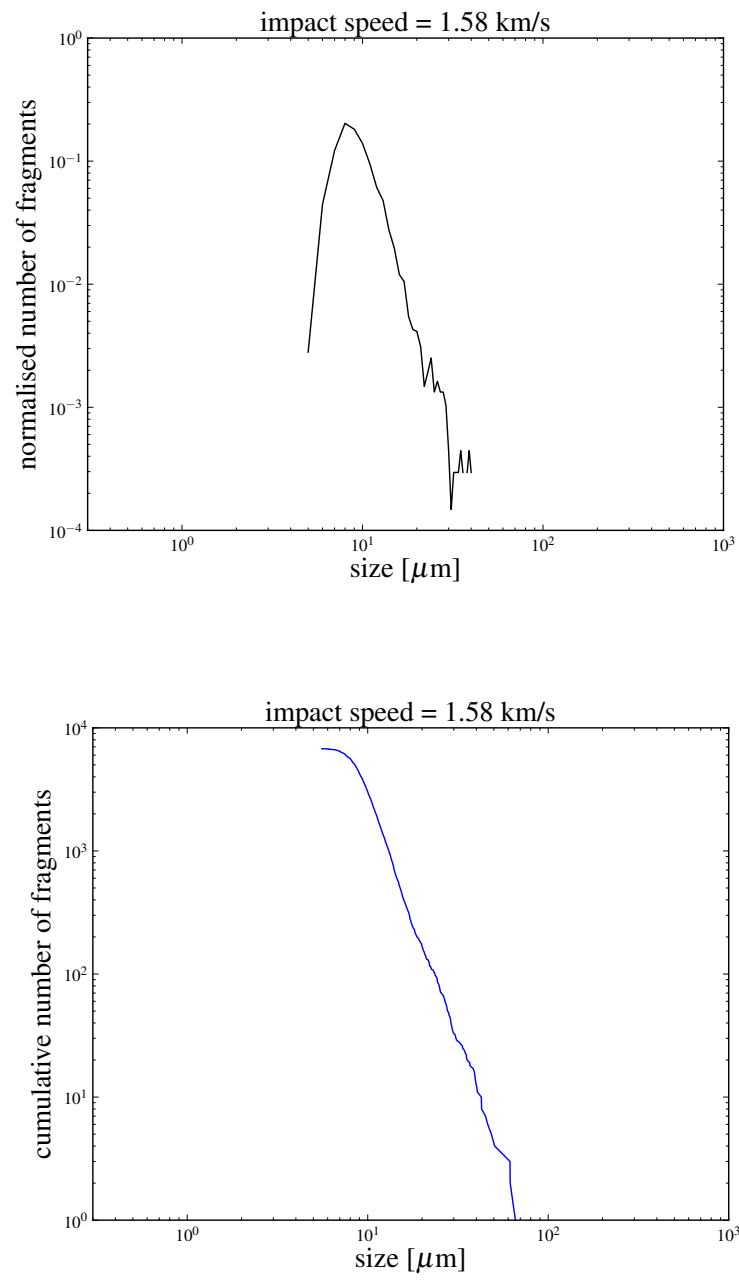


Figure B.17: Differential (top) and cumulative (bottom) SFD of Run#3 (with $z = \times 150$).

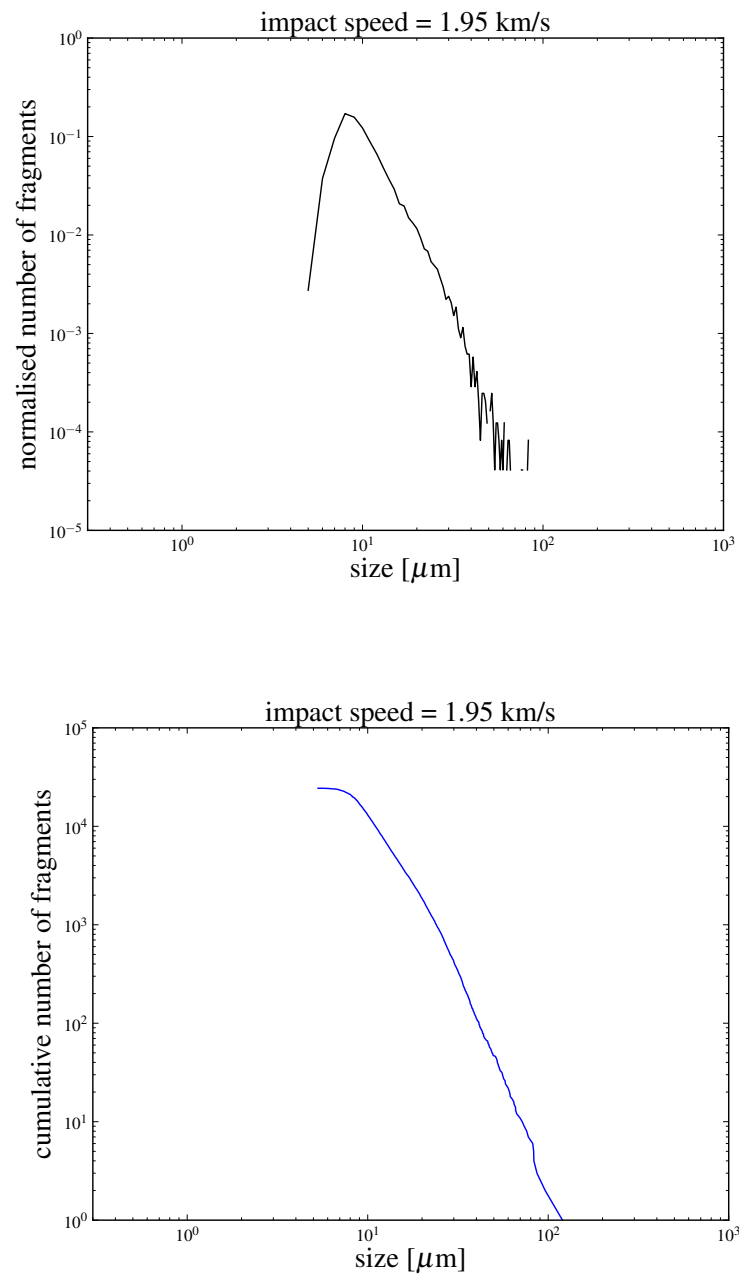


Figure B.18: Differential (top) and cumulative (bottom) SFD of Run#3 (with $z = \times 150$).

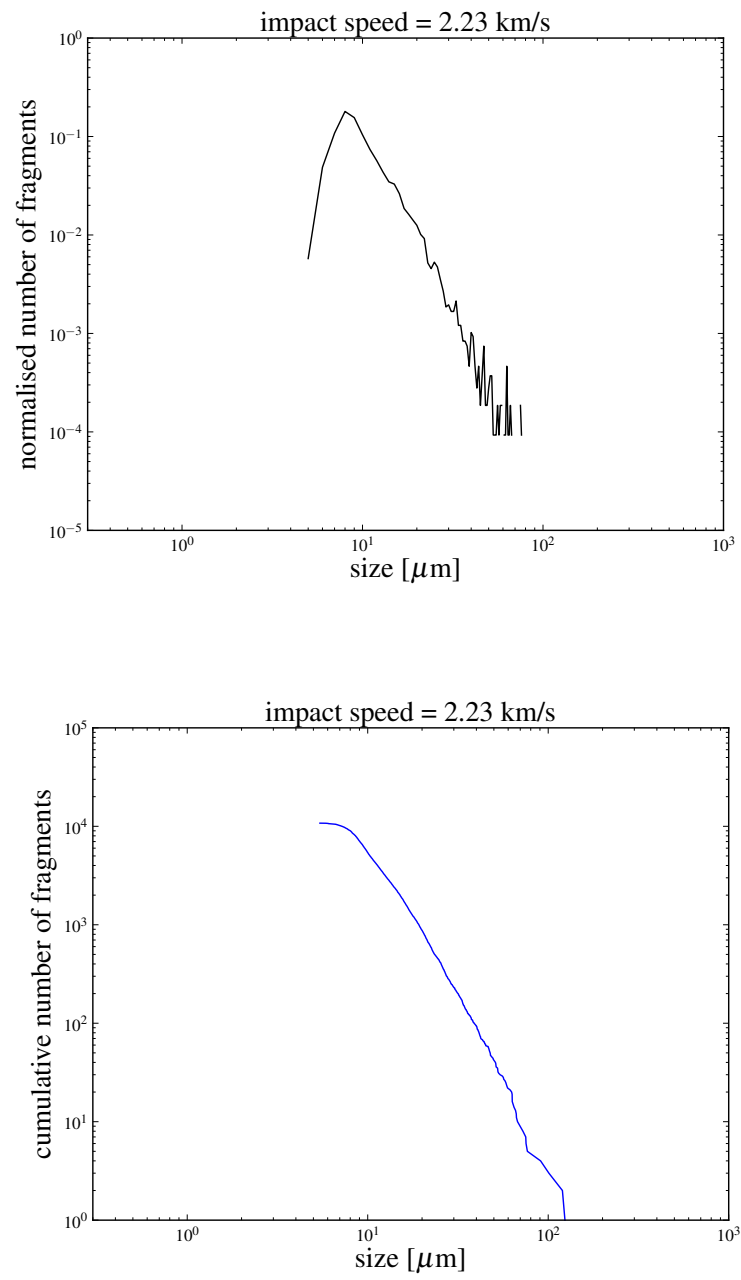


Figure B.19: Differential (top) and cumulative (bottom) SFD of Run#3 (with $z = \times 150$).

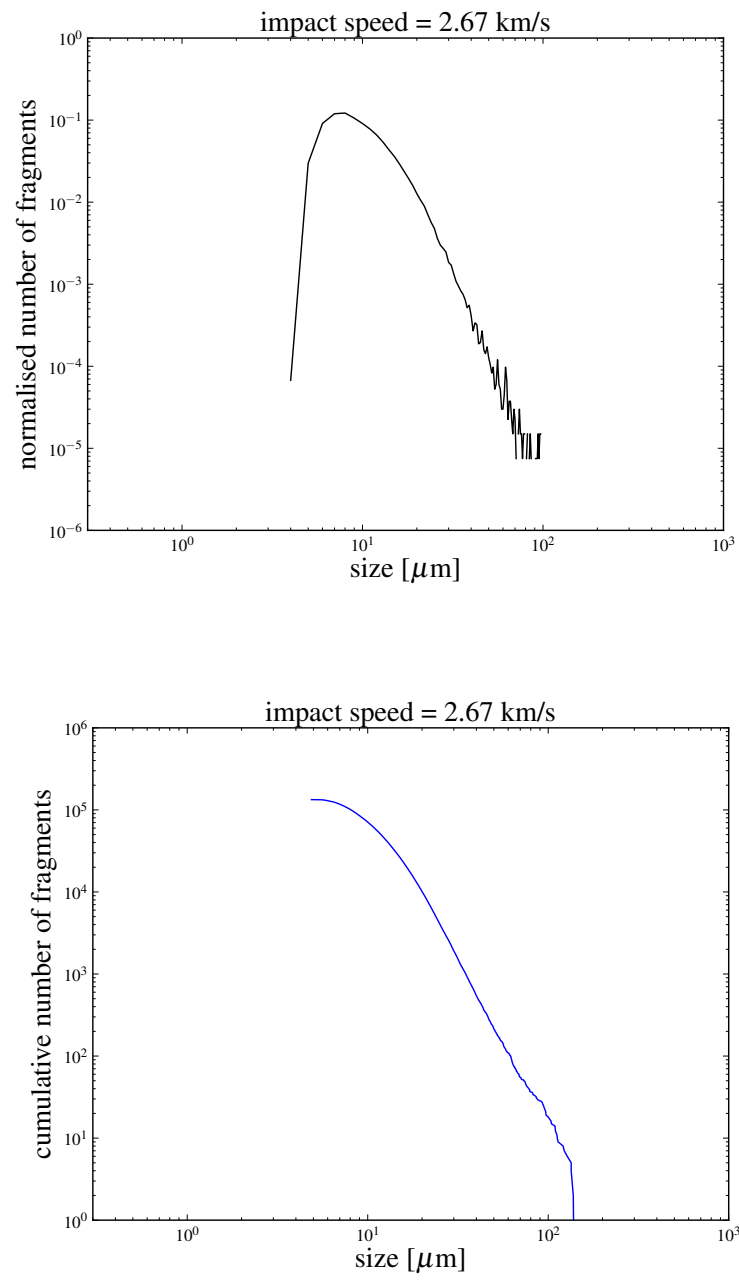


Figure B.20: Differential (top) and cumulative (bottom) SFD of Run#3 (with $z = \times 150$).

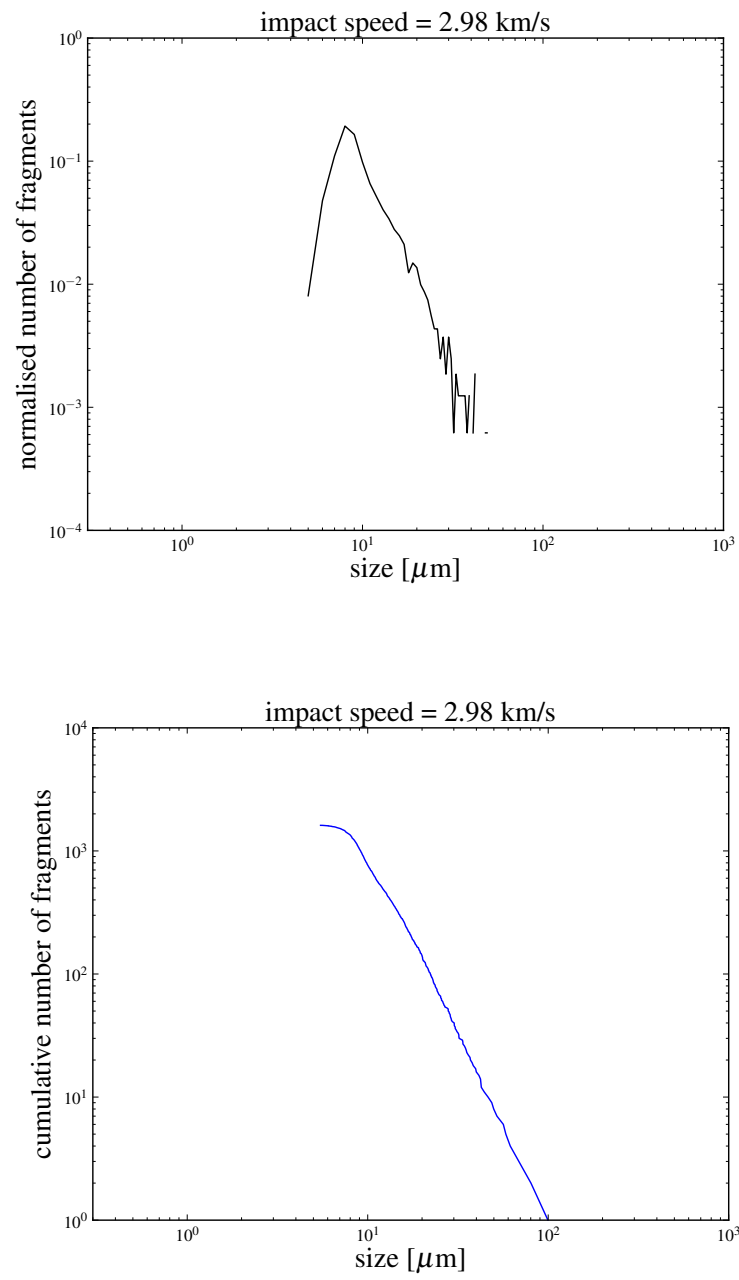


Figure B.21: Differential (top) and cumulative (bottom) SFD of Run#3 (with $z = \times 150$).

B.0.8 Raman spectra: Run#1

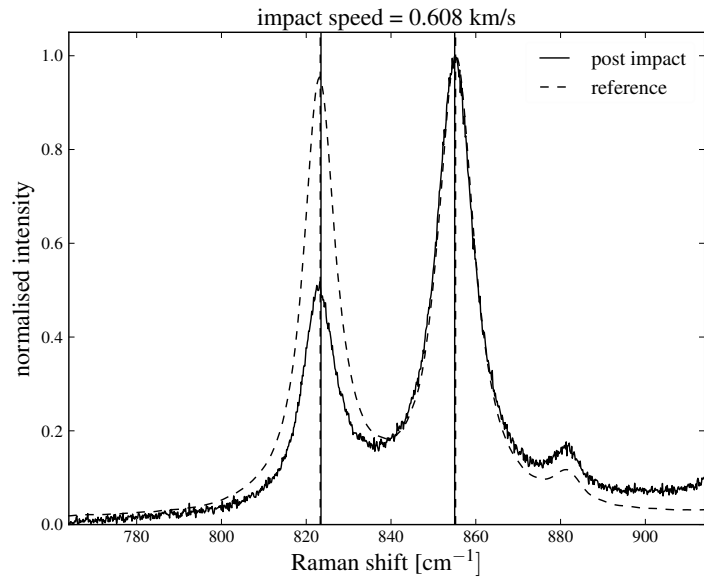


Figure B.22: Raman spectra of olivine before and after the shot with $\Delta P_1 = 0.16$ and $\Delta P_2 = 0.2$.

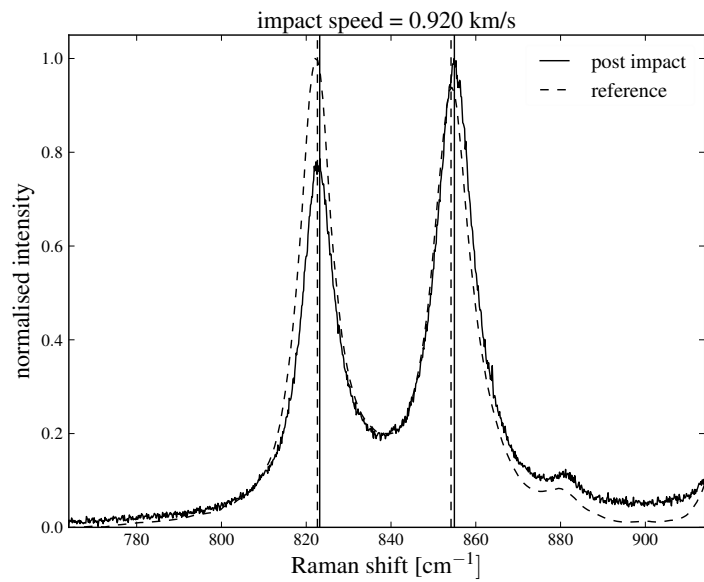


Figure B.23: Raman spectra of olivine before and after the shot with $\Delta P_1 = 0.53$ and $\Delta P_2 = 0.79$.

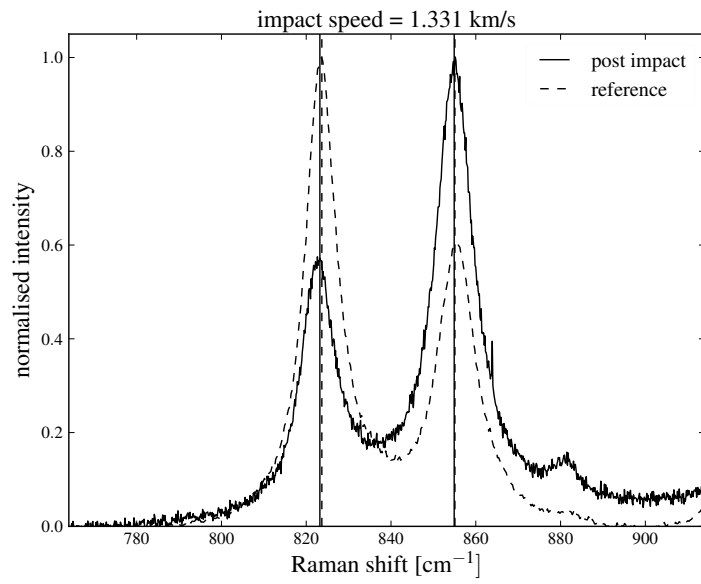


Figure B.24: Raman spectra of olivine before and after the shot with $\Delta P_1 = 0.46$ and $\Delta P_2 = 0.16$.

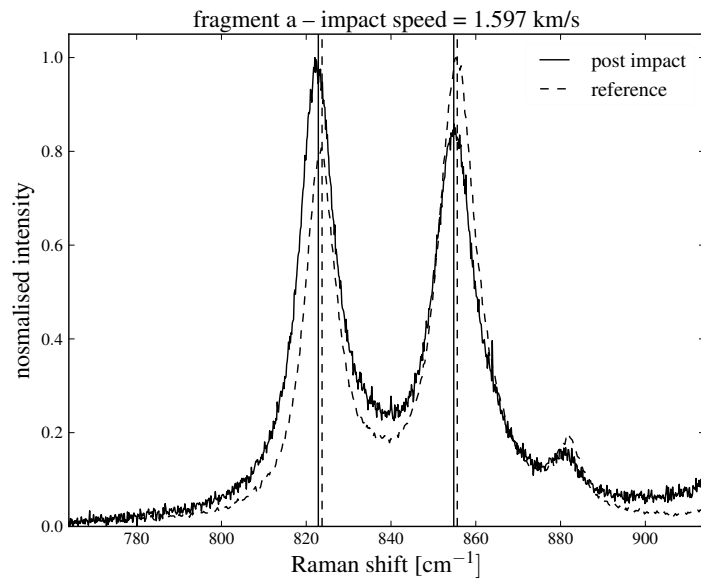


Figure B.25: Raman spectra of olivine before and after the shot with $\Delta P_1 = 0.88$ and $\Delta P_2 = 0.83$.

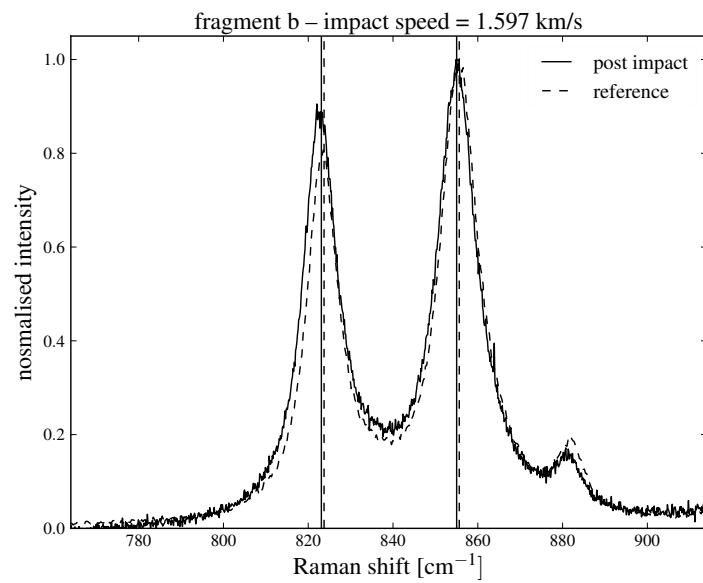


Figure B.26: Raman spectra of olivine before and after the shot with $\Delta P_1 = 0.63$ and $\Delta P_2 = 0.61$.

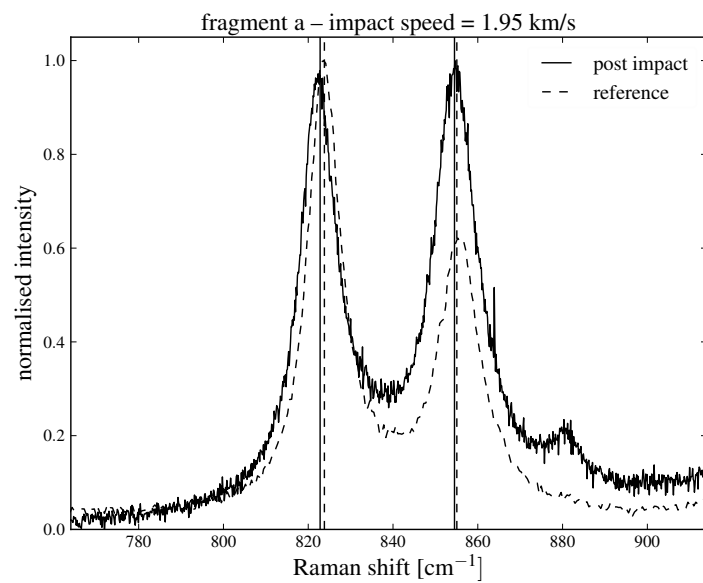


Figure B.27: Raman spectra of olivine before and after the shot with $\Delta P_1 = 1.0$ and $\Delta P_2 = 0.55$.

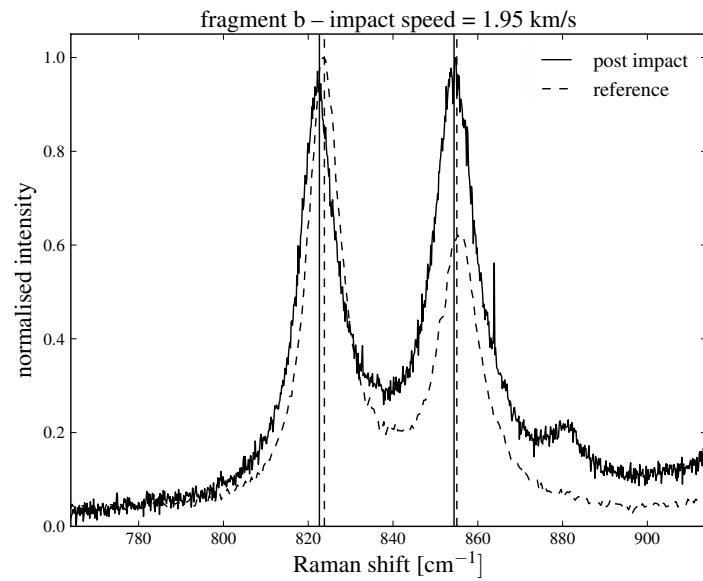


Figure B.28: Raman spectra of olivine before and after the shot with $\Delta P_1 = 1.17$ and $\Delta P_2 = 0.65$.

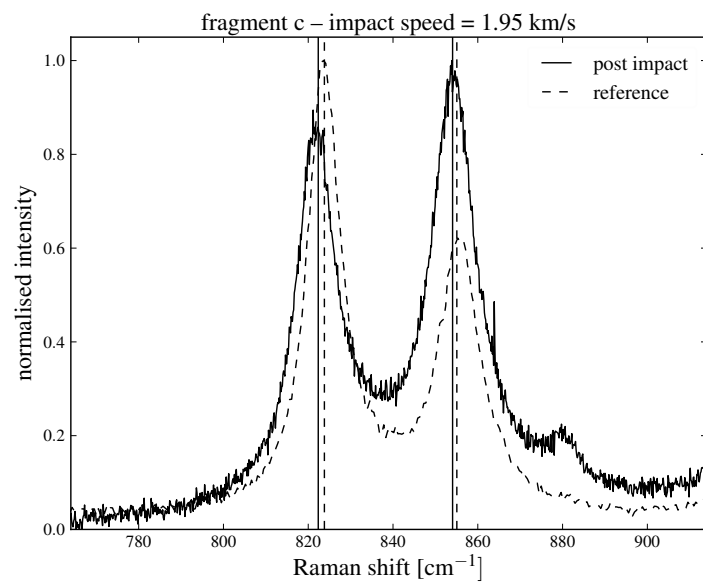


Figure B.29: Raman spectra of olivine before and after the shot with $\Delta P_1 = 1.44$ and $\Delta P_2 = 1.00$.

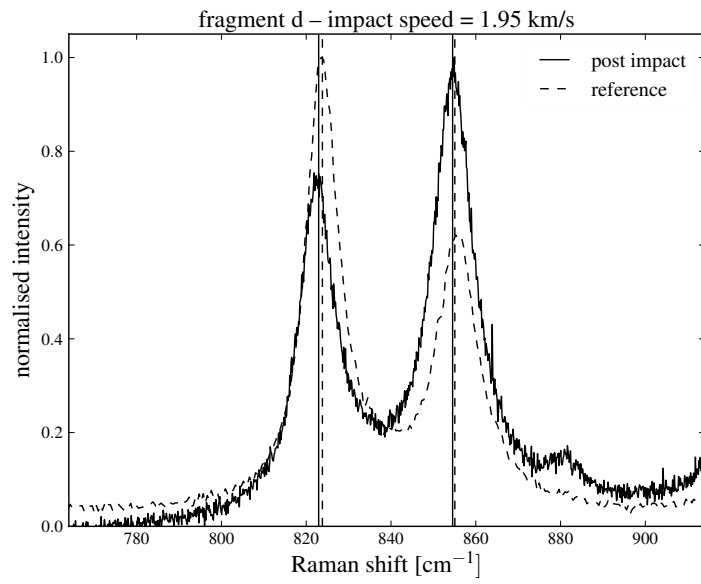


Figure B.30: Raman spectra of olivine before and after the shot with $\Delta P_1 = 0.87$ and $\Delta P_2 = 0.52$.

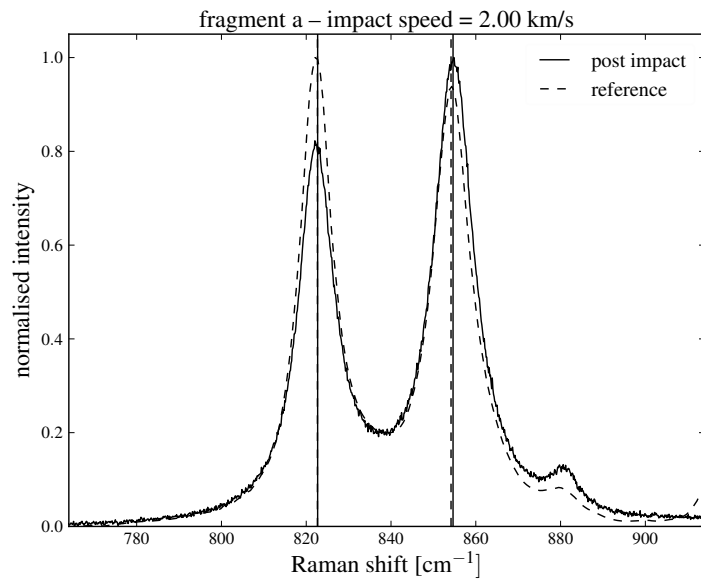


Figure B.31: Raman spectra of olivine before and after the shot with $\Delta P_1 = 0.04$ and $\Delta P_2 = 0.47$.

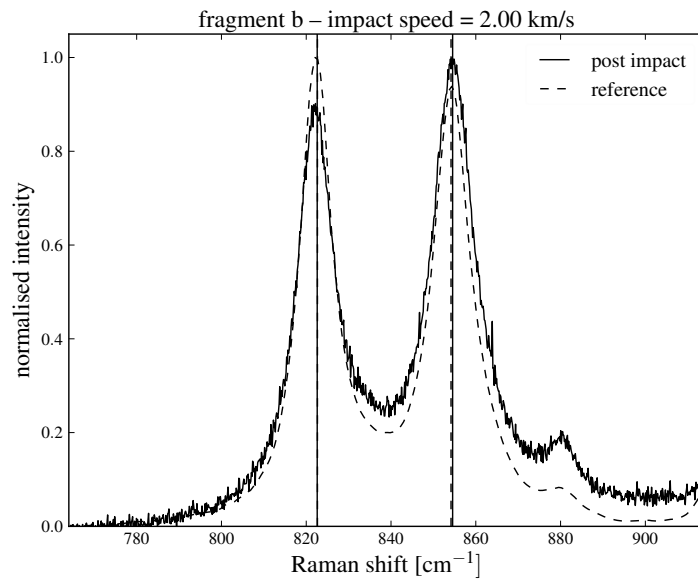


Figure B.32: Raman spectra of olivine before and after the shot with $\Delta P_1 = 0.05$ and $\Delta P_2 = 0.37$.

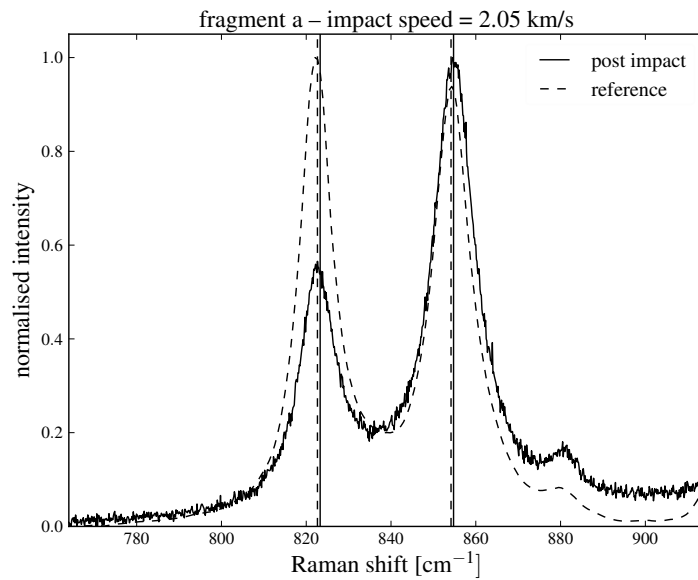


Figure B.33: Raman spectra of olivine before and after the shot with $\Delta P_1 = 0.64$ and $\Delta P_2 = 0.59$.

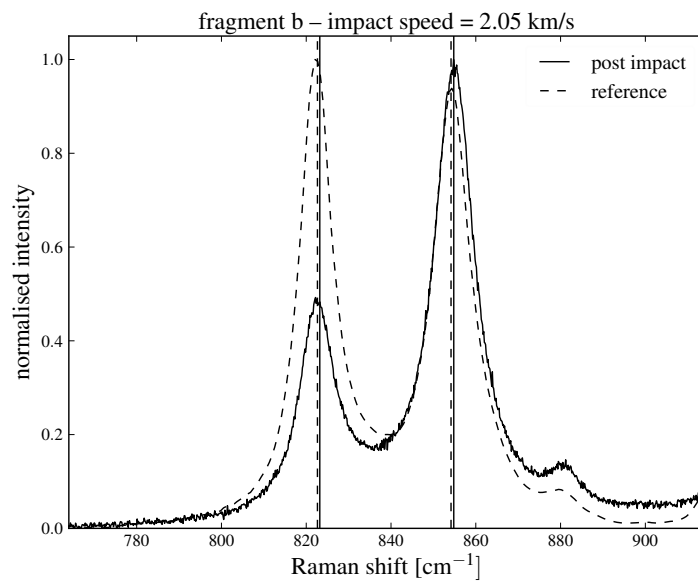


Figure B.34: Raman spectra of olivine before and after the shot with $\Delta P_1 = 0.55$ and $\Delta P_2 = 0.64$.

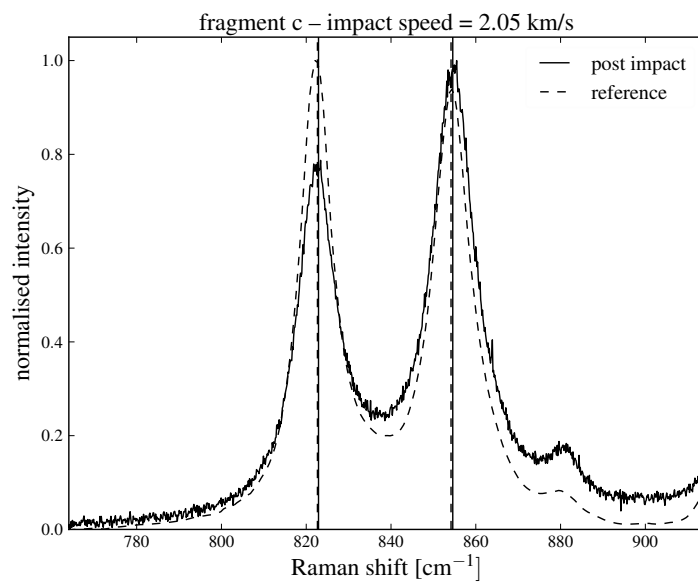


Figure B.35: Raman spectra of olivine before and after the shot with $\Delta P_1 = 0.25$ and $\Delta P_2 = 0.40$.

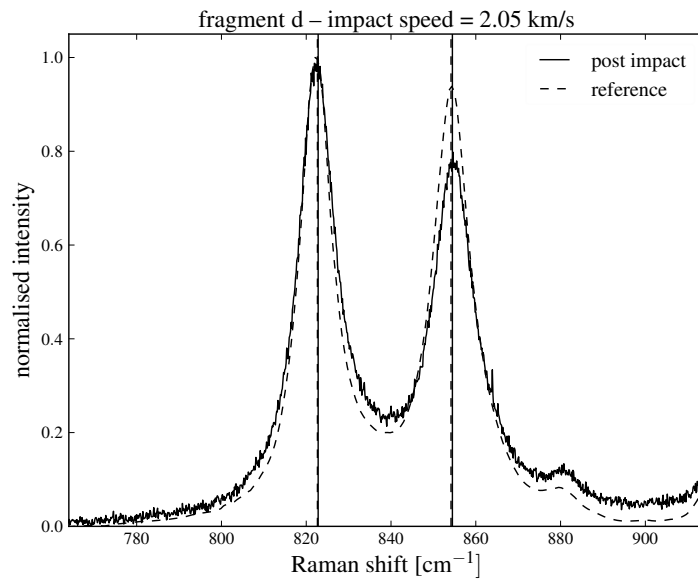


Figure B.36: Raman spectra of olivine before and after the shot with $\Delta P_1 = 0.16$ and $\Delta P_2 = 0.32$.

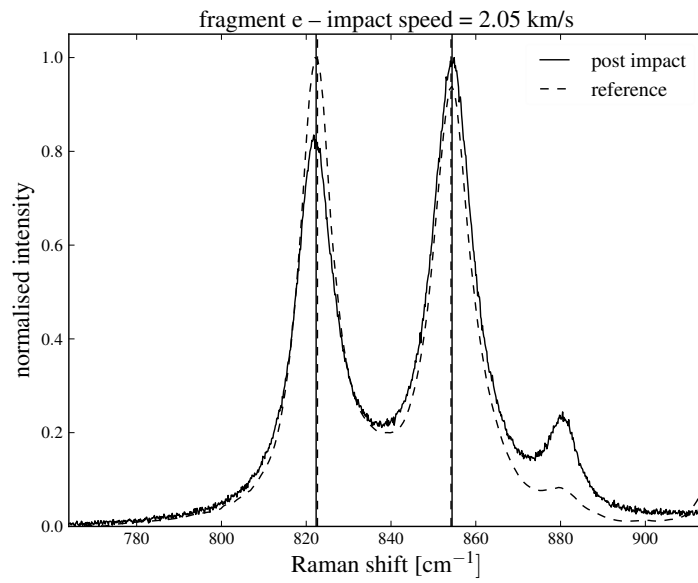


Figure B.37: Raman spectra of olivine before and after the shot with $\Delta P_1 = 0.30$ and $\Delta P_2 = 0.24$.

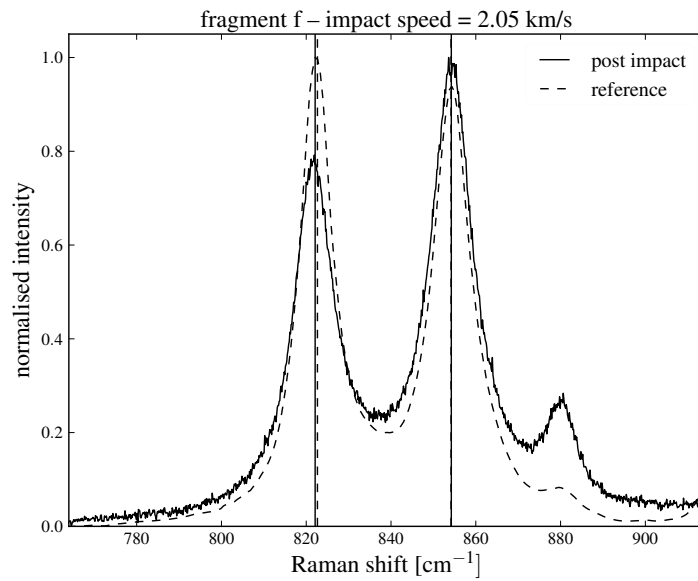


Figure B.38: Raman spectra of olivine before and after the shot with $\Delta P_1 = 0.54$ and $\Delta P_2 = 0.06$.

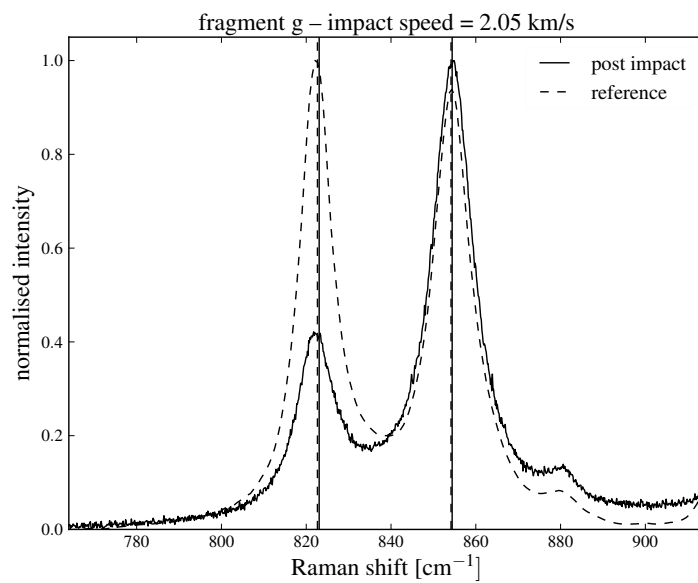


Figure B.39: Raman spectra of olivine before and after the shot with $\Delta P_1 = 0.40$ and $\Delta P_2 = 0.26$.

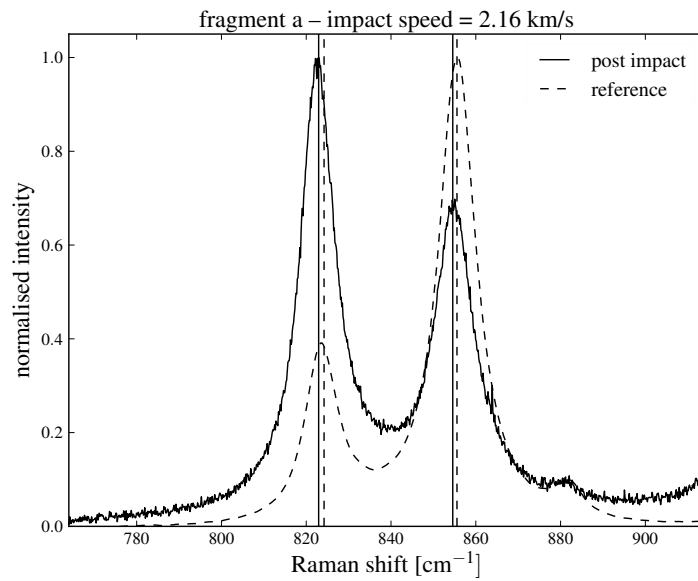


Figure B.40: Raman spectra of olivine before and after the shot with $\Delta P_1 = 1.27$ and $\Delta P_2 = 0.99$.

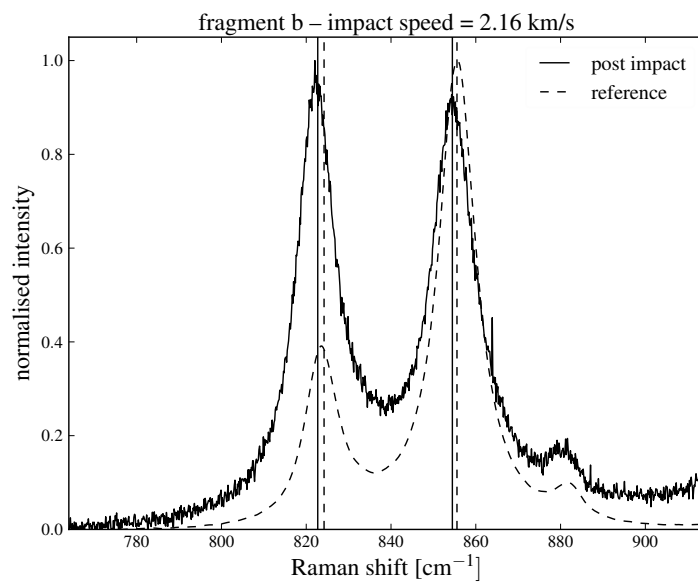


Figure B.41: Raman spectra of olivine before and after the shot with $\Delta P_1 = 1.49$ and $\Delta P_2 = 1.08$.

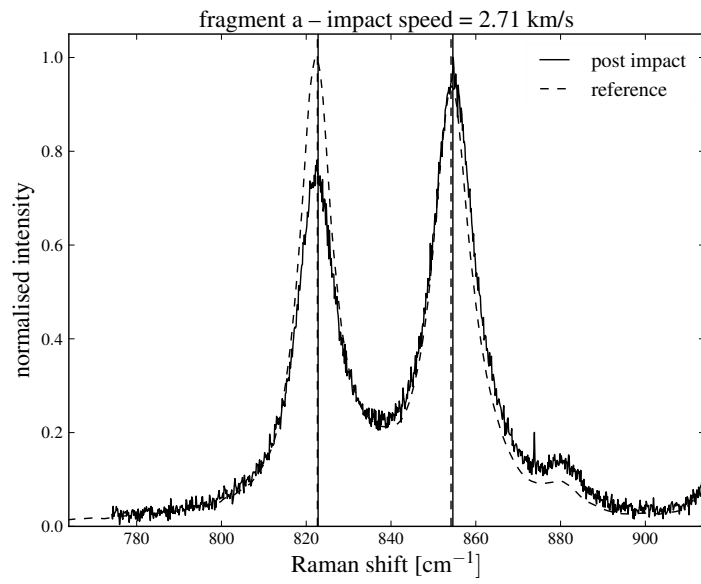


Figure B.42: Raman spectra of olivine before and after the shot with $\Delta P_1 = 0.15$ and $\Delta P_2 = 0.43$.

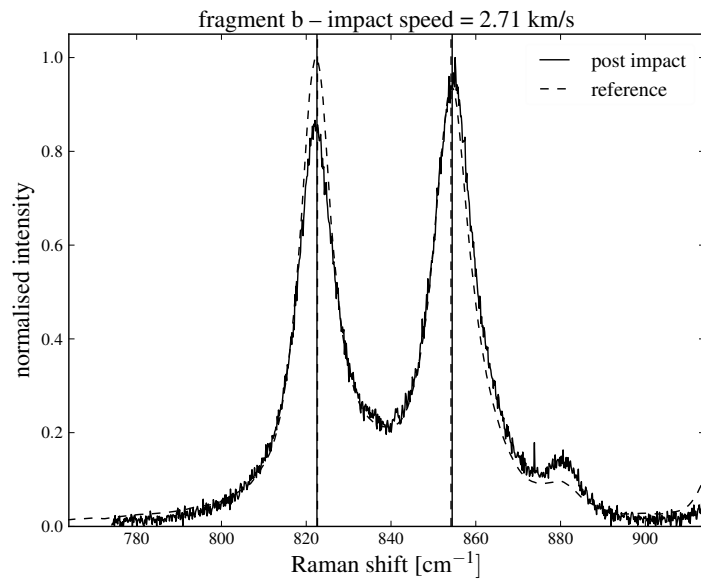


Figure B.43: Raman spectra of olivine before and after the shot with $\Delta P_1 = 0.11$ and $\Delta P_2 = 0.27$.

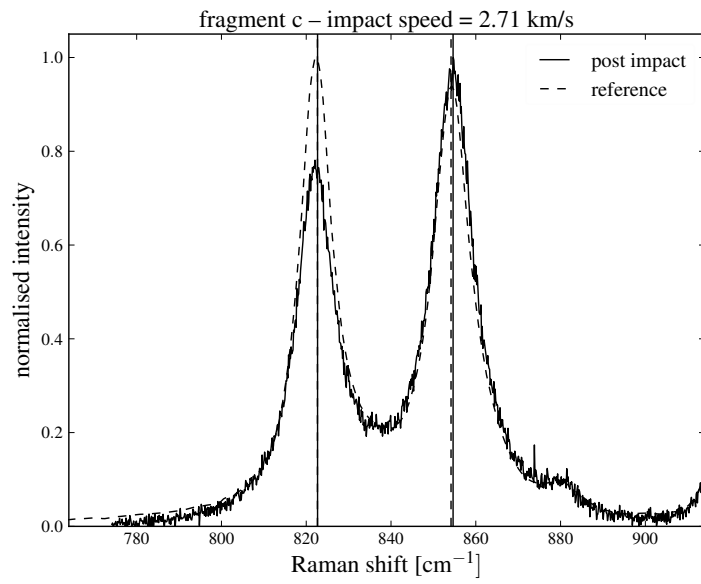


Figure B.44: Raman spectra of olivine before and after the shot with $\Delta P_1 = 0.02$ and $\Delta P_2 = 0.48$.

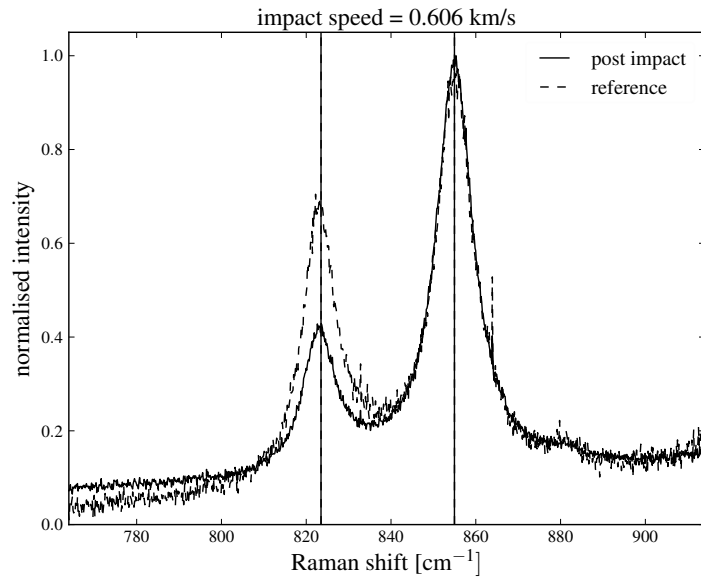
B.0.9 Raman spectra: Run#2

Figure B.45: Raman spectra of olivine before and after the shot with $\Delta P_1 = 0.01$ and $\Delta P_2 = 0$.

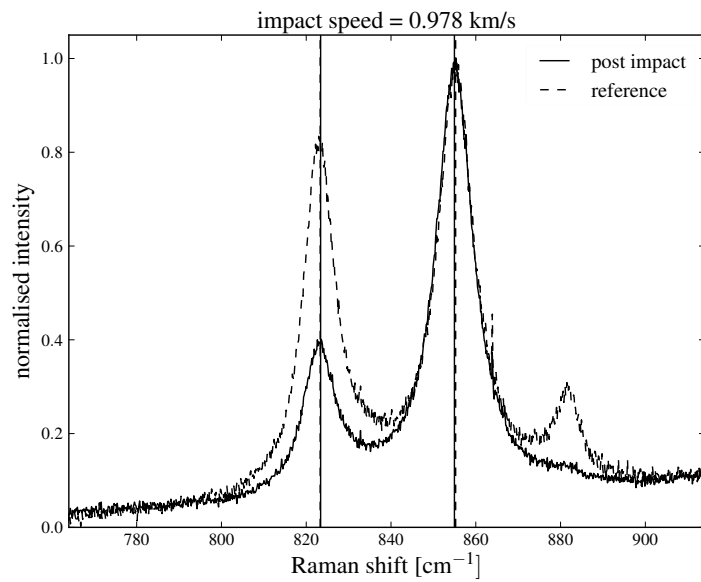


Figure B.46: Raman spectra of olivine before and after the shot with $\Delta P_1 = 0.10$ and $\Delta P_2 = 0.29$.

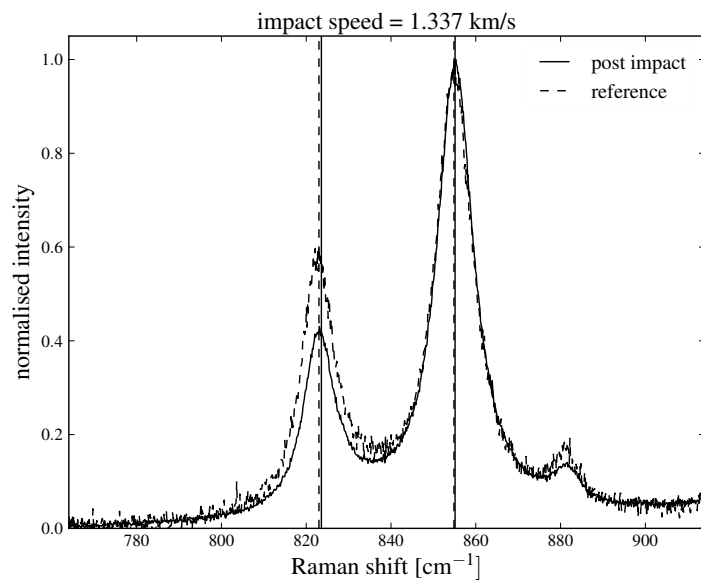


Figure B.47: Raman spectra of olivine before and after the shot with $\Delta P_1 = 0.57$ and $\Delta P_2 = 0.26$.

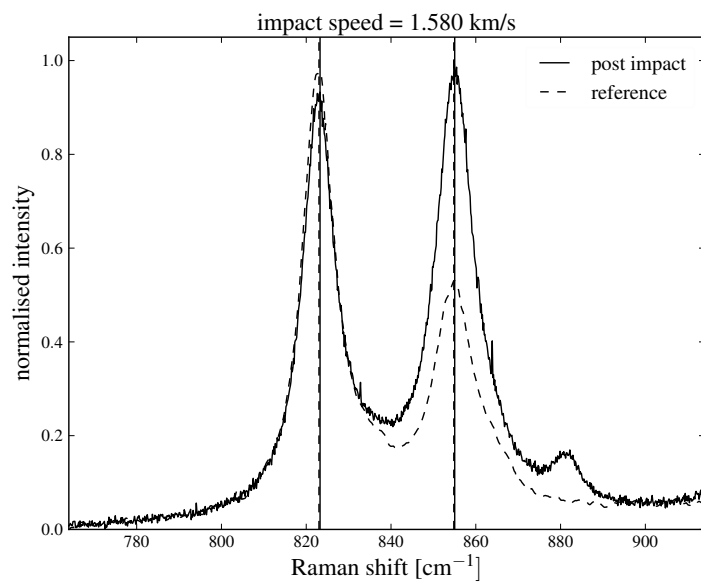


Figure B.48: Raman spectra of olivine before and after the shot with $\Delta P_1 = 0.25$ and $\Delta P_2 = 0.21$.

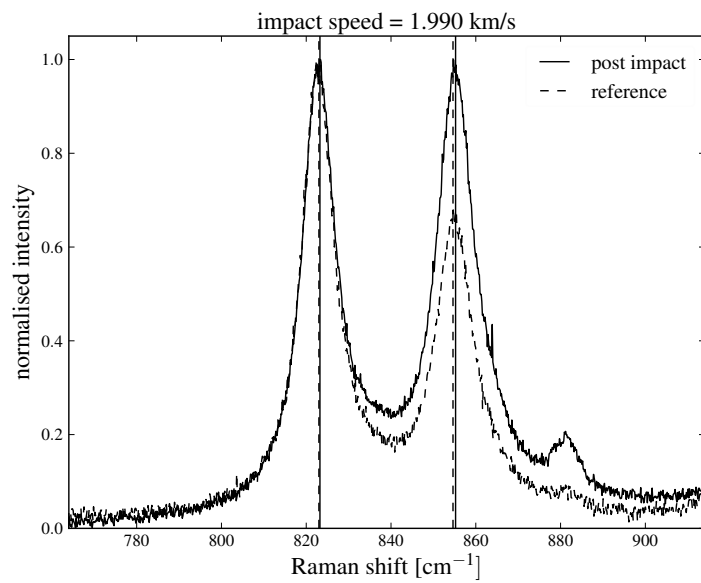


Figure B.49: Raman spectra of olivine before and after the shot with $\Delta P_1 = 0.24$ and $\Delta P_2 = 0.61$.

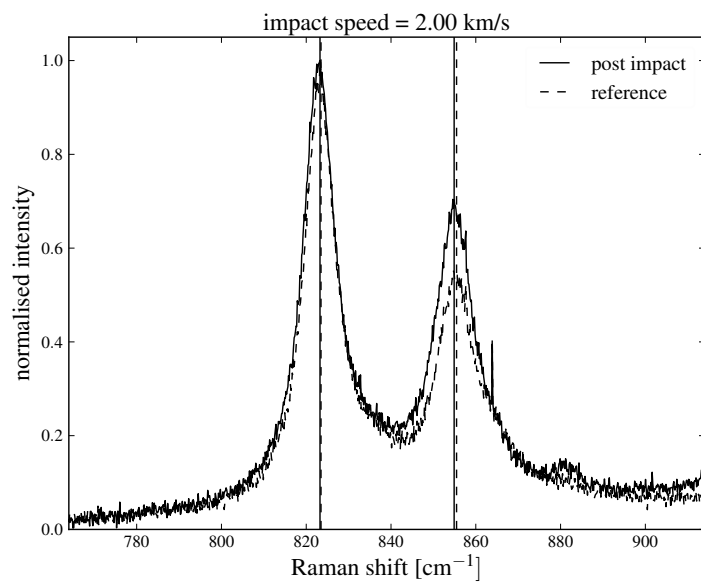


Figure B.50: Raman spectra of olivine before and after the shot with $\Delta P_1 = 0.23$ and $\Delta P_2 = 0.57$.

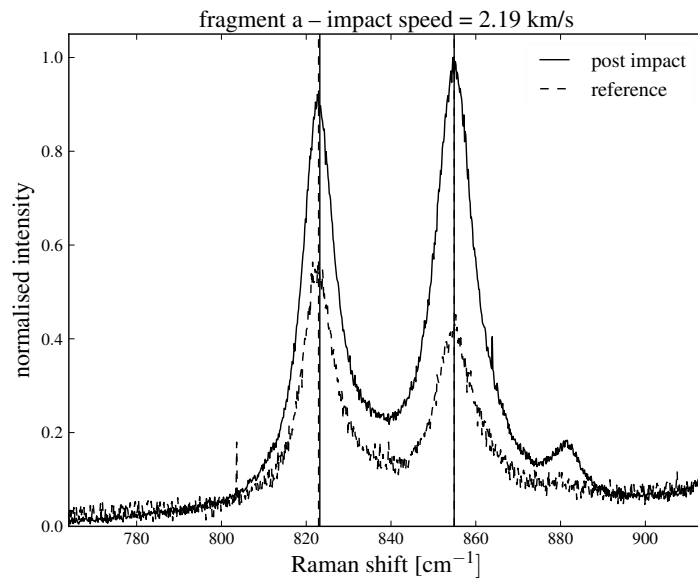


Figure B.51: Raman spectra of olivine before and after the shot with $\Delta P_1 = 0.28$ and $\Delta P_2 = 0.01$.

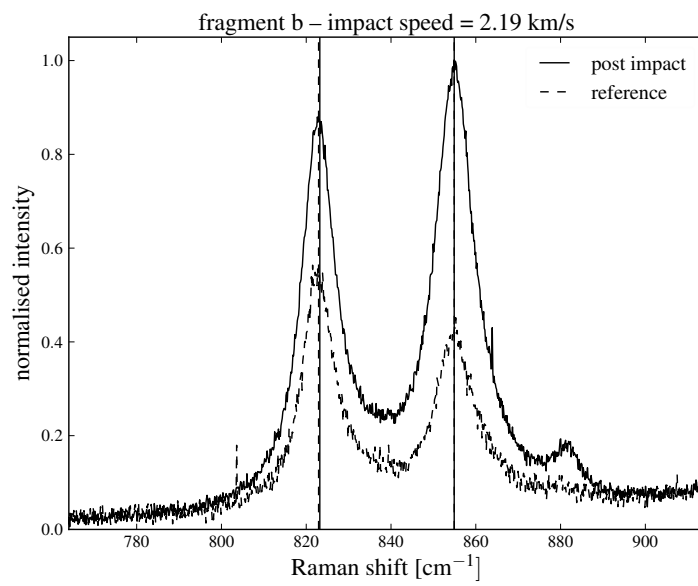


Figure B.52: Raman spectra of olivine before and after the shot with $\Delta P_1 = 0.28$ and $\Delta P_2 = 0$.

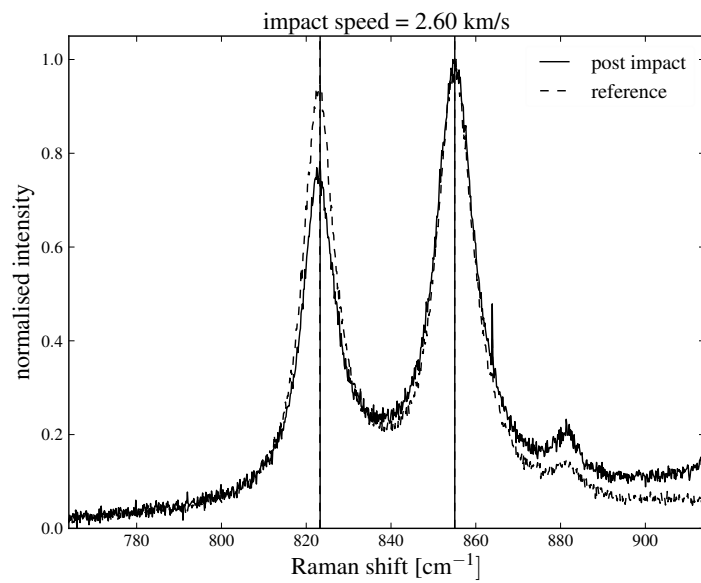


Figure B.53: Raman spectra of olivine before and after the shot with $\Delta P_1 = 0.06$ and $\Delta P_2 = 0.01$.

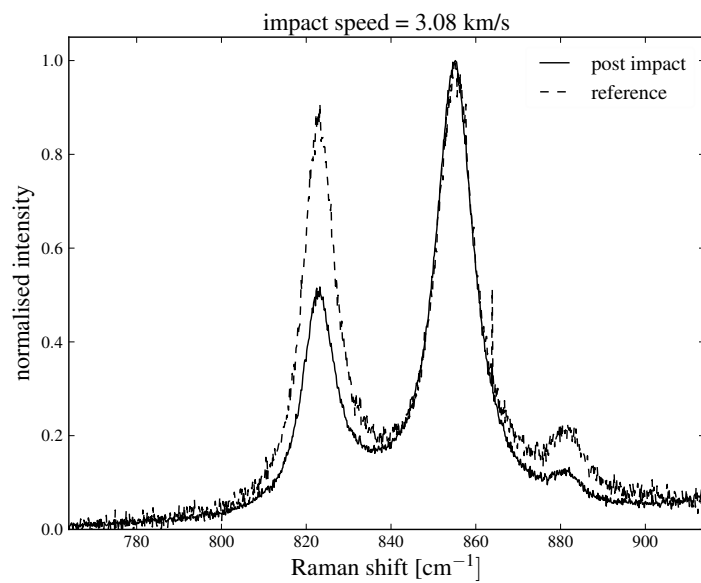


Figure B.54: Raman spectra of olivine before and after the shot with $\Delta P_1 = 0.25$ and $\Delta P_2 = 0.27$.

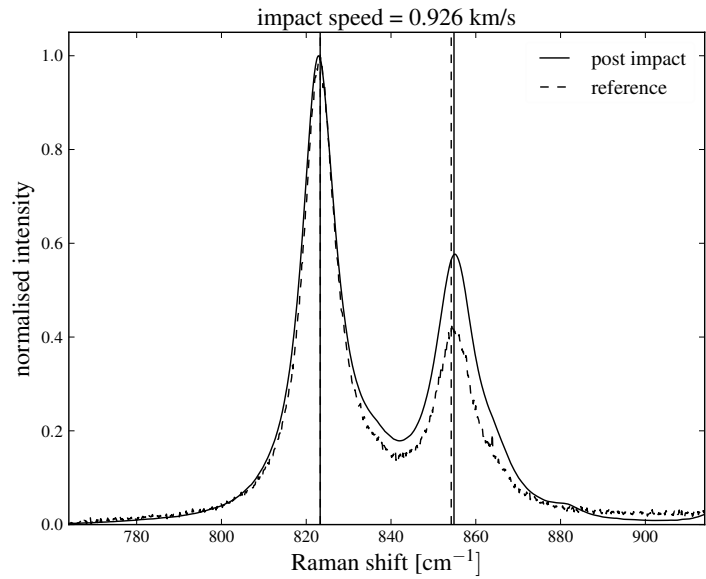
B.0.10 Raman spectra: Run#3

Figure B.55: Raman spectra of olivine before and after the shot with $\Delta P_1 = 0.02$ and $\Delta P_2 = 0.65$.

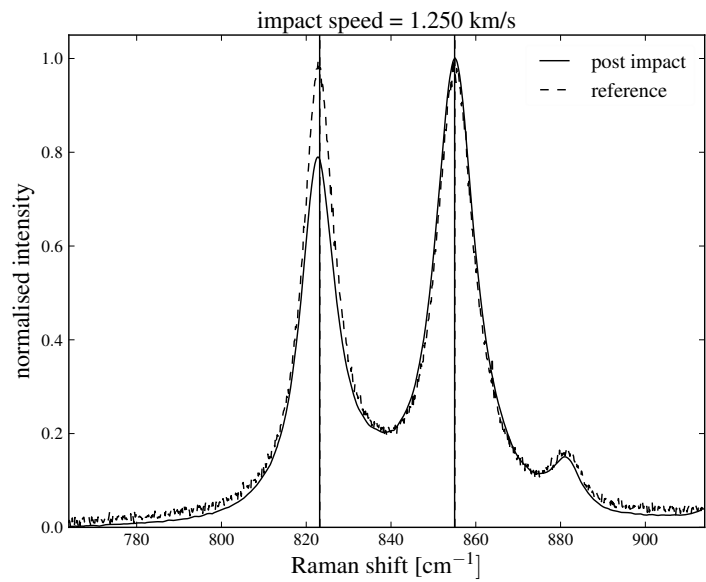


Figure B.56: Raman spectra of olivine before and after the shot with $\Delta P_1 = 0.03$ and $\Delta P_2 = 0.05$.

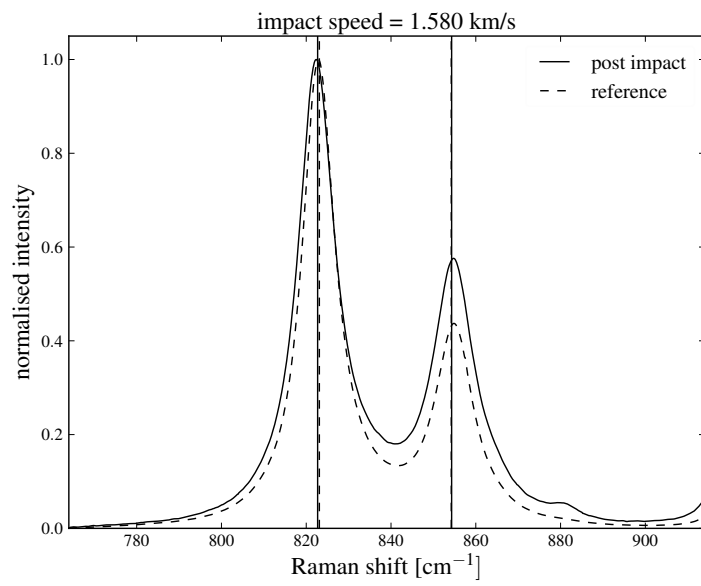


Figure B.57: Raman spectra of olivine before and after the shot with $\Delta P_1 = 0.40$ and $\Delta P_2 = 0.08$.

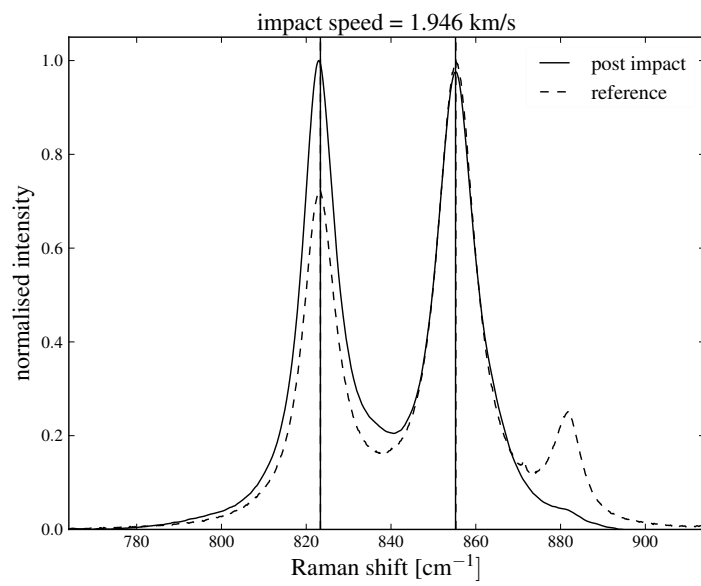


Figure B.58: Raman spectra of olivine before and after the shot with $\Delta P_1 = 0$ and $\Delta P_2 = 0.06$.

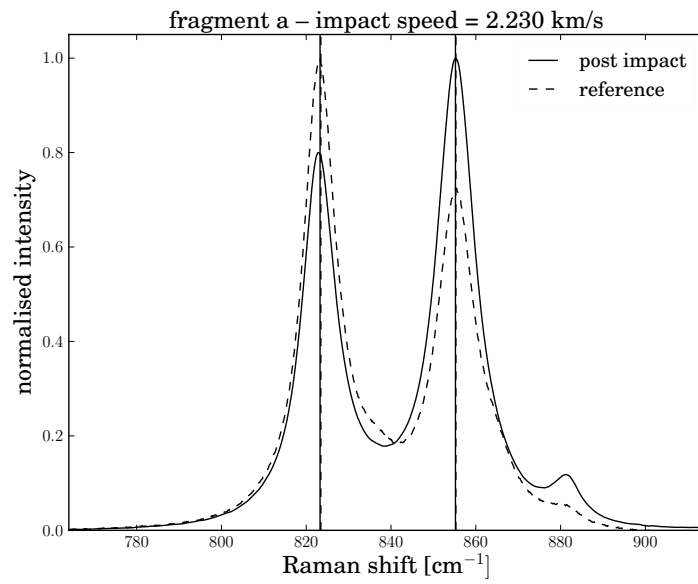


Figure B.59: Raman spectra of olivine before and after the shot with $\Delta P_1 = 0.45$ and $\Delta P_2 = 0.47$.

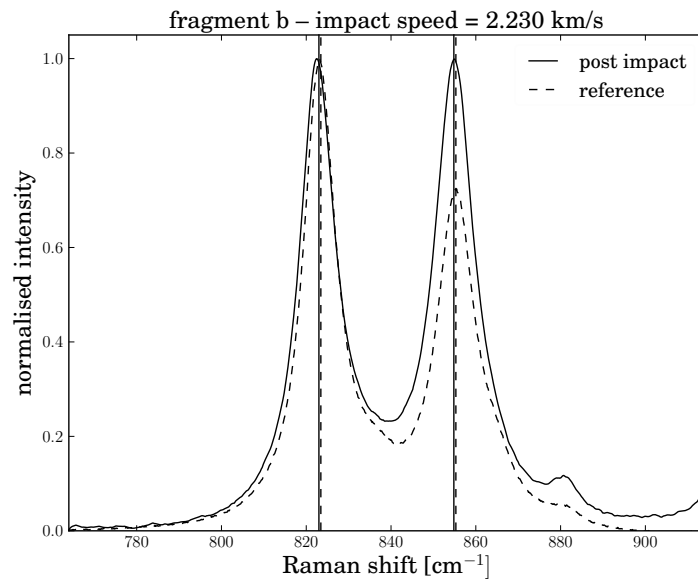


Figure B.60: Raman spectra of olivine before and after the shot with $\Delta P_1 = 0.18$ and $\Delta P_2 = 0.09$.

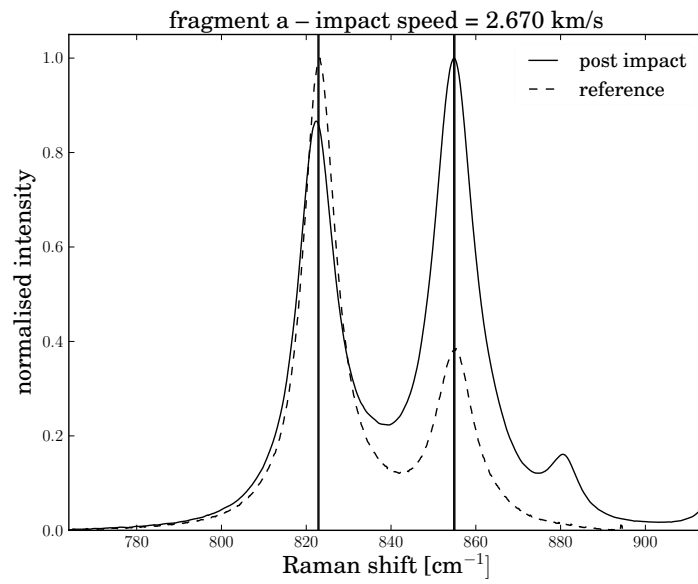


Figure B.61: Raman spectra of olivine before and after the shot with $\Delta P_1 = 0.28$ and $\Delta P_2 = 0.80$.

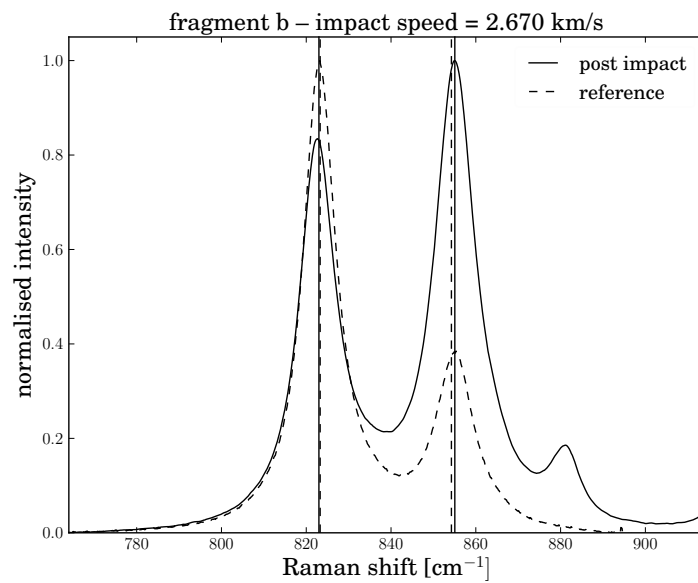


Figure B.62: Raman spectra of olivine before and after the shot with $\Delta P_1 = 0.50$ and $\Delta P_2 = 0.54$.

C

Appendix

C.0.11 List of Publications

Journal

1. **Ch. Avdellidou**, M.C. Price, M. Delbo, M.J. Cole, W.H. Smith
Survival of the impactor during hypervelocity collisions II: An analogue for high porosity targets. MNRAS, 2016 (in preparation)
2. **Ch. Avdellidou**, M.C. Price, M. Delbo, P. Ioannidis, M.J. Cole
Survival of the impactor during hypervelocity collisions I: An analogue for low porosity targets. MNRAS, 2016
3. P. Ioannidis, J.H.M.M. Schmitt, **Ch. Avdellidou**, C. von Essen, E. Agol
Kepler-210: An active star with at least two planets, A&A, 2014, 564.

Proceedings

1. **Ch. Avdellidou**, M.C. Price, M. Delbo, M. J. Cole
The effect of target's porosity on the fate of the impactor in hypervelocity collisions, LPSC 2016, The Woodlands, Houston, TX, US
2. **Ch. Avdellidou**, M.C. Price, T.M. Kinnear
Dynamical simulations of the impact rate, velocities and angles of Mars-crossing asteroids, Asteroids Comets and Meteors (ACM) 2014 Conference, Helsinki, Finland
3. P. Ioannidis, J.H.M.M. Schmitt, **Ch. Avdellidou**, C. von Essen, E. Agol
KOI-676: An active star with two transiting planets and a third possible candidate detected with TTV, The 11th Hellenic Astronomical Conference, Athens, Greece

Survival of the impactor during hypervelocity collisions – I. An analogue for low porosity targets

C. Avdellidou,¹★ M. C. Price,¹ M. Delbo,²★ P. Ioannidis³ and M. J. Cole¹

¹Centre for Astrophysics and Planetary Science, School of Physical Sciences, University of Kent, Canterbury CT2 7NH, UK

²Laboratoire Lagrange, Université Côte d’Azur, Observatoire de la Côte d’Azur, CNRS, Blvd de l’Observatoire, CS 34229, F-06304 Nice cedex 4, France

³Hamburger Sternwarte, Universität Hamburg, Gojenbergsweg 112, D-21029 Hamburg, Germany

Accepted 2015 December 2. Received 2015 November 30; in original form 2015 August 12

ABSTRACT

Recent observations of asteroidal surfaces indicate the presence of materials that do not match the bulk lithology of the body. A possible explanation for the presence of these exogenous materials is that they are products of interasteroid impacts in the Main Belt, and thus interest has increased in understanding the fate of the projectile during hypervelocity impacts. In order to gain insight into the fate of impactor, we have carried out a laboratory programme, covering the velocity range of 0.38–3.50 km s^{−1}, devoted to measuring the survivability, fragmentation and final state of the impactor. Forsterite olivine and synthetic basalt projectiles were fired on to low porosity (<10 per cent) pure water-ice targets using the University of Kent’s Light Gas Gun (LGG). We developed a novel method to identify impactor fragments which were found in ejecta and implanted into the target. We applied astronomical photometry techniques, using the SOURCE EXTRACTOR software, to automatically measure the dimensions of thousands of fragments. This procedure enabled us to estimate the implanted mass on the target body, which was found to be a few per cent of the initial mass of the impactor. We calculated an order of magnitude difference in the energy density of catastrophic disruption, Q*, between peridot and basalt projectiles. However, we found very similar behaviour of the size frequency distributions for the hypervelocity shots (>1 km s^{−1}). After each shot, we examined the largest peridot fragments with Raman spectroscopy and no melt or alteration in the final state of the projectile was observed.

Key words: techniques: image processing – techniques: photometric – minor planets, asteroids: general.

1 INTRODUCTION

Impacts have shaped the asteroids, and their size frequency distribution (SFD), over 4.5 billion years of Solar system evolution (Bottke et al. 2005) and are responsible for the formation of asteroid families. The appearance and morphology of asteroidal surfaces are also the result of impact processes, which are responsible for the formation of craters and the production of regolith (Horz & Cintala 1997, although it has been recently shown that the regolith can be efficiently produced by thermal fragmentation of surface rocks by Delbo et al. 2014). Over the last four decades, a plethora of laboratory experiments and computer simulations have provided insights into collisional processes that constitute the foundation of our current understanding of large-scale asteroid collisions (Holsapple et al. 2002). The majority of these studies focused on the fate of the target after an impact (e.g. degree of fragmentation, catas-

trophic disruption of different materials, crater sizes etc). They have provided data on the speed and size distributions of the fragments using several target materials, mostly cement mortar, basalt or ice, while the projectiles are mostly iron, copper, pyrex or basalt. Furthermore, efforts have been devoted to the study of the mass and the velocities of the ejecta (Michikami et al. 2007; Housen & Holsapple 2011).

However, the fate of the impactor at impact speeds of a few km s^{−1} is still poorly understood. The investigation of the projectile, and projectile debris, during hypervelocity impacts is crucial to explain the observations of mixed mineralogies on the surface of asteroids. Such phenomena, which have been observed only relatively recently, are the source of the olivine and dark material deposits observed on Vesta (McCord et al. 2012; Reddy et al. 2012) and probably of the ‘Black Boulder’ on (25143) Itokawa (Hirata & Ishiguro 2011). Mixing of asteroid material with different lithology through impacts is also necessary to explain the nature of the Near-Earth asteroid 2008 TC₃, a multilithology body whose formation mechanism is still not completely understood (Jenniskens

*E-mail: ca332@kent.ac.uk (CA); marco.delbo@oca.eu (MD)

et al. 2009; Bischoff et al. 2010). 2008 TC₃ impacted Earth's atmosphere on 2008 October 7 and it is estimated that it exploded approximately 37 km above the Nubian Desert in Sudan. A large number (~600) of small (0.2–379 g) meteorites were recovered from 2008 TC₃, and are collectively called Almahata Sitta. The big surprise was that those meteorites were of various mineralogical types: analysis of 110 meteorites revealed 75 ureilites, 28 enstatite chondrites (both EH and EL), five ordinary chondrites (H, L, LL), one carbonaceous chondrite (CB) and one which is a previously unknown type of chondrite related to R-chondrites. This fact has changed completely our paradigm that one meteorite fall produces meteorites of only one particular type. A recent study by Gayon-Markt et al. (2012) has shown that there is a small probability that foreign material remains on the surface of a body after low-speed collisions. However, their results were based on the assumption that, in order to preserve the impactor, an impact velocity $\leq 0.5 \text{ km s}^{-1}$ is required, which is much smaller than the typical impact velocity (about 5 km s^{-1}) among random asteroids (Bottke et al. 1994; O'Brien & Sykes 2011). The second confirmed case of heterogeneous meteorite is Benesov (Spurný et al. 2014). Surprisingly, one meteorite was H chondrite, one was LL chondrite and one was LL chondrite with embedded achondritic clast. These findings shed new light on some old meteorite finds, such as the Galim meteorite fall (LL+EH), Hajmah (ureilite+L), Gao-Guenie (H+CR), and Markovka (H+L) (Borovička, Spurný & Brown 2015). Therefore, asteroids with mixed mineralogies might be more abundant than previously thought, but their formation mechanism(s) remain mysterious (Horstmann & Bischoff 2014). One possible solution is that the heterogeneous composition of some asteroids was inherited from a time when the asteroid belt was in a different dynamical state, most likely in the very early Solar system.

These findings call for new experiments devoted to ascertaining what is the highest velocity that projectile material can be preserved and/or implanted on to asteroids via impacts. Pioneering experiments by Schultz & Gault (1984, 1990) demonstrated a change in projectile fragmentation and cratering efficiency as a function of impact velocity. Recently, Nagaoka et al. (2014) performed several laboratory experiments using pyrophyllite and basalt projectiles fired on to regolith-like sand and aluminum targets. They found that projectile material survived the impacts, although the degree of fragmentation of the projectile depended on the impact energy (Q) and the strength of the projectile, along with the strength and the porosity of the target. However, considering an average impact speed of $v = 5.3 \text{ km s}^{-1}$ for Main Belt asteroid collisions (Bottke et al. 1994), the collisional speed range that was tested ($< 1 \text{ km s}^{-1}$) in the experiments of Nagaoka et al. (2014) was at the lower end of interasteroid collision velocities. Moreover, Daly & Schultz (2013, 2014, 2015a,b, 2016) used aluminum and basalt projectiles which were fired on to pumice and highly porous water-ice trying to explain the implantation of an impactor's material on to vestan regolith, and the possibility of a similar process on to Ceres' surface. McDermott et al. (in preparation) used copper projectiles impacting porous (~50 per cent) water-ice targets at a wide range of speeds (1.00–7.05 km s^{-1}). Their results show that the projectile can be recovered completely intact at speeds up to 1.50 km s^{-1} , whereas it started to break into smaller fragments at speeds above 1.50 km s^{-1} . Increasing the impact velocity was found to produce an increasing number of projectile fragments of decreasing size. All of these recent investigations try to shed light on to the fate of the impactor. The main question that is addressed is how much of the impactor's material is embedded on/into the target by using different combinations of materials, trying to simulate collisions in the

Main Belt and on the surface of icy bodies. While the experiments of Nagaoka et al. (2014) were limited to speeds $< 1 \text{ km s}^{-1}$, the McDermott et al. (in preparation) study used only porous water-ice and a copper projectile - which is an atypical type of impactor material in the Solar System.

In this work, we advance on the investigation of the fate of the projectile during hypervelocity impacts by firing lithological projectiles, olivine and basalt, on to low-porosity water-ice targets, at a wide range of speeds between 0.38 and 3.50 km s^{-1} , and by using novel methods to detect and measure sizes of impactor fragments down to a size-scale of a few microns.

The structure of the paper is the following: in Section 2, we give a description of the materials that were used and the set-up of the experiments, along with a description of the method we established to detect, measure and analyse the impactors' fragments found both as ejecta and implanted on to/into the target. We derive the projectile fragments' volume, mass and size distribution. In Section 3, we present the results of the experiments and the calculation from hydrocode modelling of the pressures and temperatures at the time of the impact and, additionally, describe the state of the recovered fragments of the projectile. Finally, we discuss our results and give the implications for impacts to induce lithological mixing on asteroids.

2 METHODS

Our methodology consists of six steps which are as follows.

- (i) We start by carrying out a physical characterization of the projectiles pre-shot; namely we measure their sizes, masses and perform Raman spectroscopy. Raman spectroscopy is used to identify possible Raman line shifts due to deformation of the projectile's crystal structure induced by the impact shock.
- (ii) The projectiles are fired on to the ice targets. The formation of impact craters are observed, although due to the ephemeral nature of the target they were not measured. The projectile and target material, along with contaminating residues from the gun, collected by our set up (ejecta collector – see Fig. 1).
- (iii) We collect all the projectile fragments and visually identify the largest of them. The ratio between the mass of the largest fragment to the initial mass of the projectile, gives information about the degree of fragmentation of the latter.
- (iv) The ice from the target and the ejecta collector is melted and the water, plus projectile fragments, plus contaminating gun debris, is filtered.
- (v) The filters are then analysed using a Scanning Electron Microscope (SEM).

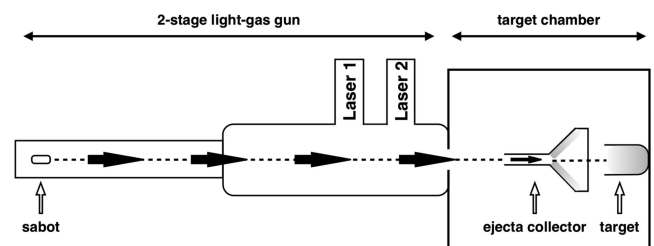


Figure 1. The experimental set-up showing the projectile, which was placed inside a sabot, inside the two-stage LGG, and the configuration of the target chamber. The projectile impacts vertically the target at 0° in respect to its trajectory (dashed line). The ejecta collection funnel was aligned with the flight path of the projectile and the centre of the target. It contained water-ice layers in order to collect the projectile's debris after the impact.

(vi) The final phase consists in analysing the data from the SEM, discriminating projectile fragments from gun detritus and allowing us to build the SFDs of the fragments and quantify the amount of projectile embedded in the target and its level of fragmentation.

In the remainder of this section, we present our projectile and target material choice and we detail each experimental and data analysis method.

2.1 The projectiles

In order to unambiguously separate projectile fragments from those of the targets and gun contamination, we used a high purity, Mg-rich olivine – in the form of a gem quality peridot – and synthetic basalt spheres as projectiles and high-purity water-ice as the target. These materials were also chosen as (a) olivine is one of the most common minerals in the Solar system. Olivine and pyroxene minerals are the primary minerals in stony and stony-iron meteorites, 75 per cent of chondrite meteorites and 50 per cent of pallasites (Petrovic 2001; Gaffey et al. 2002); (b) Mg-rich olivine (fosterite) has been detected in spectra of several cometary tails and is present in the majority of comet Wild 2 samples returned by NASA’s *Stardust Mission* (Zolensky et al. 2006); (c) parallel studies of the spectral features of the dust particles, observed in exo-planetary system β Pictoris (de Vries et al. 2012), confirm similar abundance of Mg-rich olivine in respective areas (large heliocentric distances) to our Solar system; (d) Fe-rich olivine (fayalite) is mostly encountered in asteroid mineralogies (Nakamura et al. 2011) and therefore in the warmer, inner parts, of planetary space (Olofsson et al. 2012). Possible explanations for this distribution of the different types of olivine are: (1) the presence of water on comets which leads to aqueous alteration, as the fayalite may not survive in the presence of water (Olofsson et al. 2012) and, (2) the higher abundance of heavier elements, such as Fe, in the inner Solar system; (e) Basalt is considered to be the main material on the surface of the differentiated asteroids. Differentiation, which leads to a multilayered body with core, mantle and crust and the production of basalt, occurred in the early Solar System. It is found in the basaltic eucrites and diogenites of the HED meteorites (McSween et al. 2011) which are linked with asteroid Vesta (Russell et al. 2012); (f) although initially it was commonly thought that basalt is associated only with the Vestoids (asteroids which share spectroscopic data and are dynamically connected with Vesta) observations have shown that V-type asteroids do also exist in other locations in the Main Belt (Moskovitz et al. 2008).

The peridots, roughly 3 mm in diameter, are high-quality gemstone olivine in brilliant cut, with no visible inclusions or cracks. Additionally their composition was very uniform (measured using Raman and verified by quantitative Energy-dispersive X-ray spectroscopy – EDX) and found to be $\text{Mg}_{82}\text{Fe}_{18}\text{SiO}_4$ using the simplified equations of Foster et al. (2013) with a compositional variance across the surface of 1 per cent.

The basalt projectiles, 2.0–2.4 mm spheres in diameter, were not of a natural basalt rock but synthetic spheres, sourced from ‘Whitehouse Scientific’ with a composition of SiO_2 (43 per cent), Al_2O_3 (14 per cent), CaO (13 per cent), Fe_2O_3 (14 per cent), MgO (8.5 per cent), $\text{Na}_2\text{O}/\text{K}_2\text{O}$ (3.5 per cent) and Others (4 per cent). These projectiles are homogeneous and compositionally identical and thus we maximize the reproducibility of the shots.

The compressive strength for forsterite and basalt projectiles was taken as 80 MPa and 100 MPa, respectively (Petrovic 2001).

2.2 The target

For the purposes of our work, simulating collisions at laboratory scales, it is essential to know the mechanical properties (strengths and micro/macroporosity) of small bodies. Several literature sources give the compressive and tensile strength for a series of meteorites, however the number that has been studied is very limited. Popova et al. (2011) summarizes data from several meteorites, giving the ranges of compressive and tensile strengths to be 20–450 MPa and 2–62 MPa for L ordinary chondrites, and 77–327 MPa and 26–42 MPa for H ordinary chondrites. However, the calculated bulk strengths during entry of similar type meteoroids into the Earth’s atmosphere are much lower than the above-quoted strengths. The average meteorite microporosity for the different types of ordinary and carbonaceous chondrites ranges between 6 and 16 per cent. However, only the very largest asteroids seem to have comparable bulk porosity with their equivalent meteorite microporosity. The average bulk porosity for the S-type asteroids is ~ 30 per cent, while for C-types is around ~ 40 per cent (Britt et al. 2002). As the porosity of a body increases, the strength decreases, which could be an explanation of the big difference between the calculated and observed strength of bolides. This may explain the high altitude where some meteoroids start to disrupt and also the greater abundance of ordinary chondrites compared to carbonaceous chondrites among the meteorite samples.

In order to start our study and investigate a range of porosities and strengths, we used a high purity water-ice target of low porosity, comparable to the microporosities of the examined meteorites. This was also chosen because one of the main aims of this study was to attempt to recover projectile fragments within the target. By using a water-ice target, the target only had to melt and the resulting water filtered through clean, 0.1 μm pore-size filters to recover projectile fragments. Each water-ice target was prepared and frozen (following an identical procedure for each shot) down to -130°C , before being placed into the target chamber, where the temperature at the time of the impact was approximately -50°C . The strengths of the ice (both tensile and compressive, but to different degrees) increase with decreasing temperature. In our case, the compressive and tensile strength of the targets was approximately 35 MPa and 3 MPa, respectively, using data from Petrovic (2003). The porosity of our targets was measured to be < 10 per cent and was determined by making a test sample of ice in an identical way to the targets in a cubical box. The box was slightly underfilled with water so that a void remained at the top of the box after freezing. To measure this volume, a small amount of chilled ethanol (at -30°C) was injected into the box. Since the mass and volume of the box are known, as well as the volume of injected ethanol and the temperature of pure water-ice (and hence density), the porosity can be calculated.

2.3 Experimental set-up

The gun used to perform the experiments was the horizontal two-stage Light Gas Gun (LGG) of the University of Kent (Burchell et al. 1999). It fires a shotgun cartridge in the first stage, which drives a piston to further compress a pressurized light gas in the pump tube. This gas is then suddenly released from its high pressure when a retaining disc of aluminium ruptures. This releases the gas into the second stage, where it accelerates the projectile. The projectile, which is placed in a sabot made of isoplast, is launched and travels down the gun range. Two laser light screens are placed downrange and record the time of flight. The known separation of the two lasers, plus the time taken for the projectile to cross between the

two laser screens, gives the speed (to within ± 0.2 per cent) of the projectile before it enters the chamber and impacts the target. It should be noted that since the publication of Burchell et al. (1999), the Impact Group has developed the ability to fire non-spherical projectiles such as, for example, gem-stones (as used herein) and icy projectiles (Price et al. 2013).

The pressure measured in the target chamber was no less than 50 mbar, due to the continuous sublimation of the ice target during the experiments. The impact angle was always 0° . Here, 0° is defined as impacting parallel to the impactor trajectory, and 90° to the targets ambient plane. According to numerical simulations, which were applied to craters on the Moon's surface, the biggest proportion of the impactor's material remained in the crater for impacts occurring at 0° angles (see Fig. 1). Decreasing amount of projectile material is expected to be embedded in the target with increasing impact speed, as has been demonstrated for the Moon's surface by Bland et al. (2008) and, more recently, by Daly & Schultz (2015a, 2016) for asteroid surfaces. In order to study this effect, we used impact speeds between 0.38 and 3.50 km s^{-1} .

All projectiles were weighed and Raman spectra of the peridot were taken before each shot. These initial spectra were used as a comparison to examine the state of the largest fragment after the impact. Previous impact experiments have shown shifts in Raman spectra of the shocked target – and the magnitude of this shift has potential to be used as a shock ‘barometer’ (Kuebler et al. 2006). However, as the basalt has a glassy matrix it does not give well-defined, distinguishable, peaks in the Raman spectrum and no further spectra of the synthetic basalt projectiles was undertaken.

As one of the aims of this project was to measure the size distribution of the projectile's fragments after impacting at different speeds, we constructed a setup to collect the ejecta (see Fig. 1). A funnel with an internal water-ice layer was developed. The use of a water-ice coating led to a simple recovery technique of the ejecta fragments. However, secondary fragmentation is possible, and unavoidable using any sort of practical collection technique we can employ. In these experiments, the secondary fragmentation is minimal, as the speed of ejecta is only a small fraction of the impact speed (Holsapple et al. 2002; Burchell et al. 2012). Additionally, the ejecta fragment size is smaller than the projectile's size, and therefore less prone to fragmentation due to its smaller size. Finally, we do accept that these fragments have been shocked and weakened during the primary impact process. As the projectile entered the target chamber it flew through the funnel, which completely covered the front of the target, and hit the centre of the target. Ejecta from the target was ejected and caught in the interior surface of the funnel. After each shot, the funnel was removed and the ice was

allowed to melt. In an identical way to the target, the melted ice was filtered and the majority of the projectile fragments were collected. Any ejecta that travelled backwards at small ejection angles (4.7 ± 0.3) as measured from the projectile's trajectory, was able to escape the funnel, but was collected directly from the target chamber floor which had been covered before the shot with sheets of clean aluminium foil.

2.4 Identification of fragments

The first step after each shot was to search for the largest surviving fragment of the impactor. This was done by visually examining the crater in the target, the floor of the target chamber and the ejecta collector. Interestingly, for all the peridot shots except one (shot G260215 where the largest fragment was found in the target) the largest fragment was found on the target chamber's floor, implying that this largest fragment ‘bounced’ backwards along its original flight path after impacting the target. For the spherical basalt projectiles, all the largest fragments were found in the ejecta funnel, except from shot G260515 where the largest fragment were recovered from the crater of the target. For each shot, the mass ($M_{i,f}$) of the largest recovered fragment is measured with a balance with a precision of 10^{-4} grams.

In order to identify the rest of the fragments which could not be visually inspected, we melted the ice and filtered the pure water from the target and the ejecta collection apparatus. These filters contained the projectile fragments mixed with contaminating material from the gun. These were fragments from the burst-disc, sabot, shotgun cartridge and any particulates picked up from the range during repressurization of the target chamber. The majority of this material is C, Fe, Al and Si (see Fig. 2a), but is a dust with a size (a few – 100 s of microns) comparable to the projectile fragments we were interested in. That, currently unavoidable, contamination led us to develop a novel way to discriminate, count and measure the olivine fragments.

The effective area of each filter that contained the particles was a circle with a diameter of 37 mm. Images of the projectile's fragments were obtained by scanning the filters using a Back-Scattered Electron detector (BSE) on an SEM. EDX maps were taken of the same fields in order to distinguish projectile fragments from any contaminating material. We thus recorded information about the elemental composition of the sample. Considering that; (i) the peridot projectiles have a very strong Mg signal and, (ii) there is very little Mg contamination from gun debris, we used the EDX maps of Mg to discriminate the projectile fragments from contaminating gun debris (see Fig. 2b).

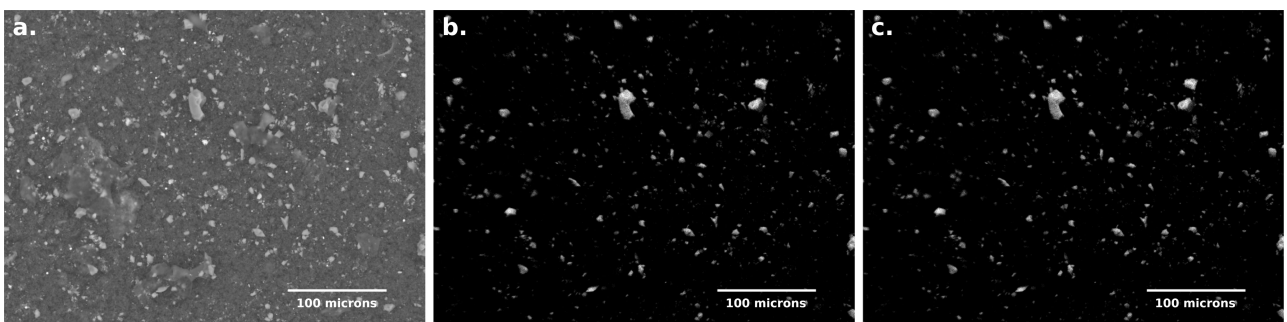


Figure 2. SEM image showing that the fragments of the projectile are mixed with other material from the gun (a). As the projectile is Mg-rich it gives a strong signal in Mg X-ray maps (b). Considering also that there are no other sources of Mg contamination, these maps are used as the main data set for the analysis. SExtractor identifies each fragment and reproduces another image containing only the pixels which contain information according to the given threshold (c).

2.5 Estimation of projectile fragmentation

The energy density has long been used to assess disruption of projectiles (Davis et al. 1979; Schultz & Gault 1990). In this work, following Nagaoka et al. (2014), the energy density at the time of the impact is Q (J/kg), and its form for the impactor is given by

$$Q_{\text{im}} = \frac{1}{2}v^2, \quad (1)$$

where v (m/s) is the impact speed. Traditionally, it is assumed that catastrophic disruption occurs when $M_{1,f}/M_{\text{im}} \leq 0.5$, with the energy threshold of Q^* . Plots of $M_{1,f}/M_{\text{im}}$ versus Q_{im} are used to give an estimate of the projectile fragmentation as a function of the impact velocity (energy).

2.6 Determination of the SFDs of the ejecta projectile fragments

Another quantity that gives crucial information about the fragmentation of the projectile is the SFD of the fragments: for instance, steep cumulative SFDs are indicative of projectiles being pulverized by the impact, whereas shallow cumulative SFDs indicate that large fragments coexist with small ones. Moreover, the size at which the differential SFD has peaks (or a peak) indicate the typical dimension of the fragments. These peaks are also called fragmentation modes.

SFD calculations were made by measuring the sizes of the impactor fragments stopped by, and accumulated on, the ejecta collector. Once the ejecta collector ice was melted and the fragments were collected on polytetrafluoroethylene (PTFE) filters (pore size 0.1 μm), we acquired two maps per filter, consisting of 50 SEM and 50 EDX frames, the latter required 30 min acquisition time per frame. Each frame contained hundreds of fragments (see Fig. 2b) and was taken with a magnification of $\times 300$, giving a pixel scale of 0.4 $\mu\text{m pixel}^{-1}$, which enabled us to detect even very small fragments. Manually counting the fragments and measuring their dimensions is extremely time consuming and prone to observer bias. To tackle this, we applied an astronomical photometry technique to each image using the SOURCE EXTRACTOR ('SETRACTOR') open source software for astronomical photometry (Bertin & Arnouts 1996). SETRACTOR is a program specifically written to automatically identify and measure extended light sources, such as galaxies, from astronomical images. To prepare the SEM-EDX images to be suitable for use by SETRACTOR, we converted the raw data to 16-bit Flexible Image Transport System (FITS) files, making sure that there was no loss of information through the transformation. Unlike most galaxies, which are well-defined elliptical sources, mineral fragments are irregular in shape. Therefore, to measure the total X-ray emission from a fragment, we used the ISO photometry setting within SETRACTOR, which is able to identify the shape irregularity of each fragment.

As the background noise from the EDX images was very close to zero counts, we were able to set a very low detection threshold in units of the background's standard deviation. By selecting pixels with counts at least three times above the mean background noise, we were able to identify the vast majority of the fragments per field. An additional threshold for the minimum detected area was defined in order to increase the detection reliability. SETRACTOR measures the semimajor and semiminor axes allowing each object to be described as an ellipse. According to the threshold, which constrains the size of the minimum area identified as a fragment, SETRACTOR

reproduces another image containing only the identified fragments, as shown in Fig. 2, not measuring anything smaller. By examining the new images, we verified that there was no false detections due to background noise.

If the field is very crowded with fragments, there is the possibility of blending the X-ray emission of several fragments. SETRACTOR comes with a sophisticated deblending algorithm which flags the initially blended fragments. SETRACTOR has the ability to discern shapes even in highly dense fields, giving good statistics by automatically counting thousands of fragments. SETRACTOR also has an edge detection algorithm and ignores fragments that lay on the edge of an image. However in order to avoid false detections due to noise, we set SETRACTOR to identify minimum fragment areas of 0.64 μm^2 .

2.7 Estimation of projectile material in the target

We used the same approach described in Section 2.6, to analyse the filters of the target melt water. These filters collected projectile material once the target ice was melted and filtered away. While mapping the target filters, in contrast with the mapping of the ejecta filters, we used low magnification ($\times 50$) in the SEM. This is because we noticed some spatial variability in the number of fragments on the filter and we choose to map the entire surface of the filter to detect all possible impactor fragments. The chosen resolution enabled us to scan a whole filter in approximately 24 h with pixel scales between 4.4 and 4.9 $\mu\text{m pixel}^{-1}$ and thus create a mosaic of the whole filter area. This means that if the fragments that remained in the target follow a similar SFD with the ejecta fragments, then we should expect to have an amount of fragments smaller than a pixel. The significant factor to consider in choosing a detection threshold in SETRACTOR is the background noise of the images, which is due to the Bremsstrahlung radiation as the electron beam decelerates within the sample. The level of this background noise is different for each element. Ideally, if there was no Bremsstrahlung background we could use an extremely low threshold for the minimum detected fragment area as every pixel with value greater than 0 corresponds to a real Mg signal. That way we could measure fragments with sizes as small as the pixel scale. However this is not possible and, in order to overcome the problem, we performed the analysis of the maps using SETRACTOR choosing several different thresholds for the minimum detected area.

After having extracted the 2D area of each fragment, as projected on the X-ray detector, an extra step was performed in order to estimate a z -length that corresponds to the fragment's height. As there was not a preferable position of the fragments we were therefore able to adopt simple estimations of the z -axis which was assumed to follow the same distribution of x - and y -axes. Several studies so far, when an estimation of a volume was demanded, use simple formulae to estimate the z -axis dimension; such as a simple average of the x - and y -dimensions.

Considering that the produced fragments are cubic-shaped, we estimate in Table 2 the total mass of the projectile by equation (2):

$$M_p = \sum_{i=0}^N x_i \times y_i \times \frac{(x_i + y_i)}{2} \times \rho, \quad (2)$$

where x_i and y_i are the big and small axis of each fragment, respectively, and $\rho = 3.217 \text{ g cm}^{-3}$, the density of the peridot.

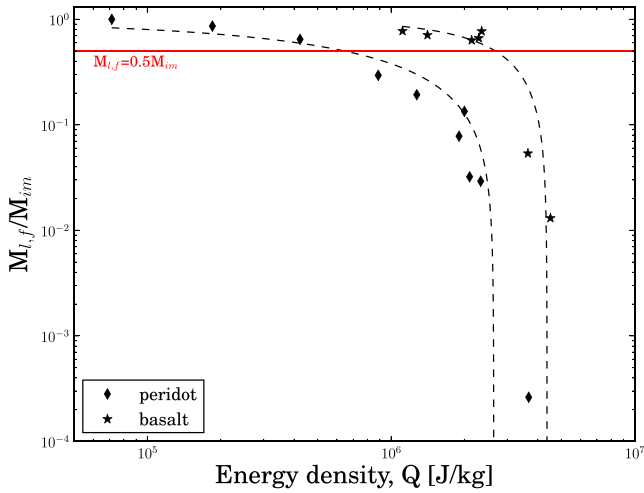


Figure 3. Mass ratio of the largest surviving fragment of the impactor versus the energy density, Q_{im} , for speed ranges $0.38\text{--}2.71\text{ km s}^{-1}$ and $1.49\text{--}3.03\text{ km s}^{-1}$ for olivine and basalt, respectively. The dashed lines correspond to the best-fitting curves using equation (3).

3 RESULTS

3.1 State of the largest projectile surviving fragments

In Fig. 3, we present the mass of the largest fragment we retrieved as a fraction of the initial impactor’s mass, in relation to the energy density Q_{im} . In order to calculate the values of the energy density at the catastrophic disruption threshold, Q_{im}^* , we fit the parameters of equation (3) to the data:

$$\frac{M_{i,f}}{M_{im}} = 1 - A Q_{im}^c. \quad (3)$$

We found that $c_p = 0.49$, $A_p = 6.80 \times 10^{-4}$ for peridot and $c_b = 1.50$, $A_b = 1.42 \times 10^{-10}$ for basalt fragments. The derived values of the catastrophic disruption threshold, Q_{im}^* , were estimated at $7.07 \times 10^5\text{ J Kg}^{-1}$ and $2.31 \times 10^6\text{ J Kg}^{-1}$ for peridot and basalt, respectively.

Raman spectra of the recovered fragments, using a near-IR laser at 785 nm , were obtained to ascertain whether the impact shock caused a shift in the main olivine lines, referred to as P_1 and P_2 . The P_1 and P_2 lines are at $822.64\text{--}824.20\text{ cm}^{-1}$ and $854.15\text{--}855.63\text{ cm}^{-1}$, respectively, at the reference spectra of the projectiles which were measured before each shot (Hibbert et al. 2014). By comparing the spectra we collected before, and after, each shot we noticed a small shift of the two prominent olivine lines which slightly increased with increasing collisional speed, as shown in Fig. 4. The greatest shift measured was 1.49 and 1.08 cm^{-1} for the P_1 and P_2 , respectively, which we interpret as not significant since the accuracy of the measurement is approximately 1 cm^{-1} .

Another interesting application of Raman spectra would be the identification of any change in the separation (ω) of the two characteristic peaks of forsterite which, together with elementary quantification of Mg and Fe, could show possible shock induced change to the crystallization and/or the elemental composition of the olivine (Kuebler et al. 2006; Foster et al. 2013). These two prominent peaks are the result of the fundamental vibration of the chemical bonds (here of Si-O bonds). Peak positions and shifts are generally used to calculate the ratio of Mg/(Mg+Fe) in olivine. The positions of the P_1 and P_2 are strongly related to Fe and Mg compositions of the olivine. For example according to Kuebler et al. (2006), the separation of the P_1 can be up to 10 cm^{-1} from fayalite to forsterite

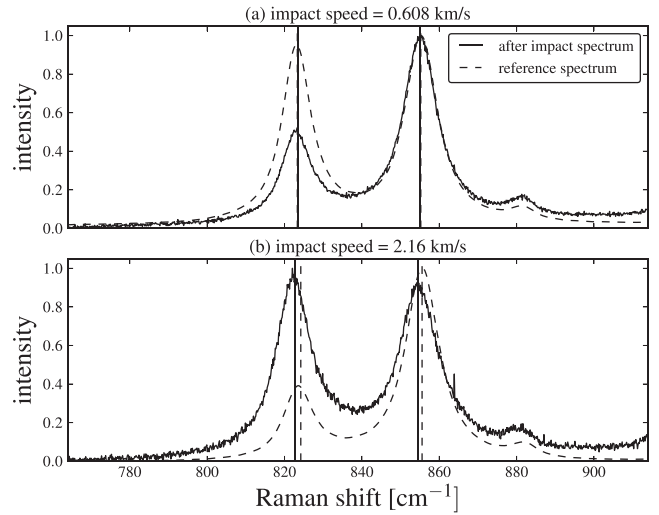


Figure 4. At 0.92 km s^{-1} , none of the shifts exceed the precision of the instrument, whilst for the 2.16 km s^{-1} shot a shift in P_1 and P_2 olivine lines was observed to be 1.49 and 1.08 cm^{-1} , respectively.

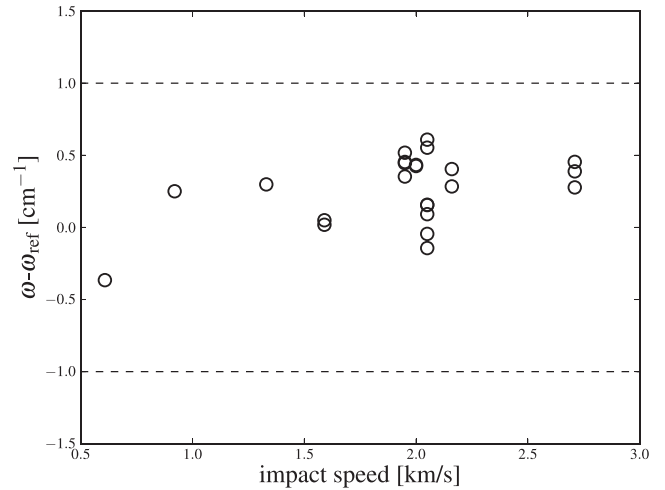


Figure 5. The change in separation, ω , of the P_1 and P_2 olivine lines was calculated for all the big surviving fragments in the range of impact speeds $0.608\text{--}2.71\text{ km s}^{-1}$.

while the separation of the P_2 can be up to 20 cm^{-1} . Up to our maximum collision speed, no change in ω was detected above the spectral resolution of the spectrometer ($\sim 1\text{ cm}^{-1}$) (Fig. 5).

3.2 Impact strength

In order to investigate the peak pressures and temperatures experienced by the projectile during impact, a complementary program of hydrocode modelling was undertaken.

Simulations were performed with the AUTODYN hydrocode (Hayhurst & Clegg 1997). A simple Lagrangian, 2D half-space model was set up, using 20 cells across the projectile’s radius. The total number of cells in the model was approximately 500 000. Material models for ice were taken from Fendyke, Price & Burchell (2013) using a five-phase equation-of-state (EoS) from Senft & Stewart (2011). Strength and EoS data were taken from Ranjith et al. (2012) and Marsh (1980), respectively. Gauges (or tracers) were placed along the axis of the projectile so that pressure and temperature

Table 1. Peak pressure, P_{\max} , peak temperature, T_{\max} , and temperature at peak pressure, T_P , are shown for the range of shots at the time of the impact. $M_{l,f}/M_{\text{im}}$ represents the proportion of the largest fragment of the impactor of its initial mass. For the shots G031214 and G121214, we were not able to identify the largest fragment. For the shots G260215 and G260515, the largest fragments were recovered from the bottom of the craters.

Peridot Shot no.	Speed (km s ⁻¹)	P_{\max} (GPa)	T_{\max} (K)	T_P (K)	$M_{l,f}/M_{\text{im}}$ (%)	Basalt Shot no.	Speed (km s ⁻¹)	P_{\max} (GPa)	T_{\max} (K)	T_P (K)	$M_{l,f}/M_{\text{im}}$ (%)
S141114	0.38	0.54	301	293	100	G010415	1.49	0.80	360	307	77.42
S180315	0.60	1.21	298	293	86.25	G260515	1.68	1.02	401	302	70.93
S211114	0.92	1.64	297	294	65.50	G240415	2.07	1.29	433	303	63.20
G060315	1.33	2.84	302	295	29.46	G050615	2.14	1.32	436	303	66.32
G260215	1.60	3.75	312	296	19.30	G260515	2.17	1.33	440	303	77
G230115	1.95	4.83	330	297	7.80	G070515	2.70	2.97	463	308	5.36
G250315	2.00	4.94	331	297	13.42	G270415	3.03	4.58	522	317	1.30
G261114	2.05	5.06	342	297	3.21						
G130315	2.16	5.59	335	298	2.92						
G180215	2.71	7.13	397	299	0.02						
G031214	2.97	8.04	407	305	–						
G121214	3.50	10.2	513	353	–						

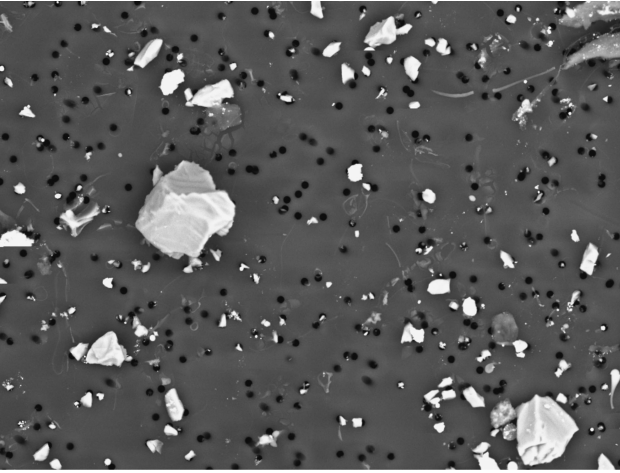


Figure 6. SEM image showing that a significant amount of olivine fragments smaller than $0.1 \mu\text{m}$, which is the pore size (black circles), remained on the filter.

could be determined during the impact. In Table 1, we present the peak pressures, P_{\max} , the temperatures at the time of the peak pressures, T_P , was experienced and the maximum temperature, T_{\max} , $1 \mu\text{m}$ below the front surface of the projectile. Note, that for the lowest speed shot (0.38 km s^{-1}) the peak pressure as modelled does not exceed the yield strength of olivine (1.5 GPa). This agrees with the observed state of the recovered projectile, that retained 100 per cent of its initial mass and showed no signs of damage.

3.3 SFDs of the ejecta projectile fragments

Following the procedures described in Sections 2.4 and 2.6, we measured the fragment SFDs for all our shots. A noticeable number of fragments smaller than $0.1 \mu\text{m}$ remained on the filter lying between the holes (see Fig. 6), but as the resolution of the SEM-EDX images was $0.4 \mu\text{m}$ per pixel, we were not able to measure fragments smaller than the resolution using our automated image analysis routines. Therefore, $\sim 0.4 \mu\text{m}$ is, effectively, the limiting spatial resolution of our SEM.

The SFDs of the size of the fragments appear to have a power-law tail, as shown in Fig. 7. There is a shift of approximately $3 \mu\text{m}$ of the principal mode of the distribution from 0.608 to 1.33 km s^{-1} shots

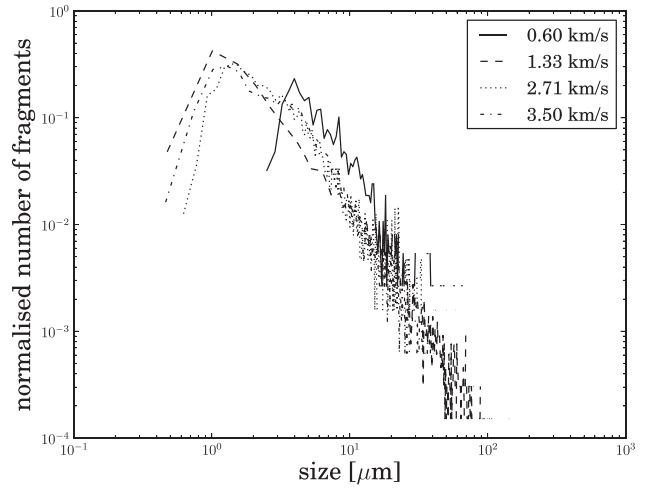


Figure 7. SFDs of indicative shots, showing no significant change in modes.

but beyond this speed the mode remains constant at around $1.5 \mu\text{m}$. Considering the size of the filters ($0.1 \mu\text{m}$) and the detection threshold of the EDX maps ($0.4 \mu\text{m}$), the turnover of the curves around $2 \mu\text{m}$ is real, and not an artefact of the detection process. It would be expected that as the impact speed increases the number of smaller fragments would increase. However, as can be seen from Figs 7 and 8, although there are differences of even an order of magnitude in the number of fragments, there is no clear trend in the fragmentation behaviour with increasing impact speed. Similarly, the slopes of the cumulative distributions in Fig. 8 also show no clear trend with increasing speed, which seems to be counter-intuitive. We found that the slopes of all SFDs lie in a range between -1.04 and -1.68 . Here, we have to point out that due to a possible secondary fragmentation that occurred on the ejecta collecting system the observed slopes of the SFDs would be steeper. However, as described in Section 2.3, we expect this phenomenon to be limited.

3.4 Implantation of material in the target

In Table 2, we present the overall masses of the fragments which were found in the target filters as a fraction of the initial projectile mass. For the identification of the fragments, we used two different photometric thresholds for the minimum detected area (4 and 6 pixel

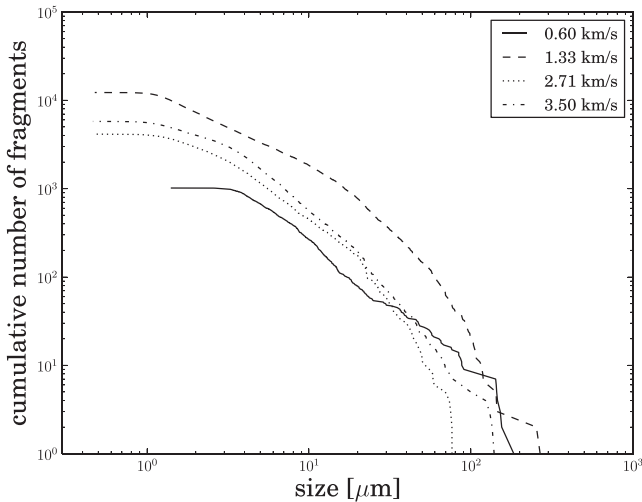


Figure 8. Cumulative SFD of the same shots shown in Fig. 7, demonstrating that the fragmentation of peridot does not change by increasing collision speed.

Table 2. The mass fraction of the olivine projectile that was found embedded in the targets using two different detection thresholds, of 4 and 6 pixels, respectively, for the minimum detected area.

Shot	Speed (km s ⁻¹)	Area 4 (%)	Area 6 (%)
S180315	0.60	0.2	0.18
S211114	0.92	0.43	0.37
G060315	1.33	1.4	1.17
G260215	1.60	24	22.4
G230115	1.95	8.29	0.58
G250315	2.00	1.71	0.55
G220515	2.04	1.15	0.48
G130315	2.16	3.5	2.6
G180215	2.71	0.17	0.12

area, respectively). Note that for the shot G260215, the largest fragment was found in the crater with a mass of 31 per cent of the initial mass, increasing the total amount implanted in the target from 53–55 per cent.

4 DISCUSSION

At impact speeds up to 3 km s⁻¹, which occur at the lower part of the velocity distribution in the Main Belt (Bottke et al. 1994; O’Brien & Sykes 2011), we observe no detectable melting of the projectile, as determined by visual observation and Raman spectroscopy (melting of olivine results in a degradation of the Raman spectra due to loss of olivine crystal structure). This observation is backed up by hydrocode modelling which demonstrates that the temperatures at maximum pressures (Table 1) experienced by the olivine and basaltic impactors do not reach their melting point, which is 2100 K and 2500 K at pressures of 10 GPa and 4.6 GPa, respectively. This is an important observation when we consider the mineralogical signature of implanted impactors on asteroids i.e. the projectile’s mineralogy (including crystallinity) will be preserved. By examining the Raman spectra of the survived fragments, and calculating the difference $\omega - \omega_{\text{ref}}$, we found that there is no alteration in the Fe abundance of the fragments as all the calculated differences lie inside the resolution limit of the instrument. However, it would be extremely important to identify the impact speed at

which the olivine starts to melt and the introduced shock is enough to change the molecular geometry in the crystal.

The size distribution of the projectile fragments has a definite turnover at a point well above the detection limit of our method. The positions of the modes and slopes of the size distributions are velocity invariant, although there is a difference between the modes at 0.608 and 1.331 km s⁻¹. This is counter to the observations made for ductile (i.e. metal) projectiles by Hernandez, Murr & Anchondo (2006), Kenkmann et al. (2013) and McDermott et al. (in preparation). This suggests that the fracturing mechanism between lithological projectiles (non-ductile) and metallic (ductile) projectiles is different.

We determine different Q^* values, with an order of magnitude difference, for forsterite olivine and synthetic basalt on to icy surfaces at speeds relevant to impacts in the asteroid belt. Comparing the results of both projectiles, it is obvious that the same portion of mass of the basaltic projectile survives at higher collisional speed than the peridot. Additionally, the data demonstrate that significant fractions of projectile material survives and escapes as ejecta. The main result is that at collision speeds close to 3 km s⁻¹ there is material implanted in the target even if its mass is only a small proportion of the initial mass of the projectile. The data points to that the portion of the mass implanted in the target is related to the type of materials which collide, and the porosity of the target. As the porosity of the same material increases, the compressive strength decreases and this, in turn, affects the result of the impact. Higher porosity leads to the formation of narrower and deeper craters because the shock-wave cannot propagate as easily as in the non-porous materials, and the energy is concentrated in a limited cross-section area. Moreover, the ejecta velocities are reduced as the porosity of the target increases, even up to two orders of magnitude, and therefore there are indications that larger amount of material will be eventually implanted in the target from the re-accumulation of the ejecta (containing projectile debris). There are already several examples from laboratory experiments on highly porous targets, trying, among others, to simulate collisions on 253 Mathilde with porosity ~ 50 per cent (Housen, Holsapple & Voss 1999), that show very limited or even no ejecta material is found around the crater. The implications of this, along with our current results and ongoing experiments, can contribute to the explanation of the formation of multilithology small bodies, considering also ejecta velocities smaller than the escape velocities of these bodies. A new set of ongoing experiments may prove this hypothesis. In these experiments peridot and basaltic projectiles, of the same sizes and strengths as in the described experiments, are being fired at water-ice targets with porosity between 35 and 40 per cent which is similar to the average bulk porosity of C-type asteroids.

Finally, It should be noted that the results presented here are for near normal impacts only, and that the observations may differ as a function of impact angle. Schultz, Ernst & Anderson (2005) and Schultz et al. (2007), who were investigating the Deep Impact impact, demonstrated that the cratering mechanism differs between normal and oblique impacts. In addition, recent work from Daly & Schultz (2016) investigated the mass implanted in a target at different impact angles and showed that the embedded projectile material is reduced with increasing impact angle.

5 CONCLUSIONS

Our experiments have demonstrated a difference in the fragmentation of the forsterite olivine and synthetic basalt projectiles, that were fired on to low porosity water-ice targets, giving catastrophic

disruption energy densities of $Q_p^* = 7.07 \times 10^5 \text{ J Kg}^{-1}$ and $Q_b^* = 2.31 \times 10^6 \text{ J Kg}^{-1}$, respectively. We note that there is no change in modes and slopes of the SFD of the olivine beyond the impact speed of 1.331 km s^{-1} . In addition, we did not record any melt or vaporization of the projectile for the range of impact speeds $0.38\text{--}3.50 \text{ km s}^{-1}$. Therefore we suggest that, for such velocities that represent the lower end of the distribution of impact velocities in the main asteroid belt (about 5 km s^{-1}), there should be significant survival of the impactors.

In this work, we also present a novel way to measure thousands of fragments autonomously and accurately, in order to study the fragmentation properties of the projectile during a hypervelocity impact with unprecedented statistical significance. Applying astronomical photometry techniques enabled us to measure fragments down to sizes of a few microns, and adequately define the 2D area (and thus inferred volume) of each fragment. This analysis method is essential to estimate SFD and masses of very small fragments, as the LGG cannot fire bigger projectiles, which will produce larger fragments suitable for weighing.

ACKNOWLEDGEMENTS

CA would like to thank the University of Kent for her 50th Anniversary PhD scholarship and Timothy Kinnear and Victor Ali-Lagoa for fruitful discussions. MCP and MJC thank the STFC, UK for funding this work. MD acknowledges support from the French Agence National de la Recherche (ANR) SHOCKS.

REFERENCES

- Bertin E., Arnouts S., 1996, *A&A*, 117, 393
- Bischoff A., Horstmann M., Packer A., Laubenstein M., Haberger S., 2010, *Meteorit. Planet. Sci.*, 45, 1638
- Bland P. A., Artemieva N. A., Collins G. S., Bottke W. F., Bussey D. B. J., Joy K. H., 2008, 39th Lunar and Planetary Science Conference, Asteroids on the Moon: Projectile Survival During Low Velocity Impact. p. 2045
- Borovička J., Spurný P., Brown P., 2015, preprint ([arXiv:1508.01011](https://arxiv.org/abs/1508.01011))
- Bottke W. F., Nolan M. C., Greenberg R., Kolvoord R. A., 1994, *Icarus*, 107, 255
- Bottke W. F., Durda D. D., Nesvorný D., Jedicke R., Morbidelli A., Vokrouhlický D., Levison H. F., 2005, *Icarus*, 179, 63
- Britt D. T., Yeomans D., Housen K., Consolmagno G., 2002, in Bottke W. F., Jr, Cellino A., Paolicchi P., Binzel R. P., Asteroids, III. Univ. Arizona Press, Tuscan, AZ, p. 485
- Burchell M. J., Cole M. J., McDonnell J. A. M., Zarnecki J. C., 1999, *Meas. Sci. Technol.*, 10, 41
- Burchell M. J., Cole M. J., Price M. C., Kearsley A. T., 2012, *Meteorit. Planet. Sci.*, 47, 671
- Daly R. T., Schultz P. H., 2013, 44th Lunar and Planetary Science Conference, Experimental Studies into the Survival and State of the Projectile. p. 2240
- Daly R. T., Schultz P. H., 2014, 45th Lunar and Planetary Science Conference, How much of the Impactor (and Its Water) Ends up in Vesta's Regolith? p. 2070
- Daly R. T., Schultz P. H., 2015a, *Geophys. Res. Lett.*, 42, 7890
- Daly R. T., Schultz P. H., 2015b, 46th Lunar and Planetary Science Conference, New Constraints on the Delivery of Impactors to Icy Bodies: Implications for Ceres. p. 1972
- Daly R. T., Schultz P. H., 2016, *Icarus*, 264, 9
- Davis D. R., Chapman C. R., Greenberg R., Weidenschilling S. J., Harris A. W., 1979, in Gehrels T., ed., *Collisional evolution of asteroids – Populations, rotations, and velocities*. Univ. Arizona, Tuscon, p. 528
- de Vries B. L. et al., 2012, *Nature*, 490, 74
- Delbo M. et al., 2014, *Nature*, 508, 233
- Fendyke S., Price M. C., Burchell M. J., 2013, *Adv. Space Res.*, 52, 705
- Foster N., Wozniakiewicz P., Price M., Kearsley A., Burchell M., 2013, *Geochim. Cosmochim. Acta*, 121, 1
- Gaffey M. J., Cloutis E. A., Kelley M. S., Reed K. L., 2002, in Bottke W. F., Jr, Cellino A., Paolicchi P., Binzel R. P., Asteroids, III. Univ. Arizona Press, Tuscan, AZ, p. 183
- Gayon-Markt J., Delbo M., Morbidelli A., Marchi S., 2012, *MNRAS*, 424, 508
- Hayhurst C. J., Clegg R. A., 1997, *Int. J. Impact Eng.*, 20, 337
- Hernandez V., Murr L., Anchondo I., 2006, *Int. J. Impact Eng.*, 32, 1981
- Hibbert R., Price M. C., Burchell M. J., Cole M. J., 2014, *Eur. Planet. Sci. Congr.*, 9, 295
- Hirata N., Ishiguro M., 2011, 42nd Lunar and Planetary Science Conference, Properties and Possible Origin of Black Boulders on the Asteroid Itokawa. p. 1821
- Holsapple K., Giblin I., Housen K., Nakamura A., Ryan E., 2002, in Bottke W. F., Jr, Cellino A., Paolicchi P., Binzel R. P., Asteroids III. Univ. Arizona Press, Tuscan, AZ, p. 443
- Horstmann M., Bischoff A., 2014, *Chemie der Erde – Geochemistry*, 74, 149
- Horz F., Cintala M., 1997, *Meteorit. Planet. Sci.*, 32, 179
- Housen K. R., Holsapple K. A., 2011, *Icarus*, 211, 856
- Housen K. R., Holsapple K. A., Voss M. E., 1999, *Nature*, 402, 155
- Jenniskens P. et al., 2009, *Nature*, 458, 485
- Kenkmann T., Trullenque G., Deutsch A., Hecht L., Ebert M., Salge T., Schriber F., Thoma K., 2013, *Meteorit. Planet. Sci.*, 48, 150
- Kuebler K. E., Jolliff B. L., Wang A., Haskin L. A., 2006, *Geochim. Cosmochim. Acta*, 70, 6201
- McCord T. B. et al., 2012, *Nature*, 491, 83
- McSween H. Y., Mittlefehldt D. W., Beck A. W., Mayne R. G., McCoy T. J., 2011, *Space Sc. Rev.*, 163, 141
- Marsh S. P., 1980, *Los Alamos Series on Dynamic Material Properties*. University of California Press, London
- Michikami T., Moriguchi K., Hasegawa S., Fujiwara A., 2007, *Planet. Space Sci.*, 55, 70
- Moskovitz N. A., Jedicke R., Gaidos E., Willman M., Nesvorný D., Fevig R., Ivezić Ž., 2008, *Icarus*, 198, 77
- Nagaoka H., Takasawa S., Nakamura A. M., Sangen K., 2014, *Meteorit. Planet. Sci.*, 49, 69
- Nakamura T. et al., 2011, *Science*, 333, 1113
- O'Brien D. P., Sykes M. V., 2011, *Space Sci. Rev.*, 163, 41
- Olofsson J., Juhász A., Henning T., Mutschke H., Tamanai A., Moór A., Ábrahám P., 2012, *A&A*, 542, A90
- Petrovic J., 2001, *J. Mater. Sci.*, 36, 1579
- Petrovic J., 2003, *J. Mater. Sci.*, 38, 1
- Popova O., Borovička J., Hartmann W. K., Spurný P., Gnos E., Nemtchinov I., Trigo-Rodríguez J. M., 2011, *Meteorit. Planet. Sci.*, 46, 1525
- Price M., Solscheid C., Burchell M., Josse L., Adamek N., Cole M., 2013, *Icarus*, 222, 263
- Ranjith P. G., Viète D. R., Chen B. J., Perera M. S. A., 2012, *Eng. Geol.*, 151, 120
- Reddy V. et al., 2012, *Icarus*, 221, 544
- Russell C. T. et al., 2012, *Science*, 336, 684
- Schultz P. H., Gault D. E., 1984, in *Lunar and Planetary Science Conference, Vol. 15, Effects of Projectile Deformation on Cratering Efficiency and Morphology*. p. 730
- Schultz P. H., Gault D. E., 1990, *Geol. Soc. Am.*, 247, 239
- Schultz P. H., Ernst C. M., Anderson J. L. B., 2005, *Space Sci. Rev.*, 117, 207
- Schultz P. H., Eberhardy C. A., Ernst C. M., A'Hearn M. F., Sunshine J. M., Lisse C. M., 2007, *Icarus*, 190, 295
- Senft L. E., Stewart S. T., 2011, *Icarus*, 214, 67
- Spurný P., Haloda J., Borovička J., Šhrbený L., Halodová P., 2014, *A&A*, 570, A39
- Zolensky M. E. et al., 2006, *Science*, 314, 1735

This paper has been typeset from a $\text{\TeX}/\text{\LaTeX}$ file prepared by the author.

Kepler-210: An active star with at least two planets[★]

P. Ioannidis¹, J. H. M. M. Schmitt¹, Ch. Avdellidou², C. von Essen¹, and E. Agol³

¹ Hamburger Sternwarte, Universität Hamburg, Gojenbergsweg 112, 21029 Hamburg, Germany
e-mail: pioannidis@hs.uni-hamburg.de

² Centre for Astrophysics and Planetary Science, School of Physical Sciences (SEPnet), The University of Kent, Canterbury, CT2 7NH, UK

³ Dept. of Astronomy, Box 351580, University of Washington, Seattle WA 98195, USA

Received 6 September 2013 / Accepted 31 January 2014

ABSTRACT

We report the detection and characterization of two short-period, Neptune-sized planets around the active host star Kepler-210. The host star's parameters derived from those planets are (a) mutually inconsistent and (b) do not conform to the expected host star parameters. We furthermore report the detection of transit timing variations (TTVs) in the O–C diagrams for both planets. We explore various scenarios that explain and resolve those discrepancies. A simple scenario consistent with all data appears to be one that attributes substantial eccentricities to the inner short-period planets and that interprets the TTVs as due to the action of another, somewhat longer period planet. To substantiate our suggestions, we present the results of *N*-body simulations that modeled the TTVs and that checked the stability of the Kepler-210 system.

Key words. planetary systems – methods: data analysis – stars: individual: Kepler 210

1. Introduction

Since the launch of the *Kepler* Mission in 2009, a large number of planetary candidates has been found using the transit method in the high precision *Kepler* lightcurves. Specifically, 2321 planetary candidates in 1790 hosts stars have been reported, from which about one third are actually hosted in multiple systems (Batalha et al. 2013). The majority of these *Kepler* planetary candidates are expected to be real planets (Lissauer et al. 2012) and therefore those stars present an excellent opportunity for a more detailed study and characterization through the method of transit timing variations (TTVs). Ever since the first proposals of the method by Agol et al. (2005) and Holman & Murray (2005), TTVs have been widely used to search for smaller, otherwise undetectable planets in systems containing already confirmed planets. In multiple systems this method can be applied in order to confirm the physical validity of the system along with a rough estimate of the components' mass, which can otherwise be obtained only through radial velocity data. For the *Kepler* candidates the *Kepler* team has carried out and reported this kind of analysis for 41 extrasolar planet systems. For the last announcement of the series see Steffen et al. (2013).

In this paper we present our in-depth analysis and results for a particular system, Kepler-210 (=KOI-676), which was previously identified and listed as a planet host candidate in the catalog by Borucki et al. (2011). The specific characteristics of Kepler-210 that enticed us to perform a detailed study of this candidate system were the high activity of its host star coupled with the fact that the system harbors two transiting planets, which we validate using spectral and TTVs analysis, as well as stability tests.

[★] Tables 5–8 are only available at the CDS via anonymous ftp to cdsarc.u-strasbg.fr (130.79.128.5) or via <http://cdsarc.u-strasbg.fr/viz-bin/qcat?J/A+A/564/A33>

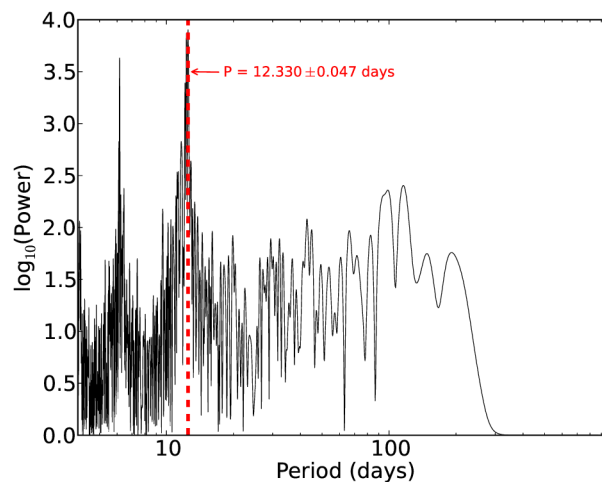


Fig. 1. Lomb-Scargle periodogram for the raw lightcurve as logarithmic power (on *y* axis) vs. period. A polynomial fit was applied to remove systematics related to the rotation of the telescope.

The plan of our paper is as follows. In the first section we describe the methods used to determine the stellar and planetary properties. In the second section we discuss various scenarios to explain the detected discrepancies in the orbital elements of the planets. Furthermore, we describe the results of our TTVs analysis for both planets, and finally, we summarize with what we believe is the most probable scenario.

2. Data analysis

2.1. Stellar activity

The *Kepler* data of Kepler-210 were obtained from the STDADS archive and contain the data recorded in the quarters Q1 to Q12.

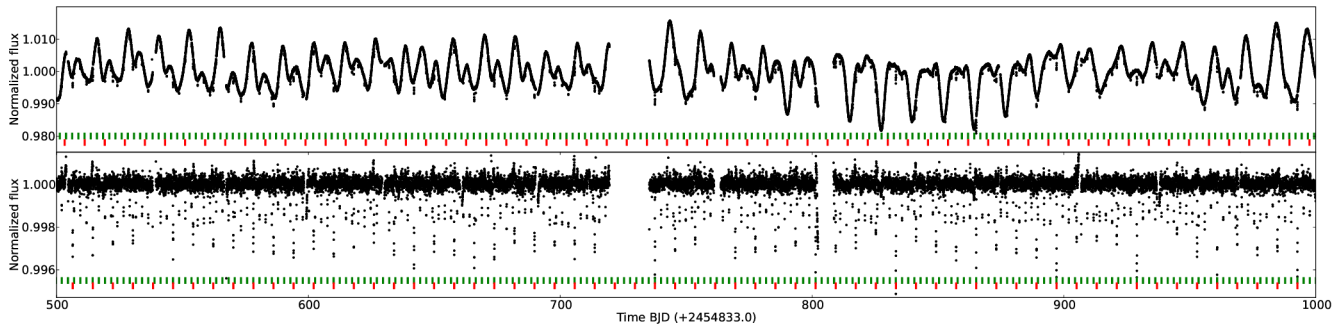


Fig. 2. Fraction of the Kepler-210 lightcurve. *Top*: part of the raw lightcurve demonstrating the activity of Kepler-210. *Bottom*: the transits of planet a (green) and b (red) for that particular time, with the stellar activity removed by using the `kepflatten` routine of the `Pyke` package for `pyraf`.

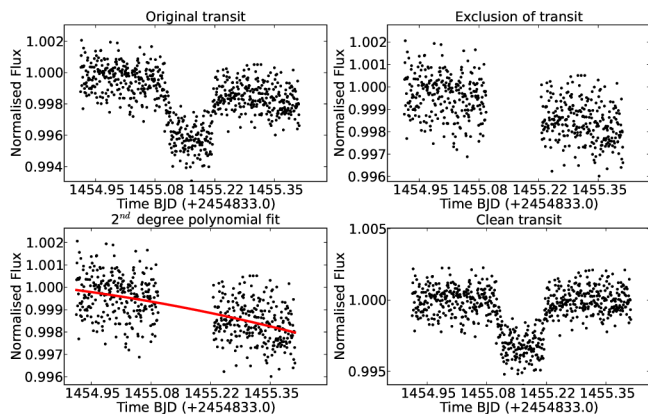


Fig. 3. Demonstration of stellar activity removal procedure; see text for details.

To achieve better temporal coverage we used both long and short cadence data. We decided to use the SAP data for our analysis to avoid any artifacts introduced by the use of SAP_PDC data, given the obvious complexity of the Kepler-210 lightcurve (cf., Fig. 2). Clearly, the host star of the Kepler-210 system is of particular interest by itself.

To give an impression of the activity of Kepler-210, a part of the overall *Kepler* lightcurve of Kepler-210 covering 500 days is shown in Fig. 2. Peak-to-peak variations on the order of 2% can easily be identified on time scales of a few days, and in addition, variations on longer time scales are also visible. To assess the dominant time scales of variability we computed a Lomb-Scargle periodogram over the full available data set, which we show in Fig. 1. Two peaks are clearly observable in the resulting periodogram. We interpret the most significant peak at 12.33 ± 0.15 days as the rotation period of the star, while the second, smaller peak at 6.15 ± 0.047 days is interpreted as an alias from the 12.33 day rotation period. We further note that both peaks are quite broad, with significant power residing at frequencies near the peak frequency.

2.2. Data preparation

For our transit and TTVs analysis we must remove all effects of stellar activity as much as possible. In order to rectify the *Kepler* lightcurve of Kepler-210 we proceed as follows: for each transit of each planet we select some part of the lightcurve centered at the estimated mid-transit time, including data points before and after ingress and egress, respectively (see Fig. 3, upper left). The obvious transit points are then removed (Fig. 3, upper right) and

Table 1. Stellar parameters of Kepler-210 taken from Batalha et al. (2013).

Kepler-210	
KIC-ID	7 447 200
KOI-ID	676
T_{eff}	4300 K
$\log g$	4.55
R_*	$0.69 R_{\odot}$
M_*	$0.63 M_{\odot}$
Linear LD	0.7181
Quadratic LD	0.0443

Notes. The limb-darkening coefficients were calculated for those values from Claret et al. (2012) for those parameters.

Table 2. MCMC analysis transit model fit results and their “ 1σ ” errors.

Planet	b	c
Period (d)	2.4532 ± 0.0007	7.9725 ± 0.0014
T_0 (LC)	134.0952 ± 0.0002	131.7200 ± 0.0002
R_{pl}/R_*	0.0498 ± 0.0004	0.0635 ± 0.0006
a/R_*	4.429 ± 0.077	11.566 ± 0.323
i	77.86 ± 0.26	85.73 ± 0.16
b	0.931 ± 0.038	0.861 ± 0.065
Transits	431 lc / 243 sc	97 lc / 51 sc

a second order polynomial fit is applied to the remaining data points (see Fig. 3 lower left). Finally, all selected data points including those obtained during transit are divided by the result of the polynomial fit (see Fig. 3 lower right) and we obtain a rectified lightcurve, normalized to unity for the data prior to the first and after the fourth contact. In this fashion we prepare the transit data for both planets for an application of our transit model fit; we consider only transits by one planet and exclude any simultaneous transits from our analysis.

2.3. Model fitting

The effects of the host star’s stellar activity are clearly visible also in the transit lightcurves, which are twofold: (see Fig. 2); star spots occulted by the planet on the one hand lead to bumps in the lightcurve as shown by Wolter et al. (2009), while star spots on the unocculted face of the star on the other hand lead to variable transit depths. Thus, both effects increase the dispersion of the transit data and the incorrect normalization leads to incorrect stellar and planetary parameters. In order to minimize

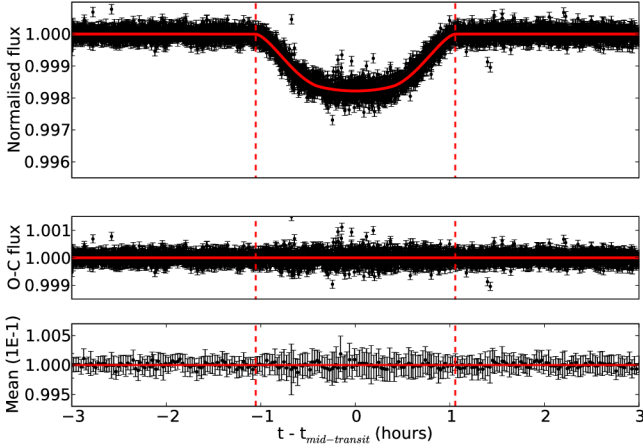


Fig. 4. Folded lightcurve of planet b, using the total number of transits and the best fit model. The lower diagram shows the model residuals and the best fit model, which in this case is less obvious than in case of planet c (see Fig. 5).

the effects of stellar activity we therefore decided to use transits, following the following two rules:

1. We select those transits occurring close to maximum flux in the activity modulations, which corresponds to smaller spot coverage of the stellar surface.
2. We model each transit separately, isolated the transit data and measure the χ^2 -test statistics. Only the transits with acceptable fits are selected.

Thus, for the transit model fit of the inner planet 89 transits were used, while for the outer planet a total of 10; we rejected 154 transits by the inner planet and 41 transits by the outer planet for this analysis. To determine the best fit model we used the analytical transit lightcurve model by Mandel & Agol (2002) and Markov-chain Monte-Carlo (MCMC) sampling¹ for the computation of the fit parameters and their errors. In this process we used the limb darkening coefficients for the model as calculated by integrating the values of the Claret catalog (Claret et al. 2012) for the parent star’s nominal parameters T_{eff} , $\log g$ and $[\text{Fe}/\text{H}]$ listed in Table 1.

2.4. Fit results

In Figs. 4 and 5 we show the full sample of the derived mean normalized *Kepler* transit lightcurves and our best fit model (red line; upper panel), the fit residuals for all data points (middle panel) and the mean values of the individual residuals as well as for blocks of twenty adjacent phase points (lower panel). The physical parameters derived from our transit analysis are listed in Table 2; note that the inner, shorter period planet is smaller than the outer planet.

3. Transit timing variations

3.1. Timing variation analysis

After completion of the transit model fit procedure and the determination of the global parameters for each planet, we recalculated the mid-transit times for all transits of each planet, i.e.,

¹ <http://www.hs.uni-hamburg.de/DE/Ins/Per/Czesla/PyA/PyA>

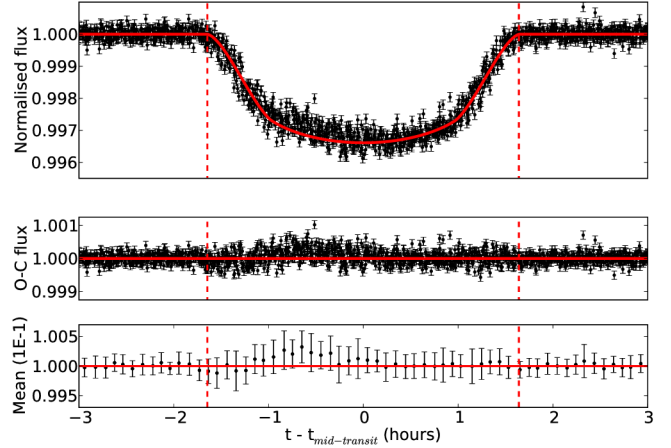


Fig. 5. Folded lightcurve of planet c, using the total number of transits and the best fit model. The transit profile is affected by spots during and after ingress.

also those that had been rejected for the best model fit. To that end we reapplied the MCMC fitting algorithm for every transit separately, keeping all model parameters fixed except for the individual mid-transit times $t_{\text{MT},i}$ $i = 1, N$. From the observed mid-transit times $t_{\text{MT},i}$, their errors σ_i and the integer transit epochs N_i we derived a mean period P and time reference T_0 , by minimizing the expression

$$\chi^2 = \sum_{i=1}^N \frac{(t_{\text{MT},i} - t_{\text{calc},i})^2}{\sigma_i^2} = \sum_{i=1}^N \frac{(t_{\text{MT},i} - P N_i - T_0)^2}{\sigma_i^2} \Rightarrow \quad (1)$$

$$\chi^2 = \sum_{i=1}^N \left(\frac{OC_i}{\sigma_i^2} \right)^2$$

with respect to P and T_0 ; the thus resulting O–C diagrams for planets b and c are shown in Fig. 6; the appropriate data for the creation of those diagrams are available at the CDS.

3.2. TTVs results

While in the O–C diagram of planet b (Fig. 6) some modulation is visible, no clear variation is apparent for planet c. In order to assess to what extent TTVs might be caused by stellar activity, as for example the observed anomaly in the ingress of the transit of planet b (Fig. 4), we calculated the transit times using two different approaches, additional to the one described in 3.1:

- We recalculated the transit times using the method described in 3.1, but by excluding the affected areas of the transit phase.
- We used the analysis described by Carter & Winn (2009) in order to remove the spot anomalies, considering them as red noise.

The results in both cases were almost identical, thus we decided to use for our analysis the transit times which were produced with the simplest method (Sect. 3.1). In addition we searched for correlations between the timing variations vs. the transit depth and duration, but in any case no correlations were found.

In order to quantify the significance of the observed O–C variations, we carried out a χ^2 -analysis on the null hypothesis that there are no timing variations, on the long and short cadence data separately and on the joined long and short cadence data. We also carried out the same analysis by averaging

Table 3. Null hypothesis χ^2 results with their P -values for the long cadence alone (left column) vs. the short cadence alone (middle column) and the combined long and short cadence data (right column) for unbinned and binned data. In the square brackets are listed the degrees of freedom.

	Long Cad.	Short Cad.	L & S Mix
b	430.6 (0.47) [430]	347.5 (>0.99) [242]	447.9 (0.71)
c	111.6 (0.77) [96]	138.7 (>0.99) [50]	185.2 (>0.99)
b_{bin}	61.2 (0.88) [43]	63.5 (>0.99) [24]	47.5 (0.67)
c_{bin}	51.9 (>0.99) [10]	76.1 (>0.99) [5]	67.9 (>0.99)

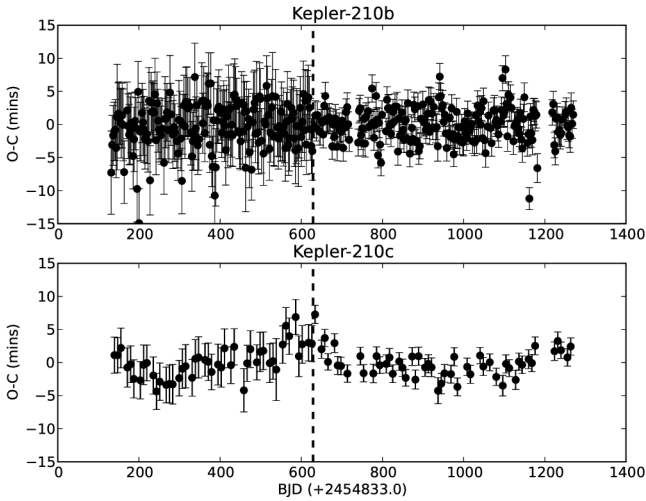


Fig. 6. O–C diagrams of planet b (upper panel) and c (lower panel), along with the best fit models. The dashed line discriminates the long from the short cadence data.

the measured O–C values over ten consecutive epochs; the respective χ^2 -values and the derived significance levels are listed in Table 3.

An inspection of Table 3 shows that the unbinned long cadence data show no evidence for any non-zero O–C values, while the short cadence data do; binning does greatly increase the significance of the non-zero O–C values.

Since the values of the χ^2 -test statistics sensitively depend on the measurement errors σ_i , we carefully checked the errors of the derived mid-transit times by using two independent methods and convinced ourselves of the internal consistency of our error determination. In addition we checked that the derived χ^2 -values are not produced by a few individual outliers. As a result we are confident that the observed TTVs are statistically significant.

4. Discussion

4.1. Examination of stellar properties

In order to better determine the stellar parameters of Kepler-210, a high resolution spectrum was acquired, using the CAFE instrument on the 2.2 m telescope of the Calar Alto Observatory in Spain. For our analysis we also used two spectra of Kepler-210, taken from the CFOP² web page. We specifically inspected the spectra for a second set of lines indicating the existence of a close unresolved companion but found none. For the same purpose we also examined the pixel area around the star using the

² <https://cfop.ipac.caltech.edu>

Kepler target fits frames, but found again no evidence of any variable star in the vicinity of the central star that could create a contaminating signal.

To measure the color index $B - V$, we observed Kepler-210 together with two standard stars (HD 14827 and HD 195919), using the 1.2 m *Oskar-Lühning*-Telescope (OLT) from Hamburg Observatory and found $B - V_{\text{Kepler-210}} = 1.131 \pm 0.064$, consistent with the color derived from CFOP (1.088 ± 0.037) and other sources; thus the spectral type of Kepler-210 is in the late K range.

We then proceeded to estimate the stars age using the gyrochronology expression 2 derived by Barnes (2007)

$$\log(t_{\text{gyro}}) = \frac{1}{n} \{ \log(P) - \log(\alpha) - [\beta \cdot \log(B - V - 0.4)] \}, \quad (2)$$

where t is in Myr, $B - V$ is the measured color, P (in days) is the rotational period, $n = 0.5189$, $\alpha = 0.7725 \pm 0.011$ and $\beta = 0.601 \pm 0.024$. By using Eq. (2) with $P = 12.33$ days and the $B - V = 1.131$, we estimate an age of 350 ± 50 Myrs for Kepler-210; this estimate appears reasonable given its high degree of activity.

4.2. Mean stellar density

When a planet is transiting in front of its parent star, we have the opportunity to accurately derive the ratio between the stellar radius R_\star and the orbital semimajor axis a (cf., Table 2). Combining this information with Kepler's third law, we can compute an expression for the mean density ρ_{mean} of the host star through

$$\rho_{\star, \text{mean}} = \frac{3\pi}{G} \frac{a^3}{R_\star^3 P^2}, \quad (3)$$

with G denoting the gravitational constant in addition to the terms containing only the observed quantities a/R_\star and period P . The value for a/R_\star is derived from the transit modeling, given the large number of transits, for both planets, the values of a/R_\star and P can be estimated with relatively high accuracy. Carrying out this computation using the observed parameters for planets b and c (cf., Table 2) we obtain densities of $\rho_{\star, b} = 0.27 \pm 0.004 \text{ g/cm}^3$ and $\rho_{\star, c} = 0.46 \pm 0.038 \text{ g/cm}^3$, respectively for the host. On the other hand, based on the nominal stellar parameters of the host star we expect a mean density of $\rho_o \approx 2.6 \text{ g/cm}^3$. Thus the mean host star densities derived from planets b and c are, first, inconsistent with each other, and second, differ by almost an order of magnitude from the expected host star density. Since we firmly believe in Kepler's third law, there must be a physical explanation for both discrepancies.

4.2.1. Ellipticity of planetary orbits

So far our analysis has implicitly assumed circular orbits for both planets. For elliptical orbits the orbital speed and hence the transit duration change during the orbit and therefore there is no unique relation between transit duration and stellar and planetary dimensions. Assuming that the orbital velocity is constant during the actual transit, Tingley & Sackett (2005) relate the transit duration D_{ell} to the period P and the impact parameter b of a transit through the expression

$$D_{\text{ell}} = \frac{\sqrt{(1 - e^2)}}{1 + e \cdot \cos(\phi_t)} \frac{P}{\pi} \frac{\sqrt{((R_\star + R_{\text{pl}})^2 - b^2)}}{a}, \quad (4)$$

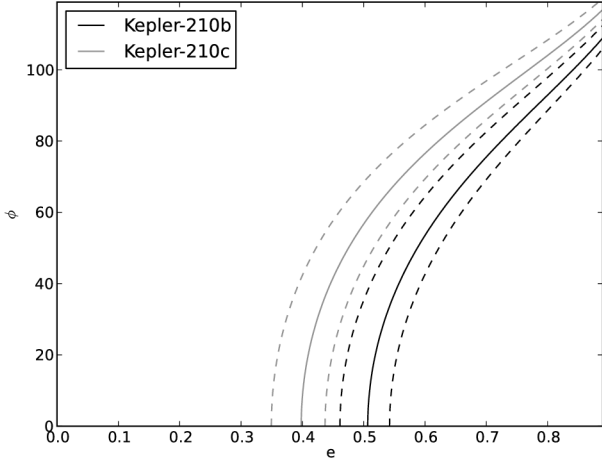


Fig. 7. Contour plot of eccentricity versus true anomaly during the mid-transit (ϕ). For a circular system ($e = 0$) the density should equal $\varrho_o \simeq 2.6 \text{ g/cm}^3$, as can be calculated for the given values of R_\star and M_\star . The TBD derived from the a/R_\star values of ϱ_\star for the planets Kepler-210b (black line) and Kepler-210c (gray line) can be explained for eccentricities $\gtrsim 0.4$ and $\gtrsim 0.51$ respectively, depending on the true anomaly of the planet during the mid-transit. The dashed lines represent the uncertainty limits.

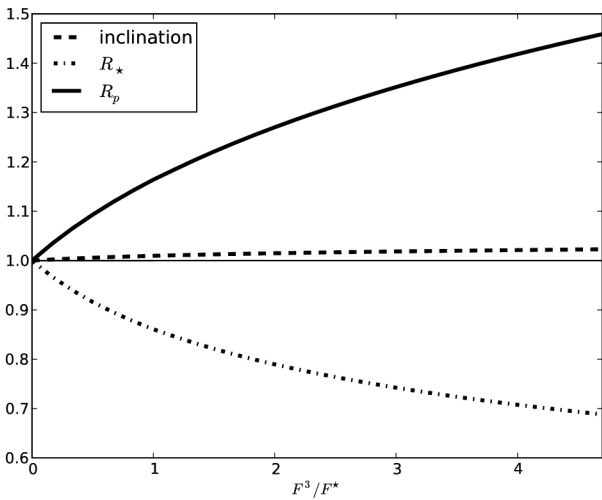


Fig. 8. Variation of inclination, R_\star and R_p , assuming third light interference F^3 for Kepler-210c.

where ϕ_t denotes the true anomaly at the mid-transit, while R_\star , R_p and a , denote stellar and planetary radii and semi-major axis respectively. Consequently, the transit duration D_{ell} of an elliptical orbit scales with the transit duration D_{circ} of a circular orbit (for the same system geometry and the same period) through

$$D_{\text{ell}} = \frac{\sqrt{1-e^2}}{1+e \cdot \cos(\phi_t)} \times D_{\text{circ}} = g(e, \cos(\phi_t)) \times D_{\text{circ}}. \quad (5)$$

It is straightforward to convince oneself that the derived sizes for star and planet scale with the scaling function $g(e, \cos(\phi_t))$ introduced in Eq. (5). Since the mean stellar density scales with R_\star^3 , we find

$$\varrho_{\star, \text{ell}} = \varrho_{\star, \text{circ}} \cdot \left(\frac{\sqrt{1-e^2}}{1+e \cdot \cos(\phi_t)} \right)^{-3} \quad (6)$$

with $\varrho_{\star, \text{circ}} = \varrho_{\star, \text{mean}}$ from Eq. (3). Hence the discrepant stellar densities can be explained by introducing suitable eccentricities

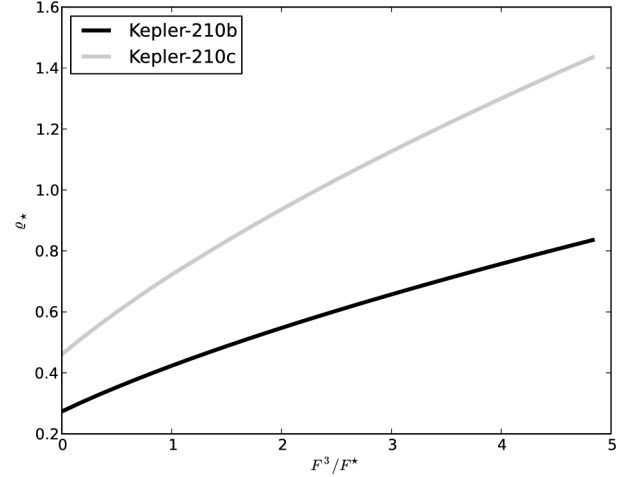


Fig. 9. Derived stellar density versus assumed third light contribution F^3 .

and true transit anomalies. By solving 6 for different values of e and ϕ_t it is thus possible to constrain the range of permissible eccentricities as well as values for ϕ_t , for which the derived stellar density becomes equal to the density expected for the spectral type of the star for both planets; the corresponding curves are shown in Fig. 7, where we plot for each planet the combination of e and ϕ_t resulting in a nominal stellar density of 2.7 g cm^{-3} . Figure 7 shows that eccentricities of 0.4 (for planet b) and 0.5 (for planet c) are required to produce the expected stellar densities.

4.2.2. Second (third) light scenario

Despite the fact that neither the optical spectrum nor the centroid analysis of the *Kepler* data have shown any evidence for a companion or blend, it might still be possible that some third object in the background or foreground with flux F_3 contributes to the system flux in a way that the observed total flux F_{obs} is given by

$$F_{\text{obs}} = F^\star + F_3, \quad (7)$$

where F^\star is the desired planet host's flux, which has to be used for the transit modeling. If this hypothetical third light contribution F_3 is substantial, the true transit depth d_{true} would be underestimated and an incorrect radius for the Kepler-210 host star would be derived. Assuming that the limb darkening coefficients are identical and equal to the values presented in Table 1 for all system sources, we calculate the influence of the third light source on the derived stellar density (as shown in Fig. 9), considering the following non-linear system of equations, which allows computing the stellar and planetary radii (each scaled by the semi-major axis) \tilde{R}_\star and \tilde{R}_p and, i , the inclination of the orbit normal with respect to the line of sight, given the observed period P , the observed time between the first and fourth contact, T_{14} , the time between the second and third contact, T_{23} and the observed (relative) transit depth at mid-transit d_{obs} .

$$\sin^2 i \cos^2 \left(\frac{\pi}{P} T_{14} \right) = 1 - (\tilde{R}_\star + \tilde{R}_p)^2 \quad (8)$$

$$\sin^2 i \cos^2 \left(\frac{\pi}{P} T_{23} \right) = 1 - (\tilde{R}_\star - \tilde{R}_p)^2 \quad (9)$$

and

$$d_{\text{true}} = \frac{(1 - c_1 - c_2) + (c_1 + 2c_2) \mu_c - c_2 \mu_c^2}{1 - \frac{c_1}{3} - \frac{c_2}{6}} \left(\frac{\tilde{R}_p}{\tilde{R}_\star} \right)^2. \quad (10)$$

Here c_1 and c_2 denote the quadratic limb darkening coefficients and μ_c denotes the expression

$$\mu_c = \sqrt{1 - \frac{\cos^2 i}{\tilde{R}_\star^2}}. \quad (11)$$

We clearly need the true transit depth d_{true} to compute the values of \tilde{R}_\star , \tilde{R}_p and i , yet only the observed transit depth d_{obs} is available; the two depths are related, however, through

$$d_{\text{true}} = (1 + d_{\text{obs}}) \frac{F_3}{F_\star}. \quad (12)$$

Therefore, given the observed values of d_{obs} , T_{14} and T_{23} and the observed periods P for both planets, the derived values for \tilde{R}_\star and hence ϱ_\star will depend on the assumed third light contribution F_3/F_\star . The resulting system of equation is quite non-linear. In order to provide a feeling on how sensitive the solutions depend on the third light contribution F_3/F_\star , we plot in Fig. 8 the variation of the derived values for the inclination and stellar and planetary radii (for the planet Kepler-210c), relative to the case of no third light. As is clear from Fig. 8, the inclination increases only slightly (it cannot exceed 90 degrees), while the stellar radius decreases (as desired) and the planetary radius increases. Finally, we can derive the stellar density, for which our results are shown in Fig. 9, where we plot the derived stellar densities for both planets as a function of the assumed third light contribution $\frac{F_3}{F_\star}$. As is clear from Fig. 9, the third light contribution would have to be substantial, and in fact the third light would have to dominate the total system flux in order to obtain values of $\varrho_{\star c}$ as expected for stars on the main sequence in the relevant spectral range. Yet, the two planets still yield discrepant densities of their host, so one would have to introduce yet another host for the second planet, which appears at least a little contrived. Therefore we conclude that the introduction of a third light source does not lead to a satisfactory solution of inconsistency in the derived stellar parameters.

4.2.3. Inflated star

Another possible scenario explaining the *Kepler* observations of Kepler-210 would be the assumption that the host is not on the main sequence, but rather evolved and in fact a giant or sub-giant. Such stars are usually not active, however, there are some classes of evolved stars which are quite active, for example, variables of the FK Com type. Those stars are highly active G-K type sub-giant stars with surface gravities $\log(g)$ of ~ 3.5 . They show strong photometric rotational modulations caused by a photosphere covered with inhomogeneously distributed spots. An other important characteristic of these objects is their rapid rotation. Generally the $v \sin i$ derived from their spectra is between ~ 50 and 150 km s^{-1} (Berdyugina 2005). In the case of Kepler-210 $v \sin i$ is $\sim 4 \text{ km s}^{-1}$, and thus we believe that a FK-com scenario does not provide a suitable explanation for the observed density discrepancy.

4.3. Kepler-210 TTVs

As described in Sect. 3, TTVs are detected in both planets. In order to further examine the properties of these variations we searched for any periodicities in the O–C data by constructing a Lomb-Scargle periodogram on every set. For the outer and larger planet, the Lomb-Scargle periodogram shows a leading period of about 690 days, which is apparent in the modulation

Table 4. χ^2 results of the model for 2 eccentric planets hypothesis, 3 non eccentric planets and 3 eccentric planets.

	2 ecc planets	3 non ecc planets	3 ecc planets
b	489.57 [420]	447.9 [415]	443.9 [415]
c	116.22 [86]	112.4 [81]	117.59 [81]

Notes. In the square brackets are listed the degrees of freedom.

of the O–C curve in Fig. 6, while for the inner and smaller planet the periodicity results remain ambiguous, most probably due to the large scatter in its O–C diagram.

What would be a physical scenario consistent with these O–C diagrams? We first note that the orbital period ratio of the system is very close to a 13/4, if we consider that the errors in periods in Table 2 are also affected by the TTVs. This ratio is not close to any low order mean motion resonance so the amplitude of any TTVs is expected to be relatively small for both planets (Agol et al. 2005).

In order to verify this and to model the TTVs we use the N -body code as presented in the same paper. The N -body code requires the planetary masses which are unknown. Assuming ad hoc that the planetary densities are below 5 g/cm^3 , it is clear that the masses of the two planets are substantially below $0.5 M_J$. Furthermore, in order to roughly estimate the planetary masses below that limit, we use a general mass vs. radius law as described by Lissauer et al. (2011) in the form

$$M_p = R_p^{2.06}. \quad (13)$$

With the masses thus specified, we first considered only the two transiting planets for our TTVs simulations. Assuming non-eccentric orbits resulted in TTVs of less than a minute, which is far from the observed variations for both planets. The TTVs would remain in that state even if we assume higher masses, under the limit of $12 M_J$. As discussed in detail by Lithwick et al. (2012), the TTVs amplitude can also be affected by eccentricity. Implementation of eccentric orbits for both planets, Kepler-210b and Kepler-210c, improved the fit substantially; the modeled TTVs together with the data are shown in Fig. 10, the fit results in terms of fit quality measured through χ^2 are given in Table 4.

Clearly, also the TTVs analysis supports a scenario of two planets with rather eccentric orbits similar to our discussion in 4.2.1. However, in order to produce the observed TTVs the system configuration must be such that the true anomaly, of both planets at the time of transit, ϕ_t , should exceed 40° , while also the difference in true anomaly $\Delta\phi_t$ should be $\sim 60^\circ$. However, this configuration appears impossible due to the physical constraints in Fig. 7. Furthermore, our stability tests, which performed with the swift_rmvs3 algorithm (Levison & Duncan 1994), show that this configuration is unstable on time scales in excess of ~ 1 Myear. Finally we note that the probability of observing a transit is higher for small values of true anomaly, i.e., for the times near periastron passage.

We therefore conclude that a scenario with only two planets with eccentric orbits is unlikely and introduce a third, hypothetical planet KOI-676.03 in order to stabilize the system. We consider both eccentric and non-eccentric orbits for Kepler-210b and Kepler-210c. In order to determine period, mass and eccentricity for the hypothetical planet KOI-676.03, we considered several possible system configurations.

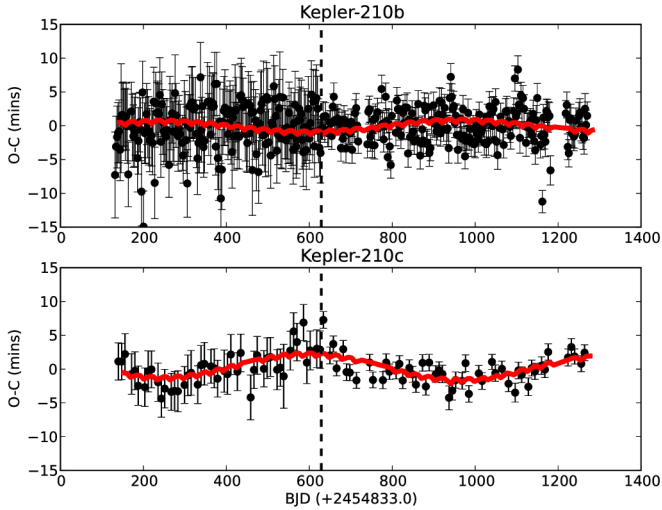


Fig. 10. TTVs expected for two planets assuming eccentric orbits with $e_b = 0.44$ and $e_c = 0.50$.

We emphasize that we cannot derive a unique solution for the physical parameters of this hypothetical planet. Most importantly, we need to assume a mass for this planet, which controls the strength of the gravitational interaction with the observed planets Kepler-210b and Kepler-210c. Thus, given the observed TTVs amplitude and given the assumed mass of KOI-676.03, a certain value of semi-major axis and hence period is derived. The higher the assumed mass, the longer the resulting period, and thus there is more than one configuration to account for the detected TTVs signal.

In order to produce possible candidate systems, we carried out simulations assuming some given mass for KOI-676.03, considering periods between 20 to 300 days, masses in the range $M_{03} \sim 0.1\text{--}0.6 M_J$ and eccentricities $e \approx 0.1\text{--}0.3$. A particularly promising configuration, but by no means unique solution, consistent with all *Kepler* data, has a period $P \approx 63$ days; in Fig. 11 and again Table 4 (for the case with zero eccentricity) and in Fig. 12 and Table 4 (for the eccentric case) we show that such a scenario provides results consistent with the available *Kepler* data. As is clear from Figs. 11 and 12, as well as Table 4, the difference between the non-eccentric and eccentric case is marginal at best, while (statistically) preferable over a two planets scenario. In addition, the eccentricities of the planets Kepler-210b and Kepler-210c give a high frequency TTVs signal, which might better explain the higher dispersion of the TTVs in Kepler-210b. In that case the model also suggests ϕ_t values around zero with $\Delta\phi < 30^\circ$, which are in line with Fig. 7. Also the system's stability exceeds 10^7 years.

In the case of non eccentric orbits the system would reach fatal instability once masses above $5 M_J$ are chosen. For eccentric orbits the upper limit for the masses of the system becomes lower. While this fact suggests a planetary nature of the system components, it also introduces an additional factor of concern about the long term stability of the system. We do point out that this third stabilizing planet does produce a radial velocity signal in the system. For our nominal case we plot in Fig. 13 the expected RV signal in a synthetic radial velocity diagram, which shows peak-to-peak variations in excess of 60 m/s; clearly such RV variations ought to be detectable despite the high activity level of the host star, and therefore, the detection of a RV-signal

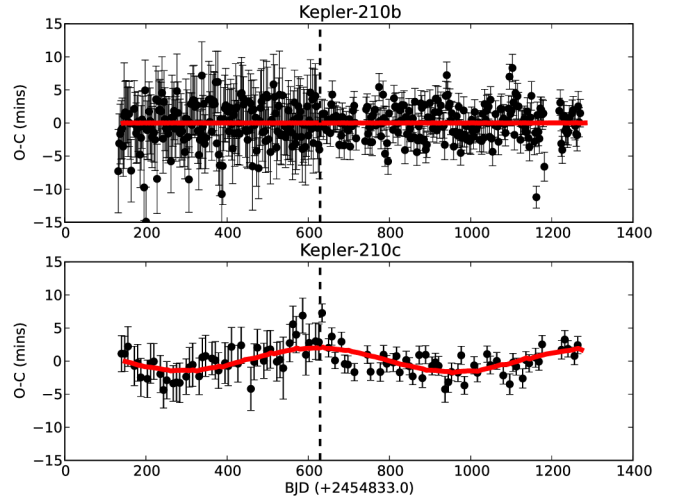


Fig. 11. TTVs expected for three planets with non-eccentric orbits for all components of the system. The third planet's period for that case is $P_{03} = 63.07$ days.

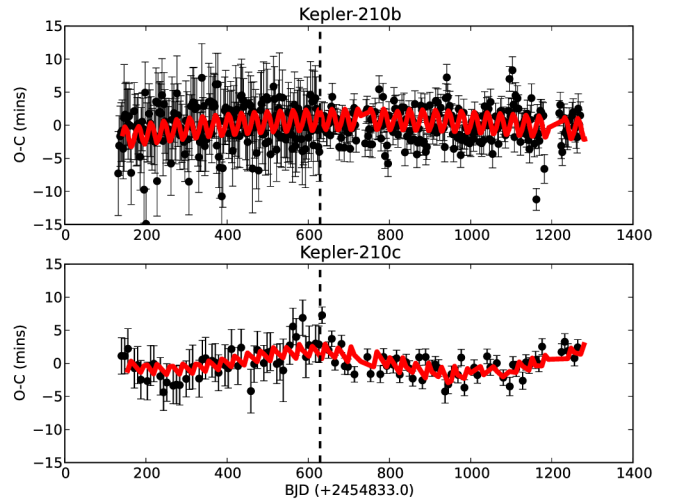


Fig. 12. TTVs expected for three planets assuming eccentric orbits with $e_b = 0.45$, $e_c = 0.51$ and $e_{03} = 0.23$. The Third planet's period for that case is $P_{03} = 63.29$ days.

would significantly constrain the possible configuration space of the system.

5. Summary

We report the detection and characterization of two transiting Neptune-sized planets, Kepler-210b and Kepler-210c with periods of 2.4532 days and 7.9723 days respectively around a presumably quite young and active K-type dwarf. These objects were first listed as planetary candidates by the *Kepler* team. We show that the transits of both planets are affected by spots. From the observed transit parameters and in particular from the observed value of a/R_* it is possible to calculate the mean density of the host star using the Kepler's 3rd law. Interestingly, the two planets yield discrepant mean host star densities, which in addition are inconsistent with the densities expected for a K-type dwarf. Having explored various scenarios we conclude that the assumption of quite eccentric orbits for both planets provides the currently most probable scenario.

In addition, both planets show transit timing variations. Using *N*-body simulations we constructed possible system

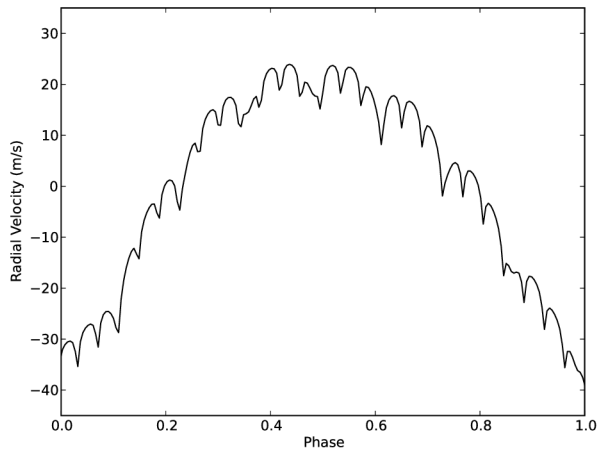


Fig. 13. Predicted, synthetic, radial velocity diagram for the system Kepler-210 for $P_{03} = 63$ days, $M_{03} = 0.4 M_J$, $e_{03} = 0.23$ and $i_{03} = 60^\circ$.

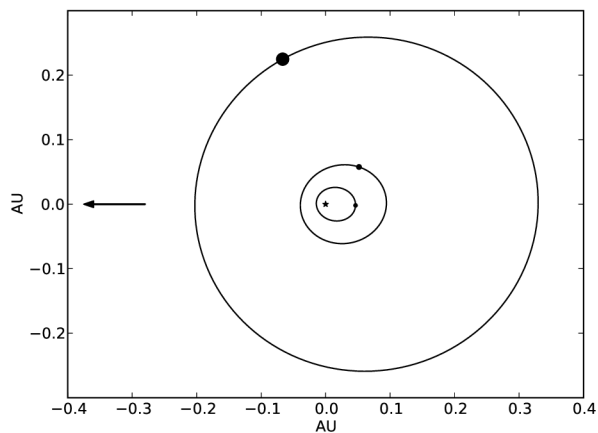


Fig. 14. Suggested system configuration. The earth is at the direction of the arrow.

configurations consistent with the *Kepler* data. While it is possible to explain the observed TTVs with a two planet scenario,

such a scenario requires a very special geometrical configuration and is unstable on time scales of 10^6 years. As a result we believe that there exists a third planet, KOI-676.03, with a mass between $\sim 0.3\text{--}0.6 M_J$ in a slightly eccentric ($e \simeq 0.2$) orbit with period ~ 63 days, which stabilizes the whole Kepler-210 planetary system.

Different configurations are also possible, yet this stabilizing hypothetical planet should produce a detectable RV signal. We therefore suggest RV monitoring of Kepler-210, which is likely to provide a substantially increased insight into the Kepler-210 planetary system.

Acknowledgements. P.I. and C.v.E. acknowledge funding through the DFG grant RTG 1351/2 “Extrasolar planets and their host stars”. The results of this publication are based on data collected by the NASA’s *Kepler* satellite. We would like to thank the director and the Calar Alto Observatory staff for the approval and execution of a DDT proposal. Finally we acknowledge the exceptional work by the CFOP team which was essential for this publication.

References

- Agol, E., Steffen, J., Sari, R., & Clarkson, W. 2005, *MNRAS*, 359, 567
 Barnes, S. A. 2007, *ApJ*, 669, 1167
 Batalha, N. M., Rowe, J. F., Bryson, S. T., et al. 2013, *ApJS*, 204, 24
 Berdyugina, S. V. 2005, *Liv. Rev. Sol. Phys.*, 2, 8
 Borucki, W. J., Koch, D. G., Basri, G., et al. 2011, *ApJ*, 736, 19
 Carter, J. A., & Winn, J. N. 2009, *ApJ*, 704, 51
 Claret, A., Hauschildt, P. H., & Witte, S. 2012, *VizieR Online Data Catalog*, J/A+A/546/A14
 Holman, M. J., & Murray, N. W. 2005, *Science*, 307, 1288
 Levison, H. F., & Duncan, M. J. 1994, *Icarus*, 108, 18
 Lissauer, J. J., Ragozzine, D., Fabrycky, D. C., et al. 2011, *ApJS*, 197, 8
 Lissauer, J. J., Marcy, G. W., Rowe, J. F., et al. 2012, *ApJ*, 750, 112
 Lithwick, Y., Xie, J., & Wu, Y. 2012, *ApJ*, 761, 122
 Mandel, K., & Agol, E. 2002, *ApJ*, 580, L171
 Steffen, J. H., Fabrycky, D. C., Agol, E., et al. 2013, *MNRAS*, 428, 1077
 Tingley, B., & Sackett, P. D. 2005, *ApJ*, 627, 1011
 Wolter, U., Schmitt, J. H. M. M., Huber, K. F., et al. 2009, *A&A*, 504, 561